

NASA
Technical Memorandum 107170

Army Research Laboratory
Technical Report ARL-TR-971

Crack Propagation Studies to Determine Benign or Catastrophic Failure Modes for Aerospace Thin-Rim Gears

David G. Lewicki
Vehicle Propulsion Directorate
U.S. Army Research Laboratory
Lewis Research Center
Cleveland, Ohio

DTIC QUALITY INSPECTED 4

May 1996



National Aeronautics and
Space Administration

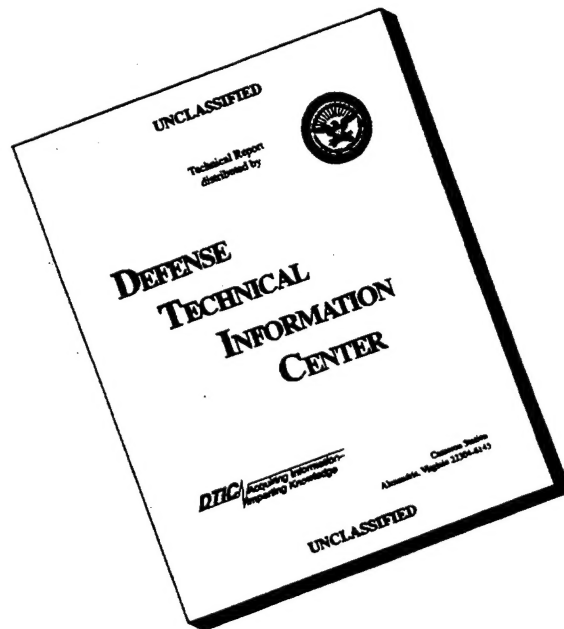
19960821 000



DISTRIBUTION STATEMENT A

Approved for public release;
Distribution Unlimited

DISCLAIMER NOTICE



**THIS DOCUMENT IS BEST
QUALITY AVAILABLE. THE
COPY FURNISHED TO DTIC
CONTAINED A SIGNIFICANT
NUMBER OF PAGES WHICH DO
NOT REPRODUCE LEGIBLY.**

CRACK PROPAGATION STUDIES TO DETERMINE BENIGN OR CATASTROPHIC FAILURE MODES FOR AEROSPACE THIN-RIM GEARS

DAVID G. LEWICKI
Vehicle Propulsion Directorate
U.S. Army Research Laboratory
NASA Lewis Research Center
Cleveland, Ohio 44135

ABSTRACT

Analytical and experimental studies were performed to investigate the effect of rim thickness on gear tooth crack propagation. The goal was to determine whether cracks grew through gear teeth (benign failure mode) or through gear rims (catastrophic failure mode) for various rim thicknesses. Gear tooth crack propagation was simulated using a finite element based computer program. Principles of linear elastic fracture mechanics were used. Quarter-point, triangular elements were used at the crack tip to represent the stress singularity. Crack tip stress intensity factors were estimated and used to determine crack propagation direction and fatigue crack growth rate. The computer program used had an automated crack propagation option in which cracks were grown numerically using an automated re-meshing scheme. In addition, experimental studies were performed in the NASA Lewis Spur Gear Fatigue Rig. Gears with various backup ratios were tested to validate crack path predictions. Also, specialized crack propagation gages were installed on the test gears to measure gear tooth crack growth rate. From both predictions and tests, gears with backup ratios (rim thickness divided by tooth height) of 3.3 and 1.0 produced tooth fractures while a backup ratio of 0.3 produced rim fractures. For a backup ratio of 0.5, the experiments produced rim fractures and the predictions produced both rim and tooth fractures, depending on the initial crack conditions. Good correlation between the predicted number of crack propagation cycles and measured number of cycles was achieved using both the Paris fatigue crack growth method and the Collipriest crack growth equation when fatigue crack closure was considered.

TABLE OF CONTENTS

	Page
Chapter 1: Introduction	
1.1 Background	1
1.2 Current Gear Analysis Methods	1
1.3 Analysis of Thin-Rim Gears	3
1.4 Introduction to Fracture Mechanics	4
1.5 Fracture Mechanics Applied to Gear Teeth	5
1.6 Dissertation Objective and Outline	6
 Chapter 2: Fundamentals of Fracture Mechanics	
2.1 Introduction	8
2.2 Stress Intensity Factors	8
2.3 Crack Propagation Directions	10
2.4 Crack Propagation Fatigue Crack Growth	13
2.5 FRANC Computer Program	15
 Chapter 3: Crack Propagation Modeling of Gears	
3.1 Introduction	17
3.2 Gear Modeling	17
3.3 Mesh Refinement	19
3.4 Gear Tooth Crack Propagation Modeling Using FRANC	19
3.5 Effects of Gear Tooth Load Position on Crack Propagation Direction	21
3.6 Effect of Rim Thickness on Crack Propagation	23
3.7 Fatigue Crack Growth of Gear Teeth	24
 Chapter 4: Experimental Studies	
4.1 Introduction	27
4.2 Test Facility	27
4.3 Test Gears	27
4.4 Instrumentation	28
4.5 Test Procedure	30
4.6 Test Results	30
 Chapter 5: Comparison of Experiments With Analysis	
5.1 Introduction	34
5.2 Modeling of Test Gears	34
5.3 Crack Path Comparison	35
5.4 Crack Propagation Life Comparison	36
5.5 Crack Initiation Life and Total Life	38
 Chapter 6: Gear Parametric Studies	
6.1 Introduction	40
6.2 Model Description	40
6.3 Analytical Results	40
 Chapter 7: Conclusions	43

Appendices	
A Nomenclature	45
B Load Vector Orientation	49
C Notch Modeling	51
 Bibliography	 52
 Tables	 58
 Figures	 70

CHAPTER 1: INTRODUCTION

1.1 Background. For aircraft applications such as helicopters or turboprops, one design goal for the gears in power transmissions is to reduce weight. To help meet this goal, some gear designs incorporate thin rims. Rims that are too thin, however, may lead to bending fatigue problems. Gear tooth bending fatigue is a failure mode in which a tooth cracks due to the repeated application of load. Depending on the geometry and load on the gear or the severity of the defect, a crack may propagate through a tooth or into the rim. In aircraft applications, a crack which propagates through a tooth would probably not be catastrophic and ample warning of a failure could be possible. On the other hand, a crack which propagates through the rim would be catastrophic and could lead to disengagement of a rotor or propeller from an engine, loss of an aircraft, and fatalities.

Gear tooth bending fatigue can usually be prevented with proper tooth design. Possible causes of gear tooth or rim fatigue failures where the tooth design itself is adequate are insufficient rim thickness in the design, a bad batch of material containing inclusions where cracks can initiate, severe operating conditions such as overload or misalignment, operation near the resonant frequency of a gear structure, or localized wear such as fretting at a gear-shaft connecting joint which could initiate a crack. A tragic example of a gear rim fatigue failure is shown in Figure 1.1.1 (McFadden, 1985). A helicopter of the Royal Australian Navy crashed due to a failure of the input spiral-bevel pinion in the main-rotor gearbox. Metallurgical investigations revealed that the pinion failed due to a fatigue crack which started at a subsurface inclusion near the root of one of the teeth. The crack then propagated through the rim of the gear and caused a catastrophic failure.

Additional examples related to gear rim failures are given by Albrecht (1988). A failure due to insufficient gear rim design is described where a fatigue crack initiated in the tooth root area and propagated through the rim. Also described is an example of a gear resonant failure where a failure initiated at the gear-to-shaft spline joint and the crack propagated due to the gear operating at a resonance condition with insufficient damping (Figure 1.1.2).

Couchan, et al. (1993) describes a failure of the main drive gear in a turboprop gearbox. An analysis of the gear led to the theory that the gear failed due to extensive misalignment caused by a failed pinion bearing. The misalignment caused stresses above the gear material yield stress and initiated a crack in the tooth root. The crack then propagated from the loads during normal operation. The crack propagated through the rim and caused catastrophic damage.

It should again be emphasized that a crack which progresses through only a tooth and not the rim can many times be detected before extensive damage would occur. However, if the crack goes through the rim, catastrophic failures and loss of aircraft may occur. A design tool to predict the orientation of crack growth of gears, especially thin-rim gears, would be extremely useful to increase the safety of current and future configurations.

1.2 Current Gear Analysis Methods. The most common methods of gear design and analysis are based on standards published by the American Gear Manufacturers Association (AGMA). Included in the standards are rating formulas for gear tooth bending. The fundamental bending stress index for spur and helical gears is (AGMA, 1990)

$$s_t = \frac{W_t K_a}{K_v} \frac{P_d}{f} \frac{K_s K_m K_B}{J} \quad (1.2.1)$$

where

- s_t = bending stress index, psi
- W_t = tangential load, lb
- K_a = application factor
- K_v = dynamic factor
- P_d = diametral pitch, teeth/in
- f = face width, in
- K_s = size factor
- K_m = load distribution factor
- K_B = rim thickness factor
- J = geometry factor

The bending stress index is related to the allowable stress index by

$$s_t \leq \frac{s_{at} K_L}{K_T K_R} \quad (1.2.2)$$

where

- s_{at} = allowable bending stress index, psi
- K_L = life factor
- K_T = temperature factor
- K_R = reliability factor

The rim thickness factor, K_B , considers the effect of the gear blank rim thickness on the load carrying capacity of the gear tooth. It is shown in Figure 1.2.1 and is based on the analysis of Drago (1982). The rim thickness factor is a function of the backup ratio, m_B , where

$$m_B = \frac{b}{h} \quad (1.2.3)$$

where

- b = rim thickness, in
- h = tooth whole depth, in

For backup ratios less than 1.2, the rim thickness factor adjusts the bending stress index to account for the increased stress in the gear rim blank of thin-rim gears. The factor was determined by photoelastic experiments and finite element analysis of thin-rim gears. More details of the stress analysis of thin-rim gears are described in the following section (1.3 Analysis of Thin-Rim Gears).

The AGMA standard for vehicle spur and helical gears (AGMA, 1976) and aircraft engine and power take-off spur and helical gears (AGMA, 1974a) recommends that the backup ratio should be at least 0.75 for external gears with webs and at least 1.0 for webless external gears. The standard for aircraft engine and power take-off spiral-bevel gears (AGMA, 1974b) recommends a backup ratio at of at least 0.8. These standards use similar formulas as in Equations 1.2.1 and 1.2.2 for tooth bending stress indexes. The standards do not give any indication of crack propagation path. In fact, no gear analysis design tool currently exists which can predict whether a crack will propagate through a tooth or through the rim.

1.3 Analysis of Thin-Rim Gears. A number of researchers have investigated the effects of thin rims on gear stress. These studies included analysis using the finite element method (FEM), experiments with strain-gaged gear teeth, and photoelastic experiments for external and internal spur gears and helical gears.

Oda, et al. (1981), performed a FEM stress analysis on external spur gears along with strain gage experiments to determine the effect of rim thickness and boundary conditions on stress. For solid gears (thick rims), the maximum tensile bending stress occurred along the tooth profile fillet in the neighborhood of the critical section determined by Hofer's method (Hofer, 1948). This critical section is located at a point on the tooth fillet where a line drawn at 30° from the tooth centerline is tangent to the tooth profile (Figure 1.3.1a). Also shown in Figure 1.3.1 are the stresses along the tooth profile (represented by straight lines drawn normal to the tooth surfaces with the lengths of the lines proportional to the magnitude of stress). The maximum compressive stress occurred on the unloaded side of the tooth fillet and the magnitude was slightly greater than the magnitude of the maximum tensile stress (Figure 1.3.1a). As the rim thickness decreased, the maximum tensile stress remained nearly constant while the maximum compressive stress significantly increased due to the increased deformation of the rim (Figures 1.3.1b - 1.3.1d). This implies that reversed loading takes place in thin-rim gears and their effect must be considered in the bending strength design of the tooth. In addition, the locations of the maximum tensile and compressive stresses moved from the Hofer 30° position toward the root area of the tooth as the rim thickness decreased. Oda also observed that the modeled boundary conditions had a significant effect on stress. For the case when the gear was constrained only at the ends, the compressive stress significantly increased as the rim thickness decreased. The stress remained nearly constant when the tooth was constrained along the rim (Figure 1.3.2).

Arai, et al. (1981), performed a FEM stress analysis along with bending endurance tests on thin-rim external spur gears with spokes. The FEM analysis produced similar results to that of Oda where a decreased rim thickness significantly increased the maximum compressive stress on the unloaded side of the tooth. Endurance tests were performed where two consecutive teeth were cyclicly loaded at a 180° phase difference to simulate reversed loading that takes place in thin-rim gears. The tests showed that the endurance limit of a thin-rim gear was less than that of a solid gear.

Drago (1982) and Drago and Lutthans (1983) performed FEM analysis and photoelastic experiments on external spur gear segments to determine the rim effect on stress. Their parameters were the alternating stresses at the fillet (Hofer's critical section) and at the root (centered between two consecutive teeth). The alternating root stress significantly increased when the rim thickness decreased while the alternating fillet stress moderately increased. They noted that the fillet tensile stresses in standard gears, which are used in the standard strength calculation, are not necessarily the most significant but will give a reasonable index for strength. For thin-rim gears, however, the fillet stresses are inadequate and the root stresses are additionally required in the analysis. The results were summarized in the rim thickness factor, K_B (Figure 1.2.1), and are currently used in the AGMA standard for spur gears (AGMA, 1990).

Other pertinent publications regarding stresses in thin-rim external spur gears were by Chang, et al. (1983), Chong and Kubo (1985), Gulliot and Tordion (1989), Von Eiff, et al. (1990), and Bibel, et al. (1991). Contrary to previous models, Gulliot and Tordion (1989) simulated a complete rim rather than a gear segment. Also, they included an iterative rim/support detachment process. In the work of Bibel, et al. (1991), a comparison study between various references on stresses in thin-rim gears was included. A notable difference among authors was observed for the knees of the stress versus backup ratio curves. The differences resulted from differences in tooth geometry (numbers of teeth, diametral pitch, pitch diameter, ...), mesh refinement, and more notably, differences in support conditions. The

effect of keys on stress in thin-rim gears was investigated by Oda and Miyachika (1984b) and Gulliot and Tordion (1989). The rim effect on stress for internal spur gears was studied by Chong and Kubo (1985), Oda, et al. (1986), and Von Eiff, et al. (1990). Thin-rim effects were also studied for helical gears (Oda and Koide, 1983) and for planet gears (Oda, et al., 1984a). The effect of webs on stress in thin-rim gears was investigated by Oda and Koide (1983) and Oda, et al. (1986). The result was that the fillet stress was greater at the center of the face width of webbed-gears than at the ends of the face.

The results of stress as a function of backup ratio from the various references on external gears are summarized in Figure 1.3.3. In the figure, the normalized stress is defined as the actual stress divided by the stress for a solid gear. All references show the same trend of increased stress with decreased backup ratio. The knees of the curves vary (as stated by Bibel, et al, 1991) but the rate of increase for thin rims appear to be fairly consistent among the references.

With respect to crack propagation direction, some information was cited in these references, all from experimental observations. In the case of thicker-rim gears, the fatigue cracks initiated in the tooth fillet of the loaded side (maximum tensile stress) and propagated through the tooth while the cracks propagated through the rim in the thinner-rim specimens (Oda, et al., 1986, and Arai, et al. 1981). Oda and Koide (1983) noticed that cracks also initiated in the tooth fillet of the loaded side for helical gears. As the load position was placed toward the tooth root, the cracks still propagated across the tooth but more into the rim area. Oda and Miyachika (1984b) reported that in tests with keys, the cracks initiated in the areas corresponding to the maximum tensile stress, which were either in the tooth fillet or in the area of the keys themselves. Oda, et al. (1984a) noted that a planet bearing assembled using a press fit of the rim to the support significantly altered the rim stress distribution and possibly caused a crack to propagate through the rim rather than the tooth.

In summary, a significant amount of work has been done in the stress analysis of thin-rim gears. However, none of the stated references relating to thin-rim gears incorporated any crack propagation prediction analysis. Such analysis using methods of fracture mechanics may prove to be a valuable design tool.

1.4 Introduction to Fracture Mechanics. The field of fracture mechanics has developed into a mature discipline since World War II. As an introduction, consider three types of loading on a cracked body (Figure 1.4.1). For mode I loading, the load is applied normal to the crack plane and tends to open the crack. Mode II refers to in-plane shear loading or sliding. Mode III corresponds to out-of-plane loading or tearing. Linear elastic fracture mechanics, as the name implies, is based on a linear elastic material with no plastic deformation. Williams (1957) demonstrated that the stress distribution ahead of a crack tip in an isotropic linear elastic material can be written as

$$\sigma_{ij} = \frac{K}{\sqrt{2\pi r}} f_{ij}(\theta) \quad (1.4.1)$$

where σ_{ij} is the stress tensor, r and θ are position coordinates (Figure 1.4.2), f_{ij} is a function of θ , and K is defined as the stress intensity factor. Three distinct stress intensity factors are possible, K_I , K_{II} , and K_{III} , which correspond to mode I, mode II, and mode III loading, respectively. For mixed-mode problems (more than one type of loading) the total stress can be determined from superposition.

Equation 1.4.1 was developed using an Airy stress function approach to the solution of an elasticity problem of a semi-infinite crack. The equation is valid for only a certain region. As seen from Equation 1.4.1, the stress distribution near the crack tip exhibits a $1/\sqrt{r}$ singularity. As r approaches zero, the stress approaches infinity. In reality, once the stress for the material exceeds the yield limit,

plastic deformation takes place. In this region, linear elastic fracture mechanics is no longer valid and elastic-plastic fracture mechanics is required. As r gets larger, higher order terms from the elastic stress solution (not included in Equation 1.4.1) become significant and must be included. Thus, Equation 1.4.1 is valid for a restricted size of r .

As can be seen from Equation 1.4.1, the stress ahead of the crack tip can be described by the stress intensity factor. The stress intensity factor is a function of geometry and load. A number of methods can be used to estimate the stress intensity factor such as Green's functions, weight functions, boundary integral equations, finite element method (FEM), or experimental techniques. For other than simple geometry and loading, closed-form solutions for the stress intensity factor are not possible and methods such as FEM or experiments are used. With the growing capacities of computers today FEM techniques have become extremely popular.

Fracture mechanics methods can be used to estimate crack propagation direction in mixed-mode applications and crack growth rate. Fracture mechanics has been applied to a variety of problems such as damage tolerance life predictions in structural components (Thomas, et al., 1986), rolling-element bearing fatigue predictions (Keer and Bryant, 1983, Mendelson and Ghosn, 1986, and Ballarini and Hsu, 1989), and more recently, gear tooth bending fatigue.

1.5 Fracture Mechanics Applied to Gear Teeth. Only a handful of references are available in which fracture mechanics was applied to gear tooth bending fatigue problems. Among the earliest, Ahmad and Loo (1977) applied fracture mechanics to gear teeth to illustrate the procedure and estimate crack propagation direction. FEM was used to calculate gear tooth stress intensity factors in which special triangular crack tip elements of Wilson (1971) were used which modeled the crack tip singularity. Also Sih's strain energy density criteria (Sih (1974), further described in Section 2.3) was used to predict the direction of crack propagation. A number of examples were given with cracks originating in the tooth fillet area for both the loaded and unloaded side of the tooth. For the case of a gear tooth loaded near the tip with an inclined crack in the fillet, K_I dominated over K_{II} and the crack was predicted to propagate in a straight path. All of this work, however, considered only an initial crack and no attempt was made to model continued crack propagation. Also, no experimental validation was made.

Honda and Conway (1979) applied fracture mechanics to gear teeth to simulate crack propagation, compute a threshold load in which cracking would cease, and calculate the life of a tooth with a crack. FEM was used and sequential square elements of zero elastic modulus were used to simulate a crack. Stress intensity factors were calculated using both the displacement extrapolation method and the strain energy release rate method. Sih's strain energy density method was used to predict crack propagation direction. For a tooth loaded at the tip and a crack in the fillet of the loaded side, K_I dominated over K_{II} and the crack was predicted to propagate in a straight path. The method of Paris (1961) was used to estimate crack propagation life and a simple example was given. Crack propagation modeling appeared to have been performed by manual remeshing of the crack region. This was a tedious process and only a few iterations were performed, representing a crack of only a small fraction of the total tooth.

Flasker and Jezernik (1983) applied fracture mechanics to gear teeth to evaluate stress intensity factors and estimate gear life. FEM was used to model the tooth and the stress intensity factors were compared using three different methods: the displacement extrapolation method, the energy release rate method, and the J-integral method. The crack propagation direction was again calculated using Sih's strain energy density method. As with Ahmad and Loo, Flasker and Jezernik's results only considered an initial crack and continued crack propagation was not considered.

For application in aircraft or automotive use where high-strength, carburized gears are used, the effect of residual stress may play an important role in crack initiation and propagation. A series of analyses and experiments were performed at Tohoku University in Japan to include these effects and expand the technology. As a first step Tobe, et al. (1985), developed a methodology to calculate the residual stress of carburized spur gears based on the hardness distribution through the tooth, amount of retained austenite, and a FEM analysis based on volume expansion. This methodology was then used by Inoue, et al. (1989a), to estimate gear tooth stress intensity factors. FEM was used and the stress intensity factors were calculated using the energy release rate method. The stress energy was the superposition of the stress due to the applied load and the residual stress. Single tooth bending fatigue tests were performed by Inoue, et al. (1989b), and were used with the stress intensity estimates to determine the effect of hardness and residual stress on crack growth rate. The results were compiled to develop a methodology to estimate the crack growth rate based on the hardness distribution of the gear tooth (Kato, et al., 1990, and Inoue, et al., 1991). The overall goal was to develop a methodology to estimate gear tooth strength of carburized gears based on fracture mechanics. Emphasis was not placed on crack propagation direction and propagation was assumed to occur in a straight path.

Daniewicz (1991) developed a comprehensive, self-contained analysis package to refine the spur gear bending fatigue life prediction theory using fracture mechanics. Gear tooth stresses were solved using the complex potential method solution of the elasticity problem. Using this method, a gear tooth anchored in a semi-infinite domain was transformed to an elastic half plane with a concentrated load (Cardou and Tordion, 1989). A cracked geometry was approximated as an elastic half-plane containing an edge crack and stress intensity factors were determined from Hartranft and Sih (1973). Additional topics such as residual stress, yielding, elastic-plastic fracture, and crack closure were considered. Predicted crack growth rates were compared to experiments of Inoue, et al. (1989b), although the correlation was not that good. Again, the goal of the work was to estimate gear tooth strength and not necessarily crack propagation direction.

Flasker and Pehan (1993) described their method for calculating crack propagation in gear teeth using fracture mechanics. FEM was used to calculate the stress intensity factors based on the virtual crack extension method. Residual stress and yielding was considered. An example gear from an automotive gearbox was analyzed and compared to experiments. Good correlation of crack propagation direction was achieved but poor correlation of crack growth life resulted. It should be noted that this work only considered a solid, thick-rim gear.

In summary, only a few references were available in which fracture mechanics was applied to gear teeth. All the citing used some form of numerical method to calculate the stress intensity factor. Much of the work considered only an initial crack and little emphasis was placed on calculating crack propagation paths. Many of the references that did consider crack propagation assumed the propagation occurred in a straight path. In addition, experimental validation of the cited analyses was sparse. Finally, no work relating to fracture mechanics was performed for thin-rim gears.

1.6 Dissertation Objective and Outline. The objective of this study was to determine the effect of gear rim thickness on crack propagation. A major emphasis was to predict the direction in which a crack would grow, either through the gear tooth or through the rim. In addition, gear tooth fatigue crack growth was investigated. Linear elastic fracture analysis was used to analyze gear tooth bending fatigue in standard and thin-rim gears. Finite element computer programs MARC and FRANC were used to determine stress distributions and model crack propagation. Experimental tests were performed in the NASA Lewis Spur Gear Fatigue Rig to validate predicted crack propagation results.

This dissertation is divided into seven chapters. Chapter 2 presents further fundamental ideas in the area of fracture mechanics. Methods to calculate stress intensity factors, crack propagation directions, and crack growth rates are discussed. Chapter 3 presents the results of the gear tooth crack propagation modeling. Fundamental principles of Chapter 2 were applied in a computer-based finite element analysis to predict crack propagation paths and fatigue growth. Chapter 4 describes the experimental studies used to measure crack propagation direction and fatigue growth. Chapter 5 presents a comparison between the analytical predictions and experimental results. Chapter 6 presents analytical parametric studies in which the effect of gear design variables on crack propagation paths was investigated. Lastly, Chapter 7 closes with conclusions of the study.

CHAPTER 2: FUNDAMENTALS OF FRACTURE MECHANICS

2.1 Introduction. This chapter presents further fundamental ideas in the area of fracture mechanics. Stress intensity factors are used in fracture mechanics to characterize the stress distribution near a crack tip. Methods to calculate stress intensity factors are presented with an emphasis on the use of the finite element method. Furthermore, methods are presented which use the stress intensity factors to estimate crack propagation direction and crack growth rate. Finally, the computer program FRANC, which numerically simulates crack propagation, is briefly discussed.

2.2. Stress Intensity Factors. Linear fracture mechanics can be used for predicting strength and life of cracked structures. Knowledge of the crack tip stress intensity factors is necessary for such predictions. A solution to the elasticity problem formulated for a cracked structure is one method to determine stress intensity factors. In most cases, however, an exact solution to an actual elasticity problem is very difficult or even impossible to solve. The finite element method has become a very popular approach in calculating stress intensity factors in actual engineering applications. It should be noted that this discussion will be limited to two-dimensional problems.

One of the earlier applications of the finite element method to cracked structures was performed by Chan, et al. (1970). Here, conventional first-order triangular finite elements were used throughout the model. It was concluded that this method was feasible in determining stress intensity factors, but a large number of elements were needed, not only in the crack tip region, but throughout the model, to achieve high accuracy. This was due to the stress singularity at the crack tip.

Work has been done in developing special finite elements used near the crack tip to model the singular elastic stress distribution. Tracey (1971) used special four-node quadrilateral elements with two nodes coincident at the crack tip and the element displacement functions prescribed as a $1/\sqrt{r}$ relationship (where r was the distance from the crack tip). This type of modeling produced accurate predictions of the stress intensity factors using an order of magnitude decrease in the number of degrees of freedom compared to Chan's analysis. Similarly, Wilson (1971) investigated two different types of special finite elements near a crack tip. The first was a high-order, circular crack tip element with prescribed displacements of the element circumference which matched the solution of the first four terms of the Williams expansion (Williams, 1957). The second type was similar to the Tracey approach which used triangular crack tip elements. Again, better accuracy and convergence was obtained compared to conventional elements. Other works in which special crack tip finite elements were investigated were by Tong and Pian (1973a) and Tong, et al. (1973b).

It was concluded that improved accuracy with less degrees of freedom was achieved with special crack tip elements. However, specialized code must be written to assemble the stiffness matrix for these elements. In addition, compatibility must be maintained for the special crack tip elements and surrounding conventional elements. To overcome these deficiencies, work was performed by two independent sources to model the region in the vicinity of the crack tip with conventional isoparametric finite elements (Henshell and Shaw, 1975, and Barsoum, 1976). Here, standard six-node triangular elements or eight-node quadrilateral elements were used, with the mid-side nodes on sides adjacent to the crack tip moved from the nominal mid-position to one-quarter of the length (Figure 2.2.1). It was shown by these studies that this type of mesh modeled the inverse square-root singularity of stress distribution near a crack tip. It should be noted that the work by Barsoum and further work by Shih, et al. (1976) concluded that the six-node triangular element configuration gave more accurate results than the eight-node quadrilateral configuration. Also, once the mid-side nodes of these elements were moved to the

quarter-point positions, conventional methods to assemble the stiffness matrices for standard six-node and eight-node elements could be used, providing a versatile method for use in crack tip analysis.

Regardless of the type of finite element used, the direct output of the finite element method is calculated nodal displacements for which nodal forces, and stress and strains can be determined. For fracture mechanics, stress intensity factors are of primary interest and can also be estimated based on the nodal displacements and forces. A variety of methods have been developed based on the finite element nodal values.

One method to calculate the stress intensity factors is called the displacement correlation method. This method is based directly on the nodal displacements (Tracey, 1977, and Wawrzynek, 1991). Here the mode I and II stress intensity factors are given by (with respect to Figure 2.2.2)

$$K_I = \frac{\mu}{\kappa+1} \sqrt{\frac{2\pi}{L}} [4(v_b - v_d) + v_e - v_c] \quad (2.2.1)$$

$$K_{II} = \frac{\mu}{\kappa+1} \sqrt{\frac{2\pi}{L}} [4(u_b - u_d) + u_e - u_c] \quad (2.2.2)$$

$$\mu = \frac{E}{2(1+\nu)} \quad (2.2.3)$$

$$\kappa = \begin{cases} 3-4\nu & \text{for plane strain} \\ \frac{3-\nu}{1+\nu} & \text{for plane stress} \end{cases} \quad (2.2.4)$$

where E is the modulus of elasticity, ν is Poisson's ratio, L is the element length, and the u 's and v 's are nodal displacements in the x and y directions, respectively.

A second method to calculate stress intensity factors is called the modified crack closure method. This method is an indirect method based on the energy release rate. The method used classical principles developed by Irwin (1957) which were used by Rybicki and Kanninen (1977) in a finite element application using conventional quadrilateral elements. Ramamurthy, et al. (1986) later refined this method using quarter-node elements. Here, the energy release rates for mode I and II are

$$G_I = \frac{1}{2L} [(c_{11}F_{y,j} + c_{12}F_{y,j+1} + c_{13}F_{y,j+2})v_{j-1} + (c_{21}F_{y,j} + c_{22}F_{y,j+1} + c_{23}F_{y,j+2})v_{j-2}] \quad (2.2.5)$$

$$G_{II} = \frac{1}{2L} [(c_{11}F_{x,j} + c_{12}F_{x,j+1} + c_{13}F_{x,j+2})u_{j-1} + (c_{21}F_{x,j} + c_{22}F_{x,j+1} + c_{23}F_{x,j+2})u_{j-2}] \quad (2.2.6)$$

$$\begin{aligned} c_{11} &= \frac{33\pi}{2} - 52 & c_{12} &= 17 - \frac{21\pi}{4} & c_{13} &= \frac{21\pi}{2} - 32 \\ c_{21} &= 14 - \frac{33\pi}{8} & c_{22} &= \frac{21\pi}{16} - \frac{7}{2} & c_{23} &= 8 - \frac{21\pi}{8} \end{aligned} \quad (2.2.7)$$

where the F_x 's and F_y 's are nodal forces in the x and y directions, respectively, and the u 's and v 's are nodal displacements in the x and y directions, respectively (Figure 2.2.3). From the energy release rates, the stress intensity factors are defined as

$$K_I = \sqrt{G_I E^*} \quad (2.2.8)$$

$$K_{II} = \sqrt{G_{II} E^*} \quad (2.2.9)$$

$$E^* = \begin{cases} \frac{E}{(1-\nu^2)} & \text{for plane strain} \\ E & \text{for plane stress} \end{cases} \quad (2.2.10)$$

A third method to calculate stress intensity factors is called the J-integral method. The J-integral (Rice, 1968) is a path-independent, line integral which indicates the change in energy for a crack extension and can be applied in cases where plasticity effects are not negligible. Even though originally derived for a self-similar crack (crack moves in a straight path), the mixed-mode formulation of the J-integral has been formulated and the symmetric and antisymmetric components can be defined as

$$J_1 = \int_{\Gamma} (W dy - T \cdot \frac{\delta u}{\delta x} ds) \quad (2.2.11)$$

$$J_2 = \int_{\Gamma} (W dx - T \cdot \frac{\delta u}{\delta y} ds) \quad (2.2.12)$$

where Γ is a curve surrounding the crack tip, W is the strain energy density, T is the traction vector with respect to the outward normal along Γ , u is the displacement vector, and ds is an elemental arc length along Γ . The stress intensity factors can be derived from (Wawrzynek, 1991)

$$J_1 = \frac{1}{E^*} (K_I^2 + K_{II}^2) \quad (2.2.13)$$

$$J_2 = \frac{2}{E^*} (K_I + K_{II}) \quad (2.2.14)$$

The J-integral method can be applied to numerical finite element calculations by transforming the above contour integral to an equivalent domain integral, then integrating the stresses over an area (Wawrzynek, 1991).

In summary, stress intensity factors are needed to analyze the strength and life of a cracked structure. The finite element method can be used along with special quarter-node elements to accurately and efficiently model the conditions of a crack tip. Three different methods (displacement correlation, modified crack closure, and J-integral) were presented which calculate the stress intensity factors based on the nodal displacements and forces. The stress intensity factors will now be used to calculate crack propagation direction and crack propagation fatigue crack growth rate.

2.3 Crack Propagation Directions. For the case of a static load on a cracked structure, the crack will propagate when the stress intensity factor due to the applied load reaches a critical value. Here

if the loading is purely mode I ($K_I > 0$, $K_{II} = 0$), the crack will extend from the tip in a straight path parallel to the original crack (Figure 2.3.1a). However, for mixed-mode crack problems ($K_I > 0$, K_{II} not equal to zero), the crack will extend from the tip and propagate at some angle, θ_m , from the original crack trajectory (Figure 2.3.1b).

One of the earliest but still popular theories to predict crack propagation angle for mixed-mode problems was postulated by Erdogan and Sih (1963). Their work considered two-dimensional static loads applied to thin, brittle materials. Their theory states that the crack extension starts at the crack tip and grows in the radial direction in the plane perpendicular to the direction of the greatest tangential tensile stress. From Williams (1957), the tangential stress in the neighborhood of the crack tip is

$$\sigma_{\theta\theta} = \frac{1}{\sqrt{2\pi r}} \left[K_I \cos^3 \frac{\theta}{2} - 3K_{II} \sin \frac{\theta}{2} \cos^2 \frac{\theta}{2} \right] \quad (2.3.1)$$

Setting $d\sigma_{\theta\theta}/d\theta = 0$ and solving for $\theta = \theta_m$ gives

$$\theta_m = 2 \tan^{-1} \left[\frac{\frac{K_I}{K_{II}} \pm \sqrt{\left(\frac{K_I}{K_{II}} \right)^2 + 8}}{4} \right] \quad (2.3.2)$$

where θ_m is the predicted crack propagation angle. The sign to use in Equation 2.3.2 should be that which gives a tensile (positive) tangential stress in Equation 2.3.1. Examples of the crack tip tangential stress distribution as a function of the θ -coordinate for various K_I and K_{II} loading schemes are given in Figure 2.3.2. For purely mode I (Figure 2.3.2a), the maximum tangential stress occurs at $\theta_m = 0^\circ$ and the crack would propagate parallel to the original crack. For a mixed-mode case (Figure 2.3.2b), the predicted crack propagation angle is at $\theta_m = -40.2^\circ$ for the case of $K_I = 10 \text{ ksi}\sqrt{\text{in}}$ and $K_{II} = 5 \text{ ksi}\sqrt{\text{in}}$. For purely mode II (Figure 2.3.2c), the predicted crack propagation angle is $\theta_m = -70.5^\circ$.

A second popular method to predict crack propagation angle for mixed-mode problems was developed by Sih (1974). Sih developed the strain-energy-density factor, S , where

$$S = a_{11} K_I^2 + 2a_{12} K_I K_{II} + a_{22} K_{II}^2 \quad (2.3.3)$$

and

$$\begin{aligned} a_{11} &= \frac{1}{16\mu} [(1 + \cos \theta)(\kappa - \cos \theta)] \\ a_{12} &= \frac{1}{16\mu} \sin \theta [2 \cos \theta - (\kappa - 1)] \\ a_{22} &= \frac{1}{16\mu} [(\kappa + 1)(1 - \cos \theta) + (1 + \cos \theta)(3 \cos \theta - 1)] \end{aligned} \quad (2.3.4)$$

Sih's criteria for crack propagation in a two-dimensional stress state are: 1) a crack will propagate in a direction, $\theta = \theta_m$, in which the strain-energy-density factor is a minimum ($\delta S / \delta \theta = 0$), and 2) a crack will propagate when the strain energy factor reaches a critical value, $S = S_{cr}$. Note that for Sih's strain-energy-density theory, the predicted crack propagation angle is a function of Poisson's ratio as well as the stress intensity factors. Also as noted by Swedloy (1976) in follow-up work, the predicted crack propagation angle occurs when the strain-energy-density factor is a minimum and the tangential stress near the crack tip is tensile.

A third popular method to predict crack propagation angle for mixed-mode problems assumes the crack will propagate at an angle where the energy release rate is maximum. For a crack having a main branch and a propagation branch at an arbitrary angle $\theta = \theta_m$, the elasticity solution for the energy release rate becomes an extremely complicated problem for mixed-mode loading. Hussain, et al. (1974) developed a solution for the energy release rate for such a problem using the complex potential elasticity method with the results

$$G(\gamma) = \frac{4}{E} \left[\frac{1}{3 + \cos^2 \gamma} \right]^2 \left[\frac{1 - \frac{\gamma}{\pi}}{1 + \frac{\gamma}{\pi}} \right]^{\frac{\gamma}{\pi}} [(1 + 3\cos^2 \gamma) K_I^2 + 8 \sin \gamma \cos \gamma K_I K_{II} + (9 - 5\cos^2 \gamma) K_{II}^2] \quad (2.3.5)$$

where $\gamma = -\theta$. From these results, the predicted crack propagation angle occurs at an angle, $\theta = -\gamma_m$ where γ_m occurs when the energy release rate from Equation 2.3.5 is a maximum.

Other researchers have investigated crack propagation angle for mixed-mode problems using a crack-kinking analysis. Cotterell and Rice (1980) used first-order solution approximations using a perturbation procedure and calculated crack propagation angle based on the assumption that the crack would propagate in the direction (with respect to the crack tip) where the local K_{II} was zero. Hayashi and Nemat-Nasser (1981) investigated the crack propagation angle using a complex potential elasticity analysis of a kinked crack for the maximum energy release rate similar to Hussain. Both Cotterell and Rice (1980) and Hayashi and Nemat-Nasser (1981) concentrated on a predominately mode I loaded problem, and both derived the expression for the crack propagation angle as

$$\theta_m = - \frac{2K_{II}}{K_I} \quad (2.3.6)$$

which is valid for $K_I \gg |K_{II}|$.

All the methods previously mentioned to predict crack propagation angle for mixed-mode problems considered stationary static loads. Mendelson and Ghosn (1986) investigated mixed-mode crack propagation for applications of aerospace rolling element bearings and considered crack propagation for a moving load. Here the roller bearing was modeled as a plate with an edge crack in which a Hertzian load was positioned at various locations with respect to the crack. The energy release rate was derived from the energy required to close an increment, δ , of the crack tip (Figure 2.3.3) where

$$G = \lim_{\delta \rightarrow 0} \frac{2}{\delta} \int_0^{\delta} \frac{1}{2} [\sigma_{\theta\theta}(r) u_{\theta}(\delta-r) + \sigma_{r\theta}(r) u_r(\delta-r)] dr \quad (2.3.7)$$

The stresses of Equation 2.3.7 were based on the stress intensity factors of the crack tip of C (Figure 2.3.3a) and the displacements were based on the stress intensity factors of the extended crack tip C' (Figure 2.3.3b). Mendelson and Ghosn used relationships developed by Cotterell and Rice to convert the stress intensity factors in the x', y', z' coordinate system to that of the x, y, z system and derived the relationship for the energy release rate as

$$G = G_{\theta\theta} + G_{r\theta} \quad (2.3.8)$$

where

$$\begin{Bmatrix} G_{\theta\theta} \\ G_{r\theta} \end{Bmatrix} = \frac{(1+\nu)(\kappa+1)}{4E} \begin{Bmatrix} [K_I \cos^3 \frac{\theta}{2} - 3K_{II} \sin \frac{\theta}{2} \cos^2 \frac{\theta}{2}]^2 \\ [K_I \sin \frac{\theta}{2} \cos^2 \frac{\theta}{2} + K_{II} \cos \frac{\theta}{2} (1 - 3 \sin^2 \frac{\theta}{2})]^2 \end{Bmatrix} \quad (2.3.9)$$

The term $G_{\theta\theta}$ was labeled as the tangential crack extension force and was predominately used to determine crack propagation angle. Mendelson and Ghosn used the criteria that the crack would propagate in the direction which gave the maximum change in the tangential crack extension force, $G_{\theta\theta}$. It should be noted that the tangential crack extension force criteria of Mendelson and Ghosn gives the same results for the predicted crack propagation angle as the maximum tangential stress criteria of Erdogan and Sih.

A comparison of the predicted crack propagation angle using the maximum tangential stress theory (Erdogan and Sih), minimum strain-energy-density theory (Sih), and maximum energy release rate (Hussain) is given in Figure 2.3.4. All the methods mentioned to predict crack propagation angle converge to $\theta_m = -2K_{II}/K_I$ for the case when mode I is dominant. The largest divergence for the predicted crack angle takes place for the case when mode II is dominant. Various experiments have been performed to validate crack angle predictions but no one method is currently predominantly favored over another.

2.4 Crack Propagation Fatigue Crack Growth. Many machine elements, such as gear teeth, are cyclicly loaded in application. The overall fatigue life of such components may be represented by three distinct phases: 1) crack initiation, 2) crack propagation, and 3) final failure. Once crack initiation has occurred, fracture mechanics may be used to estimate crack propagation fatigue growth rate and time to final failure.

The most universally used method to calculate crack propagation fatigue crack growth was postulated by Paris (Paris, et al., 1961, Paris and Erdogan, 1963). Here, considered were purely mode I loaded specimens subjected to cyclic load (Figure 2.4.1a). Further considered was unstable crack growth such that the stress intensity factor grew with increasing crack size (Figure 2.4.1b). Paris postulated that the rate of crack growth with respect to number of stress cycles was a logarithmic relationship with the stress intensity factor range where

$$\frac{da}{dN} = C (\Delta K)^n \quad (2.4.1)$$

where da is the change in crack length for dN number of stress cycles, ΔK is the range of the stress intensity factor at a given time, and C and n are material constants. This theory was compared to experiments primarily using aluminum alloys for aircraft structural use and found to give good correlation (Figure 2.4.2). It is still in use today due to its simplicity. The material constants, C and n , however, must still be determined by some experimental means. Standard test methods to determine crack growth rates are given in ASTM E-647-93 (1993).

The final failure for a specimen undergoing crack propagation is defined when the maximum value of the stress intensity factor equals the material fracture toughness property, K_{IC} (Figure 2.4.1b). K_{IC} is a material property and can be experimentally determined using the method described in ASTM E-399-90 (1990).

Some discrepancies were discovered in the Paris fatigue crack growth theory considering three effects not previously addressed. First was the effect of load ratio, R , on crack growth ($R = P_{min}/P_{max}$).

Second was the instability of crack growth observed when the stress intensity factor range approached K_{IC} . Third was the presence of a stress intensity threshold factor, ΔK_{th} . The stress intensity threshold factor is the highest stress intensity factor in which no crack growth would occur.

Early work considering some of these effects were by Roberts and Erdogan (1967), Forman, et al. (1967), and Walker (1970). Forman and Hu (1984) describe the fracture mechanics computer program FLAGRO 4 used in the analysis of the NASA space shuttle. The Collipriest crack growth model (Collipriest, 1972) was used in this analysis where

$$\frac{da}{dN} = C (K_{IC} \Delta K_{th})^{\frac{n}{2}} \cdot \exp \left\{ \ln \left[\frac{K_{IC}}{\Delta K_{th}} \right]^{\frac{n}{2}} \right. \\ \left. \cdot \tanh^{-1} \left[\frac{\ln \left[\frac{\Delta K^2}{(1-R) K_{IC} \Delta K_{th}} \right]}{\ln \left[\frac{(1-R) K_{IC}}{\Delta K_{th}} \right]} \right] \right\} \quad (2.4.2)$$

The Collipriest equation accounts for the effect of load ratio, instability near K_{IC} , and the stress intensity threshold factor, ΔK_{th} . Crack growth rate using the Collipriest equation is shown in Figure 2.4.3 for a variety of load ratios. Also shown for comparison is the crack growth rate using the Paris equation.

In actual applications of gears, Inoue, et al. (1991) describes fatigue crack growth of gear bending fatigue tests. Here, crack growth equations were derived as a function of crack depth through a gear tooth. The expressions derived for crack growth rate da/dn (in units of mm/cyc), as a function of stress intensity range, ΔK (in units of $\text{MPa} \sqrt{\text{m}}$), were

$$\frac{da}{dN} = \begin{cases} \frac{\lambda}{(1-\alpha^\eta)} (\Delta K^\eta - \Delta K_{th}^\eta) & \text{for } \Delta K_{th} \leq \Delta K \leq \Delta K_C \\ \frac{\lambda}{(1-\alpha^\eta)} \frac{\Delta K^\eta K_{IC}^\eta}{(K_{IC}^\eta - \Delta K^\eta)} & \text{for } \Delta K_C < \Delta K < K_{IC} \end{cases} \quad (2.4.3)$$

where

$$\Delta K_C = \sqrt{\Delta K_{th} K_{IC}} \quad (2.4.4)$$

$$\alpha = \frac{\Delta K_{th}}{K_{IC}} \quad (2.4.5)$$

These parameters were all estimated as a function of the hardness of the tooth where

$$\Delta K_{th} = 2.45 + (3.41 \times 10^{-3})H \quad (2.4.6)$$

$$K_{IC} = 141 - (1.64 \times 10^{-1})H \quad (2.4.7)$$

$$\eta = 4.31 - (8.66 \times 10^{-3})H + (1.17 \times 10^{-5})H^2 \quad (2.4.8)$$

$$\log(\lambda) = -10.0 + (1.09 \times 10^{-2})H - (1.40 \times 10^{-5})H^2 \quad (2.4.9)$$

Furthermore, the hardness distribution, H (in units of Vickers hardness, Hv), along the depth of the gear tooth, d (in units of mm), was estimated as

$$H = (H_2 - H_3) \exp[-A(d-d_2)^2] + H_3 \quad (2.4.10)$$

$$A = \begin{cases} \frac{-1}{d_2^2} \ln \left[\frac{H_1 - H_3}{H_2 - H_3} \right] & \text{for } d \leq d_2 \\ \frac{-1}{(d_{eff} - d_2)^2} \ln \left[\frac{550 - H_3}{H_2 - H_3} \right] & \text{for } d > d_2 \end{cases} \quad (2.4.11)$$

where H_1 was the hardness at the tooth surface, H_2 was the maximum hardness which occurred at depth d_2 , H_3 was the hardness of the tooth core, and d_{eff} was the effective depth which occurred at $H=550$ Hv. A typical example of the calculated hardness distribution using Equation 2.4.10 is given in Figure 2.4.4a. Various crack growth curves using Equation 2.4.3 for this range of hardness distributions is given in Figure 2.4.4b.

It was shown in this section and the previous section that stress intensity factors were used to predict crack propagation direction for mixed-mode loading and crack growth rate. In the next section, the computer program FRANC (FRacture ANalysis Code), a unique analysis package which uses these principles to calculate stress intensity factors and crack propagation direction, is described.

2.5 FRANC Computer Program. The analysis of this present study used the FRANC (FRacture ANalysis Code) computer program developed by Wawrzynek (1991). FRANC is a general purpose finite element code for the static analysis of cracked structures. FRANC is designed for two-dimensional problems and is capable of analyzing plane strain, plane stress, or axisymmetric problems. To start FRANC, a finite element mesh consisting of element conductivity data (definition of what nodes belong to what elements) and nodal coordinate data of an uncracked structure must be imported to FRANC using an external mesh generator. FRANC can accept conventional eight-node, isoparametric quadrilateral elements or six-node triangular elements. Once a model is imported into FRANC, boundary conditions, externally applied loads, and element material property data can be defined. Conventional finite element analysis for deflections as well as post-processing calculations of nodal forces, stresses, and strains can be performed.

Among the variety of capabilities, a unique feature of FRANC is the ability to model a crack in a structure. FRANC used a method called "delete and fill" to accomplish this. To illustrate the principle, first consider a finite element mesh of an uncracked structure (Figure 2.5.1a). The user would first define an initial crack by identifying the node of the crack mouth and coordinates of the crack tip (Figure 2.5.1b). FRANC will then delete the elements in the vicinity of the crack tip (Figure 2.5.1c). FRANC will next insert a rosette of quarter-point, six-node triangular elements around the crack tip to model the inverse square-root stress singularity (Figure 2.5.1d). Finally, FRANC will fill the remaining area between the rosette and original mesh with conventional six-node triangular elements (Figure 2.5.1e). The user can then run the finite element equation solver to determine nodal displacements, forces,

stresses, and strains. FRANC can then calculate stress intensity factors using the previously described methods: 1) the displacement correlation method, 2) modified crack-closure method, or 3) J-integral method.

A further unique feature of FRANC is the automatic crack propagation capability. FRANC uses crack length as the independent variable rather than time. FRANC calculates stress intensity factors and crack propagation angles for various discrete increments of crack length to simulate crack propagation. To illustrate, first consider an initial crack as imputed by the user in the manner described above. Once the initial crack is imputed, the user would input a crack increment size. FRANC runs the equation solver and calculates stress intensity factors, K_I and K_{II} , for the initial crack. Next, FRANC calculates the crack propagation angle based on one of the previously described methods as specified by the user: 1) maximum tangential stress theory of Erdogan and Sih, 2) minimum strain-energy-density of Sih, or 3) maximum energy release rate of Hussain. The location of the new crack tip is determined based on the calculated propagation angle and imputed crack increment size (Figure 2.5.2). After the new crack tip is determined, FRANC deletes the elements near the new crack tip, inserts a rosette of quarter-point triangular elements at the new crack tip, inserts conventional triangular "fill" elements, and runs the equation solver to calculate the stress intensity factors of the new crack tip. This process is repeated as many times as specified by the user. This process allows the automated calculation of crack propagation path of a cracked structure (Figure 2.5.3).

In summary, this chapter presented methods to calculate stress intensity factors using the finite element method. The stress intensity factors were then used to calculate crack propagation direction and crack growth rate. In addition, various methods to calculate crack propagation direction and crack growth rate were presented. Finally, the computer program FRANC was described which uses these principles to simulate crack propagation. In the next chapter, crack propagation of gear teeth is modeled.

CHAPTER 3: CRACK PROPAGATION MODELING OF GEARS

3.1 Introduction. In this chapter, gear tooth crack propagation modeling is presented. Gear finite element modeling is discussed along with a mesh refinement study. The principles discussed in Chapter 2 (stress intensity factors, crack propagation direction, and crack growth rate) are applied to the gear model and gear tooth crack propagation is simulated. Lastly, the effect of rim thickness on crack propagation direction and fatigue crack growth is discussed.

A flow chart of the procedure used in the modeling of a gear is shown in Figure 3.1.1. Basic gear tooth geometry data was input to a tooth coordinate generation program called GPAT. The output of GPAT was tooth coordinate and rim coordinate data which defined a single-tooth sector of a gear. This output was used by P3/PATRAN (1993), a pre- and post-processing finite element analysis software package, which created the finite element mesh of the complete gear. The P3/PATRAN output was used by two separate finite element programs. The first was the MARC finite element program (MARC, 1992). Here, a static, linear, structural finite element analysis was performed. The MARC output was used by P3/PATRAN as well as a PC spreadsheet for post-processing of displacement, stress, and strain information.

The second finite element program was FRANC, as described in Chapter Two. FRANC was used to simulate crack propagation using linear elastic fracture mechanics. The output of FRANC was crack tip stress intensity factors as well as predicted crack path coordinates. In addition, crack propagation fatigue growth was calculated based on the predicted stress intensity factors. More details of the analysis procedure is given in the following sections.

3.2 Gear Modeling. Computer program GPAT was written to calculate tooth coordinate data and prepare an input file for the P3/PATRAN program. GPAT used, as a subroutine, the method of Hefeng, et al. (1985) to determine the tooth coordinates of an external spur gear. For this method, the gear tooth was generated from a rack-form type of cutting tool, such as a hob. The generated tooth was defined as the envelope of successive positions of the rack as the rack was rolled on the pitch circle of the gear. At any roll position, the rack and the resulting tooth were tangent to each other at the cutting point and can be described mathematically as

$$\mathbf{n} \cdot \mathbf{v} = 0 \quad (3.2.1)$$

where \mathbf{n} is the unit normal vector of the rack surface at the cutting point, and \mathbf{v} is the relative velocity between the cutting point on the rack and the coincident point on the gear blank. Equation 3.2.1 is satisfied by those points on the rack surface for which the surface normal passes through the mesh pitch point, O (Figure 3.2.1).

The generated tooth geometry can be divided into four sections: 1) top land, 2) involute section, 3) trochoid section, and 4) bottom land (Figure 3.2.2). The top land section is defined by the outer radius of the gear blank where

$$\mathbf{r} = [(r_p + a_g) \cos \omega] \mathbf{i} - [(r_p + a_g) \sin \omega] \mathbf{j} \quad (3.2.2)$$

where r_p is the pitch radius of the gear tooth, a_g is the addendum of the tooth, and ω is the rotation of the gear blank (Figure 3.2.1). Note that \mathbf{r} is defined in the x, y, z coordinate system which rotates with the gear blank. The involute section is defined as

$$\begin{aligned} r = & [r_p \cos \omega + r_p \omega \sin \omega - r_p \omega \cos(\omega - \phi)] i \\ & + [-r_p \sin \omega + r_p \omega \cos \omega + r_p \omega \sin \phi \sin(\omega - \phi)] j \end{aligned} \quad (3.2.3)$$

where ϕ is the pressure angle of the rack. The trochoid section of the tooth is defined as

$$\begin{aligned} r = & [r_p \cos \omega + r_p \omega \sin \omega - a_c \frac{\cos(\omega - \phi)}{\cos \phi} \\ & - r_c \sin(\omega - \phi) + r_c \sin(\omega - \beta)] i \\ & + [-r_p \sin \omega + r_p \omega \cos \omega + a_c \frac{\sin(\omega - \phi)}{\cos \phi} \\ & - r_c \cos(\omega - \phi) + r_c \cos(\omega - \beta)] j \end{aligned} \quad (3.2.4)$$

where a_c is the rack cutter addendum, r_c is the rack cutter radius, and

$$\beta = \tan^{-1} \left[\frac{a_c - r_c \sin \phi}{r_p \omega - a_c \tan \phi - r_c \cos \phi} \right] \quad (3.2.5)$$

Finally, the bottom land is defined as

$$r = [(r_p - d_g) \cos \omega] i - [(r_p - d_g) \sin \omega] j \quad (3.2.6)$$

where d_g is the dedendum of the gear tooth.

User input to GPAT for standard gears were number of teeth on gear, N_g , pressure angle, ϕ , and diametral pitch, P_d . Figure 3.2.3a shows an example of a tooth for $N_g=28$, $\phi=20^\circ$, $P_d=8$ teeth/in. As a default, GPAT used $a_g \cdot P_d=1.0$ and $d_g \cdot P_d=1.35$. GPAT also includes the capability to model non-standard teeth as described by Hefeng, et al. (1985). Here, the user may define values for tooth addendum, dedendum, cutter tip radius, or tool shift ratio. The tool shift ratio, e , is defined as

$$a_g' = a_g + e, \quad d_g' = d_g - e \quad (3.2.7)$$

where a_g' and d_g' are the actual generated addendum and dedendum, respectively. Figures 3.2.3b through 3.2.3e show the effects of parametric variations of the addendum, dedendum, cutter tip radius, and tool shift ratio on the generated tooth geometries.

The strategy used to assemble the tooth coordinate data into a P3/PATRAN input file was similar, in principle, to that used by Valco (1992). First, the tooth coordinate data was used to define "grid" points in P3/PATRAN. Next, selected grid points were used to form "lines" noting that lines were both straight and curved. Finally, lines were connected to form "patches" where a patch was defined as a four-sided surface (two-dimensional) consisting of four intersecting lines. The output of GPAT was the appropriate P3/PATRAN definition of grids, lines, and patches to form a single-tooth sector of a gear as shown in Figure 3.2.4a.

Once a single-tooth sector was imported, P3/PATRAN was used to generate a finite element mesh of the complete gear. This was done by a "seed-and-mesh" method. Seeds were placed along patch edges to define the number of elements along each edge. The meshing process then created the appropriate number of finite elements for each patch. A powerful capability of P3/PATRAN was the ability to copy and rotate patches and finite elements. This was done to construct the complete gear model based on a single-tooth sector. A sample mesh of a gear along with the load and boundary conditions is shown in Figure 3.2.4b. As stated by many references (see Chapter 1), the maximum tensile stress occurred in the fillet region of the loaded tooth. This was also the location of crack

initiation. For these reasons, a finer mesh was employed in this region. Details of the mesh refinement strategy are given in the next section.

3.3 Mesh Refinement. The objective of the mesh refinement was to reduce the size of the elements in the fillet region until convergence of the maximum stress occurred. The input parameters used in this analysis to create the mesh is given in Table 3.3.1. The tooth geometry used was the nominal geometry for the test gears of the NASA Lewis Spur Gear Fatigue Rig later used in experimental studies (described in Chapter 4). The analysis used 8-node, plane stress, quadrilateral finite elements. The material used was steel. The tooth was loaded at the tip (see Appendix A for the derivation of the load vector orientation). The hub corner nodes were fixed in both the x and y directions.

Four different mesh refinements were investigated. The coarsest mesh had 1692 elements and 5676 nodes and is pictured in Figures 3.2.4b and 3.3.1a. The second case had 3216 elements and 10,348 nodes (Figure 3.3.1b). The third case had 7276 elements and 22,644 nodes (Figure 3.3.1c). Lastly, the fourth case had 8348 elements and 25,800 nodes (Figure 3.3.1c). The MARC program was used for the analysis.

The stress distribution for the elements located on the tooth fillet surfaces for both the loaded side (tensile stress) and unloaded side (compressive stress) is given in Figure 3.3.2. The stresses plotted were maximum principle stresses for the loaded side and minimum principle stresses for the unloaded side. All stresses were normalized with respect to the largest magnitude of minimum principle stress. The angle ψ ranged from 5° to 83° and represented elements from the top of the fillet to the root. The results for all refinement cases showed a gradual increase in stress as ψ varied from 5° to $\approx 30^\circ$, a maximum value in the range of $30^\circ < \psi < 40^\circ$, and a gradual decrease in stress as ψ varied from 40° to 83° . Table 3.3.2 gives the results of the largest magnitude of maximum and minimum principle stresses for the refinement study. A significant difference of the largest magnitude of maximum and minimum principle stresses was observed for the 3216-element model compared to the 1692-element model (6.9% and 7.0%, respectively). A significant difference was also observed for the 7276-element model compared to the 3216-element model (6.4% and 5.7%, respectively). The difference decreased as the mesh grew finer to the 8348-element model (2.3% and 2.8%, respectively). It was thus decided to use the 7276-element model for further studies to maximize the accuracy and minimize the computational requirements.

An initial attempt was made to analyze the 7276-element model using FRANC. The model, however, exceeded the memory size limit of FRANC. Thus, the 7276-element model was further reduced in size by reducing the number of elements away from the loaded tooth region. The resulting mesh had 2364 elements and 7334 nodes (Figure 3.3.3). This new model was compared to the previous 7276-element model using MARC and the stress distributions in the loaded tooth fillet region were essentially the same. Figure 3.3.4 is a plot of the Von Mises stresses for the loaded tooth region of the 2364-element model. Again, the tooth was loaded at the tip as stated in Table 3.3.1. The figure depicts a stress concentration on the surface of the fillet region on the loaded side (tensile stress) and on the unloaded side (compressive stress). The 2364-element model was then used in crack propagation studies using FRANC as described in the next section.

3.4 Gear Tooth Crack Propagation Modeling Using FRANC. The 2364-element model was used with FRANC to model crack propagation. The mouth of the initial crack was placed at the element corner node on the surface of the tooth fillet closest to the location of the maximum tensile stress ($\psi = 35^\circ$). The tip of the initial crack was arbitrarily placed at the adjacent corner node of the same element, approximately inward normal to the tooth surface, to give an initial crack length of 0.0104 in. The automatic crack propagation option of FRANC was used with a crack increment size of 0.0104 in.

The J-integral method to calculate crack tip stress intensity factors was used along with the maximum tangential stress theory for predicting crack propagation direction.

Figure 3.4.1 shows the mode I and II stress intensity factors as a function of crack length for 15 steps of predicted crack propagation. The mode I stress intensity factor gradually increased with increasing crack length, indicating unstable crack growth. Also, the values of the mode I stress intensity factors were significantly larger than the mode II stress intensity factors (K_{II}/K_I for each step ranged from 2 to 4 percent), indicating a relatively straight crack path. This was consistent with other reported results (Ahmad and Loo, 1977, Honda and Conway, 1979, and Flasket and Jezernik, 1983), but is unique in that an actual crack propagation path was predicted.

Figure 3.4.2 shows the mesh and the predicted crack path after 15 steps. Note that even though K_{II} was much less than K_I , it did have an influence as the predicted path had a slight curvature to it. Initially, the crack propagated toward the tooth root, then gradually changed direction and propagated only through the tooth itself. This type of propagation would cause only the tooth to crack off and lead to a benign failure mode, desirable in a design. For this case, the gear was solid and had a backup ratio of $m_B=3.3$.

A study was performed comparing the predicted stress intensity factors using the modified crack closure method, displacement correlation method, and J-integral method. Here, the same initial 2364-element mesh (before insertion of a crack) and same initial crack conditions were used. Also, the maximum tangential stress crack direction theory was used for all cases. There was virtually no difference in the K_I results (Figure 3.4.3a). In addition, there was virtually no difference in the K_{II} results for the displacement correlation method compared to the J-integral method, but a slight difference compared to the modified crack closure method (Figure 3.4.3b). This led to a slight deviation in crack propagation path predictions of the modified crack closure method compared to the other two methods, but in all practicality, all three methods predicted the same path (Figure 3.4.4).

A comparison was also made between the maximum tangential stress ($\sigma_{\theta\theta, max}$) crack propagation direction theory, strain-energy-density factor (S_{min}) theory, and maximum energy release rate (G_{max}) theory. Here once again, the same initial 2364-element mesh (before insertion of a crack) and same initial crack conditions were used. Also, the J-integral stress intensity factor method was used. Table 3.4.1 depicts the predicted stress intensity factors and crack propagation directions for all three theories. Note that even though the J-integral method was used for all cases, the predicted stress intensity factors were slightly different for each case since the different theories predicted slightly different crack tip positions. In all practicality, however, all three theories predicted the same crack propagation path. This was due to the fact that, as previously mentioned, all three theories converged to $\theta_m = -2 K_{II} / K_I$ (in radians) for the case when K_I was much greater than K_{II} (Figure 2.3.4).

As a final comparison, the effect of crack increment size on crack propagation path was investigated. The J-integral method and maximum tangential stress theory were used along with the initial 2364-element mesh (before insertion of a crack) and same initial crack conditions. Figure 3.4.5 gives the results of the predicted stress intensity factors and Figure 3.4.6 depicts the predicted crack paths. Crack increment sizes of 0.0052, 0.0104, and 0.0208 in. were used. Note that 0.0104 in. was the element size of the refined mesh in the tooth fillet region which produced maximum and minimum stress convergence. Also, 0.0208 in. was double this value and 0.0052 in. was half this value. All three crack increment sizes produced basically the same K_I results, slightly different K_{II} results, but in all practicality, same crack propagation paths.

In summary of the gear tooth crack propagation modeling, the J-integral method, displacement correlation method, and modified crack closure method produced similar results for predicted crack tip stress intensity factors. In addition, the $\sigma_{\theta\theta, \max}$ crack propagation direction theory, S_{\min} theory, and G_{\max} theory produced similar results for predicted crack directions since K_I was much greater than K_{II} . Also, a crack increment size equal to the length of an element of a refined mesh to accurately predict maximum stress gave consistent crack path predictions when compared to perturbations in size. Unless otherwise stated, all further results in this study will use the J-integral stress intensity factor method, maximum tangential stress crack propagation direction theory, and a crack increment size equal to the element length of the refined mesh.

It should be noted that the analysis in this section was all for a stationary load located at the gear tooth tip. In actual applications, the load on a gear tooth is not stationary but moves along the tooth as the tooth goes through mesh. The next section describes the analysis of a load at various positions along the tooth and its effect on crack propagation direction.

3.5 Effects of Gear Tooth Load Position on Crack Propagation Direction. A manual crack propagation procedure (Figure 3.5.1) was used instead of FRANC's automated method in order to analyze the effect of load position on gear tooth crack propagation. First, an analysis was performed which determined the proper load orientations on a gear tooth at various positions along the tooth profile (Appendix A). Next, the gear mesh with an initial crack as described in the previous section was analyzed using FRANC. Eighteen separate cases were run with unit loads placed at various nodes of three consecutive teeth (Figure 3.5.2a). Note that an initial crack was placed in the fillet (loaded side) of tooth 2 in Figure 3.5.2a even though it is not shown in the figure. Also, Figure 3.5.2b shows the load angle, ξ , and the roll angle, ϵ , for the eighteen different cases.

The crack tip mode I and II stress intensity factors for the unit load cases are shown in Figure 3.5.3. The symbols in the figure represent the actual stress-intensity-factor data points calculated by FRANC. The curves connecting the points were polynomial curve fits. The stress intensity factors are presented in three graphs corresponding to the cases where the loads were on tooth 1 (cases 1 through 6, Figure 3.5.3a), tooth 2 (cases 7 through 12, Figure 3.5.3b), or tooth 3 (cases 13 through 18, Figure 3.5.3c). For loads on tooth 2 (the cracked tooth), K_I was much larger than K_{II} , similar to the results of the previous section. Also, K_I increased as the roll angle increased. This was due to the increased tensile stresses caused by the increased load lever-arm. For loads on tooth 1, K_I was negative due to compressive stresses in the crack tip region. K_I was positive for loads on tooth 3 due to tensile stresses in the crack tip region. Note that the values of the mode I stress intensity factors were much lower for loads on teeth 1 and 3 compared to those for loads on the cracked tooth 2. This was due to the rather rigid gear rim structure for this model where the backup ratio was $m_B=3.3$.

Next considered were the actual loads on a gear tooth as it went through mesh. Computer program DANST (Dynamic ANalysis of Spur gear Transmissions) was used for this analysis. DANST was originally developed by Lin (Lin, et al., 1988a, and Lin, et al., 1988b) and its installation and use was described by Oswald, et al. (1993). DANST is based on a four-degree-of-freedom, torsional, lumped-mass model of a gear transmission. The model includes driving and driven gears, connecting shafts, motor, and load. The equations of motion for this model were derived from basic gear geometry and elementary vibration principles. The solution of dynamic tooth loads were found by numerically integrating the equations of motion.

For simplicity, however, the static gear tooth loads of the DANST solution were used. The static loads were determined from well-established gear tooth stiffness principles and static equilibrium. The static gear tooth load as a function of gear rotation angle, ω , for the gear as defined in Table 3.3.1 and

Figure 3.5.2 and a driving torque of 599 in-lb is shown in Figure 3.5.4. Tooth 2 began contact at a gear rotation of $\omega=10^\circ$. As the gear rotation increased, the load on tooth 2 gradually increased. In the region $10^\circ < \omega < 18^\circ$, teeth 1 and 2 shared the load. At $\omega=18^\circ$, tooth 2 carried the complete load (single-tooth contact) until a gear rotation angle of 23° . Then the load on tooth 2 gradually decreased as teeth 2 and 3 shared the load. For tooth 2, $\omega=18^\circ$ was considered the lowest point of single tooth contact (LPSTC) and $\omega=23^\circ$ was considered the highest point of single tooth contact (HPSTC).

The gradual increase and decrease of load on the teeth were due to profile modifications (deviations from a true involute) used in the model. Linear profile modifications (tooth profile relief as a linear function of gear roll angle) were used with the modifications starting at the HPSTC and ending with a maximum deviation at the tooth tip of 0.0005 in. These were the specifications of the test gears of the NASA Lewis Spur Gear Fatigue Rig later used in experimental studies (Chapter 4).

The actual gear tooth crack tip stress intensity factors as a function of gear rotation were then determined by multiplying the stress intensity factors previously determined using unit loads (Figure 3.5.3) by the actual tooth loads (Figure 3.5.4) and applying superposition since linear elastic fracture mechanics was used. Figure 3.5.5 gives the mode I results for the initial crack of 0.0104 in. Superposition was used to determine the stress intensity factors based on the combined loads of teeth 1, 2, and 3 (Figure 3.5.5d). The largest value of K_I occurred at the HPSTC ($\omega=23^\circ$). In a similar approach, Figure 3.5.6 gives the mode II results.

Figures 3.5.5d and 3.5.6d give the mode I and II stress intensity factors as a function of gear rotation. These results were used to determine crack propagation direction. The criteria of Mendelson and Ghosn (1986) was used. Again, the criteria stated that a crack propagated in the direction which gave the maximum change in tangential crack extension force. Figure 3.5.7 gives the tangential stress factor (proportional to the tangential crack extension force) as a function of gear rotation and θ -position where

$$\sigma_{\theta\theta} \sqrt{2\pi r} = K_I(\omega) \cos^3 \frac{\theta}{2} - 3K_{II}(\omega) \sin \frac{\theta}{2} \cos^2 \frac{\theta}{2} \quad (3.5.1)$$

where $K_I(\omega)$ and $K_{II}(\omega)$ were functions of gear rotation. For these results, the maximum change in the tangential stress factor occurred at $\theta_m=4.3^\circ$. Note that negative (compressive) tangential stress factors were not considered since they did not contribute to crack propagation. Also note that $\theta_m=4.3^\circ$ occurred at values of K_I and K_{II} where the tooth was loaded at the HPSTC ($\omega=23^\circ$).

After the analysis of the initial crack, the crack was then extended at a crack increment size of 0.0104 in. and an angle of $\theta_m=4.3^\circ$ using FRANC. FRANC re-meshed the vicinity of the new crack tip and the crack propagation direction of the new crack tip was determined using the procedure as described in the section. This procedure was repeated for a total of nine steps. Figure 3.5.8 gives the mode I and II stress intensity factors for each crack length, a . For all cases, the maximum K_I occurred at the HPSTC ($\omega=23^\circ$). Table 3.5.1 gives the predicted crack propagation angles for each step.

As a final note, the results using the cumbersome, manual, crack propagation procedure were compared to the results using FRANC's automated procedure. For the automated procedure, the tooth load was placed at the HPSTC which was the location which produced the largest K_I value. The stress intensity factor results and the predicted crack propagation directions were nearly the same as the results of the manual method. This occurred since K_I was much greater than K_{II} , and thus, the maximum tangential stress factor of Equation 3.5.1 was controlled by K_I . It was thus concluded that the automated crack propagation using FRANC could be used to model gear teeth if the load was placed at the location of the greatest K_I stress intensity factor.

3.6 Effect of Rim Thickness on Crack Propagation. In this section, the effect of rim thickness on crack propagation was investigated. Six different backup ratios were studied: $m_B=3.3, 1.0, 0.5, 0.4, 0.3,$ and 0.2 . The first case ($m_B=3.3$) was the solid gear which used the 2364-element model as described in Sections 3.3 and 3.4. All parameters, including location and length of the initial crack, were the same as described in Section 3.4, except the tooth load was placed at the HPSTC with components $F_x=341$ lb and $F_y=-129$ lb.

For the other five backup ratios, the same basic finite element model as that for $m_B=3.3$ was used except slots were inserted into the gear rim to locally model the loaded tooth as a thin rim gear. The tooth models were exactly the same for all cases, and thus, the parametric variation of backup ratio was a result of the various rim thicknesses. Figure 3.6.1 depicts two cases ($m_B=1.0$ and 0.3) and illustrates the insertion of slots in the models. The models had 2119 elements and 6668 nodes for $m_B=1.0$ and 0.5 , 1783 elements and 5660 nodes for $m_B=0.4$, 1615 elements and 5156 nodes for $m_B=0.3$, and 1351 elements and 4364 nodes for $m_B=0.2$.

Figure 3.6.2 shows the stress distribution on the loaded tooth fillet surfaces when no crack were considered (as predicted using the MARC program). The stresses plotted were maximum principle stresses for the loaded side and minimum principle stresses for the unloaded side. All stresses were normalized with respect to the largest magnitude of minimum principle stress for $m_B=3.3$. For all cases, the magnitude of the compressive stresses on the unloaded side of the teeth increased with decreasing backup ratio (Figure 3.6.2b). For the tensile stresses on the loaded side of the teeth, the magnitude slightly decreased as the backup ratio varied from 3.3 to 1.0, then slightly increased as $m_B<0.4$. Table 3.6.1 depicts the largest magnitude of maximum and minimum principle stresses for the various backup ratios modeled. As the backup ratio decreased to become thin-rim gears, the location of the largest magnitude of principle stresses moved toward the root area. This is significant in crack studies since crack initiation usually occurs at the location of the maximum tensile stress.

The six different backup ratios were re-analyzed using FRANC to include crack propagation. Initial cracks of 0.0104 in. were used in all cases. For each case, the initial crack mouths were placed at the tooth surface nodes closest to the locations of the maximum tensile stresses. Figure 3.6.3 shows the mode I and mode II stress intensity factors as a function of crack length. Figure 3.6.4 shows the predicted crack propagation paths. For $m_B=3.3$ and 1.0 , the crack propagated only through the tooth. For $m_B\leq 0.5$, the crack propagated through the rim.

From Figure 3.6.3, K_I was much greater than K_{II} for all cases. K_{II} , however, played an important role in crack propagation even though it was relatively small in magnitude. For the case of $m_B=0.5$, K_{II} was nearly zero throughout the simulation and the crack propagated in a straight path. For cases of $m_B>0.5$, K_{II} was negative which produced a positive crack propagation angle (relative to the x-y coordinate axes of Figure 2.5.2). This lead to a crack trajectory which cracked only the tooth off. For cases of $m_B<0.5$, K_{II} was positive which produced a negative crack propagation angle. This lead to crack propagation through the gear rim which should be avoided in the design of a gear set.

To gain further understanding of the effect of rim thickness on crack propagation direction, an analysis was performed in which the orientation of the initial crack was varied in the models of $m_B=3.3, 0.5,$ and 0.2 (Figure 3.6.5). For $m_B=3.3$, the crack propagated through the tooth, not the rim, for all orientation angles of the initial crack. Conversely, the crack propagated through the rim for all crack angle orientations of $m_B=0.2$. The predicted crack propagation path for $m_B=0.5$, however, was unstable. For a 0° initial crack (horizontal crack), the crack propagated through the tooth. For $30, 60,$ and 90° , the crack propagated through the rim. Thus, the case of $m_B=0.5$ for these studies was the transition point. For $m_B>0.5$, the crack propagated through the tooth. For $m_B<0.5$, the crack

propagated through the rim. For $m_B=0.5$, the crack path was unstable and depended on the initial conditions.

3.7 Fatigue Crack Growth of Gear Teeth. In this section, the predicted number of crack propagation cycles was investigated. The materials used in the analysis were AISI 9310 and SCM415. AISI 9310 is a relatively high hardenable, case-hardening steel with high core strength and good fracture toughness properties. It is commonly used for high-strength, low-weight applications such as helicopter or turboprop drive trains. AISI 9310 was also the material used in the experimental studies (Chapter 4). As previously stated, fatigue crack growth is based on material constants derived from experimental tests. Because of this, various results on AISI 9310 reported in the literature will now be presented.

Au and Ke (1981) reported on extensive studies conducted on consumable-electrode vacuum-melted AISI 9310 using the compact tension specimen. Carburized and non-carburized specimens were tested at a variety of load ratios, load cycle frequencies, and environment conditions (controlled dry air or wet air). The carburized specimens were through-hardened and tempered to a hardness of R_c 60 (Rockwell C scale) and representative of the case of a gear tooth. The non-carburized specimens had a hardness of R_c 37 and were representative of the core of a tooth.

Figure 3.7.1 gives the fatigue crack growth rate results from the Au and Ke tests. Plotted are linear curve fits (Paris equation) of the experimental data points. Also given are the Paris equation constants (for use in Equation 2.4.1) for the non-carburized specimens. The carburized specimens (lines 1 and 2) exhibited a higher slope than the non-carburized ones (lines 3 through 6), indicating a greater crack growth rate due to its increased hardness and increased brittleness compared to the non-carburized specimens. Good correlation was observed between lines 4, 5, and 6 of the non-carburized specimens. In a gear tooth, the non-carburized specimens are more applicable in fatigue crack growth predictions due to the relatively small hardened layer of the case.

Binder and Mack (1980) presented results for vacuum-arc-remelted (VAR) and vacuum-induction-melted, vacuum-arc-remelted (VIM-VAR) AISI 9310 steel. Again, compact tension specimens were used. Figure 3.7.2 gives the fatigue crack growth data along with the results from Au and Ke. Good correlation between the two references was observed for some cases (lines 7 and 9 with lines 4, 5, and 6).

Forman and Hu (1984) tabulated constants for a variety of materials using the Collipriest crack growth rate relationship (Equation 2.4.2). For AISI 9310, the material constants were: $n=1.63$, $C=8.36 \times 10^{-9}$ in/cyc/(ksi $\sqrt{\text{in}}$) n , $\Delta K_{th}=3.5$ ksi $\sqrt{\text{in}}$, and $K_{IC}=200$ ksi $\sqrt{\text{in}}$. Figure 3.7.3 presents these results compared to Au and Ke. The crack growth rate of Forman and Hu was significantly lower than that of Au and Ke, which would lead to a larger number of predicted life cycles. In contrary, DiRusso (1986) and Hanink (1979) report on a fracture toughness value of $K_{IC}=100$ ksi $\sqrt{\text{in}}$ for AISI 9310 at 300° F, compared to 200 ksi $\sqrt{\text{in}}$ from Forman and Hu. Thus, the material constants for crack growth rate reported by Forman and Hu appear to overestimate crack propagation life.

Lastly, crack growth studies on actual gears from Inoue, et al. (1991) were considered. Here, the Japanese steel SCM415 was used. SCM415 is also a high-hardenable, high-strength steel. Table 3.7.1 gives a comparison of the chemical composition of AISI 9310 (from Townsend and Bamberger, 1991) and SCM415 (Inoue, et al., 1991). The chemical composition along with the properties between the two materials are similar.

Figure 3.7.4 gives the crack growth rate of SCM415 using Inoue's method compared to Au and Ke's AISI 9310 results. The crack growth rate using Inoue's method was calculated for a variety of

hardnesses using Equations 2.4.3 through 2.4.9. The hardnesses ranged from 750 Hv (R_c 62), typical of a gear case, to 300 Hv (R_c 30), typical of a gear core. Fairly good correlation occurred between the lower hardness (300 Hv) SCM415 results and the non-carburized AISI 9310 specimens (lines 4, 5, and 6).

The predicted crack propagation cycles using the results of Au and Ke, Forman and Hu, and Inoue were compared. The crack growth rates, da/dN , were of the form

$$\frac{da}{dN} = g(\Delta K) \quad (3.7.1)$$

where $g(\Delta K)$ is given by Equation 2.4.1 for the Paris relationship, Equation 2.4.2 for the Collipriest relationship, or Equation 2.4.3 for Inoue's method. The predicted number of crack propagation cycles for the i_{th} crack increment, N_i , was estimated by

$$N_i = \frac{a_i - a_{i-1}}{g(\overline{\Delta K}_i)} + N_{i-1} \quad (3.7.2)$$

where a_i was the crack length of the i_{th} increment, a_{i-1} was the crack length of the $(i-1)_{th}$ increment, N_{i-1} was the number of cycles of the $(i-1)_{th}$ increment, and

$$\overline{\Delta K}_i = \frac{\Delta K_i + \Delta K_{i-1}}{2} \quad (3.7.3)$$

where ΔK_i and ΔK_{i-1} were the mode I stress intensity factor ranges of the i_{th} and $(i-1)_{th}$ increments, respectively. Note that a_1 was the initial crack length, $N_1=0$, and i varied from 2 to the total number of increments.

The predicted number of crack propagation cycles is given in Figure 3.7.5. The comparison was made for $m_B=3.3$ and the mode I stress intensity factor ranges were taken from Figure 3.6.3a. Six different cases were considered. The first four used the Paris equation and the Au and Ke material constants of the non-carburized specimens (lines 3, 4, 5, and 6). The fifth case used the Collipriest equation and the AISI 9310 material constants from Forman and Hu (line 10). The sixth case used Inoue's method for SCM415 (line 11). Note that a special algorithm was developed when Inoue's method was applied. First, the depth of the crack tip to the tooth surface was calculated at each crack increment. Next, the hardness of the material at each increment was estimated using the calculated depths and Equations 2.4.10 and 2.4.11. The crack growth rate was then calculated at each increment based on the hardness. Values used in Equations 2.4.10 and 2.4.11 were $H_1=H_2=710$ Hv (R_c 61), $H_3=375$ Hv (R_c 38), $d_2=0$ mm, and $d_{eff}=0.81$ mm (0.032 in). These values were based on hardness measurements of the tests gears from the NASA Lewis Spur Gear Fatigue Rig (Townsend and Bamberger, 1991). From Figure 3.7.5, a significant difference in the predicted number of stress cycles for the different cases was observed.

Lastly, the effect of rim thickness on crack propagation life was investigated (Figure 3.7.6). Six cases were compared ($m_B=3.3, 1.0, 0.5, 0.4, 0.3, 0.2$). For all cases, the Paris equation was used with $n=2.555$ and $C=2.721 \times 10^{-17}$ in/cyc/(psi \sqrt{in})ⁿ (line 5 of Au and Ke). The stress intensity factor ranges were taken from Figure 3.6.3a. The highest life occurred for $m_B=0.5$ since it had the lowest stress intensity factors. Also, a rather small difference in stress intensity factors between cases results in a significant difference in predicted life. This was caused by the stress intensity factor ranges being raised to some power in the crack growth rate equations.

In summary, this chapter presented results from crack propagation modeling of gear teeth. Gear finite element modeling was discussed and principles of linear fracture mechanics were used to simulate crack propagation. The effect of rim thickness on crack propagation direction and fatigue crack growth was investigated. In the next chapter, experimental results to validate the simulated predictions are discussed.

CHAPTER 4: EXPERIMENTAL STUDIES

4.1 Introduction. The objective of the experimental studies was to determine the effect of rim thickness on gear crack propagation direction and fatigue crack growth. In this chapter, the results of the gear tooth crack propagation experiments are presented. A description of the test facility, test gears, instrumentation, and test procedure is discussed along with the results of the tests.

4.2 Test Facility. The crack propagation experiments were performed in the NASA Lewis Spur Gear Fatigue Rig (Figure 4.2.1). The test stand operated on a torque-regenerative principle in which torque was circulated in a loop of test gears and slave gears. Oil pressure was supplied to load vanes in one slave gear which displaced the gear with respect to its shaft. This produced a torque on the test gears, slave gears, and connecting shafts proportional to the amount of applied oil pressure. A 25-hp, variable-speed motor provided speed to the drive shaft using a belt and pulley. Note that in a torque-regenerative principle, the required input drive power needs only to overcome the frictional losses in the system.

Separate lubrication systems were provided for the test gears and the main gearbox. The test gears were lubricated using a single oil jet at the in-to-mesh location. The main gearbox lubrication system provided oil to the loading vanes using a high-pressure pump. Also, the main gearbox lubrication system provided oil to the slave gears and support bearings. The test gear and main gearbox lubrication systems were separated by labyrinth seals on the gear shafts pressurized with nitrogen gas. Even though two separate systems existed, a common oil was used for both since some leakage occurred between the two. The lubricant used was a synthetic paraffinic oil and its properties are listed in Table 4.2.1. In addition, the test gear lubricant was filtered through a 5-micron fiberglass filter.

The NASA Lewis Spur Gear Fatigue Rig was primarily developed for surface pitting fatigue life investigations. For surface pitting fatigue tests, the test gears are run offset as shown in Figure 4.2.1 to increase the tooth contact stress and promote surface fatigue. For the current crack propagation studies, however, the desired failure mode was tooth bending fatigue. Therefore, the gears were run full contact, not offset.

4.3 Test Gears. The test gears are shown in Figure 4.3.1. The test gear geometry data are given in Table 4.3.1. The gears were external spur gears. The teeth had involute profiles with linear tip relief starting at the HPSTC and ending at the tooth tip. The maximum amount of tip relief was 0.0005 in. at the tooth tip.

All gears used in the experiments were fabricated and machined from a single batch of material. The test gear material was consumable-electrode vacuum-melted AISI 9310 steel. The gears were case-carburized and ground. The teeth were hardened to a case hardness of R_c 61 and a core hardness of R_c 38. The effective case depth (depth at a hardness of R_c 50) was 0.032 in.

To determine the effect of rim thickness on crack propagation, slots were machined in some gears to emulate various rim thicknesses. Backup ratios of $m_B=3.3$ (no slots), 1.0, 0.5, and 0.3 were tested (Figure 4.3.2).

The maximum load capacity of the test rig was approximately 700 lb normal tooth force. The parameters for the AGMA bending stress index (Equation 1.2.1) at this load were: $W_t=700 \cos 20^\circ = 658$ lb, $P_d=8$ teeth/in., $f=0.25$ in., and $J=0.36$ (AGMA, 1989). Setting $K_a=K_v=K_s=K_m=K_B=1$ gave a bending stress index of

$$s_t = \frac{(658)(1)}{(1)} \frac{(8)}{(.25)} \frac{(1)(1)(1)}{(.36)} = 58 \text{ ksi} \quad (4.3.1)$$

An accepted value of the AGMA allowable bending stress index for AISI 9310 gears was $s_{at}=65$ ksi (AGMA, 1988). Based on these findings, it was believed that tooth bending fatigue cracks would be difficult to initiate. Due to this, notches were fabricated in the fillet region (loaded side) on one tooth of each of the test gears to promote crack initiation.

Table 4.3.2 gives the notch dimensions of the test gears used in the experiments. Figure 4.3.3 shows a magnified view of a typical notched tooth. The notches were fabricated using electrodischarge machining (EDM) with a 0.004-in. diameter wire electrode. The measured notch dimensions ranged from lengths of 0.005 to 0.013 in. and widths from 0.004 to 0.009 in. The notches were located at the same location for all the gears. This location was at a radius of 1.594 in. on the fillet which was the position of the greatest tensile stress for the solid gear ($m_B=3.3$). The notches produced a stress concentration factor of approximately three as determined using a finite element analysis (Chapter 5).

4.4 Instrumentation. The standard test rig instrumentation monitored test gear speed, oil load pressure, test gear and slave gear oil pressure, and oil temperatures. Also, overall test stand vibration was monitored using an accelerometer mounted on the top housing. In addition to the standard facility vibration sensor, an advanced vibration processing system was installed in the test stand to help assist in crack detection.

A schematic of the advanced vibration processing system is shown in Figure 4.4.1. Here, a high-frequency accelerometer was mounted on the test gear oil-seal cap near the shaft support bearing. The accelerometer had integral electronics, a sensitivity of ≈ 12 mV/g, and a resonant frequency of 100 kHz. The accelerometer output was connected to an anti-aliasing filter. The filter was set at either 20 or 40 KHz, depending on the test. The filter output was routed to an analog-to-digital (A/D) board of a personal computer. The A/D board was programmed at 125-kHz acquisition rate. An infrared sensor was also connected to the computer. The infrared sensor produced a tach pulse for every rotation of the test gear shaft and its filter and A/D settings were the same as that for the accelerometer.

Gear fault detection techniques used in the vibration processing system were those studied by Zakrajsek (Zakrajsek, 1989, Zakrajsek, et al., 1993, and Zakrajsek, et al., 1994). First, vibration data were time-averaged. For this, the computer concurrently collected accelerometer and tach pulse data. The digitized accelerometer data were assembled in blocks corresponding to test gear shaft rotations using the tach pulse signal as a reference. For each block, data were interpolated to 1024 points per revolution. One-hundred blocks were collected and then averaged in the time domain. The time-domain averaging allowed the vibration of the test gears to be separated from the vibration of the complete system.

A variety of gear fault detection techniques were applied to the time-averaged signals. The first was the FM0 parameter developed by Stewart (1977). FM0 was defined as

$$FM0 = \frac{\text{peak-peak level of the time-averaged signal}}{\sum \text{amplitudes of gear mesh frequencies/ harmonics}} \quad (4.4.1)$$

FM0 was formulated to be a robust indicator of major faults in a gear mesh by detecting major changes in the meshing pattern.

A second technique was the FM4 parameter, also developed by Stewart (1977). FM4 was defined as

$$FM4 = \frac{(1024) \sum_{i=1}^{1024} (D_i - D_M)^4}{\left[\sum_{i=1}^{1024} (D_i - D_M)^2 \right]^2} \quad (4.4.2)$$

where D_i was the i_{th} data point of the difference signal defined as

$$D_i = A_i - M_i \quad (4.4.3)$$

where A_i was the i_{th} point of the time-averaged signal, and M_i was the i_{th} point of the regular-meshing-components signal. The regular-meshing-components signal was defined as the time-averaged vibration at the gear mesh fundamental frequency and harmonics, first-order sidebands about the gear mesh fundamental frequency and harmonics, and gear shaft fundamental and second and third harmonic frequencies. D_M was defined as the mean value of the difference signal where

$$D_M = \frac{1}{1024} \sum_{i=1}^{1024} D_i \quad (4.4.4)$$

FM4 was developed to indicate initial localized gear tooth damage. FM4 is dimensionless and has a nominal value of three for an undamaged gear.

Another method used was the NA4 parameter. NA4 was a method developed by Zakrajsek, et al. (1993) not only to detect the onset of damage, as FM4 does, but also to continue to react as damage spreads. NA4 was defined as

$$NA4(T) = \frac{(1024) \sum_{i=1}^{1024} (D_{i,T} - D_{M,T})^4}{\left[\frac{1}{T} \sum_{j=1}^T \left[\sum_{i=1}^{1024} (D_{i,j} - D_{M,j})^2 \right] \right]^2} \quad (4.4.5)$$

where T was the current time record of the run, $D_{i,T}$ was the i_{th} data point of the difference signal for the T_{th} time record, $D_{M,T}$ was the mean value of the difference signal for the T_{th} time record, $D_{i,j}$ was the i_{th} point of the difference signal for the j_{th} time record, and $D_{M,j}$ was the mean value of the difference signal for the j_{th} time record. The difference signal used for NA4 was the same as that used for FM4 except the first-order sidebands about the gear mesh fundamental and harmonic frequencies were included. The denominator of NA4 allowed the difference signal to be constantly compared to the running average of a gear system in good condition. This allowed NA4 to grow with the severity of the fault until the average of the gear system grew itself. As with FM4, NA4 is dimensionless and has a nominal value of three for an undamaged gear.

The parameters FM0, FM4, and NA4, along with the root-mean-square (rms) value of the time-averaged signal were processed on-line during the gear tests to help indicate crack initiation. The accelerometer data were continuously monitored and the data were processed as quickly as possible on a 486/33 MHz personal computer. This resulted in output of the vibration parameters every one minute.

In addition to the advanced vibration processing, crack propagation gages were used in the experiments to estimate fatigue crack growth. Special gages were fabricated for installation in the tooth fillet region of the test gears. The gages had ten circular strands with an inner radius of 0.060 in. and

an outer radius of 0.120 in. (Figure 4.4.2a). The strands were designed to break as the crack propagated through them, which in turn, increased the electrical resistance of the gage (Figure 4.4.2b). Figure 4.4.3 shows the installation of a gage in the fillet region of a notched tooth. A gage was installed on each side of the tooth flank for each gear instrumented with crack gages. Figure 4.4.4 shows the data acquisition setup for the crack gages. The electrical resistance of the crack gages were monitored along with the load cycle count to estimate cycles as a function of crack length. The information from the rotating crack gages was transferred through brush-type slip rings. Also, the same infrared sensor from the vibration processing was used for the cumulation of load cycles.

Lastly, the test rig did not have a direct indication of shaft torque. A static calibration was performed to correlate oil load pressure with shaft torque. For this, the test gears were assembled in the rig with the test-gear cover removed. The test gears were assembled in an offset condition such that engagement did not occur. The left test gear was locked to the rig support frame to prohibit rotation. A torque wrench with a dial indicator was installed on the shaft of the right test gear. The high-pressure lubrication system was started and load pressure was applied. The load pressure rotated the right test gear clockwise until the vane in the slave gear reached its stop. Torque was manually applied on the right test gear using the torque wrench in the opposite direction of the load pressure until slippage occurred. At slippage, the torque indicated from the torque wrench equalled the applied torque. This torque was recorded at a variety of load pressures. Figure 4.4.5 gives the results of the calibration.

4.5 Test Procedure. The objective of the tests was to determine the effect of rim thickness on gear crack propagation direction and fatigue crack growth. The results would then be used to validate the analytical predictions (Chapter 5). Eleven tests were performed and the corresponding test gear serial numbers (S/N's) are given in Table 4.3.2. For tests 1 through 8, the notched gears were the driver gears of the test pair. Unmodified gears fabricated from the same batch of material as the notched gears were used as the driven gears. For tests 9 through 11, the notched gears were instrumented with crack propagation gages. The notched gears for these tests were installed on the driven side due to slip ring considerations. Unmodified gears fabricated from the same batch of material were used as driver gears.

The test procedure for all tests was basically the same. First, the test gears were cleaned to remove any protective coating from original manufacturing or debris caused from the notch fabrication, and installed in the rig. Next, an oil-scavenging vacuum system and a high-pressure nitrogen system were energized. Next, the test gear and main gearbox oil pumps were started. The load pressure on the vanes was set at 50 psi to apply a light torque in the system and the drive motor was started. The test gear speed was adjusted to 10,000 rpm for all tests. After reaching full speed, the load pressure was adjusted to obtain the desired stress level of the gear teeth. After reaching the desired load pressure, a strip chart recorder monitoring oil temperatures was turned on along with the vibration processing system.

At the start of each test, all gears were initially run at 50 psi load pressure for one hour as a break-in procedure. After break-in, the load pressure was set for the required test conditions. These conditions ranged from 100 to 475 psi, depending on the test. The gears were run at a steady load condition until failure occurred or a different load level was desired. Test gear oil inlet temperature was $102 \pm 3^\circ \text{F}$. Test gear oil outlet temperature was stable (fluctuation $< \pm 1^\circ \text{F}$) and was a function of the load pressure. As an example, the oil outlet temperature was 140°F at 100 psi load pressure and 175°F at 475 psi load pressure. After occurrence of a failure (tooth or rim breakage), the gears were removed from the rig, cleaned, and photographed.

4.6 Test Results. The load history and vibration results for test 1 (S/N 01, $m_B=3.3$) are shown in Figure 4.6.1. The load was gradually increased in step increments as the run progressed. It was desired to run the tests at the lightest possible load that would still produce crack initiation. This was

desired to minimize rig wear (bearings and splines), retard crack propagation once it started (in order to enhance it's measurement), and for general safety concerns since tooth or rim fractures were the failure modes. After the 1-hr. break-in, the test was run for 4.2 hr. at 100 psi load pressure, 2.8 hr. at 250 psi, and 0.4 hr. at 475 psi (maximum load available from rig). Tooth fracture occurred at 8.4 hr. total run time and at 475 psi load pressure (Figure 4.6.2). Fracture originated at the tip of the fabricated notch and propagated through only the tooth and not the gear rim. The fracture occurred uniformly throughout the gear tooth face width.

During the test it was desired to initiate a crack, record the initial crack geometry, then propagate the crack until tooth or rim failure occurred. With this in mind, the notched test gear was removed from the rig and inspected under a microscope at 5.2 and 8.0 hr. run time. No crack initiation, however, was detected at these inspections. It appeared from the vibration parameters that the tooth fracture occurred rapidly at the end of the test. Table 4.6.1 gives a listing of the vibration parameter results for the last 0.4-hr. of testing. All vibration parameters (rms, FM0, FM4, and NA4) gave clear indication once the tooth was completely broken off from the gear. NA4 gave the most robust indication. From the time interval 8.2333 to 8.2500 hr., the NA4 parameter significantly increased (3.30 to 3.88) indicating start of fracture. At a run time of 8.2667 hr., complete tooth fracture had occurred.

The load history and vibration parameters for test 2 (S/N 02, $m_B=3.3$) are given in Figure 4.6.3. Again, the load was gradually increased during the test. The gears were run at 250 psi load pressure for 9.0 hr., 300 psi for 7.0 hr., 350 psi for 7.0 hr., and 400 psi for 3.4 hr. Fracture occurred at 27.4 hr., originated at the notch tip, and propagated through the tooth uniformly throughout the tooth face width (Figure 4.6.4). Table 4.6.2 gives the vibration parameters for the last 0.4 hours of testing. Again, NA4 gave the most robust indication of failure. The value of NA4 significantly rose at 27.2250 hr. indicating start of fracture. Complete tooth fracture had occurred by 27.4333 hr.

Based on the experience of test 1 and 2, it was decided to perform the majority of the remaining tests at 400 psi load pressure. For test 3 (S/N 03, $m_B=1.0$), the gears were run at 400 psi load pressure for a total of 3.9 hr. (Figure 4.6.5). At approximately 2.5 hr. total run time, the load pressure began to gradually decrease. The decrease in load pressure was due to excessive rig vibration (and resulting load vane oil leakage) due to worn shaft bearings. It was also noticed that the NA4 parameter reacted to changes in applied load, and thus, decreased as the load pressure decreased. The test rig was completely disassembled and refurbished with new bearings. The test gears were re-installed and testing resumed at 400 psi load pressure. The test concluded at 4.9 hr. run time at which tooth fracture occurred. Tooth fracture again originated at the fabricated notch and propagated through the tooth (Figure 4.6.6). Unfortunately, drive belt slippage occurred during the last hour of running which affected the tach pulse of the vibration processing system. Due to this, the vibration results of the last hour of running were erroneous.

Test 4 (S/N 04, $m_B=1.0$) was also run at 400 psi load pressure but was inconclusive. At 22.9 hr. total run time, no crack initiation occurred and the test was suspended. Test 5 (S/N 05, $m_B=0.5$) was run at 400 psi load pressure and was concluded after 5.4 hr. total run time (Figure 4.6.7). At 5.4 hr., a crack originated at the fabricated notch, propagated in a straight path for a short distance, then turned direction and propagated through the gear rim (Figure 4.6.8). All vibration parameters except FM4 gave clear indication of the rim failure (Figure 4.6.7).

Test 6 (S/N 06, $m_B=0.5$) was run at 400 psi load pressure for 27.0 hr. and then 475 psi for 0.9 hr. At this time, rim failure occurred (Figure 4.6.9). A crack started at the fabricated notch and propagated through the rim similar to test 5. In addition, secondary rim damage occurred due to the high

dynamic loads caused by the rim failure. The rim was broken in two pieces as a result. The vibration results for test 6 were not available due to tach pulse instrumentation problems.

Test 7 (S/N 07, $m_B=0.3$) ended after only 9 min. of testing at 400 psi load pressure (Figure 4.6.10). A crack started at the notch and propagated directly through the rim (Figure 4.6.11). The crack propagated too quickly to be detected by the vibration system in the 1-min. intervals. Test 8 (S/N 08, $m_B=0.3$) was run at only 300 psi load pressure (Figure 4.6.12) due to the sudden failure of test 7. After 3.8 hr. at this load, rim fracture occurred similar to test 7 (Figure 4.6.13).

The objective of tests 9 through 11 was to experimentally measure fatigue crack growth of gear teeth. Test 9 (S/N 11, $m_B=0.3$) was run at 300 psi load pressure (Figure 4.6.14). Rim fracture occurred at 7.5 hr. total run time (6.5 hr. at 300 psi load pressure). A 486/60 MHz personal computer was used for collection of the vibration data for tests 9 through 11. The data collection was increased from once every minute (as was done in the previous tests) to once every fifteen seconds due to the increased computer speed. Permanent data was saved every 5 minutes. In addition, data was saved every fifteen seconds for the last 25 minutes of the test. Again, NA4 gave the most robust indication of failure.

Two crack propagation gages were installed on test gear S/N 11, one on the front tooth flank and one on the rear flank. The inner radii of the crack gages were positioned at the notch tip. Figure 4.6.15 gives the crack gage electrical resistances as a function of load cycles. Note that the figure was for the run time at 300 psi load pressure only and neglected the 1-hr. break-in. The gage resistances as a function of load cycles were noisy at times. The noise was due to a combination of slip ring noise and crack gage noise. Slip ring noise resulted from changes in resistance of the brush contacts during shaft rotation. Crack gage noise resulted from cyclic compression in the rim of the gear tooth during mesh (from rim deformation) which caused broken strands to contact. Even with the noise, however, discrete steps in the response were obtainable.

The discrete steps in the response of the crack propagation gages lead to measurement of gear tooth crack propagation rate (Table 4.6.3). The electrical resistance measurements of each step increment lead to calculation of the number of broken strands for the increment using the calibration curve of Figure 4.4.2b. Once the number of broken strands was known, the crack length was estimated from an enlarged photograph (64X) of the cracked gear. The crack length was then correlated to cycle count using the start and end cycles of the step increment. Figure 4.6.16 gives the measured crack propagation cycles for test 9 (S/N 11, $m_B=0.3$).

The crack gage results indicated the crack growth was non-uniform throughout the tooth face width. A crack started on the rear flank of the tooth at the tip of the notch and reached an initial size of 0.018 in. at 1,060,000 cycles (Table 4.6.3). The crack continued to propagate through the rear flank but did not reach the front flank until approximately 2,680,000 cycles. At 2,910,000 cycles, the crack reached a size of 0.025 in. on the front flank, but completed propagated through the rear gage by this time. Even though the crack initiation time was not uniform throughout the tooth face width, the crack propagation rate was uniform. This was indicated by the similarity in slopes of the curves in Figure 4.6.16 for gages 1 and 2. Figure 4.6.17 shows a photo of the cracked rim for test 9. For all the previous tests (test 1 through 8), the cracks were rather uniform throughout the tooth face widths. For test 9, the crack paths on the front and rear flanks (Figure 4.6.17a and 4.6.17b, respectively) were rather different. Figure 4.6.17c shows an isometric view of the rim failure and emphasizes the three-dimensional effects.

Test 10 (S/N 12, $m_B=0.3$) was also run at 300 psi load pressure and produced a rim fracture at 2.6 hr. total run time (Figure 4.6.18). The test gear was instrumented with two crack propagation gages

similar to that of test 9. The results were inconclusive with respect to crack growth measurements due to excessive slip ring noise in the crack gage signals. An interesting observation, however, was noted during the test. At 2.5 hr. total run time, the crack gages indicated that fracture occurred through the rear gage and just started through the front gage, similar to that of test 9. At that time, the test gear was removed from the rig and photographed. Sure enough, a crack started on the front flank (Figure 4.6.19a) and completely broke through the gage on the rear flank (Figure 4.6.19b). This was a visual verification of the integrity of the crack propagation gage. The test gear was re-installed in the test stand and the crack quickly broke through the complete rim (Figure 4.6.20).

For the last test (test 11), a solid gear (S/N 13, $m_B=3.3$) was instrumented with crack gages and run at 450 psi load pressure (Figure 4.6.21). Before the test, a replacement slip ring was installed in the rig. The signals from the crack propagation gages had significantly less noise than the previous tests (Figure 4.6.22). There were two reasons for this. The first reason was the reduced noise of the replacement slip ring. The second reason was the stiffer rim of the test gear which resulted in reduced compression of the crack gages during mesh.

Table 4.6.4 and Figure 4.6.23 give the processed crack propagation results for test 11. At 1.30 hr. total run time, tooth fracture occurred. The crack initiation and crack propagation was uniform throughout the tooth face width for this test. Figure 4.6.24 gives a photo of the front and rear tooth flanks after failure.

Table 4.6.5 summarizes the crack initiation and crack propagation lives for tests 9 through 11. It was difficult to define the exact number of cycles when crack initiation occurred, and then, crack propagation began, since an initial crack had to exist in order to measure it. Thus, the measurement of crack initiation cycles had some uncertainty to it. Regardless, the crack propagation life was a significant portion of the total life. The advanced vibration diagnostics system gave little indication of crack propagation and only reacted at the end of the tests when significant crack propagation had already occurred.

In summary, this chapter presented results from the crack propagation experiments. The objective was to determine the effect of rim thickness on crack propagation direction and crack propagation life. In the next chapter, the experimental results are compared to analytical predictions.

CHAPTER 5: COMPARISON OF EXPERIMENTS WITH ANALYSIS

5.1 Introduction. In this chapter, predicted crack propagation modeling is compared with the experimental studies. The modeling technique described in Chapter 3 was refined to closely match the test gears used in the experiments. Crack propagation paths for various rim thicknesses were compared. In addition, predicted crack propagation cycles as well as crack initiation cycles were compared to the experiments.

5.2 Modeling of Test Gears. The test gears used in the experimental studies (Chapter 4) were analyzed using the finite element method. The finite element models were the same as the models presented in Chapter 3 with two exceptions. First, the tooth profiles were modified to closely match those of the test gears. Second, notches were introduced into the models.

The first step in modeling the test gears was to accurately determine the tooth, fillet, and root profiles. The actual profiles of sample test gears taken from the same batch as tested in Chapter 4 were measured using an optical coordinate measuring machine. The optical coordinate measuring machine produced an image of the tooth magnified to 20-times the original size. This image was compared to analytical profiles produced from the GPAT program.

The tooth, fillet, and root profiles produced by GPAT using the input parameters of Table 3.3.1 were slightly different than the measured test gear profiles. A study was performed varying the GPAT input parameters and the following combinations produced the closest profile to that of the test gears: 28-tooth gear, $P_d = 8$ teeth/in., $\phi = 20^\circ$, $a_g \cdot P_d = 1.05$, $d_g \cdot P_d = 1.35$, $r_c \cdot P_d = 0$, and $e \cdot P_d = -0.05$. It should be noted that the fillet profile produced using these parameters still slightly deviated from that of the tests gears. With this in mind, the fillet coordinates produced from the GPAT program were manually adjusted to accurately model the test gears. Figure 5.2.1 shows the tooth profiles produced from the original model of Chapter 3 and the revised model which matched that of the test gears.

In addition to the revised tooth coordinates, a notch was introduced into the finite element model. An algorithm was developed which used the measured notch lengths, widths, and angles (Table 4.3.2) as input and assembled the appropriate P3/PATRAN commands to incorporate the notch in the finite element model. The methodology behind the algorithm is given in Appendix C.

A close-up of the notch from a sample finite element model is given in Figure 5.2.2a. This model was for S/N 01, $m_B = 3.3$ (solid gear). The complete model for this example was similar to that shown in Figure 3.3.3, but had the modified tooth and root profiles as described earlier in this section in addition to the notch. One goal of incorporating the notch in the model was to calculate the stress concentration factor at the notch tip. A mesh refinement study was performed to determine the effect of element size on maximum tensile stress. Refinement 1 (Figure 5.2.2b) split each quadrilateral element on the notch surface into four smaller quadrilateral elements. Refinement 2 (Figure 5.2.2c) split each of the notch surface elements of refinement 1 into four elements. The original notch model had 2850 elements and 8806 nodes, while refinement 1 had 2878 elements and 8898 nodes, and refinement 2 had 2926 elements and 9052 nodes. The calculated maximum principle stress (using the MARC program) for the original notch model was 111.5 ksi, located at the notch tip. The calculated maximum principle stress for refinement 1 was 124.9 ksi (12.1% increase). The calculated maximum principle stress for refinement 2 was 128.9 ksi (3.2% increase compared to refinement 1). Refinement 1 was a relatively straight forward procedure using P3/PATRAN. Refinement 2, however, required considerably more effort due to the extremely small element sizes. Refinement 1 was therefore chosen as the method for further studies based on the accuracy and ease of model development.

Figure 5.2.3 shows the calculated Von Mises stress distribution of the notched and un-notched models of test gear S/N 01 ($m_B=3.3$). As previously stated, the tensile stress was concentrated on the fillet surface for the un-notched model (Figure 5.2.3a, maximum principle stress of 42.2 ksi). The effect of the notch was to further concentrate the tensile stress at the notch tip (Figure 5.2.3b, maximum principle stress of 124.9 ksi). This produced a stress concentration factor of $124.9/42.2 = 2.96$ for the notched specimen. The notched model used the refinement 1 mesh configuration. The notch had no effect on the compressive stress distribution for the unloaded side of the tooth.

Finite element models were created to analyze test gears S/N 02 through 08. In addition, notches were introduced in these models. For the slotted gears (S/N 03 through 08), finite element models similar to those shown in Figure 3.6.1 were used. In all cases, the models used the tooth profiles as described earlier in this section. Table 5.2.1 lists the calculated principle stresses with and without the notches. The stress concentration factors were functions of notch length, notch width, and backup ratio, and ranged from 2.41 to 3.38.

5.3 Crack Path Comparison. FRANC was used to simulate crack propagation for test gears S/N 01 through 08. The finite element models with notches as previously described were used. For all cases, the mouths of the initial cracks were placed at the nodes located at the tip of the notches. The lengths of the initial cracks were all 0.01 in. and at the same angles as the notches as stated in Table 4.3.2. As before, the tooth load was placed at the HPSTC and the hub corner nodes were fixed in the x and y -directions for all cases.

The mode I and II stress intensity factors for the simulated crack propagation of test gears S/N 01 through 08 are shown in Figure 5.3.1. The overall trends were similar to those presented in Chapter 3 (Figure 3.6.3). There was a slight increase in the mode I stress intensity factors due to the narrower tooth width in the fillet region of the test gears compared to those of Chapter 3. In Figure 5.3.1, the only difference between the models of similar backup ratios were notch dimensions, and thus, initial crack locations. That is, the model for gear S/N 01 was the same as that for S/N 02 except for the notch, S/N 03 was same as S/N 04 except for the notch, and so on. The differences were rather minor and the calculated stress intensity factors for identical backup ratios were nearly the same.

The predicted crack propagation paths for the models of the test gears are shown in Figure 5.3.2. Also shown for comparison are the results of the experiments. For backup ratios $m_B \geq 1.0$, the cracks propagated through the teeth and the correlation between predicted crack paths and experiments was rather good (Figures 5.3.2a, 5.3.2b, and 5.3.2c). For the other extreme of $m_B=0.3$, the cracks propagated through the rim, and again, the correlation between predictions and experiments was good (Figures 5.3.2f and 5.3.2g). A discrepancy occurred for the $m_B=0.5$ cases (Figures 5.3.2d and 5.3.2e). The predicted crack paths for these cases propagated in a fairly straight path with a slight tendency back toward the tooth. The crack paths from the experiments, however, propagated through the rims.

As was previously addressed, the predictions for the $m_B=0.5$ case was unstable and the crack paths were dependent on initial conditions. Figure 5.3.3 shows the predicted paths for $m_B=3.3$, 0.5, and 0.3 at various initial crack angles. This analysis was similar to that of Figure 3.6.5 except the modified tooth profile to match that of the test gears was used as well as notches. The results were similar in that the paths for $m_B=3.3$ were all through the tooth, the paths for $m_B=0.3$ were all through the rim, and those for $m_B=0.5$ were dependent on the initial conditions. Figure 5.3.4 shows the predicted crack paths when the backup ratio was slightly varied from the $m_B=0.5$ case. This was accomplished by removing layers of elements in the rim-slot region of the $m_B=0.5$ model. The result was that a small variation in backup ratio significantly affected the predicted crack path directions. Figure 5.3.5 shows the effect of tooth load location on predicted crack paths for $m_B=0.5$. These locations of tooth load may possibly be

the load locations which give the greatest stress intensity factors if dynamic loads are incorporated in the analysis. The load position had a slight effect on predicted crack path.

The purpose of Figures 5.3.3, 5.3.4, and 5.3.5 was to demonstrate the instability of the predicted crack paths for $m_B=0.5$. At $m_B=0.5$, various conditions such as initial crack angles, load positions, or small perturbations of the backup ratio affected the stress field in the tooth and rim region enough to significantly alter crack path direction. It is obvious from Figures 5.3.2d and 5.3.2e that the stress fields of the gears during testing were slightly different than that modeled since the predicted crack paths diverged from the experimental results. It was not known exactly what these differences were. One possibility could have been residual stress fields in the test gears due to the fabrication of the slots. Another possibility could have been slight deviations in the model and notch dimensions and initial crack locations compared to the tested gears due to measurement errors. Overall, considering all cases modeled and tested, the predictions correlated well with the experiments. Care and conservatism should be used, however, when modeling thin-rim gears where the transition from tooth failure to rim failure occurs.

Figure 5.3.6 presents one last thought on crack propagation modeling with notched specimens. This case was for $m_B=3.3$ and compared the notched-tooth model with an un-notched model. As before with the notched model, the initial crack mouth was placed at the node located at the notch tip and the initial crack tip was placed at a 0.01-in. length. For the un-notched model, the initial crack tip was placed at the same location as the notched model and the initial crack mouth was placed on the node of the tooth surface closest to the notch mouth. The predicted mode I and II stress intensity factors were virtually the same. It was concluded that the notch itself had no influence on the crack propagation other than locating the position of the initial crack.

5.4 Crack Propagation Life Comparison. In this section, crack propagation life predictions are compared to experimental results. FRANC was used to simulate crack propagation of test gears S/N 11 and 13. The calculated mode I stress intensity factors from FRANC were used to calculate fatigue crack propagation cycles based on the methods presented in Section 3.7 and the results were compared to the experiments.

The finite element model of S/N 11 ($m_B=0.3$) was based on the model previously developed for S/N 07, but without a notch. Two cases were analyzed for S/N 11. The first case modeled the front tooth flank of test 9 and the results were compared to crack propagation gage 1. The second case modeled the rear tooth flank and was compared to the results of gage 2. For case 1, the mouth of the initial crack in the analysis was placed at the same location as the mouth of the notch of test gear S/N 11 (this was at a radius of 1.5947 in. on the tooth fillet surface). The tip of the initial crack was placed at a distance of 0.025 in. from the crack mouth and at the same angle as the crack observed from test 9 ($\approx 40^\circ$). This corresponded to point 2 for gage 1 in Table 4.6.3. For case 2, the mouth of the initial crack was also placed at the location of the mouth of the notch of test gear S/N 11. The initial crack tip, however, was placed at the location corresponding to the crack position of gage 2 point 2 in Table 4.6.3 (0.018 in. initial crack length).

The finite element model of S/N 13 ($m_B=3.3$) was based on the model previously developed for S/N 01, but without a notch. The mouth of the initial crack for this analysis was placed at the same location as the notch mouth for S/N 01 (also at a 1.5947-in. radius). The initial crack tip was placed at a distance of 0.008 in. from the crack mouth corresponding to an average of the front and rear flank cracks observed from test 11 (Table 4.6.4, point 2 for gages 1 and 2).

The calculated mode I stress intensity factors for the models of S/N 11 case 1, S/N 11 case 2, and S/N 13 are given in Table 5.4.1. The stress intensity factors for S/N 11 were calculated for a 300-

psi load pressure which corresponded to a 478-lb tooth normal load using the calibration of Figure 4.4.5. For S/N 13, the stress intensity factors were calculated for a 730-lb tooth normal force (450 psi load pressure). Six different prediction schemes were used to estimate fatigue crack propagation cycles. The first four schemes used the Paris equation (Equation 2.4.1) and used the constants of the non-carburized AISI 9310 material tests of Au and Ke (1981) (lines 3 through 6 of Figure 3.7.1). The fifth scheme used the Collipriest equation (Equation 2.4.2) and the AISI 9310 material constants referenced by Forman and Hu (1984) (line 10 of Figure 3.7.3). The sixth scheme used the method of Inoue (Equation 2.4.3) for SCM415 steel. For the Inoue method, the special algorithm as well as the material hardness constants described in Section 3.7 were used.

The calculated number of crack propagation cycles using the sixth schemes and the stress intensity factors of Table 5.4.1 was, on the most part, extremely low compared to the measured number of cycles from the experiments. To account for this, the concept of fatigue crack closure was investigated. Elber (1971) performed crack experiments on aluminum alloys and deduced that residual compressive stresses existed near the crack tip region due to plastic deformation. These residual stresses reduced the effective stress intensity factor range (and thus, increased predicted crack propagation life) and provided a better fit to experimental data than other empirical expressions. Elber proposed an effective stress intensity range ratio, U , such that

$$\Delta K_{eff} = U (\Delta K) \quad (5.4.1)$$

where ΔK_{eff} was the effective stress intensity factor range. The effective stress intensity factor range was then used in the Paris fatigue crack growth model as

$$\frac{da}{dN} = C (\Delta K_{eff})^n \quad (5.4.2)$$

Elber further defined U through experimental studies as

$$U = 0.5 + 0.4 (R) \quad (5.4.3)$$

for 2024-T3 aluminum alloys and $-0.1 < R < 0.7$ where R was the load ratio.

The concept of fatigue crack closure was applied to the current gear crack experiments and predictions. First the load ratios of tests 9 and 11 were determined. From the effect of gear tooth load position on crack direction analysis (Section 3.5), the load ratio for test 11 (S/N 13, $m_B=3.3$) was estimated as $R=-0.1$ (see Figure 3.5.8a). In a similar fashion, a load position-crack analysis was performed on a gear with $m_B=0.3$. From this, the estimated load ratio for test 9 (S/N 11, $m_B=0.3$) was $R=-2.6$. Note that the thinner rim caused increased flexibility in the tooth support structure and significantly increased the compressive stress in the crack region when the tooth ahead of the cracked tooth was loaded.

Since steel was used in the experiments (rather than aluminum used by Elber) and since different load ratios than that used by Elber were tested, Equation 5.4.3 was not valid for the current studies. A study was then conducted to estimate the effective stress intensity factor range ratio for the gear crack experiments. The predicted number of crack propagation cycles using the previously mentions six schemes were plotted versus crack length at a variety of arbitrarily chosen U ratios. Figure 5.4.1 shows the plots for the model of test gear S/N 11, case 1, and gives the results measured from gage 1 (front tooth flank) of test 9. Seven different U ratios were used: 1.0, 0.9, 0.8, 0.7, 0.6, 0.5, and 0.4. Good correlation between predicted crack cycles and the experiment was obtained at $U=0.5$ using the Collipriest equation (Figure 5.4.1f). Good correlation was also obtained at $U=0.4$ using the Paris equation and curve 2 constants (Figure 5.4.1g).

Figure 5.4.2 gives the results for S/N 11, case 2, and test 9, gage 2 (rear tooth flank). For this, good correlation was obtained at $U=0.5$ for the Collipriest equation (Figure 5.4.2f), and at $U=0.4$ using the Paris equation and curve 2 constants (Figure 5.4.2g). Figure 5.4.3 gives the results for the model of test gear S/N 13. Also plotted are the results of gages 1 and 2 of test 11. Good correlation between predicted crack cycles and the experiment were obtained at $U=1.0$ using the Collipriest equation (Figure 5.4.3a). Also, good correlation was obtained at $U=0.8$ using the Paris equation with the curve 2 and curve 3 constants (Figure 5.4.3b). Since both the Collipriest equation and the Paris equation (using the curve 2 constants) produced good correlation for all cases when appropriate U -ratios were used, these two schemes were further investigated.

For the Collipriest equation, good correlation between predicted crack cycles and the experiments was achieved when: 1) $U=0.5$ for $R=-2.6$, and 2) $U=1.0$ for $R=-0.1$. Assuming a linear relationship between U and R (as deduced by Elber for his aluminum alloys tests) gives

$$U_{\text{Collipriest}} = 1.02 + 0.20 (R) \quad (5.4.4)$$

Figure 5.4.4 summarizes the correlation between the experiments and the predictions using the Collipriest equation.

For the Paris equation and curve 2 constants, good correlation between predicted crack cycles and the experiments occurred when: 1) $U=0.4$ for $R=-2.6$, and 2) $U=0.8$ for $R=-0.1$. Again, assuming a linear relation between U and R produced

$$U_{\text{Paris},2} = 0.82 + 0.16 (R) \quad (5.4.5)$$

Figure 5.4.5 summarizes the correlation for these cases.

5.5 Crack Initiation Life and Total Life. The total life of a structure, N_T , is given by

$$N_T = N_i + N_p \quad (5.5.1)$$

where N_i is the crack initiation life and N_p is the crack propagation life. This section presents crack initiation life predictions for test gears S/N 11 and 13 and compares them with the experimental results.

The predicted crack initiation lives were based on S-N (stress versus cycles) data from gear single tooth bending tests (Heath and Bossler, 1993). Here, the test gears were external, involute spur gears with 20 teeth, 8 pitch, and a 25° pressure angle. The gears were installed in a special fixture which was mounted on a conventional hydraulic load machine. Four teeth on each test gear were loaded, one tooth at a time, until crack initiation occurred. Crack initiation was detected by crack wires installed on the test gear flanks.

Figure 5.5.1 shows the single tooth bending test results for AISI 9310 from Heath and Bossler. The calculated AGMA bending stress indexes at the appropriate tooth loads (located at the HPSTC) were plotted versus crack initiation cycles. A logarithmic regression curve fit gave

$$s_t = 377 - 15.24 \ln N_i \quad (5.5.2)$$

or solving for crack initiation life gives

$$N_i = \exp \left[\frac{377 - s_t}{15.24} \right] \quad (5.5.3)$$

For both test 9 and 11, the 1-hr. break-in period at 50 psi load pressure was neglected from the analysis since it did not contribute to the fatigue damage. For test 9 (S/N 11, $m_B=0.3$), the parameters for the AGMA bending stress index (Equation 1.2.1) were: $W_t=478 \cos 20^\circ = 449$ lb, $P_d=8$ teeth/in., $f=0.25$ in., $J=0.36$, and setting the parameters $K_a=K_v=K_s=K_m=K_B=1$ gave a bending stress index of

$$s_t = \frac{(449)(1)}{(1)} \frac{(8)}{(.25)} \frac{(1)(1)(1)}{(.36)} [4] = 160 \text{ ksi} \quad (5.5.4)$$

The factor of four in the square brackets was a combination notch stress concentration factor and a rim thickness factor. It was determined by dividing the value of the maximum principle stress (calculated by finite element analysis) of the $m_B=0.3$ gear with a notch by the maximum principle stress of a $m_B=3.3$ gear without a notch. The predicted number of crack initiation cycles was

$$N_i = \exp \left[\frac{377 - 160}{15.24} \right] = 1,530,000 \text{ cycles} \quad (5.5.5)$$

For test 11 (S/N 13, $m_B=3.3$), the tangential tooth load was 686 lb, which lead to

$$s_t = \frac{(686)(1)}{(1)} \frac{(8)}{(.25)} \frac{(1)(1)(1)}{(.36)} [3] = 183 \text{ ksi} \quad (5.5.6)$$

and

$$N_i = \exp \left[\frac{377 - 183}{15.24} \right] = 340,000 \text{ cycles} \quad (5.5.7)$$

where a value of 3 was used for the notch stress concentration factor. Table 5.5.1 summarizes the predicted crack initiation and propagation lives, as well as the measured lives from tests 9 and 11.

For test 9, the measured crack initiation life of the front tooth flank was nearly 3/4 of the total life, while the measured crack initiation life of the rear flank was only 1/4 of the total life. The measured total life of the rear flank, however, was probably overestimated since the crack probably propagated along the complete rim of the rear flank before final fracture of the rim occurred. The predicted crack initiation life was about 2/3 of the total predicted life. Also, the total number of predicted life cycles was 58-percent that of the total number of measured cycles.

For test 11, the measured crack initiation life was about 1/2 of the total life of the experiment. The predicted number of crack initiation cycles for this case was about three times greater than the measured crack initiation life. This lead to an overestimation of the total number of predicted cycles.

CHAPTER 6: PARAMETRIC STUDIES

6.1 Introduction. In this chapter, analytical parametric studies were performed to determine the effect of gear design parameters on crack propagation paths. Finite element computer programs MARC and FRANC were used to calculate stress distributions, stress intensity factors, and crack propagation directions. The effect of diametral pitch, pitch radius, tooth pressure angle, and reduction ratio were investigated.

6.2 Model Description. The procedure in developing the finite element model for use in the parametric studies was similar to that previously described. Computer program GPAT was used to define appropriate P3/PATRAN grids, lines, and patches of a single tooth sector based on user defined design data. P3/PATRAN was used to create the finite element mesh of the gear. A nine-tooth sector was used in the analysis rather than a complete gear to simplify the model development when parametric changes in the gear design parameters (such as diametral pitch and number of teeth) were made. Figure 6.2.1 shows a sample finite element model used in the analysis. Once again, the mesh was refined in the tooth fillet area. The same level of refinement as that previously described was used.

For each design condition studied, backup ratios of $m_B=0.7$ and 0.5 were considered. The models for both $m_B=0.7$ (Figure 6.2.1a) and $m_B=0.5$ (Figure 6.2.1b) used 2350 8-node quadrilateral elements with 7287 nodes (before cracks were inserted). Since the same number of elements was used for the $m_B=0.7$ and 0.5 cases, the $m_B=0.5$ models were further refined in the rim region (Figure 6.2.1b). This refinement was not required for analysis purposes and was actually an overkill of the number of elements. This procedure was used, however, to aid in the model development by allowing the same element and node numbering scheme amongst the different cases studied. This simplified the MARC input deck assemblage and also simplified the MARC data reduction for maximum stress location.

For each design condition studied, the location of the HPSTC along with the appropriate tooth load orientation at this location was determined using the method described in Appendix B. A point force in the finite element was placed at the node on the tooth boundary closest to this location at the calculated angle. For boundary conditions, the four corner nodes of the rim were fixed in the x and y directions. The material used in the analysis was steel ($E=30 \times 10^6$, $\nu=0.3$) with a 1.0-in. thickness. A two-dimensional, plane stress condition was assumed.

After the models were developed, the MARC program was then used. For each design condition studied, MARC was used to locate the node closest to the location of maximum principle stress (tensile stress) on the tooth fillet. Once the location of maximum stress was determined for the particular case, the model was imported to FRANC and simulated crack propagation was performed. For each case, the initial crack mouth was placed at the element corner node closest to the location of maximum stress. The initial crack tip was placed at the adjacent corner node (inward from the tooth boundary) of the same element of the initial crack mouth. The J-integral stress intensity factor calculation method was used for all cases as well as the maximum tangential stress crack direction theory. In addition, the crack increment sizes were set equal to the lengths of the initial cracks.

6.3 Analytical Results. A total of 18 runs was performed (Table 6.3.1). Parametric variations of diametral pitch, pitch radius, pressure angle, and reduction ratio were studied. Table 6.3.2 lists the calculated locations of the HPSTC and the tooth load orientations at these locations for the cases studied. The tooth load components were defined in the coordinate system as shown in Figure B.2 (Appendix B). For runs 1 through 14, the analysis considered identical driver and driven gears (with the exception of

a crack inserted in the driver gear). In all cases, only the driver gear (with the crack) was modeled. It was assumed that the backup ratio had no effect on the location or orientation of the tooth load. Also shown in Table 6.3.2 are the locations of the nodes on the tooth fillet closest to the maximum principle stresses where the initial crack mouths were inserted. In all but one case, decreasing the backup ratio from 0.7 to 0.5 moved the location of the maximum principle stress (and thus the location of the initial crack) slightly toward the root (comparing runs 1 and 2, 3 and 4, 5 and 6, and so on). In most cases, decreasing the backup ratio from 0.7 to 0.5 slightly decreased the maximum principle stress. In all cases, decreasing the backup ratio from 0.7 to 0.5 increased the magnitude of minimum principle stress (compressive stress), and in most cases, rather significantly.

The first parameter studied was the effect of diametral pitch on predicted crack propagation path. Runs 1 and 2 ($P_d=8$ teeth/in.), runs 3 and 4 ($P_d=4$ teeth/in.), and runs 5 and 6 ($P_d=16$ teeth/in.) were considered. The finite element models for runs 1 and 2 are shown in Figure 6.2.1. Figure 6.3.1 shows the finite element models for runs 3 and 4 while Figure 6.3.2 shows the models for runs 5 and 6. Once again, all models had the same number of elements and nodes. Also, the pitch radii of all these cases were the same ($r_p=1.75$ in.). As seen from Figures 6.2.1, 6.3.1, and 6.3.2, increasing the diametral pitch decreased the tooth size. Also, from Table 6.3.2, increasing the pitch decreased the radius to the HPSTC and also increased the tangential tooth load component (x-component). The effect of diametral pitch on crack propagation path is shown in Figure 6.3.3. For all cases when $m_B=0.7$, the cracks propagated through the teeth. For $m_B=0.5$, the cracks propagated through the rims for $P_d=8$ and 16 teeth/in., and propagated through the tooth for $P_d=4$ teeth/in. Thus, the increased amount of material in the $P_d=4$ rim stiffened the support structure and influenced the stress distribution enough to produce only tooth fracture.

The next parameter studied was the effect of pitch radii on crack propagation path. Figure 6.3.4 shows the finite element models for run 1 ($r_p=1.75$ in.), run 7 ($r_p=3.50$ in.), and run 9 ($r_p=7.00$ in.), all for $m_B=0.7$. The diametral pitch was the same for these cases ($P_d=8$ teeth/in.) as well as the relative rim thickness. From Table 6.3.2, the load orientations were nearly the same for these cases. The stress distributions were significantly different, however. As the pitch radius increased, the maximum tensile stress significantly decreased and the magnitude of the minimum principle stress (maximum compression) significantly increased. This implied significant rim deformation with increased pitch radius. Figure 6.3.5 shows the effect of pitch radius on crack propagation path. Pitch radius had little effect on predicted crack path for $m_B=0.7$. For $m_B=0.5$, increased pitch radius from $r_p=1.75$ to 3.50 in. tended to propagate the crack even more through the rim. At $r_p=7.00$ in., the crack propagated through the tooth.

The models investigating the effect of tooth pressure angle on crack path are shown in Figure 6.3.6. Shown are the $m_B=0.7$ cases only (runs 1, 11, and 13). Increased pressure angle increased the tooth thickness at the root of the gear tooth, and decreased thickness at the tooth tip. Thus, the advantage of increased pressure angle was to decrease fillet tensile stress (Table 6.3.2). The disadvantage of increased pressure angle was, however, to increase the separating tooth force (y-component of Table 6.3.2), which leads to decreased torque available and increased bearing reaction forces. Surprisingly, tooth pressure angle had little effect on predicted crack directions (Figure 6.3.7).

Lastly, the effect of reduction ratio was investigated. Reduction ratio was defined as the speed of the driver gear divided by the speed of the driven gear where

$$\text{Reduction ratio} = \frac{N_{g,2}}{N_{g,1}} = \frac{r_{p,2}}{r_{p,1}} \quad (6.3.1)$$

Reduction ratios of 1:1 (runs 1 and 2), 2:1 (runs 15 and 16), and 4:1 (runs 17 and 18) were studied. The only effect of reduction ratio on crack modeling was on the location and orientation of the tooth load since the cracked tooth (driven gear) was the same for all cases. From Table 6.3.2, increased reduction ratio reduced the radius to the HPSTC, but increased the tangential tooth force (x-component). The net effect was no change in the location of the maximum principle stress and no change in the predicted crack propagation paths (Figure 6.3.8).

In closing, this chapter provided some insight of the effect of gear design variables on crack propagation paths. As seen from Figure 6.3.3, the actual amount of rim thickness itself affected crack direction as well as backup ratio. The thicker rim of the $P_d=4$ teeth/in. case prevented the crack propagation through the rim. From Figure 6.3.5, pitch radius also had a significant effect on predicted crack path. As a final note, care should be used in the modeling of thin rim gears. As the rim thickness is decreased, significant deformation takes place in the gear structure. Care must be given in modeling the boundary conditions for these cases to accurately account for rim, web, or slots, and their effect on the stiffness of the support structure.

CHAPTER 7: CONCLUSIONS

Analytical and experimental studies were performed to investigate the effect of rim thickness on gear tooth crack propagation. A major emphasis was to determine the direction in which cracks grew, through the teeth or through the rims. Gear tooth fatigue crack growth rates were also studied.

Gear tooth crack propagation was simulated using a finite element based computer program. The program used principles of linear elastic fracture mechanics to model crack tip characteristics for a two-dimensional analysis. Quarter-point, triangular elements were used at the crack tip to represent the stress singularity. Crack tip stress intensity factors were estimated and used to determine crack propagation direction and fatigue crack growth rate. The computer program used had an automated crack propagation option in which cracks were grown numerically using an automated re-meshing scheme. From the analytical crack simulation, the following conclusions were made:

1) For the cases studied, cracks which started in the tooth fillet at the location of maximum tensile stress propagated through the tooth and not the rim for backup ratios (defined as rim thickness divided by tooth height) of $m_b \geq 1.0$. Cracks which started in the tooth fillet at the location of maximum tensile stress propagated through the rim for $m_b \leq 0.4$. The transition point was at $m_b = 0.5$, and the crack propagation direction there was dependent on the initial crack conditions.

2) Three different methods of calculating crack tip stress intensity factors (displacement correlation method, modified crack closure method, and J-integral method) produced similar results for the gear tooth analysis, probably due to the fine mesh refinement in the tooth fillet region. Three different methods of calculating crack propagation direction (maximum tangential stress theory, minimum strain-energy-density theory, and maximum energy release rate theory) produced similar predicted crack paths. This was due to the fact that the predicted mode I stress intensity factors, K_I , were much larger than the mode II stress intensity factors, K_{II} .

3) The location of the point force in the finite element model was determined to be positioned at the highest point of single tooth contact (HPSTC) on the tooth profile. This resulted from an analytical study in which the effect of tooth load position on crack propagation direction was investigated.

4) Three different models for calculating crack propagation cycles (Paris equation, Colliapriest equation, and Inoue equation) produced results that were significantly different from each other. In this analysis, material constants for AISI 9310 and SCM415 steels were gathered from the literature and applied to the gear tooth model.

In addition to the analysis, experimental studies were performed in the NASA Lewis Spur Gear Fatigue Rig. Gears with various backup ratios were tested to validate crack path predictions. Also, specialized crack propagation gages were installed on the test gears to measure gear tooth crack growth rate. From the experiments, the following conclusions were made:

1) For the tests performed, gears with $m_b = 3.3$ and 1.0 resulted in tooth fractures. Gears with $m_b = 0.5$ and 0.3 produced rim fractures. All tests gears had notches machined in one tooth to promote crack initiation during the tests. In all cases, the cracks initiated at the notch tips.

2) The crack propagation gages were effective in measuring gear tooth fatigue crack growth rate. In a test of $m_b = 3.3$, fatigue crack growth rates for the front and rear tooth flanks were similar, validating the use of a two-dimensional analysis approach. Also from this test, crack initiation time was

approximately 43-percent of the total life and crack propagation time was 57-percent of the total life. In a test of $m_B=0.3$, crack growth rates for the front and rear tooth flanks were also similar, but the crack initiation cycles as well as the crack paths were noticeably different. For this test, the time to the earliest detection of crack initiation was 27-percent of the total life.

3) An advanced vibration diagnostics systems installed in the test facility was effective in detecting tooth or rim fracture, but did not give very much warning of impending failures.

A study was performed comparing the analytical predictions with the experimental results. In the analysis, the gears were re-modeled to closely match the profiles of the test gears as well as incorporating a notch in the model. From the comparison study, the following conclusions were made:

1) For $m_B=3.3$ and 1.0, the analysis produced cracks which propagated through the teeth and not the rims. This was validated by the experiments. For $m_B=0.3$, the analysis produced cracks which propagated through the rim, which was also validated by experiments. For $m_B=0.5$, however, the analysis predicted tooth fracture while the experiments produced rim fractures. Further investigation of the analysis for this case showed instability (tooth or rim fracture) when various initial conditions were changed. The analytical results at the transition point of tooth to rim failure should be viewed with conservatism to produce a safe gear design.

2) The initial analytical predictions for number of crack propagation cycles were extremely lower than the measured values from the crack gage tests. To compensate for this, an effective stress intensity ratio factor was defined based on the fatigue crack closure method. Good correlation between the predicted number of cycles and the measured was then achieved using both the Paris fatigue crack growth method and the Collipriest crack growth equation.

Lastly, parametric studies were performed to determine the effect of gear design variables on predicted crack propagation paths. Based on the studies, the following conclusions were made:

1) Increased gear tooth diametral pitch increased the gear tooth size as well as the rim thickness. This lead to cracks which propagated through the tooth and not the rim (for the $m_B=0.5$ cases studied). Also, increased gear pitch diameter lead to increased rim deformation for $m_B=0.5$. This also produced cracks which propagated through the teeth for the cases studied.

2) Gear tooth pressure angle and reduction ratio had no effect on predicted crack propagation paths for the cases studied.

APPENDIX A - NOMENCLATURE

A	time-averaged vibration signal
a	crack length, mm (in)
a_{11}, a_{12}, a_{22}	see Equation 2.3.4
a_c	rack cutter addendum, mm (in)
a_g	gear tooth addendum, mm (in)
b	rim thickness, mm (in)
C	crack growth rate material constant, mm/cyc/[MPa \sqrt{m}] ⁿ (in/cyc/[ksi \sqrt{in}] ⁿ)
c_{ij}	see Equation 2.2.7
D	difference signal
D_M	mean value of difference signal
d	gear tooth depth, mm (in)
d_g	gear tooth dedendum, mm (in)
da/dN	crack growth rate, mm/cyc (in/cyc)
E	modulus of elasticity, MPa (psi)
E^*	see Equation 2.2.10
e	tool shift ratio, mm (in)
F	nodal force, N (lb)
FM0	gear mesh course fault indicator
FM4	localized gear tooth fault indicator
f	tooth face width, mm (in)
f_{ij}	position function
G_I	mode I energy release rate, N/m (lb/in)
G_{II}	mode II energy release rate, N/m (lb/in)
H	Vicker's hardness, Hv
h	tooth whole depth, mm (in)
i	unit normal vector in x-direction
J	geometry factor
J_1	J-integral, symmetric component, N/m (lb/in)
J_2	J-integral, antisymmetric component, N/m (lb/in)
j	unit normal vector in y-direction
K_a	application factor

K_B	rim thickness factor
K_I	mode I stress intensity factor, MPa $\sqrt{\text{m}}$ (psi $\sqrt{\text{in}}$)
K_{IC}	material fracture toughness, MPa $\sqrt{\text{m}}$ (ksi $\sqrt{\text{in}}$)
K_{II}	mode II stress intensity factor, MPa $\sqrt{\text{m}}$ (psi $\sqrt{\text{in}}$)
K_{III}	mode III stress intensity factor, MPa $\sqrt{\text{m}}$ (psi $\sqrt{\text{in}}$)
K_L	life factor
K_m	load distribution factor
K_R	reliability factor
K_T	temperature factor
K_v	dynamic factor
K_s	size factor
L	element length, mm (in)
l	notch length, mm (in)
M	regular-meshing-components signal
m_B	backup ratio
N_g	number of teeth on gear
N_i	crack initiation life, cyc
N_p	crack propagation life, cyc
N_T	total life, cyc
NA4	gear tooth damage indicator
n	unit normal vector of rack cutter
n	crack growth rate material constant exponent
P	load, N (lb)
P_d	diametral pitch, teeth/in
p_b	base pitch, mm (in)
R	load ratio
r	gear tooth coordinate vector, mm (in)
r, θ, z	polar coordinate frame
r_b	base radius, mm (in)
r_c	rack cutter radius, mm (in)
r_o	outside radius, mm (in)
r_p	pitch radius, mm (in)
r_t	chordal tooth thickness, mm (in)

S	strain-energy-density factor, N/m (lb/in)
s_{at}	allowable bending stress, MPa (psi)
s_t	bending stress index, MPa (psi)
T	traction vector, MPa (psi)
T	current time record of run
t	time, sec
U	effective stress intensity factor ratio
u	displacement in x -direction
v	relative velocity between rack cutter and generated tooth, mm/sec (in/sec)
v	displacement in y -direction
W	strain energy density, MPa (psi)
W_t	tangential tooth load, N (lb)
w	notch width, mm (in)
x, y, z	cartesian coordinate frame
x', y', z'	cartesian coordinate frame
x_1, x_2, x_3	cartesian coordinate frame
α	see Equation 2.4.5
β	see Equation 3.2.5
β_r	angle of recess, deg
β_t	half-sector angle for chordal tooth thickness, deg
γ_m	predicted crack propagation angle (= $-\theta_m$, deg)
ΔK	stress intensity factor range, MPa \sqrt{m} (ksi \sqrt{in})
ΔK_c	see Equation 2.4.4
ΔK_{eff}	effective stress intensity factor range, MPa \sqrt{m} (ksi \sqrt{in})
ΔK_{th}	stress intensity threshold factor, MPa \sqrt{m} (ksi \sqrt{in})
δ	crack length increment, mm (in)
ϵ	roll angle, deg
ζ	notch angle, deg
η	see Equation 2.4.8
θ_m	predicted crack propagation angle, deg
κ	plane strain/stress factor, see Equation 2.2.4
λ	see Equation 2.4.9
μ	modulus of rigidity, see Equation 2.2.3, MPa (psi)

ν	Poisson's ratio
ξ	load angle, deg
σ_{ij}	stress tensor, MPa (psi)
$\sigma_{r\theta}$	crack tip shear stress, MPa (psi)
$\sigma_{\theta\theta}$	crack tip tangential stress, MPa (psi)
τ_{ij}	shear stress, MPa (psi)
ϕ	rack pressure angle, rad (deg)
ϕ_r	see Equation B.12
ψ	root element position angle, deg
ω	gear blank rotation, rad

APPENDIX B - LOAD VECTOR ORIENTATION

In this section, the orientation of the load vector at various locations on the gear tooth is derived. Consider the two gears in mesh as shown in Figure B.1. Gear 1 is the driver gear and gear 2 is the driven gear. Given are pitch radii of gear 1 and 2, $r_{p,1}$ and $r_{p,2}$, respectively, the addendums of gears 1 and 2, $a_{g,1}$ and $a_{g,2}$, respectively, the pressure angle, ϕ , the number of teeth on gear 1, $N_{g,1}$, and the chordal tooth thickness of gear 1, $r_{t,1}$. The base radii are

$$r_{b,1} = r_{p,1} \cos \phi \quad (\text{B.1})$$

$$r_{b,2} = r_{p,2} \cos \phi \quad (\text{B.2})$$

The outside radii are

$$r_{o,1} = r_{p,1} + a_{g,1} \quad (\text{B.3})$$

$$r_{o,2} = r_{p,2} + a_{g,2} \quad (\text{B.4})$$

The various lengths along the line of action are

$$\overline{B_1 P_2} = \sqrt{r_{o,1}^2 - r_{b,1}^2} \quad (\text{B.5})$$

$$\overline{B_1 P} = r_{p,1} \sin \phi \quad (\text{B.6})$$

$$\overline{B_1 B_2} = (r_{p,1} + r_{p,2}) \sin \phi \quad (\text{B.7})$$

$$\overline{P_1 B_2} = \sqrt{r_{o,2}^2 - r_{b,2}^2} \quad (\text{B.8})$$

The angle of recess for gear 1 is

$$\beta_{r,1} = \frac{\overline{B_1 P_2} - \overline{B_1 P}}{r_{b,1}} \quad (\text{B.9})$$

The half-sector angle for the chordal tooth thickness of gear 1 is

$$\beta_{t,1} = \frac{r_{t,1}}{2 r_{p,1}} \quad (\text{B.10})$$

The orientation of the load vector when the load is located at the tooth tip of gear 1 is

$$\xi_{tip,1} = \phi + \beta_{r,1} - \beta_{t,1} \quad (\text{B.11})$$

where $\xi_{tip,1}$ is defined in the x,y -coordinate system shown in Figure B.2.

This analysis can be extended to determine the orientation of the load vector at any position on the tooth of gear 1 as gear 1 is in contact with gear 2 along the line of action. The angle $\phi_{r,1}$ is defined as

$$\phi_{r,1} = \cos^{-1} \left[\frac{r_{b,1}}{r_1} \right] \quad (\text{B.12})$$

where r_1 is the distance from the center of gear 1 to an arbitrary point of the tooth profile of gear 1. For $r_1 = r_{o,1}$ (the tooth tip of gear 1),

$$\phi_{tip,1} = \cos^{-1} \left[\frac{r_{b,1}}{r_{o,1}} \right] \quad (\text{B.13})$$

and the orientation of the load vector at any position on the tooth of gear 1 as it is in contact is

$$\xi_{r,1} = \xi_{tip,1} - \phi_{tip,1} + \phi_{r,1} \quad (\text{B.14})$$

Lastly, consider contact at the highest point of single tooth contact (HPSTC) for gear 1. The distance from the center of gear 1 to the position of the HPSTC on the line of action is

$$r_{HPSTC,1} = \sqrt{(\overline{B_1 B_2} - \overline{P_1 B_2} + p_{b,1})^2 + (r_{b,1})^2} \quad (\text{B.15})$$

where the base pitch, $p_{b,1}$ is defined as

$$p_{b,1} = \frac{2 \pi r_{b,1}}{N_{g,1}} \quad (\text{B.16})$$

This produces

$$\phi_{HPSTC,1} = \cos^{-1} \left[\frac{r_{b,1}}{r_{HPSTC,1}} \right] \quad (\text{B.17})$$

$$\xi_{HPSTC,1} = \xi_{tip,1} - \phi_{tip,1} + \phi_{HPSTC,1} \quad (\text{B.18})$$

APPENDIX C - NOTCH MODELING

In this section, the details of incorporating a notch in the fillet region of the finite element model of a gear tooth is discussed. The inputs to the analysis are notch length, l , notch width, w , notch angle, ζ , and notch mouth coordinates, x_1 and y_1 , at P_1 (Figure C.1). Point P_2 is defined as

$$x_2 = x_1 - \frac{w}{2} \cos \zeta + (l - \frac{w}{2}) \sin \zeta \quad (C.1)$$

$$y_2 = y_1 - \frac{w}{2} \sin \zeta - (l - \frac{w}{2}) \cos \zeta \quad (C.2)$$

Point P_3 is defined as

$$x_3 = x_1 + \frac{w}{2} \cos \zeta + (l - \frac{w}{2}) \sin \zeta \quad (C.3)$$

$$y_3 = y_1 + \frac{w}{2} \sin \zeta - (l - \frac{w}{2}) \cos \zeta \quad (C.4)$$

The notch tip, P_4 , is defined as

$$x_4 = x_1 + l \sin \zeta \quad (C.5)$$

$$y_4 = y_1 - l \cos \zeta \quad (C.6)$$

Once points P_2 , P_3 , and P_4 are defined, a polynomial curve fit is used to create a curve through these points to define the notch tip surface. In addition, P_5 is chosen from the existing P3/PATRAN grid points on the tooth fillet surface to create line P_2P_5 which is as close to parallel to line P_1P_4 as possible. Similarly, P_6 is chosen from the existing P3/PATRAN grid points on the tooth fillet surface to create line P_3P_6 which is as close to parallel to line P_1P_4 as possible. After the notch surface $P_5P_2P_4P_3P_6$ is defined, appropriate P3/PATRAN patches are defined in the tooth fillet region (Figure C.2a). As with the conventional model, seeds are placed along patch edges to define the number of elements along each patch edge. The P3/PATRAN meshing process then creates the appropriate finite element mesh for this region (Figure C.2b).

BIBLIOGRAPHY

- AGMA, 1974a, "Design Procedure for Aircraft Engine and Power Take-Off Spur and Helical Gears", AGMA 411.02, American Gear Manufacturers Association, Alexandria, VA.
- AGMA, 1974b, "Design Procedure for Aircraft Engine and Power Take-Off Bevel Gear", AGMA 431.01, American Gear Manufacturers Association, Alexandria, VA.
- AGMA, 1976, "Standard - Design Guide for Vehicle Spur and Helical Gears", AGMA 170.01, American Gear Manufacturers Association, Alexandria, VA.
- AGMA, 1988, "Fundamental Rating Factors and Calculation Methods for Involute Spur and Helical Gear Teeth", AGMA 2001-B88, American Gear Manufacturers Association, Alexandria, VA.
- AGMA, 1989, "Geometry Factors for Determining the Pitting Resistance and Bending Strength of Spur, Helical, and Herringbone Gear Teeth", AGMA 908-B89, American Gear Manufacturers Association, Alexandria, VA.
- AGMA, 1990, "Fundamental Rating Factors and Calculation Methods for Involute Spur and Helical Gear Teeth", ANSI/AGMA 2001-B88, American Gear Manufacturers Association, Alexandria, VA.
- Ahmad, J., and Loo, F.T., 1977, "On the Use of Strain Energy Density Fracture Criterion in the Design of Gears Using Finite Element Method", ASME Paper No. 77-DET-158, presented at the Design Technical Conference, Chicago, IL, Jun.
- Albrecht, C., 1988, "Transmission Design Using Finite Element Method Analysis Techniques", Journal of American Helicopter Society, Vol. 33, No. 2, Apr., pp 3-14.
- Arai, N., Harada, S., and Aida, T., 1981, "Research on Bending Strength Properties of Spur Gears With a Thin Rim", Bulletin of the JSME, Vol. 24, No. 195, Sep., pp. 1642-1650.
- ASTM E-399-90, 1990, "Standard Test Method for Plane-Strain Fracture Toughness of Metallic Materials", Annual Book of ASTM Standards, Metals Test Methods and Analytical Procedures, Vol. 03.01, pp. 407-437.
- ASTM E-647-93, 1993, "Standard Test Method for Measurement of Fatigue Crack Growth Rates, Annual Book of ASTM Standards, Metals Test Methods and Analytical Procedures, Vol. 03.01, pp. 569-596.
- Au, J.J., and Ke, J.S., 1981, "Correlation Between Fatigue Crack Growth Rate and Fatigue Striation Spacing in AISI 9310 (AMS 6265) Steel", Fractography and Materials Science, ASTM STP 733, pp. 202-221.
- Ballarini, R., and Hsu, Y., 1989, "Three-Dimensional Analysis of Surface Crack-Hertzian Stress Field Interaction", NASA CR-4254, Grant No. NAG3-396, Oct.
- Barsoum, R.S., 1976, "On the Use of Isoparametric Finite Elements in Linear Fracture Mechanics", International Journal for Numerical Methods in Engineering, Vol. 10, No. 1, pp. 25-37.

- Bibel, G.D., Reddy, S.K., Savage, M., and Handschuh, R.F., 1991, "Effects of Rim Thickness on Spur Gear Bending Stress", NASA TM-104388, AVSCOM TR-91-C-015.
- Binder, S., and Mack, J.C., 1980, "Experience with Advanced High Performance Gear Steel", ASME Paper No. 80-C2/DET-77.
- Cardou, A., and Tordion, G.V., 1989, "A Study of Spur Gear Geometry Factor Through Complex Potential Analysis", *Journal of Mechanisms, Transmissions, and Automation in Design*, Vol. 111, No. 3, Sep., pp. 433-438.
- Chan, S.K., Tuba, I.S., and Wilson, W.K., 1970, "On the Finite Element Method in Linear Fracture Mechanics", *Engineering Fracture Mechanics*, Vol. 2, No. 1-A, pp. 1-17.
- Chang, S.H., Huston, R.L., and Coy, J.J., 1983, "A Finite Element Stress Analysis of Spur Gears Including Fillet Radii and Rim Thickness Effects", *Journal of Mechanisms, Transmissions, and Automation in Design*, Vol. 105, No. 3, Sep., pp. 327-330.
- Chong, T.H., and Kubo, A., 1985, "Simple Stress Formulae for a Thin-Rimmed Spur Gear", *Journal of Mechanisms, Transmissions, and Automation in Design*, Vol. 107, No. 3, Sep., pp. 406-423.
- Collipriest, J.E., 1972, "An Experimentalist's View of the Surface Flaw Problem", *The Surface Crack: Physical Problems and Computational Solutions*, American Society of Mechanical Engineers, pp. 43-61.
- Cotterell, B., and Rice, J.R., 1980, "Slightly Curved or Kinked Cracks", *International Journal of Fracture*, Vol. 16, No. 2, pp. 155-169.
- Couchan, D.C., Barnes, G.K., and Cedoz, R.W., 1993, "Shot-Peened Gear Failures Due to Operation in a Misaligned Condition", AIAA Paper No. AIAA-93-2147, presented at the 29th Joint Propulsion Conference, Monterey, CA, Jun.
- Daniewicz, S., 1991, "Conception and Development of Improved Analytical Prediction Models for Fatigue Induced Tooth Breakage Due to Cyclic Bending in Spur Gear Teeth", Ph.D. Dissertation, Ohio State University.
- DiRusso, R., 1986, "Advances and Applications of Pyrowear 53 in Helicopter Transmission Systems", American Helicopter Society Pre-print No. 8, presented at the Rotary Wing Propulsion Systems Specialist Meeting, Williamsburg, VA, Nov.
- Drago, R.J., 1982, "An Improvement in the Conventional Analysis of Gear Tooth Bending Fatigue Strength", AGMA Paper No. P229.24, Oct.
- Drago, R.J., and Lutthans, R.V., 1983, "Combined Effects of Rim Thickness and Pitch Diameter on Spur Gear Tooth Stresses", *Journal of the American Helicopter Society*, Vol. 28, Jul., pp 13-19.
- Elber, W., 1971, "The Significance of Fatigue Crack Closure", *Damage Tolerance in Aircraft Structures*, ASTM STP 486, pp. 230-242.
- Erdogan, F., and Sih, G.C., 1963, "On the Crack Extension in Plates Under Plane Loading and Transverse Shear", *Journal of Basic Engineering*, Vol. 85, pp. 519-527.

- Flasker, J., and Jezernik, A., 1983, "The Comparative Analysis of Crack Propagation in the Gear Tooth", Proceedings of the International Conference of Application of Fracture Mechanics to Materials and Structures, Freiburg, West Germany, Jun., pp. 971-982.
- Flasker, J., and Pehan, S., 1993, "Crack Propagation in Tooth Root With Variable Loading", Communications in Numerical Methods in Engineering, Vol. 9, No. 2, Feb., pp. 103-110.
- Forman, R.G., Kearney, V.E., and Engle, R.M., 1967, "Numerical Analysis of Crack Propagation in Cyclic-Loaded Structures", Journal of Basic Engineering, Vol. 89D, pp. 459-464.
- Forman, R.G., and Hu, T., 1984, "Application of Fracture Mechanics on the Space Shuttle", Damage Tolerance of Metallic Structures: Analysis Methods and Applications, ASTM STP 842, pp. 108-133.
- Gulliot, M., and Tordion, G.V., 1989, "Stress Analysis of Thin-Rim Spur Gears By Finite Element Method", Proceedings of the 1989 International Power Transmission and Gearing Conference, Chicago, IL, Apr., pp. 167-172.
- Hanink, D.K., et al., 1979, "Materials for Helicopter Gears", Report of The Committee on Helicopter Transmission Gear Materials, Publication NMAB-351, National Materials Advisory Board, National Research Council.
- Hartranft, R.J., and Sih, G.C., 1973, "Solving Edge and Surface Crack Problems by an Alternate Method", Methods of Analysis and Solutions of Crack Problems, G.C. Sih, ed., Noordhoff International Publishing.
- Hayashi, K., and Nemat-Nasser, S., 1981, "Energy Release Rate and Crack Kinking", International Journal of Solids and Structures, Vol. 17, pp 104-114.
- Heath, G.F., and Bossler, R.B., 1993, "Advanced Rotorcraft Transmission (ART) Program - Final Report", NASA CR-191057, Army Research Laboratory ARL-CR-14.
- Hefeng, B., Savage, M., and Knorr, R.J., 1985, "Computer Modeling of Rack-Generated Spur Gears", Mechanism and Machine Theory, Vol. 20, No. 4, pp. 351-360.
- Henshell, R.D., and Shaw, K.G., 1975, "Crack Tip Finite Elements Are Unnecessary", International Journal for Numerical Methods in Engineering, Vol. 9, pp. 495-507.
- Hofer, H., 1948, "Verzahnungskorrekturen an Zahnradern", Automobiltechnische Zeitschrift 50, Nr. 3, S. 44-45.
- Honda, H., and Conway, J.C., 1979, "An Analysis by Finite Element Techniques of the Effects of a Crack in the Gear Tooth Fillet and its Applicability to Evaluating Strength of the Flawed Gears", Bulletin of the JSME, Vol. 22, No. 174, Dec., pp. 1848-1855.
- Hussain, M.A., Pu, S.L., and Underwood, J., 1974, "Strain Energy Release Rate for a Crack Under Combined Mode I and Mode II", Fracture Analysis, ASTM STP 560, pp. 2-28.
- Inoue, K., Deng, G., and Kato, M., 1989a, "Evaluation of the Strength of Carburized Spur Gear Teeth Based on Fracture Mechanics (Report No. 1 - Stress Intensity Factor Taking the Effects of

- Residual Stress Distribution in Gear Surface Into Consideration", Transactions of the Japanese Society of Mechanical Engineers, Sec. C, Vol. 55, No. 514, Jun., pp. 1488-1493.
- Inoue, K., Kato, M., and Yamanaka, M., 1989b, "Fatigue Strength and Crack Growth of Carburized and Shot Peened Spur Gears", Proceedings of the 1989 International Power Transmission and Gearing Conference, Chicago, IL, Apr., pp. 663-668.
- Inoue, K., Kato, M., Deng, G., and Takatsu, N., 1991, "Fracture Mechanics Based Evaluation of Strength of Carburized Gear Teeth", Proceedings of the JSME International Conference on Motion and Power Transmissions, Hiroshima, Japan, Nov., pp. 801-806.
- Irwin, G.R., 1957, "Analysis of Stresses and Strains Near the End of a Crack Traversing a Plate", Journal of Applied Mechanics, Vol. 24, pp. 361-364.
- Kato, M., Inoue, K., Deng, G., and Jeong, B.S., 1990, "Strength Evaluation of Carburized Gear Teeth Based on Fracture Mechanics", Proceedings of the KSME/JSME Joint Conference "Fracture and Strength '90", Seoul, Korea, pp. 248-253.
- Kerr, L.M., and Bryant, M.D., 1983, "A Pitting Model for Rolling Contact Fatigue", Journal of Lubrication Technology, Vol. 105, No. 2, Apr., pp. 198-205.
- Lin, H.H., Huston, R.L., and Coy, J.J., 1988a, "On Dynamic Loads in Parallel Shaft Transmissions: Part I - Modeling and Analysis", Journal of Mechanisms, Transmissions, and Automation in Design, Vol. 110, No. 2, pp. 221-225.
- Lin, H.H., Huston, R.L., and Coy, J.J., 1988b, "On Dynamic Loads in Parallel Shaft Transmissions: Part II - Parametric Study", Journal of Mechanisms, Transmissions, and Automation in Design, Vol. 110, No. 2, pp. 226-229.
- MARC, 1992, MARC Reference Library, MARC Analysis Research Corporation, Palo Alto, CA.
- McFadden, P.D., 1985, "Analysis of the Vibration of the Input Bevel Pinion in RAN Wessex Helicopter Main Rotor Gearbox WAK143 Prior To Failure", Aeronautical Research Laboratories Report No. AR-004-049.
- Mendelson, A., and Ghosn, L.J., 1986, "Analysis of Mixed-Mode Crack Propagation Using the Boundary Integral Method", NASA CR-179518, Grant No. NAG3-396, Sep.
- Oda, S., Nagamura, K., and Aoki, K., 1981, "Stress Analysis of Thin Rim Spur Gears by Finite Element Method", Bulletin of the JSME, Vol. 24, No. 193, Jul., pp. 1273-1280.
- Oda, S., and Koide, T., 1983, "Study on Bending Fatigue Strength of Helical Gears", Bulletin of the JSME, Vol. 26, No. 211, Jan., pp. 146-153.
- Oda, S., and Miyachika, K., and Takeda, A., 1984a, "Root Stresses and Bending Fatigue Breakage of Planet Gear", Bulletin of the JSME, Vol. 27, No. 227, May., pp. 995-1001.
- Oda, S., and Miyachika, K., 1984b, "Effects of Key on Bending Fatigue Breakage of Thin-Rimmed Spur Gears", Bulletin of the JSME, Vol. 27, No. 232, Oct., pp. 2279-2286.

- Oda, S., and Miyachika, K., and Sayama, T., 1986, "Effects of Rim and Web Thicknesses on Bending Fatigue Strength of Internal Gear", *Bulletin of the JSME*, Vol. 29, No. 248, Feb., pp. 586-592.
- Oswald, F.B., Lin, H.H., Liou, C.H., and Valco, M.J., 1993, "Dynamic Analysis of Spur Gears Using Computer Program DANST", NASA TM-106211, Army Research Laboratory ARL-TR-171.
- Paris, P.C., Gomez, R.E., and Anderson, W.E., 1961, "A Rational Analytical Theory of Fatigue", *The Trend in Engineering*, Vol. 13, No. 1, pp. 9-14.
- Paris, P.C., and Erdogan, F., 1963, "A Critical Analysis of Crack Propagation Laws", *Journal of Basic Engineering*, Vol. 85, pp. 528-534.
- P3/PATRAN, 1993, P3/PATRAN User Manual, PDA Engineering, Costa Mesa, CA.
- Ramamurthy, T.S., Krishnamurthy, T., and Narayana, K.B., 1986, "Modified Crack Closure Integral Method with Quarter Point Elements", *Mechanics Research Communications*, Vol. 13(4), pp. 179-186.
- Roberts, R., and Erdogan, F., 1967, "The Effect of Mean Stress on Fatigue Crack Propagation in Plates Under Extension and Bending", *Journal of Basic Engineering*, Vol. 89, pp. 885-892.
- Rice, J.R., 1968, "A Path Independent Integral and the Approximate Analysis of Strain Concentration by Notches and Cracks", *Journal of Applied Mechanics*, Vol. 35, pp. 379-386.
- Rybicki, E.F., and Kanninen, M.F., 1977, "A Finite Element Calculation of Stress Intensity Factors By a Modified Crack Closure Integral", *Engineering Fracture Mechanics*, Vol. 9, pp. 931-938.
- Shih, C.F., DeLorenzi, H.G., and German, M.D., 1976, "Crack Extension Modeling with Singular Quadratic Isoparametric Elements", *International Journal of Fracture*, Vol. 12, pp. 647-651.
- Sih, G.C., 1974, "Strain-Energy Density Factor Applied to Mixed Mode Crack Propagation", *International Journal of Fracture*, Vol. 10, No. 3, Sep., pp. 305-321.
- Stewart, R.M., 1977, "Some Useful Data Analysis Techniques for Gearbox Diagnostics", Report MHM/R/10/77, Machine Health Monitoring Group, Institute of Sound and Vibration Research, University of Southampton.
- Swedlow, J.L., 1976, "Criteria for Growth of the Angled Crack", *Cracks and Fractures*, ASTM STP 601, pp. 506-521.
- Thomas, J.M., Harris, D.O., and Besuner, P.M., 1986, "Fracture Mechanics Life Technology", *Proceedings of the 27th Structures, Dynamics, and Materials Conference*, San Antonio, TX, May, pp. 562-578.
- Tobe, T., Kato, M., and Inoue, K., 1985, "A Method Estimating Residual Stresses From Hardness Distributions in View of Fatigue Strength of Carburized Gear Teeth", *International Journal of Vehicle Design*, pp. D18.2-D18.18.
- Tong, P., and Pian, T.H.H., 1973a, "On the Convergence of the Finite Element Method for Problems with Singularity", *International Journal of Solids and Structures*, Vol. 9, pp. 313-321.

- Tong, P., Pian, T.H.H., and Lasry, S.J., 1973b, "A Hybrid-Element Approach to Crack Problems in Plane Elasticity", *International Journal for Numerical Methods in Engineering*, Vol. 7, pp. 297-308.
- Townsend, D.P., and Bamberger, E.N., 1991, "Surface Fatigue Life of Carburized and Hardened M50NiL and AISI 9310 Spur Gears and Rolling-Contact Test Bars", *Journal of Propulsion and Power*, Vol. 7, No. 4, pp. 642-649.
- Tracey, D.M., 1971, "Finite Elements for Determination of Crack Tip Elastic Stress Intensity Factors", *Engineering Fracture Mechanics*, Vol. 3, No. 3-E, pp. 255-265.
- Tracey, D.M., 1977, "Discussion of 'On the Use of Isoparametric Finite Elements in Linear Fracture Mechanics' by R.S. Barsoum", *International Journal for Numerical Methods in Engineering*, Vol. 11, pp. 401-402.
- Valco, M.J., 1992, "Planetary Gear Train Ring Gear and Support Structure Investigation", Ph.D. Dissertation, Cleveland State University.
- Von Eiff, H., Hirschmann, K.H., and Lechner, G., 1990, "Influence of Gear Tooth Geometry on Tooth Stress of External and Internal Gears", *Journal of Mechanical Design*, Vol. 112, No. 4, Dec., pp. 575-583.
- Walker, K., 1970, "The Effect of Stress Ratio During Crack Propagation and Fatigue for 2024-T3 and 7075-T6 Aluminum", *Effects of Environment and Complex Load History on Fatigue Life*, ASTM STP 462, pp. 1-14.
- Wawrzynek, P.A., 1991, "Discrete Modeling of Crack Propagation: Theoretical Aspects and Implementation Issues in Two and Three Dimensions", Ph.D. Dissertation, Cornell University.
- Williams, M.L., 1957, "On the Stress Distribution at the Base of a Stationary Crack", *Journal of Applied Mechanics*, Vol. 24, No. 1, Mar., pp. 109-114.
- Wilson, W.K., 1971, "Some Crack Tip Finite Elements for Plane Elasticity", *Stress Analysis and Growth of Cracks*, Proceedings of the 1971 National Symposium on Fracture Mechanics, Part I, ASTM STP 513, pp. 90-105.
- Zakrajsek, J.J., 1989, "An Investigation of Gear Mesh Failure Prediction Techniques", NASA TM-102340, AVSCOM TM-89-C-005.
- Zakrajsek, J.J., Townsend, D.P., and Decker, H.J., 1993, "An Analysis of Gear Fault Detection Methods as Applied to Pitting Fatigue Failure Data", NASA TM-105950, AVSCOM TM-92-C-035.
- Zakrajsek, J.J., Handschuh, R.F., and Decker, H.J., 1994, "Application of Fault Detection Techniques to Spiral Bevel Gear Fatigue Data", NASA TM-106467, Army Research Laboratory Memorandum ARL-TR-345.

Table 3.3.1.- Gear model input parameters used in mesh refinement analysis.

Number of teeth on gear	28
Pressure angle, deg	20
Diametral pitch, teeth/in	8
Addendum, in	0.125
Dedendum, in	0.169
Tool shift, in	0.0
Cutter radius, in	0.0
Finite element type	8-node quadrilateral, plane stress
Modulus of elasticity, psi	30×10^6
Poisson's ratio	0.3
Tooth and rim thickness, in	0.25
Hub thickness, in	0.75
Tooth load, lb	$F_x=323, F_y=-168$ at tooth tip node
Boundary conditions	Hub corner nodes fixed in x and y directions

Table 3.3.2.- Mesh refinement results.

Number of elements	Largest magnitude of maximum principle stress			Largest magnitude of minimum principle stress		
	Max stress (ksi)	Percent change (%)	Location (deg)	Max stress (ksi)	Percent change (%)	Location (deg)
1692	41.9	—	38	51.1	—	38
3216	44.8	6.9	32	54.7	7.0	32
7276	47.7	6.4	35	57.8	5.7	35
8348	48.8	2.3	37	59.4	2.8	37

Table 3.4.1.- Effect of different crack propagation direction theories on predicted crack path.

Crack length in	$\sigma_{\theta\theta, max}$ theory			S_{min} theory			G_{max} theory		
	K_I ksi \sqrt{in}	K_{II} ksi \sqrt{in}	θ_m deg	K_I ksi \sqrt{in}	K_{II} ksi \sqrt{in}	θ_m deg	K_I ksi \sqrt{in}	K_{II} ksi \sqrt{in}	θ_m deg
0.0104	6808	97.6	-1.6	6808	97.6	-1.6	6808	97.6	-1.8
0.0208	7948	-321.5	4.6	7948	-321.5	4.6	7945	-332.5	5.3
0.0312	8691	-293.1	3.9	8690	-294.3	3.9	8697	-262.4	3.8
0.0416	9366	-362.0	4.4	9366	-362.2	4.4	9381	-323.5	4.3
0.0520	10030	-332.0	3.8	10020	-332.7	3.8	10050	-295.6	3.7
0.0624	10740	-304.8	3.2	10730	-317.9	3.4	10760	-277.1	3.3
0.0728	11490	-314.6	3.1	11490	-329.4	3.3	11510	-296.8	3.3
0.0832	12310	-338.2	3.1	12310	-327.3	3.0	12330	-297.0	3.0
0.0936	13230	-332.2	2.9	13240	-314.7	2.7	13270	-297.6	2.8
0.1040	14260	-350.9	2.8	14270	-363.8	2.9	14300	-315.3	2.8
0.1144	15480	-348.6	2.6	15490	-332.5	2.5	15520	-297.8	2.4
0.1248	16860	-337.9	2.3	16880	-383.2	2.6	16890	-334.4	2.5
0.1352	18560	-398.4	2.5	18540	-363.3	2.2	18600	-337.2	2.3
0.1456	20450	-396.7	2.2	20460	-435.2	2.4	20520	-348.6	2.1
0.1560	22840	-457.7	2.3	22860	-425.5	2.1	22940	-402.3	2.2
0.1664	25730	-484.9	2.2	25740	-471.3	2.1	25810	-448.6	2.2

Table 3.5.1.- Crack direction predictions considering the effect of gear tooth load position.

Step number	$K_{I, max}(\omega)$ (ksi \sqrt{in})	$K_{II}(\omega)$ at $K_{I, max}$ (ksi \sqrt{in})	θ_m (deg)
1	4.8	-.18	4.3
2	5.6	.09	-1.9
3	6.0	.13	-2.4
4	6.3	.17	-3.0
5	6.6	.17	-3.0
6	7.0	.15	-2.5
7	7.4	.16	-2.5
8	7.8	.19	-2.8
9	8.2	.18	-2.5

Table 3.6.1.- Effect of rim thickness on maximum and minimum principle stresses.

Backup ratio	Largest magnitude of maximum principle stress		Largest magnitude of minimum principle stress	
	Max stress (ksi)	Location (deg)	Max stress (ksi)	Location (deg)
3.3	33.1	43	40.1	43
1.0	30.7	36	48.9	43
0.5	26.5	43	72.5	54
0.4	28.6	49	88.4	54
0.3	36.9	60	118.3	60
0.2	61.0	68	182.8	64

Table 3.7.1.- Chemical composition comparison between AISI 9310 and SCM415 materials.

Element	Composition by weight, %	
	AISI 9310 ^a	SCM415 ^b
Carbon	0.11	0.15
Chromium	1.38	1.04
Copper	0.21	—
Manganese	0.58	0.77
Molybdenum	0.13	0.18
Nickel	3.20	—
Phosphorous	0.003	<0.02
Silicon	0.26	0.31
Sulfur	0.004	<0.02
Iron	Balance	Balance

^aTownsend and Bamberger (1991) ^bInoue, et al. (1991)

Table 4.2.1.- Test gear lubricant properties.

Base stock	Synthetic paraffinic oil
Extreme pressure (EP) additive	Lubrizol 5002 ^a
Kinematic viscosity, cSt	
at (-20° F)	2500
at (100° F)	31.6
at (210° F)	5.5
at (400° F)	2.0
Flash point, °F	455
Fire point, °F	500
Pour point, °F	-65
Specific gravity	0.8285
Specific heat, Btu/lb/°F	0.523

^a EP additive: Lubrizol 5002 (5% vol) containing 0.03% vol phosphorous and 0.93% vol sulfur.

Table 4.3.1.- Test gear geometry. (Gear tolerance per AGMA class 12)

Number of teeth	28
Diametral pitch, teeth/in	8
Circular pitch, in	0.393
Whole depth, in	0.300
Addendum, in	0.125
Chordal tooth thickness, in	0.191
Pressure angle, deg	20
Pitch diameter, in	3.500
Outside diameter, in	3.750
Root fillet, in	0.040 to 0.060
Measurement over pins, in	3.781 to 3.792
Pin diameter, in	0.216
Backlash reference, in	0.010
Tip relief (at tooth tip), in	0.0005
Tooth profile surface finish, μ in rms	16
Tooth and rim width, in	0.250
Hub width, in	0.750

Table 4.3.2.- Notch dimensions of test gears.

Test	Serial number, S/N	Backup ratio, m_B	Notch dimensions		
			Length, in	Width, in	Angle, deg
1	01	3.3	0.006	0.007	37
2	02	3.3	0.011	0.006	33
3	03	1.0	0.012	0.006	29
4	04	1.0	0.005	0.004	40
5	05	0.5	0.010	0.008	34
6	06	0.5	0.010	0.007	34
7	07	0.3	0.013	0.004	31
8	08	0.3	0.009	0.009	30
9	11	0.3	0.010	0.006	64
10	12	0.3	0.006	0.005	60
11	13	3.3	0.005	0.005	63

Table 4.6.1.- Vibration parameters for last portion of test 1, S/N 01, $m_B=3.3$, 475 psi load pressure.

Run time, hr	rms, g's	FM0	FM4	NA4
8.0167	11.62	13.27	3.29	3.28
8.1000	10.50	13.06	3.03	2.62
8.1833	10.73	14.47	3.27	3.36
8.2000	10.71	13.35	3.34	3.33
8.2167	10.66	13.83	3.34	3.23
8.2333	10.64	13.58	3.38	3.30
8.2500	11.37	14.57	3.39	3.88
8.2667	20.17	42.90	4.31	57.22
8.2833	25.54	37.86	4.27	94.69
8.3000	26.38	40.67	4.31	72.06
8.3167	27.02	40.39	4.40	59.80
8.3333	27.16	40.51	4.45	47.39
8.3500	27.29	41.14	4.61	38.84
8.3667	26.54	46.22	4.56	28.85

Table 4.6.2.- Vibration parameters for last portion of test 2,
S/N 02, $m_B=3.3$, 400 psi load pressure.

Run time, hr	rms, g's	FM0	FM4	NA4
27.0416	13.81	20.56	2.52	2.90
27.1250	13.76	21.20	2.32	2.89
27.1416	13.87	19.36	2.40	2.99
27.1583	13.87	18.78	2.36	3.01
27.1750	14.26	20.39	2.42	3.24
27.1916	14.25	19.81	2.43	3.03
27.2083	13.97	19.75	2.38	3.14
27.2250	14.34	18.27	2.40	3.50
27.2416	14.59	20.33	2.42	3.51
27.2583	14.68	20.30	2.46	3.77
27.2750	14.67	20.58	2.49	3.96
27.3833	16.97	18.30	2.29	4.98
27.4000	16.62	16.95	2.26	4.77
27.4167	16.41	17.21	2.26	4.76
27.4333	20.50	15.14	2.88	19.09

Table 4.6.3.- Measured gear tooth/rim crack propagation growth
for test 9, test gear S/N 11, $m_B=0.3$.

Pt	Start cycles	End cycles	ohms	Δ ohms	Broken strands	Crack length, (in)	Propa- gation Cycles
Gage 1 (front tooth flank)							
1	0	2,680,000	3.3	0.0	0	—	—
2	2,680,000	2,910,000	4.5	1.2	3	0.025	0
3	2,910,000	3,380,000	6.4	3.1	5	0.039	470,000
4	3,380,000	3,450,000	8.1	4.8	7	0.053	540,000
5	3,450,000	3,540,000	16.0	12.7	8	0.060	630,000
Gage 2 (rear tooth flank)							
1	0	700,000	3.3	0.0	0	—	—
2	700,000	1,060,000	4.0	0.7	2	0.018	0
3	1,060,000	1,370,000	4.5	1.2	3	0.025	310,000
4	1,370,000	1,440,000	5.0	1.7	4	0.031	380,000
5	1,440,000	1,710,000	6.0	2.7	5	0.038	650,000
6	1,710,000	1,980,000	11.9	8.6	7	0.052	920,000
7	1,980,000	2,180,000	15.0	11.7	8	0.058	1,120,000
8	2,180,000	2,290,000	24.0	20.7	9	0.064	1,230,000

Table 4.6.4.- Measured gear tooth crack propagation growth
for test 11, test gear S/N 13, $m_B=3.3$.

Pt	Start cycles	End cycles	ohms	Δ ohms	Broken strands	Crack length, (in)	Propa- gation Cycles
Gage 1 (front tooth flank)							
1	0	76,400	3.5	0.0	0	—	—
2	76,400	100,300	3.7	0.2	1	0.009	0
3	100,300	118,700	4.1	0.6	2	0.015	18,400
4	118,700	134,400	4.5	1.0	3	0.021	34,100
5	134,400	143,100	5.1	1.6	4	0.028	42,800
6	143,100	150,000	5.8	2.3	5	0.034	49,700
7	150,000	158,800	7.0	3.5	6	0.040	58,500
8	158,800	164,500	10.0	6.5	7	0.046	64,200
Gage 2 (rear tooth flank)							
1	0	66,900	3.5	0.0	0	—	—
2	66,900	78,300	3.8	0.3	1	0.007	0
3	78,300	91,000	4.1	0.6	2	0.013	12,700
4	91,000	104,900	4.6	1.1	3	0.020	26,600
5	104,900	118,200	5.1	1.6	4	0.027	39,900
6	118,200	131,000	5.7	2.2	5	0.033	52,700
7	131,000	142,000	7.0	3.5	6	0.039	63,700
8	142,000	148,500	8.3	4.8	7	0.045	70,200

Table 4.6.5.- Crack initiation and crack propagation lives from tests 9 and 11.

Test gear	Crack initiation cycles	Crack propagation cycles through crack gage	Remaining crack propagation cycles	Total crack propagation cycles	Total cycles
Test 9, test gear S/N 11, gage 1 (front flank)	2,910,000 (73.5%)	630,000 (15.9%)	420,400 (10.6%)	1,050,400 (26.5%)	3,960,400
Test 9, test gear S/N 11, gage 2 (rear flank)	1,060,000 (26.7%)	1,230,000 (31.1%)	1,670,400 (42.4%)	2,900,400 (73.3%)	3,960,400
Test 11, test gear S/N 13, gage 1 (front flank)	100,300 (55.0%)	64,200 (35.2%)	17,900 (9.8%)	82,100 (45.0%)	182,400
Test 11, test gear S/N 13, gage 2 (rear flank)	78,300 (42.9%)	70,200 (38.5%)	33,900 (18.6%)	104,100 (57.1%)	182,400

Table 5.2.1.- Calculated principle stresses for finite element models
of test gears S/N 01 through 08.

S/N	m_B	Notch dimensions			Max prin stress			Min prin stress, ksi
		Length, in.	Width, in.	Angle, deg	Without notch, ksi	With notch, ksi	Stress con. factor	
01	3.3	0.006	0.007	37	42.2	124.9	2.96	50.9
02	3.3	0.011	0.006	33	42.2	138.8	3.29	50.9
03	1.0	0.012	0.006	29	38.8	127.7	3.29	57.9
04	1.0	0.005	0.004	40	38.8	125.0	3.22	57.9
05	0.5	0.010	0.008	34	35.3	107.1	3.03	87.5
06	0.5	0.010	0.007	34	35.3	110.6	3.13	87.5
07	0.3	0.013	0.004	31	52.4	177.2	3.38	149.2
08	0.3	0.009	0.009	30	52.4	126.2	2.41	149.2

Table 5.4.1.- Calculated mode I stress intensity factors
for test gears S/N 11 and 13.

Step	Crack length (in)	Crack tip x-coor (in)	Crack tip y-coor (in)	K_I (ksi $\sqrt{\text{in.}}$)
Test gear S/N 11, front tooth flank				
1	0.0252	-0.101	1.571	10.3
2	0.0352	-0.095	1.563	11.8
3	0.0452	-0.089	1.555	13.5
4	0.0552	-0.084	1.546	15.5
5	0.0652	-0.080	1.537	18.1
6	0.0752	-0.077	1.528	21.3
7	0.0852	-0.074	1.518	25.1
Test gear S/N 11, rear tooth flank				
1	0.0177	-0.106	1.577	9.0
2	0.0277	-0.099	1.570	10.5
3	0.0377	-0.092	1.562	12.0
4	0.0477	-0.087	1.554	13.7
5	0.0577	-0.082	1.545	15.8
6	0.0677	-0.078	1.536	18.5
7	0.0777	-0.074	1.527	21.8
Test gear S/N 13				
1	0.0079	-0.110	1.587	11.0
2	0.0179	-0.101	1.583	13.2
3	0.0279	-0.092	1.578	14.5
4	0.0379	-0.084	1.573	15.6
5	0.0479	-0.075	1.569	16.6
6	0.0579	-0.066	1.565	17.6
7	0.0679	-0.056	1.556	17.6

Table 5.5.1.- Comparison of predicted crack initiation cycles, predicted crack propagation cycles, and total predicted cycles to experiments.

	Experimental results			Predictions		
	Crack initiation cycles	Crack propagation cycles	Total cycles	Crack initiation cycles	Crack propagation cycles	Total cycles
Test 9, S/N 11, front flank	2,910,000	1,050,400	3,960,400	1,530,000 66.8%	760,000 ^a 33.2%	2,290,000
	73.5%	26.5%		1,530,000 62.4%	920,000 ^b 37.6%	2,450,000
Test 9, S/N 11, rear flank	1,060,000	2,900,400	3,960,400	1,530,000 55.0%	1,250,000 ^a 45.0%	2,780,000
	26.8%	73.2%		1,530,000 53.7%	1,320,000 ^b 46.3%	2,850,000
Test 11, S/N 13, front flank	100,300	82,100	182,400	340,000 75.6%	110,000 ^c 24.4%	450,000
	55.0%	45.0%		340,000 81.0%	80,000 ^d 19.0%	420,000
Test 11, S/N 13, rear flank	78,300	104,100	182,400	340,000 75.6%	110,000 ^c 24.4%	450,000
	42.9%	57.1%		340,000 81.0%	80,000 ^d 19.0%	420,000

^a Collipriest fatigue crack growth model, $n=1.63$, $C=8.36 \times 10^{-9}$ in/cyc/(ksi $\sqrt{\text{in}}$)ⁿ, $\Delta K_{th}=3.5$ ksi $\sqrt{\text{in}}$, $K_{IC}=200$ ksi $\sqrt{\text{in}}$, $U=0.47$.

^b Paris fatigue crack growth model, $n=2.954$, $C=6.027 \times 10^{-19}$ in/cyc/(psi $\sqrt{\text{in}}$)ⁿ, $U=0.38$.

^c Collipriest fatigue crack growth model, $n=1.63$, $C=8.36 \times 10^{-9}$ in/cyc/(ksi $\sqrt{\text{in}}$)ⁿ, $\Delta K_{th}=3.5$ ksi $\sqrt{\text{in}}$, $K_{IC}=200$ ksi $\sqrt{\text{in}}$, $U=0.94$.

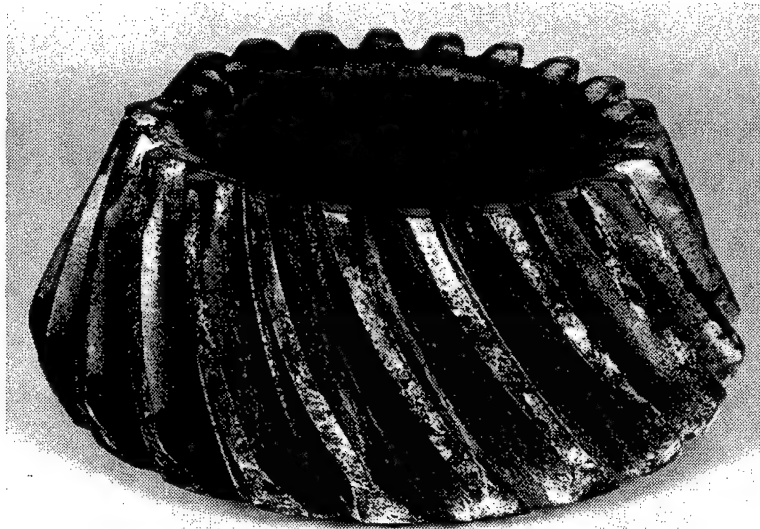
^d Paris fatigue crack growth model, $n=2.954$, $C=6.027 \times 10^{-19}$ in/cyc/(psi $\sqrt{\text{in}}$)ⁿ, $U=0.85$.

Table 6.3.1.- Gear tooth design variables used in the analytical parametric studies.

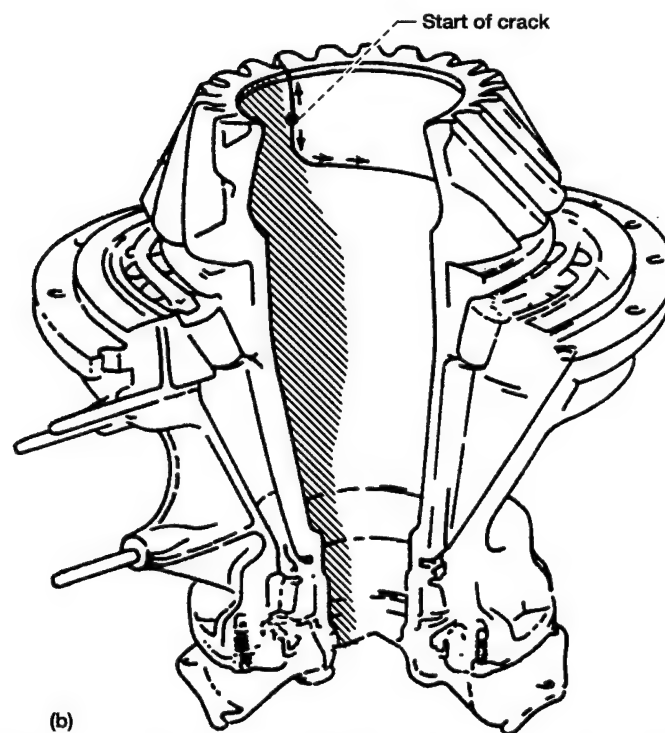
Run	Backup ratio m_B	Pitch P_d	Pressure angle ϕ (deg)	Driver gear (with crack)		Driven gear	
				Number of teeth $N_{g,1}$	Pitch radius $r_{p,1}$ (in)	Number of teeth $N_{g,2}$	Pitch radius $r_{p,2}$ (in)
1	0.7	8	20	28	1.750	28	1.750
2	0.5	8	20	28	1.750	28	1.750
3	0.7	4	20	14	1.750	14	1.750
4	0.5	4	20	14	1.750	14	1.750
5	0.7	16	20	56	1.750	56	1.750
6	0.5	16	20	56	1.750	56	1.750
7	0.7	8	20	56	3.500	56	3.500
8	0.5	8	20	56	3.500	56	3.500
9	0.7	8	20	112	7.000	112	7.000
10	0.5	8	20	112	7.000	112	7.000
11	0.7	8	25	28	1.750	28	1.750
12	0.5	8	25	28	1.750	28	1.750
13	0.7	8	14.5	28	1.750	28	1.750
14	0.5	8	14.5	28	1.750	28	1.750
15	0.7	8	20	28	1.750	56	3.500
16	0.5	8	20	28	1.750	56	3.500
17	0.7	8	20	28	1.750	112	7.000
18	0.5	8	20	28	1.750	112	7.000

Table 6.3.2.- Tooth load locations and orientations, initial crack mouth locations, and maximum and minimum tooth fillet principle stresses for runs used in the analytical parametric studies.

Run	Unit tooth load			Max prin stress		Min prin stress (psi)
	Location of HPSTC (in)	x-component (lb)	y-component (lb)	Location (in)	Stress (psi)	
1	1.774	0.936	-0.352	1.591	23.4	48.2
2	1.774	0.936	-0.352	1.587	23.0	63.8
3	1.827	0.917	-0.399	1.466	12.1	17.6
4	1.827	0.917	-0.399	1.459	10.4	19.8
5	1.757	0.941	-0.340	1.669	32.1	108.0
6	1.757	0.941	-0.340	1.668	33.3	150.5
7	3.514	0.941	-0.340	3.334	17.4	59.0
8	3.514	0.941	-0.340	3.332	17.7	82.0
9	7.009	0.941	-0.340	6.837	9.0	73.4
10	7.009	0.941	-0.340	6.844	5.9	106.5
11	1.792	0.893	-0.450	1.588	16.7	51.8
12	1.792	0.893	-0.450	1.586	15.2	71.1
13	1.754	0.973	-0.229	1.600	24.9	36.9
14	1.754	0.973	-0.229	1.597	25.4	46.3
15	1.765	0.940	-0.340	1.591	21.3	45.1
16	1.765	0.940	-0.340	1.587	20.3	59.6
17	1.759	0.943	-0.332	1.591	21.8	45.0
18	1.759	0.943	-0.332	1.587	21.1	59.4



(a)



(b)

Figure 1.1.1.—Failed Royal Australian Navy helicopter spiral-bevel pinion (McFadden, 1985). (a) Failed spiral-bevel input pinion. (b) Path of fatigue crack.

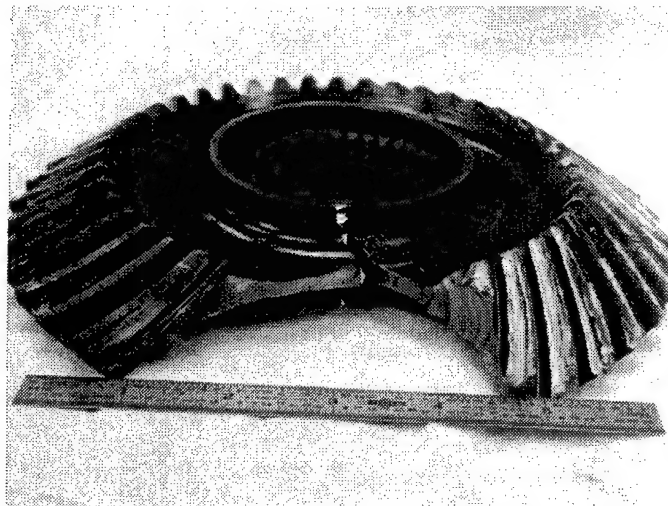


Figure 1.1.2.—Gear resonance failure (Albrecht, 1988).

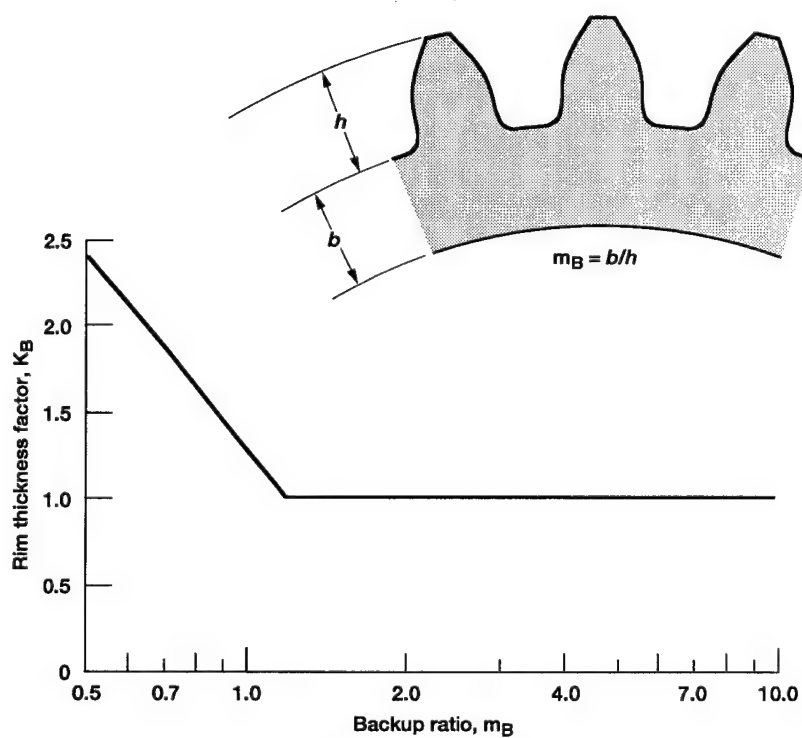


Figure 1.2.1.—Gear tooth bending stress index rim thickness correction factor (AGMA, 1990).

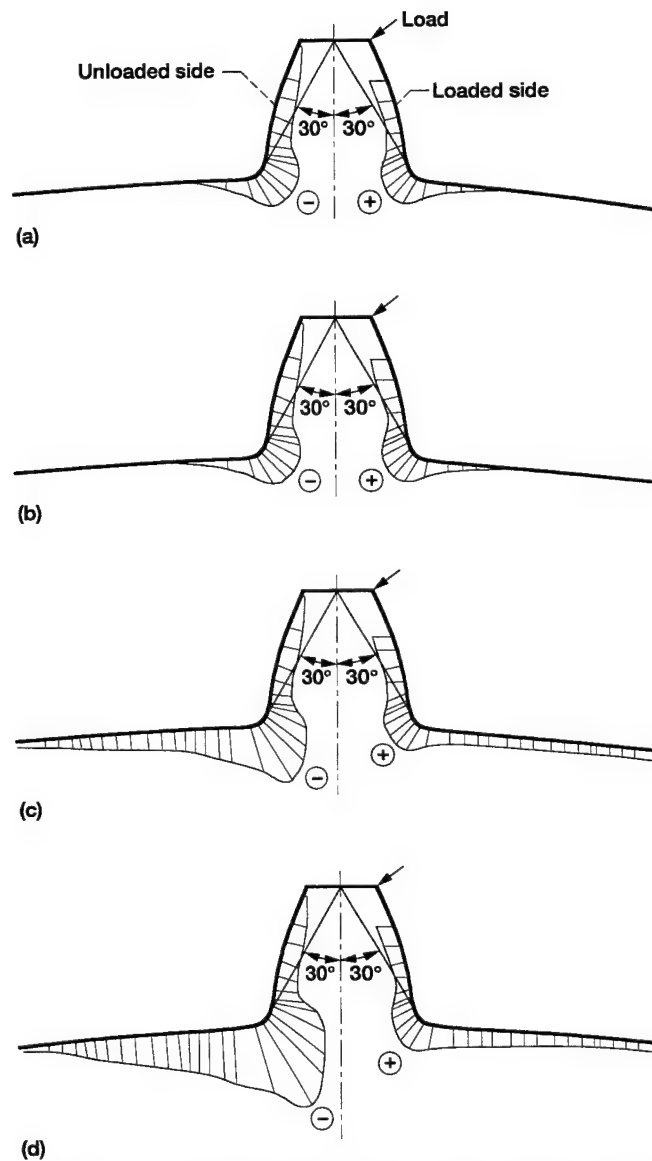


Figure 1.3.1.—Finite element stress analysis of a thin-rim gear (Oda, et al., 1981. (a) Backup ratio = 4.44. (b) Backup ratio = 0.89. (c) Backup ratio = 0.67. (d) Backup ratio = 0.44.

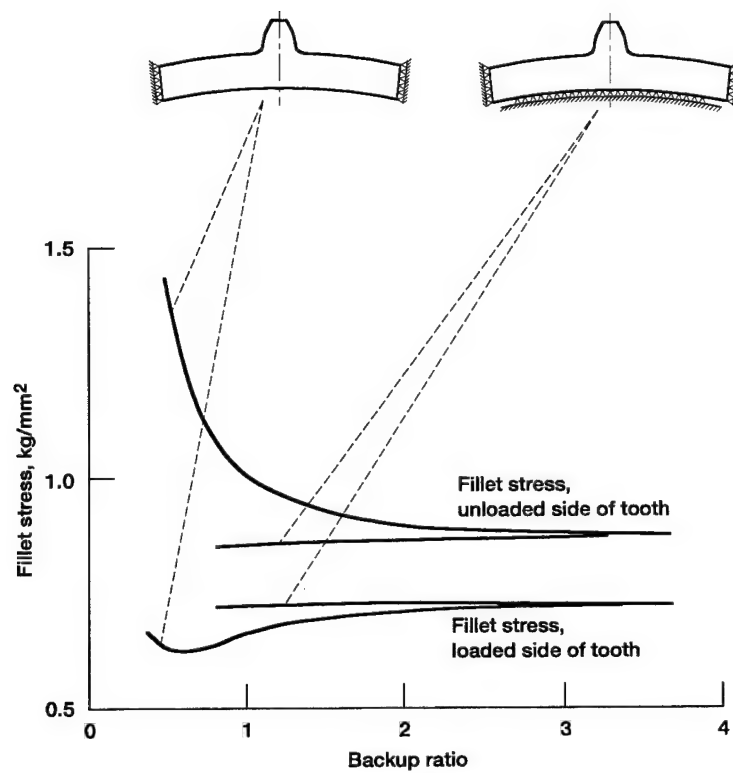


Figure 1.3.2.—Effect of boundary conditions on stress of a thin-rim gear (Oda, et al., 1981).

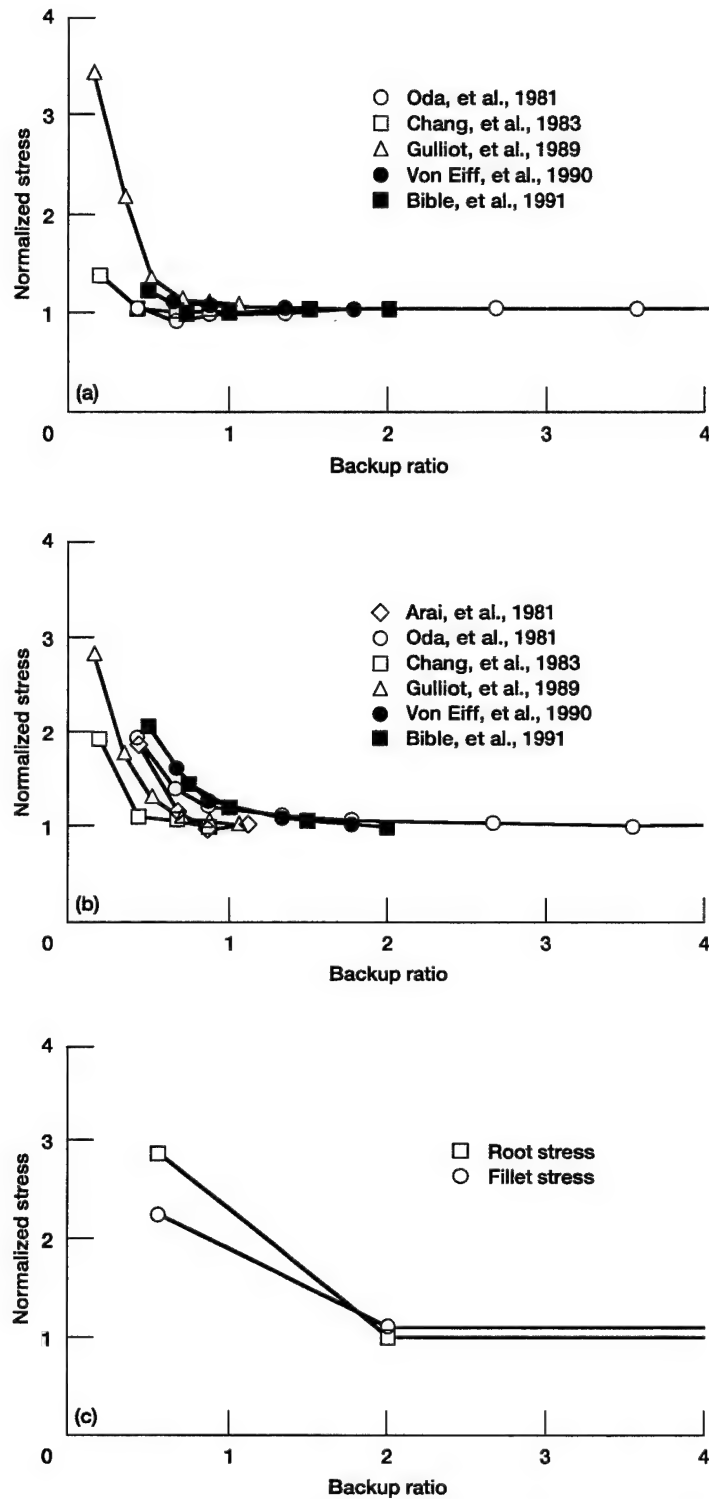


Figure 1.3.3.—Summary of effect of rim thickness on stress. (a) Fillet stress, loaded side of tooth. (b) Fillet stress, unloaded side of tooth. (c) Alternating stress (Drago and Lutthans, 1983).

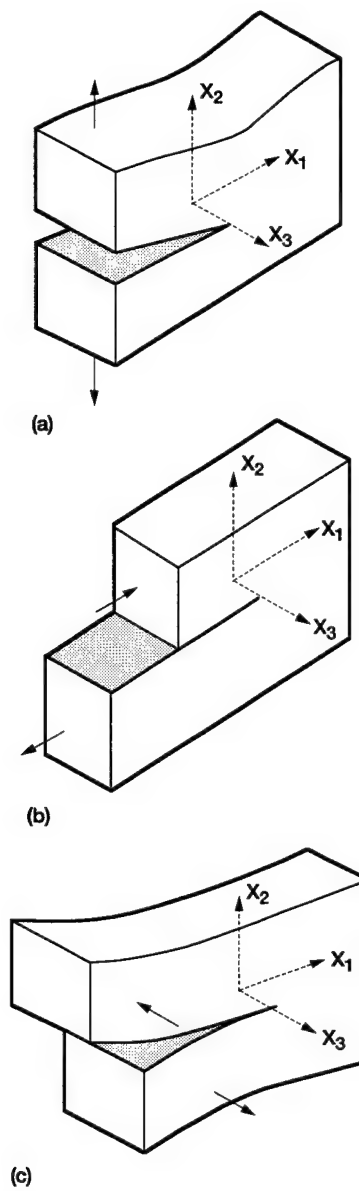


Figure 1.4.1.—Three types of loading on a cracked body. (a) Mode I. (b) Mode II. (c) Mode III.

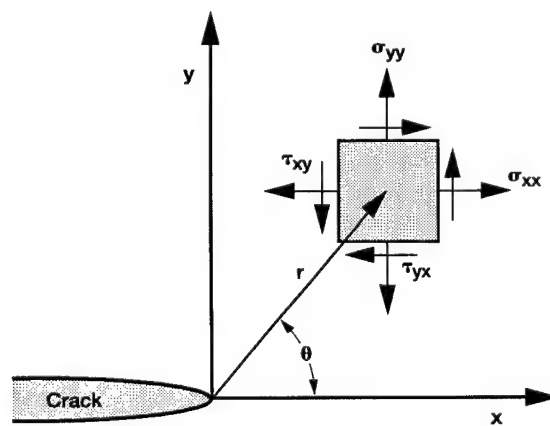


Figure 1.4.2.—Coordinate axes ahead of crack tip.

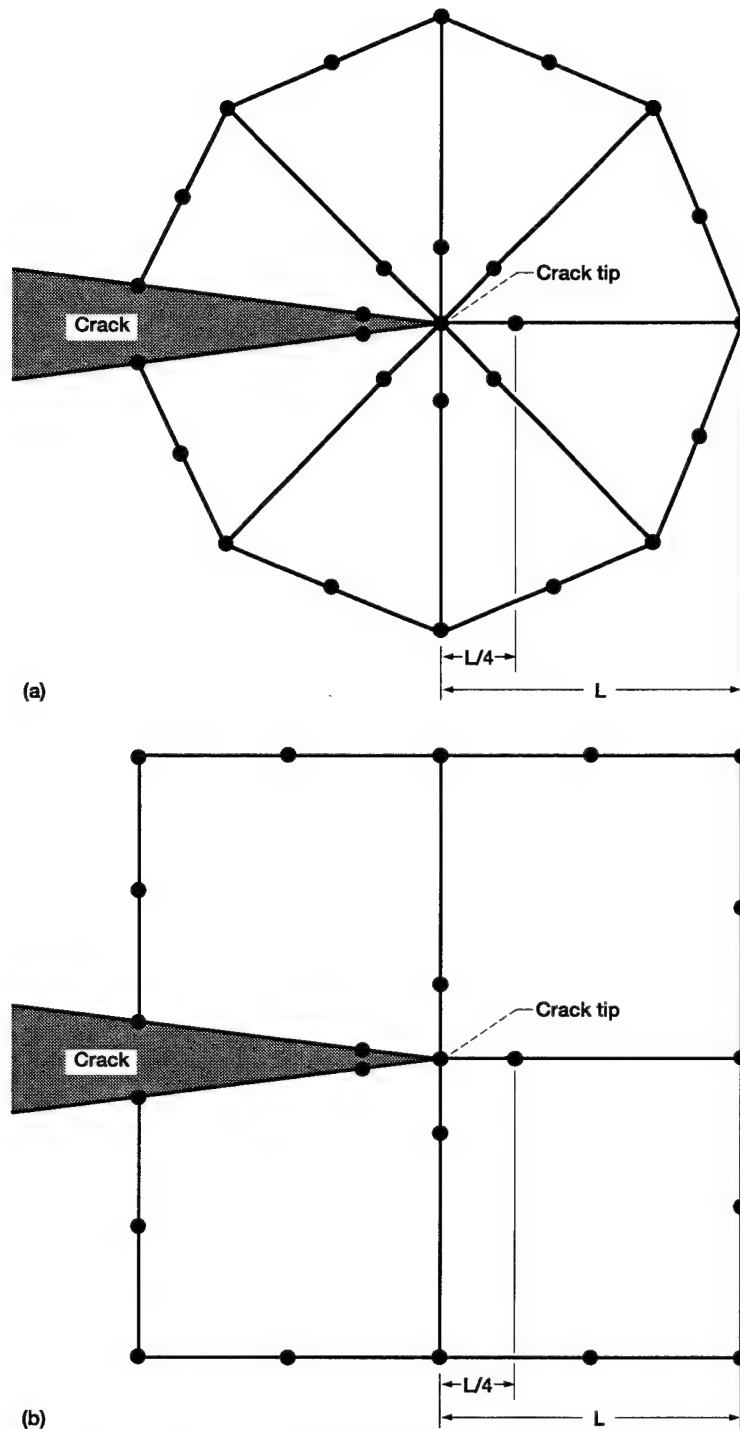


Figure 2.2.1.—Quarter-node, isoparametric finite elements used for the region near a crack tip. (a) Six-node triangular elements. (b) Eight-node quadrilateral elements.

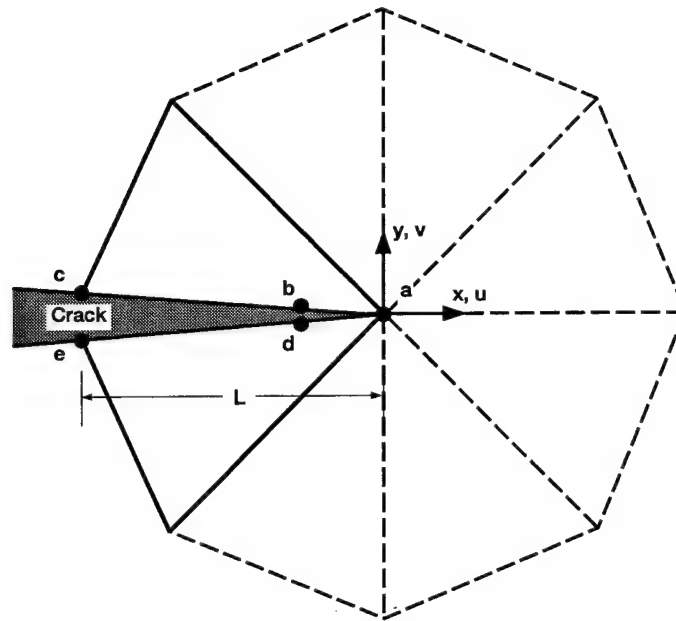


Figure 2.2.2.—Nomenclature used for stress intensity factor calculation using the displacement correlation method.

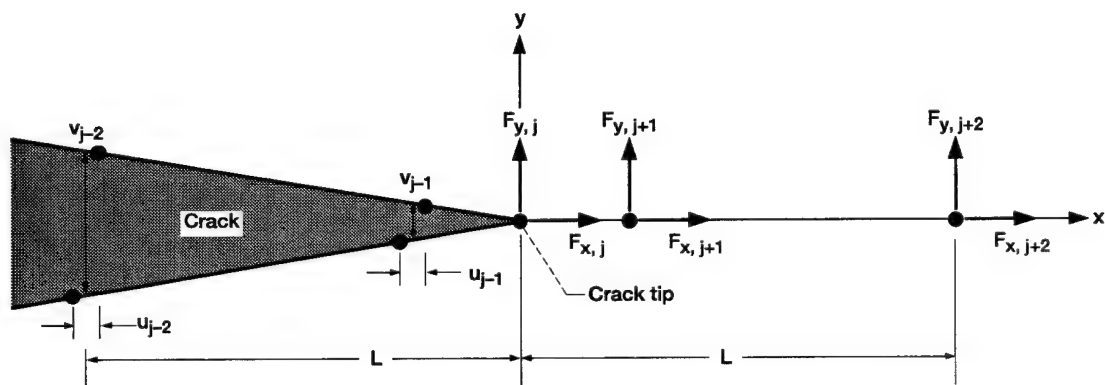


Figure 2.2.3.—Nomenclature used for stress intensity factor calculation using the modified crack closure method.

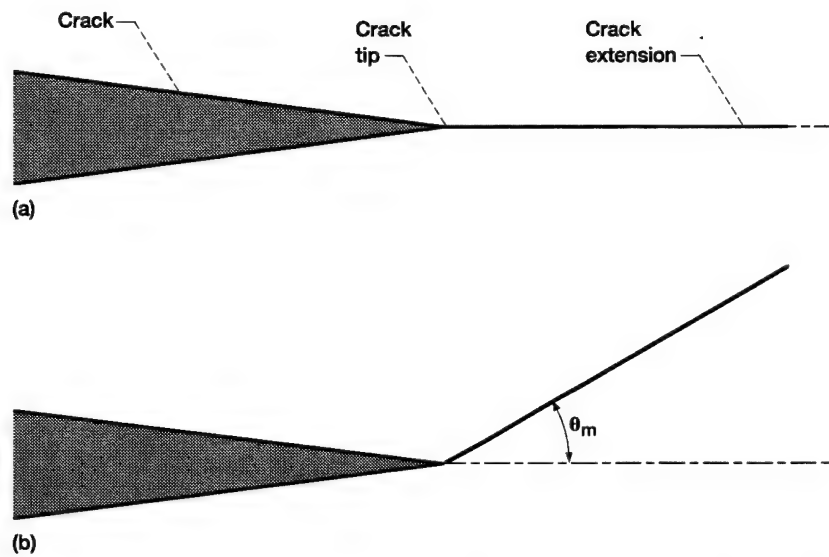


Figure 2.3.1.—Crack extension for pure mode I and mixed-mode loading. (a) Crack extension due to pure mode I loading. (b) Crack extension due to mixed-mode loading.

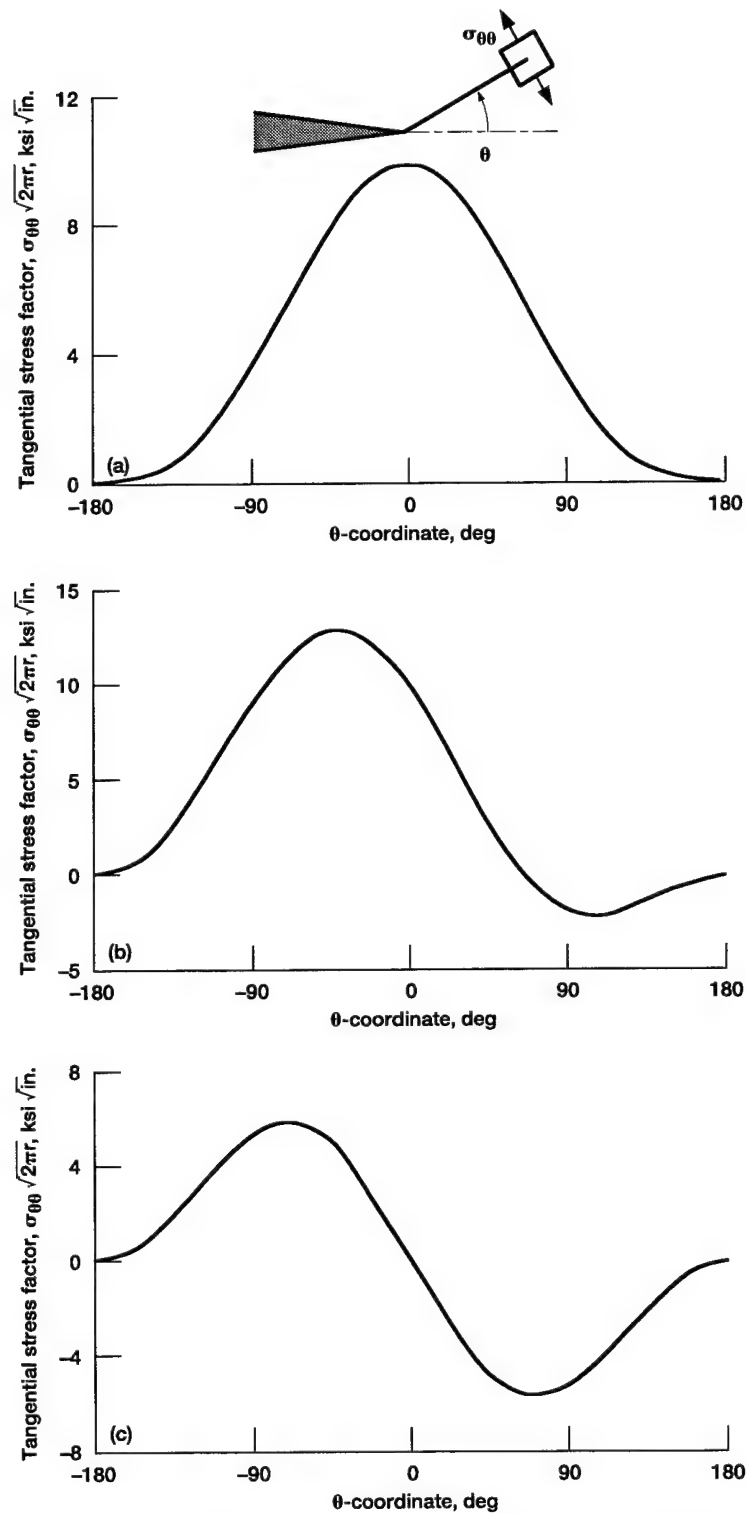


Figure 2.3.2.—Crack tip tangential stress factor for various load conditions.
 (a) $K_I = 10 \text{ ksi} \sqrt{\text{in.}}$, $K_{II} = 0$, $\theta_M = 0^\circ$. (b) $K_I = 10 \text{ ksi} \sqrt{\text{in.}}$, $K_{II} = 5 \text{ ksi} \sqrt{\text{in.}}$, $\theta_M = -40.2^\circ$. (c) $K_I = 0$, $K_{II} = 5 \text{ ksi} \sqrt{\text{in.}}$, $\theta_M = -70.5^\circ$.

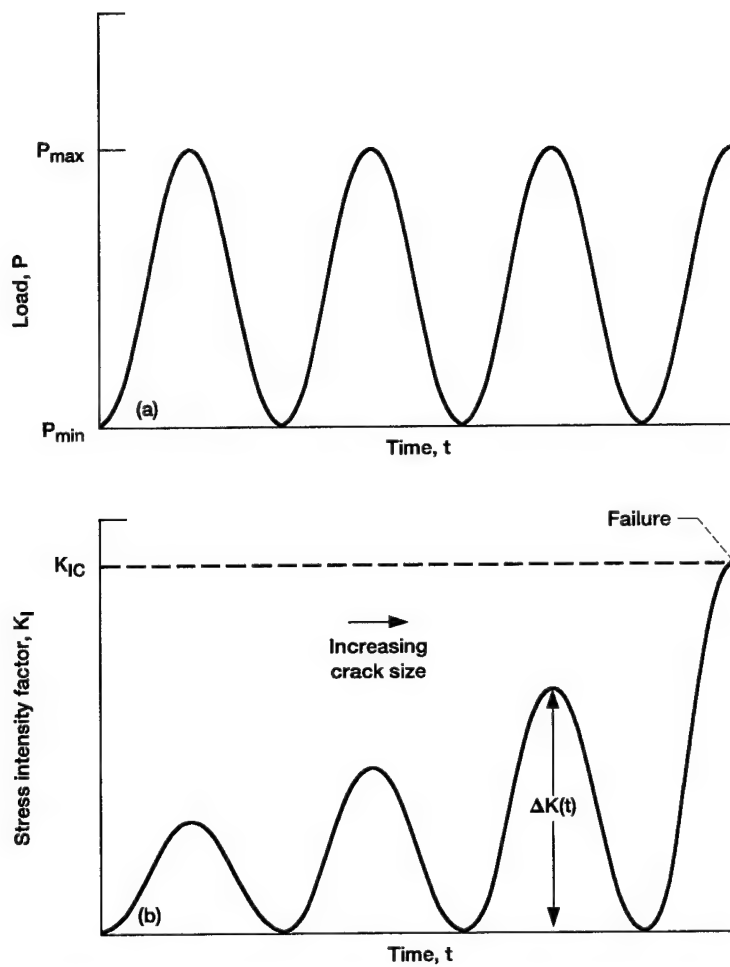


Figure 2.4.1.—Cyclic externally applied load and mode I stress intensity factor. (a) Load. (b) Stress intensity factor.

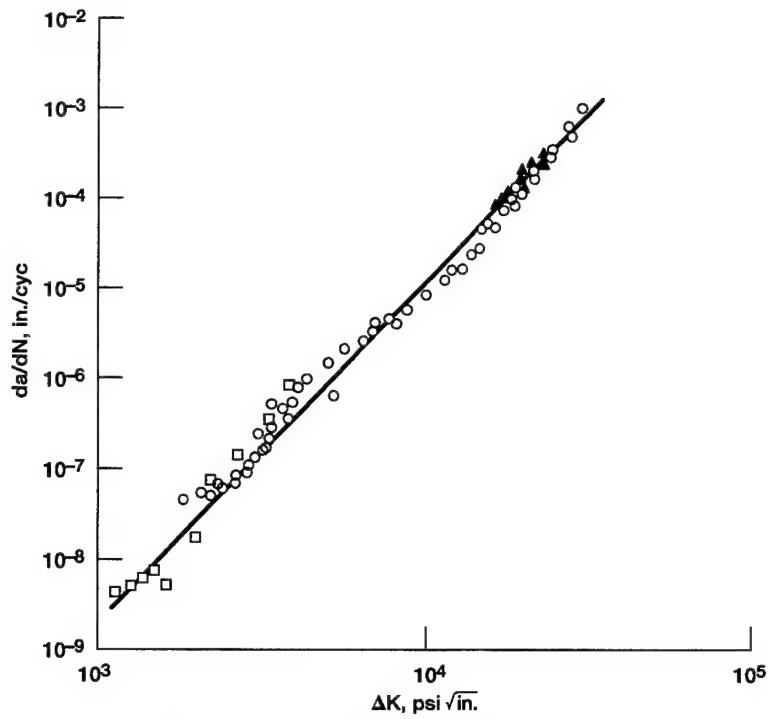


Figure 2.4.2.—Fatigue crack growth data for 7075-T6 aluminum alloy (Paris and Erdogan, 1963).

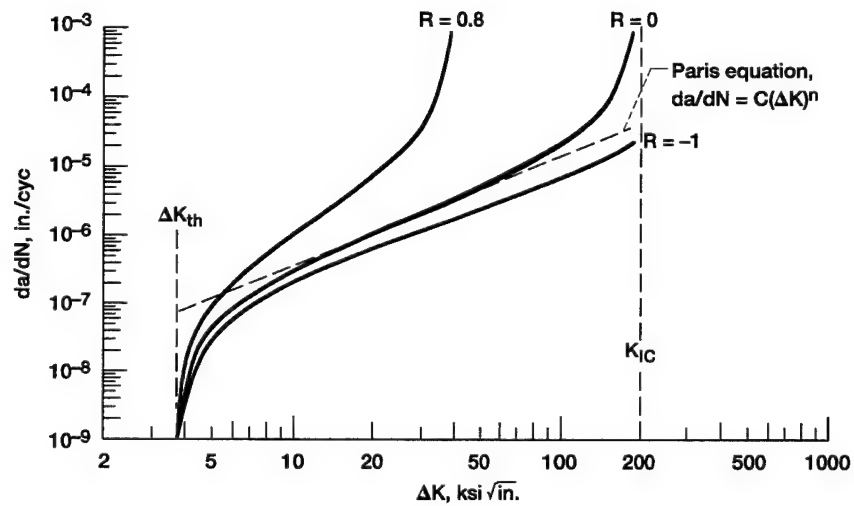


Figure 2.4.3.—Fatigue crack growth rate using Colli Priest equation: $n = 1.63$, $C = 8.36 \times 10^{-9}$, $\Delta K_{th} = 3.5$ ksi $\sqrt{\text{in.}}$, $K_{IC} = 200$ ksi $\sqrt{\text{in.}}$.

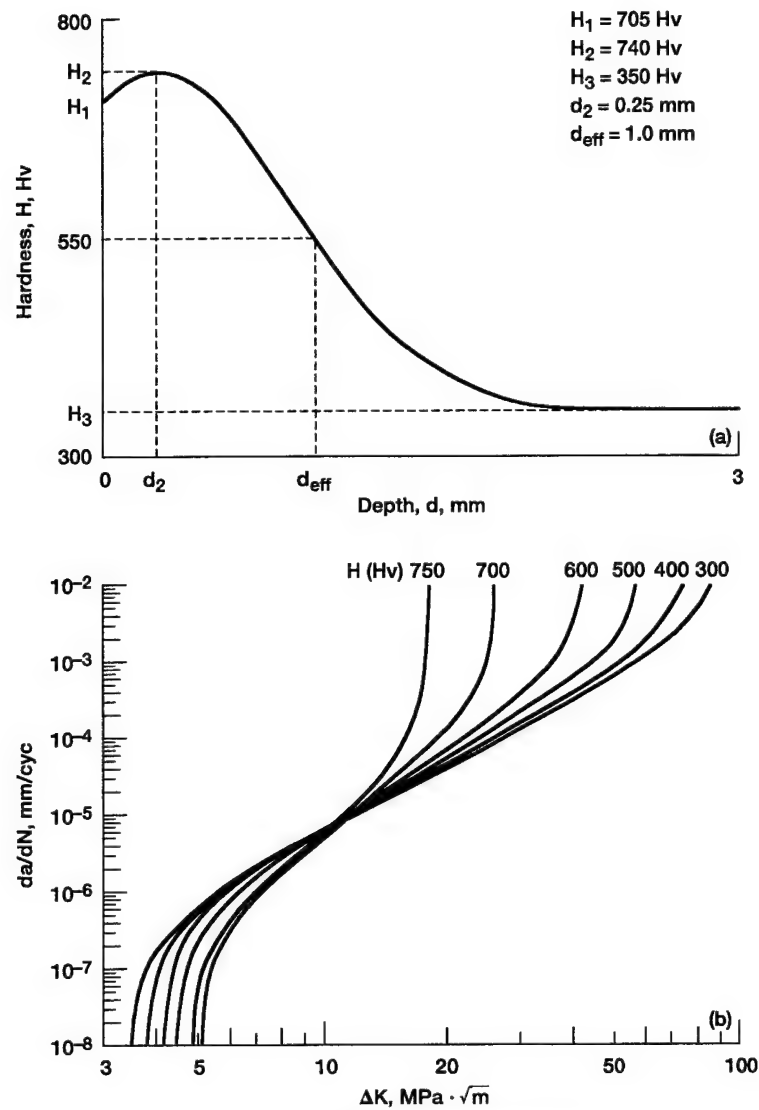


Figure 2.4.4.—Gear tooth hardness distribution and bending fatigue crack growth analysis. (a) Hardness distribution. (b) Fatigue crack growth.

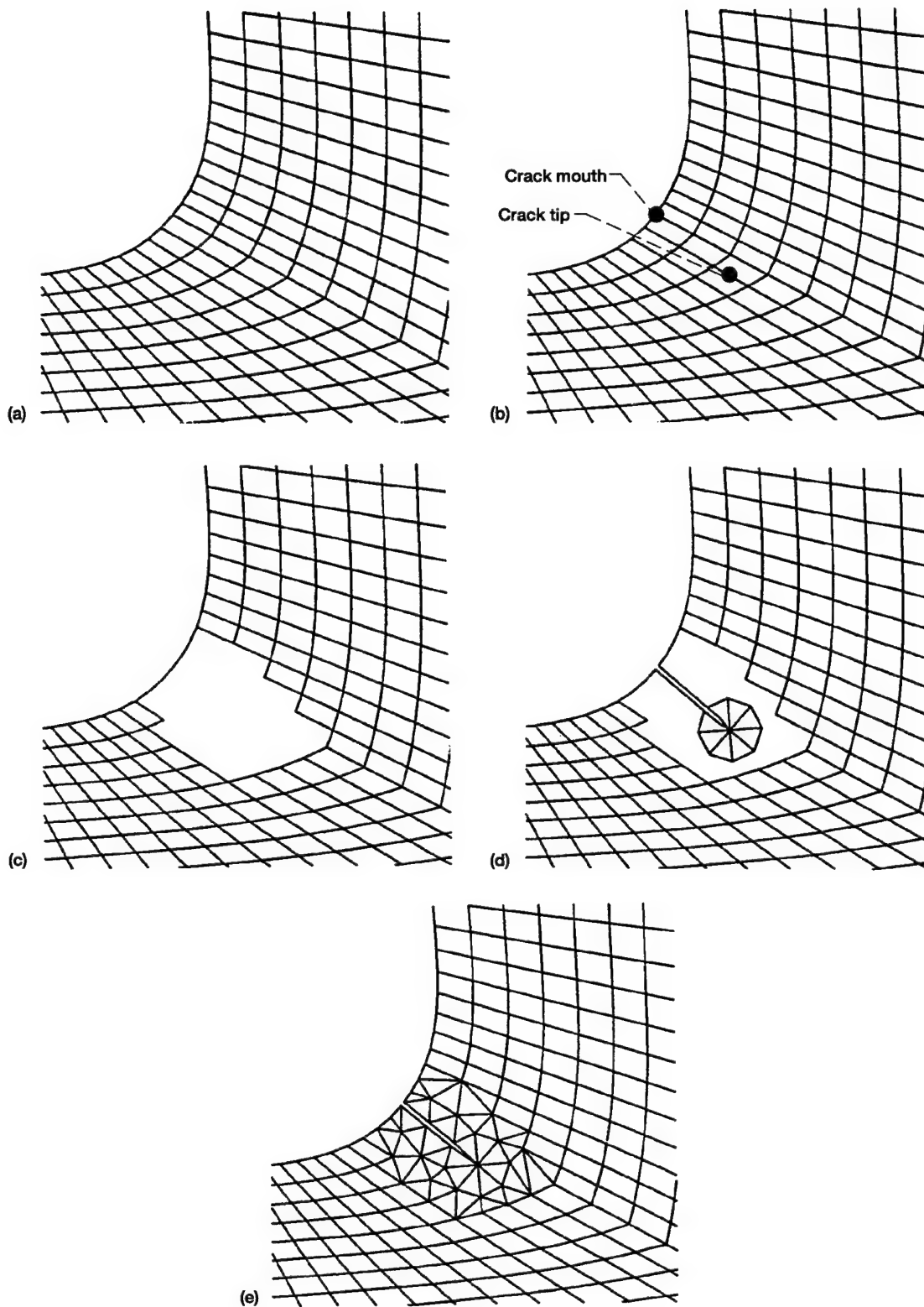


Figure 2.5.1.—FRANC computer program crack modeling scheme. (a) Initial uncracked mesh. (b) User defined mouth and tip of initial crack. (c) Deletion of elements near crack tip. (d) Rosette of quarter-point, triangular elements. (e) Final mesh of cracked surface.

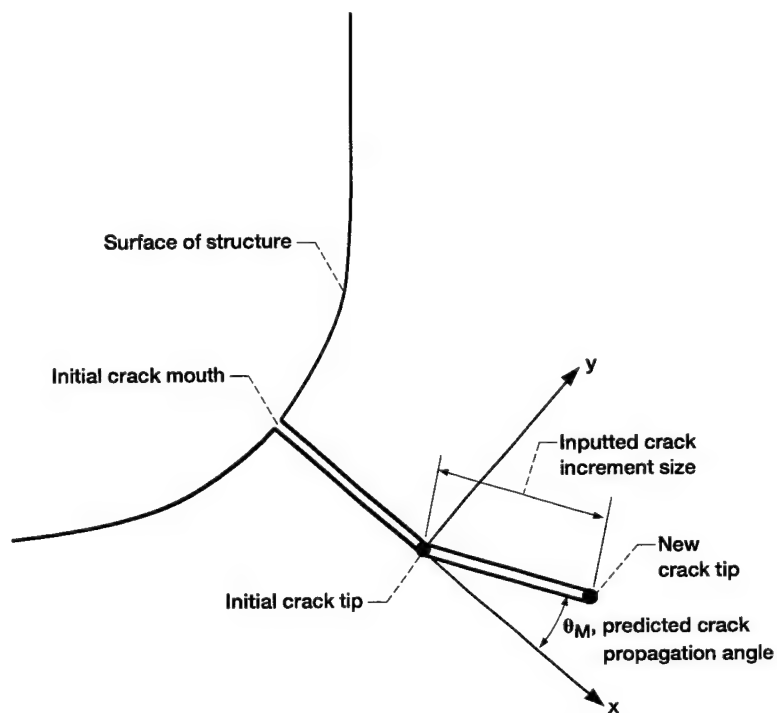


Figure 2.5.2.—Extension of initial crack in FRANC computer program.

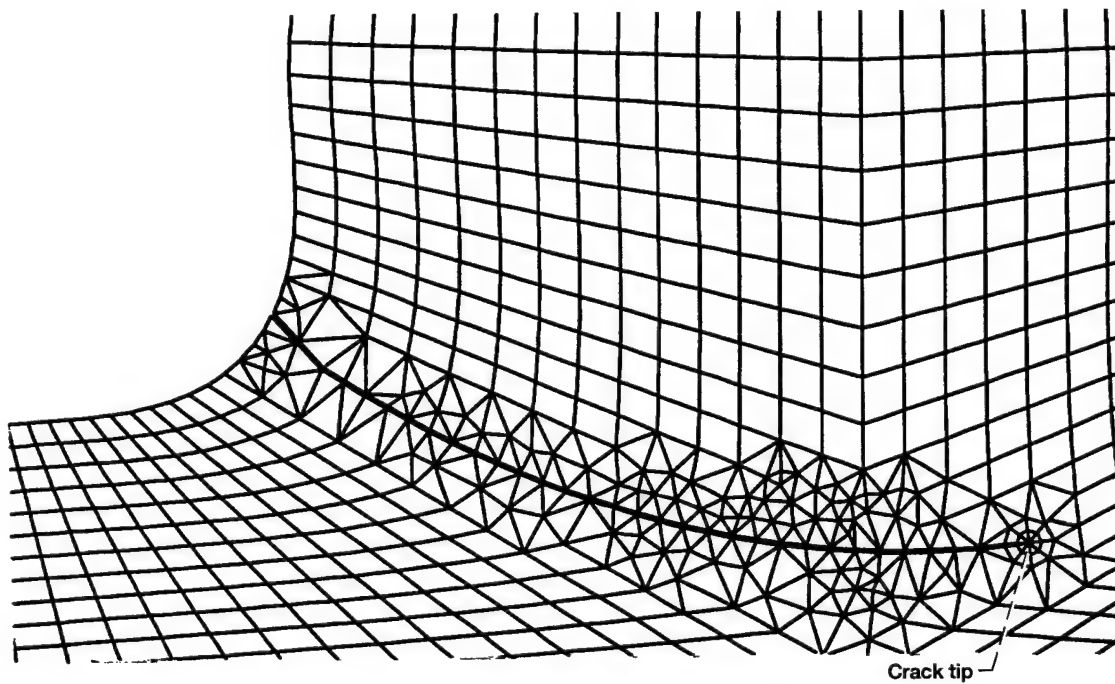


Figure 2.5.3.—FRANC computer program crack propagation modeling.

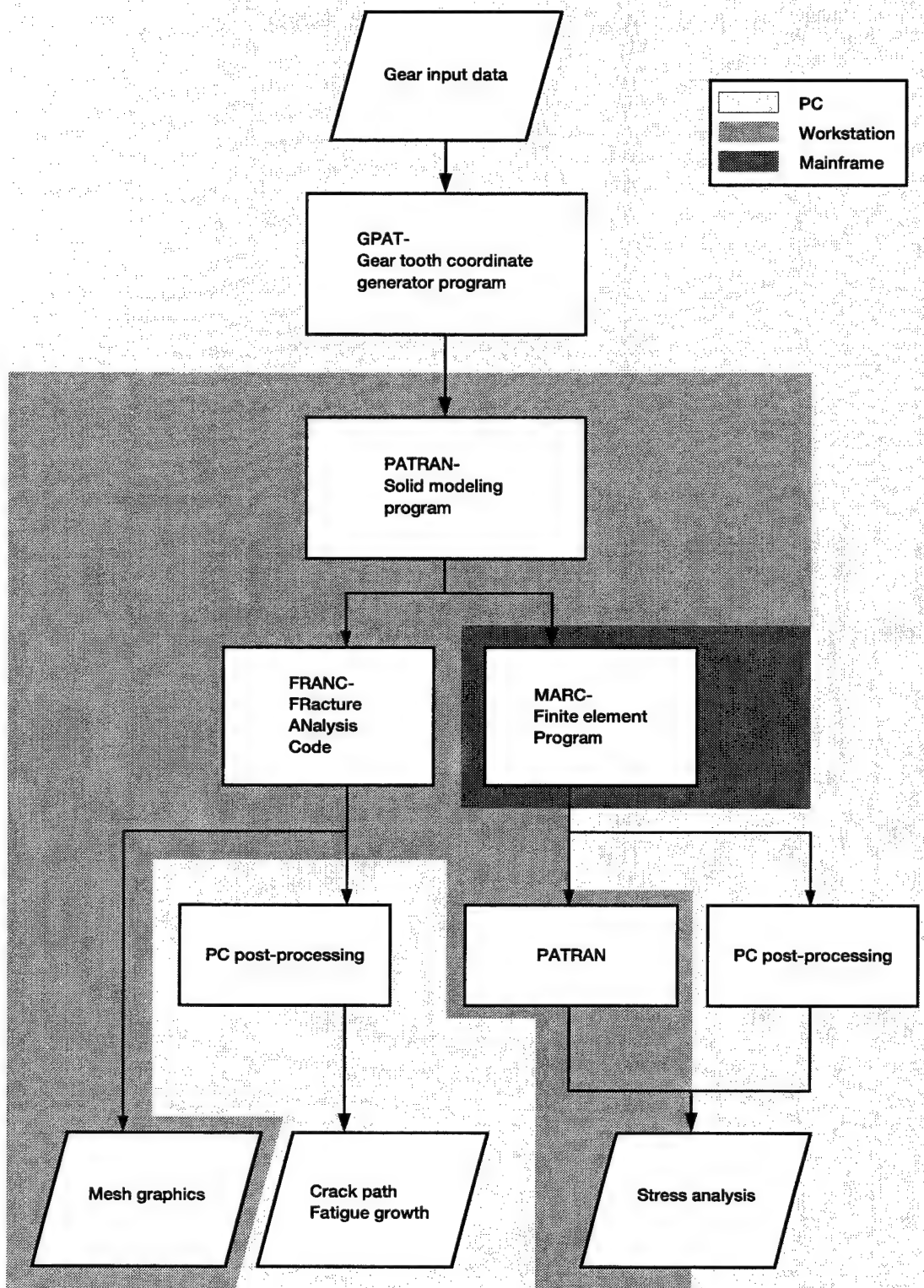


Figure 3.1.1.—Flow chart of analytical stress analysis and crack propagation calculation procedure.



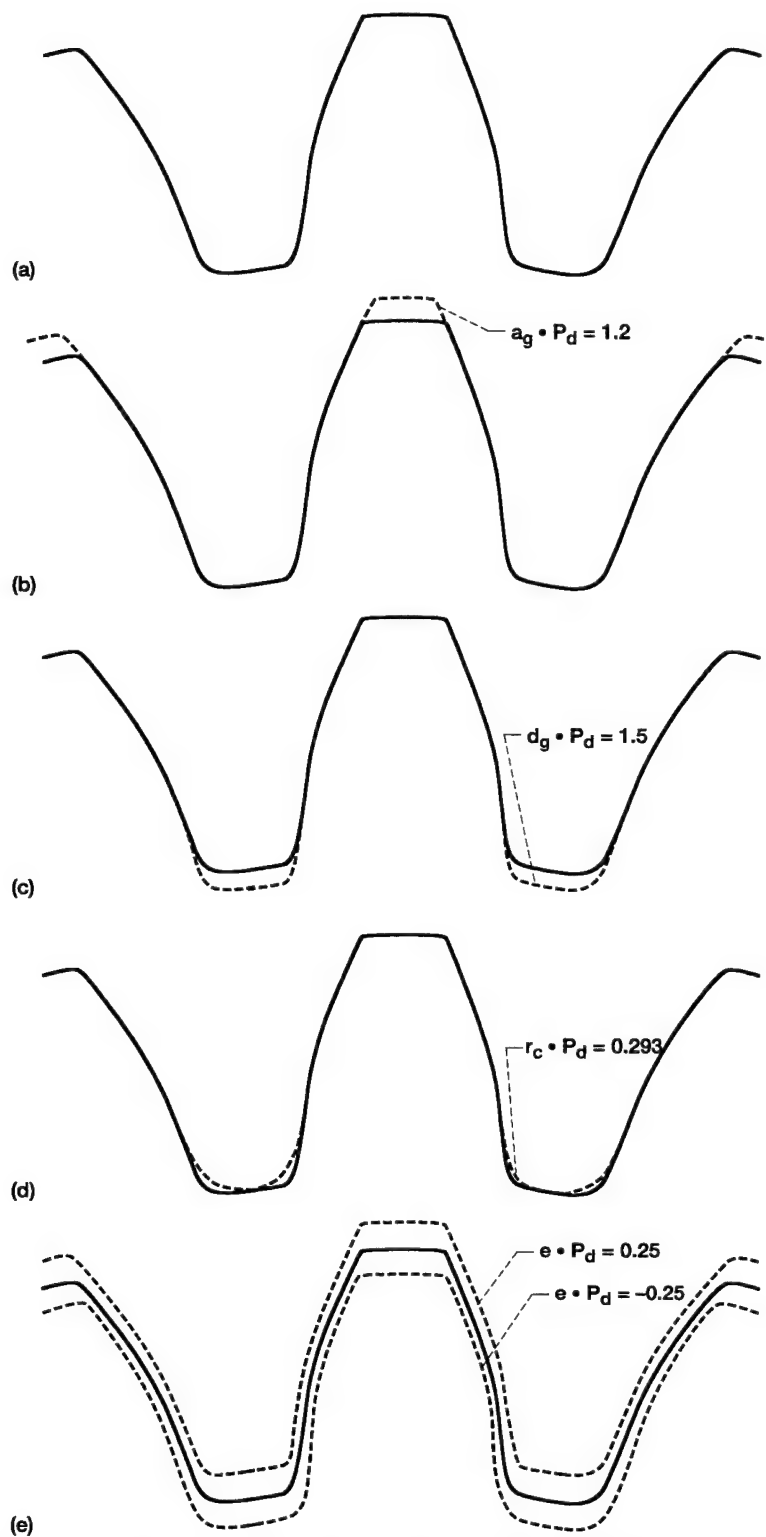


Figure 3.2.3.—Effect of input parameters on tooth geometry. (a) Standard 28-tooth gear with $P_d = 8$ teeth/in., $\phi = 20^\circ$, $a_g \cdot P_d = 1.0$, $d_g \cdot P_d = 1.35$, $r_c = 0$, $e = 0$. (b) Addendum effect. (c) Dedendum effect. (d) Cutter tip radius effect. (e) Tool shift effect.

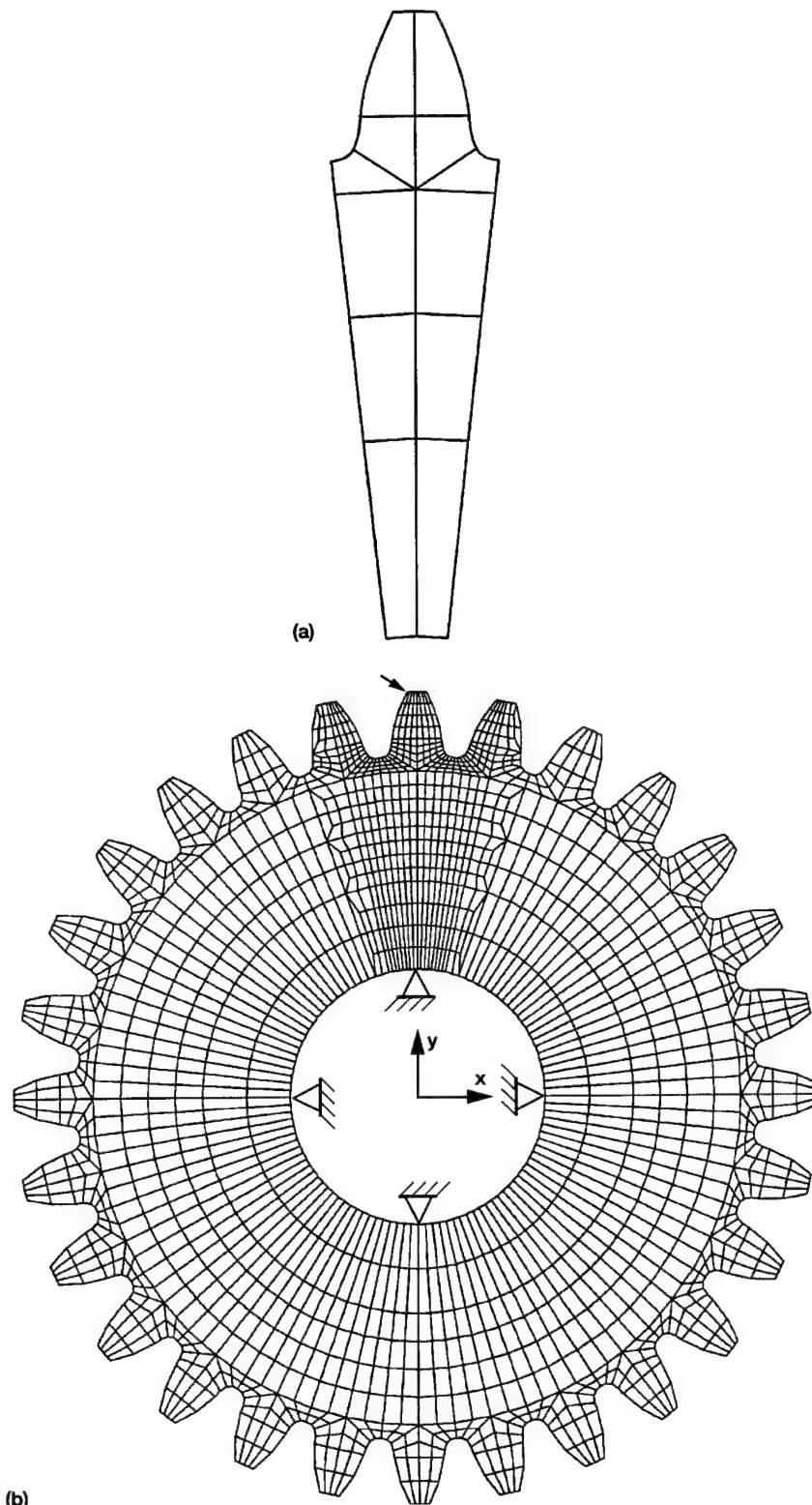
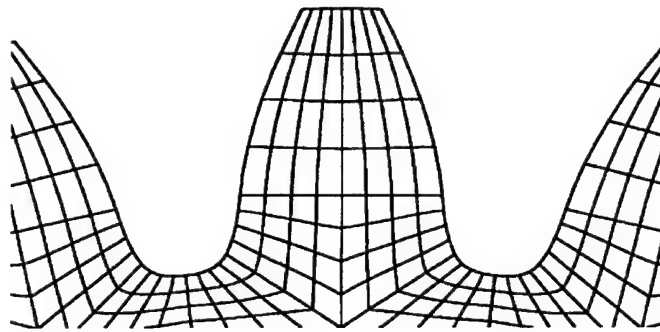
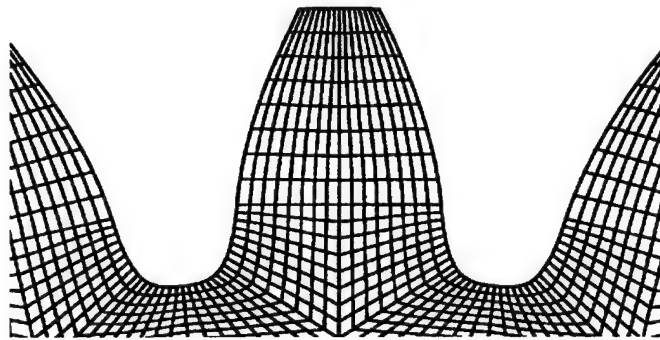


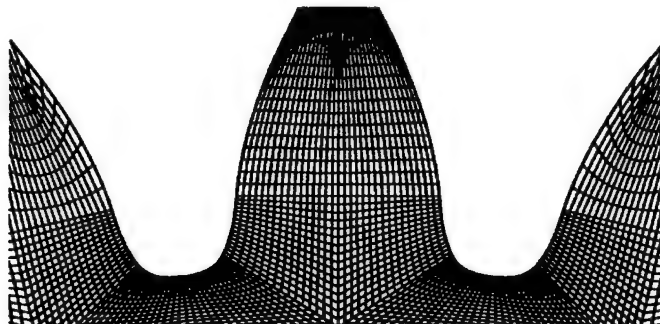
Figure 3.2.4.—Gear finite element modeling. (a) Single-tooth sector of P3/PATRAN patches. (b) Complete gear with load and boundary conditions.



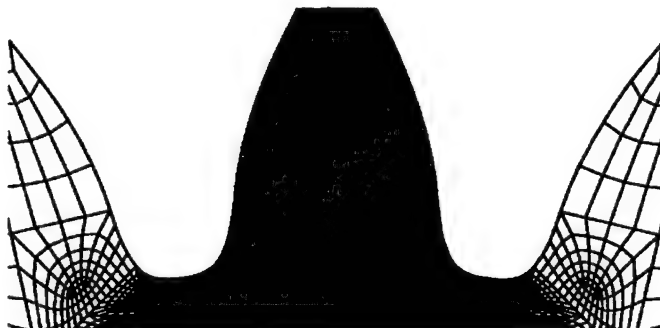
(a)



(b)



(c)



(d)

Figure 3.3.1.—Gear tooth finite element mesh refinement study. (a) 1692 elements. (b) 3216 elements. (c) 7276 elements.(d) 8348 elements.

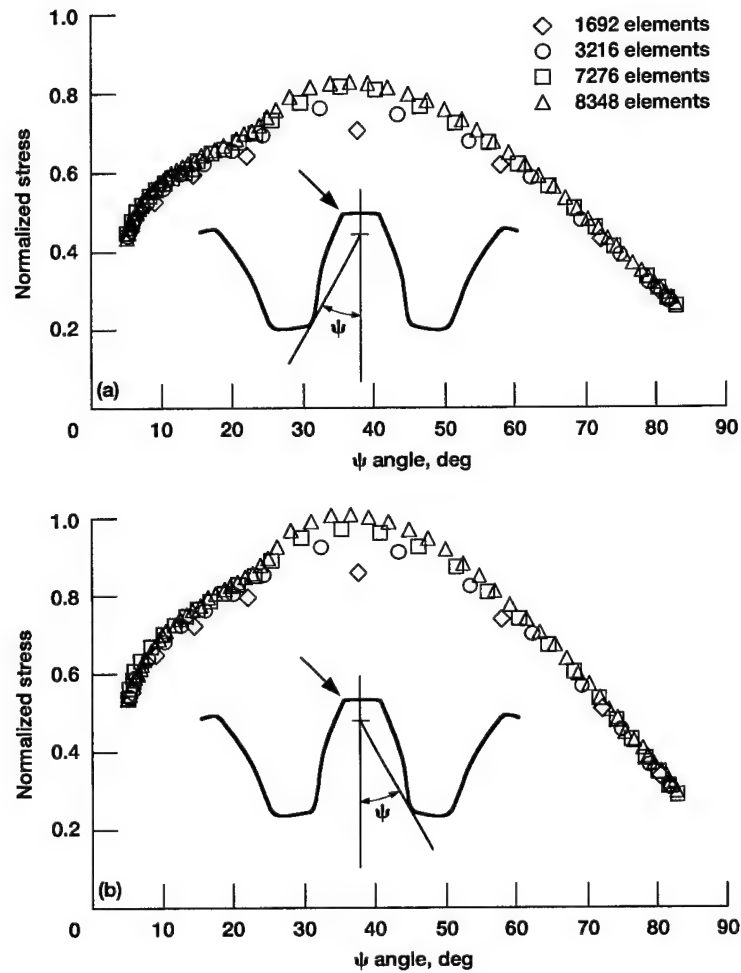


Figure 3.3.2.—Stress distribution of gear tooth fillet surface elements. (a) Loaded side of tooth (tensile stress). (b) Unloaded side of tooth (compressive stress).

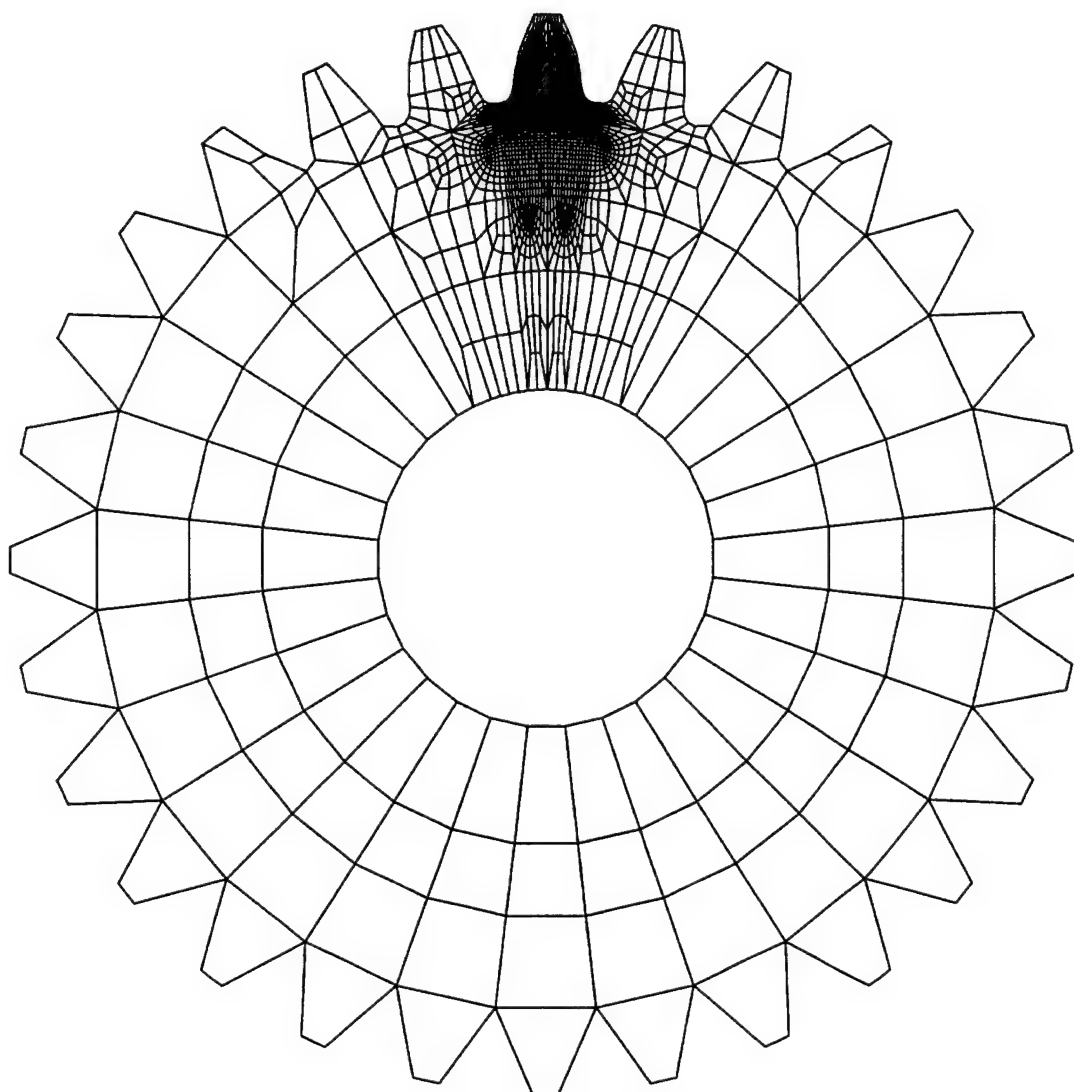


Figure 3.3.3.—2364-element model of gear used in crack propagation studies.

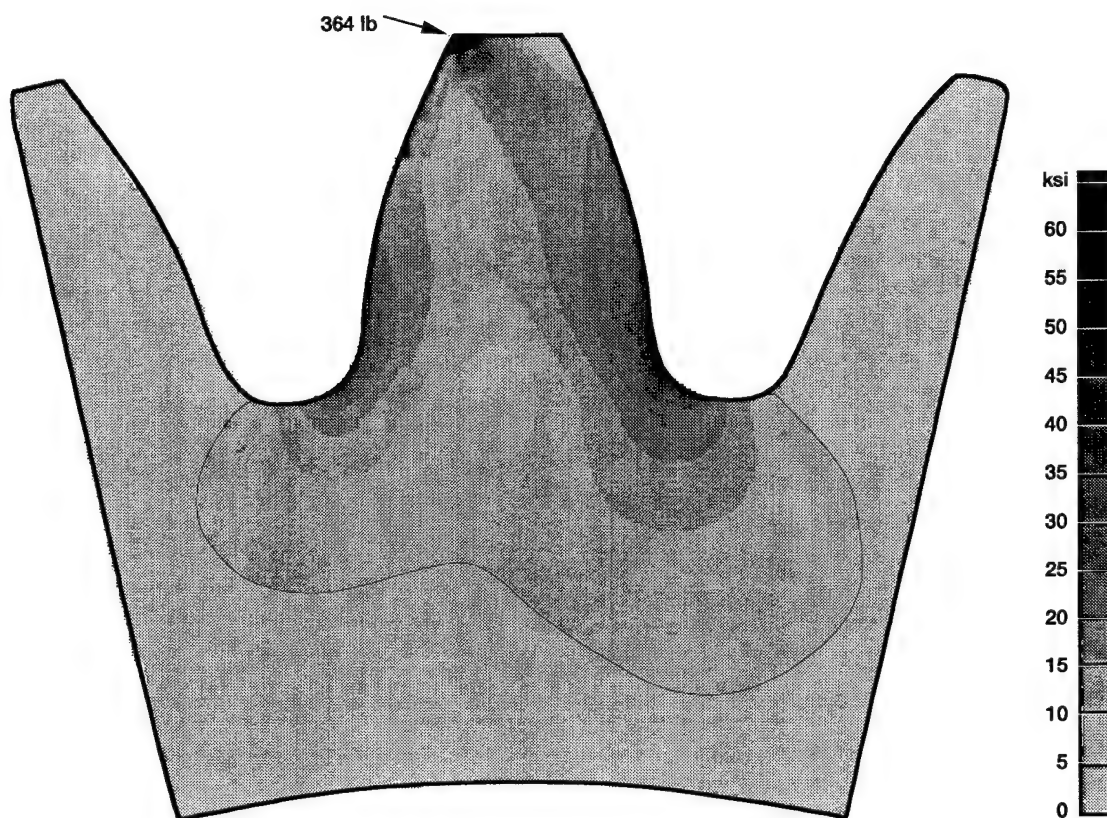


Figure 3.3.4.—Von Mises stresses of loaded gear tooth region for 2364-element model.

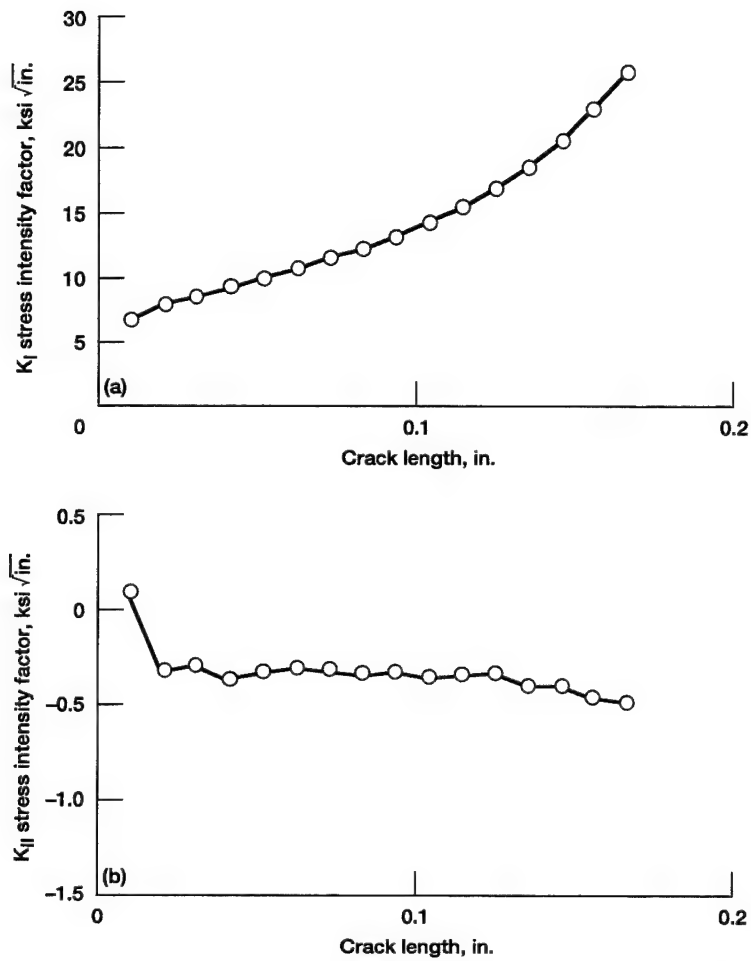


Figure 3.4.1.—Stress intensity factors for 15 steps of automated gear tooth crack propagation. (a) Mode I stress intensity factors. (b) Mode II stress intensity factors.

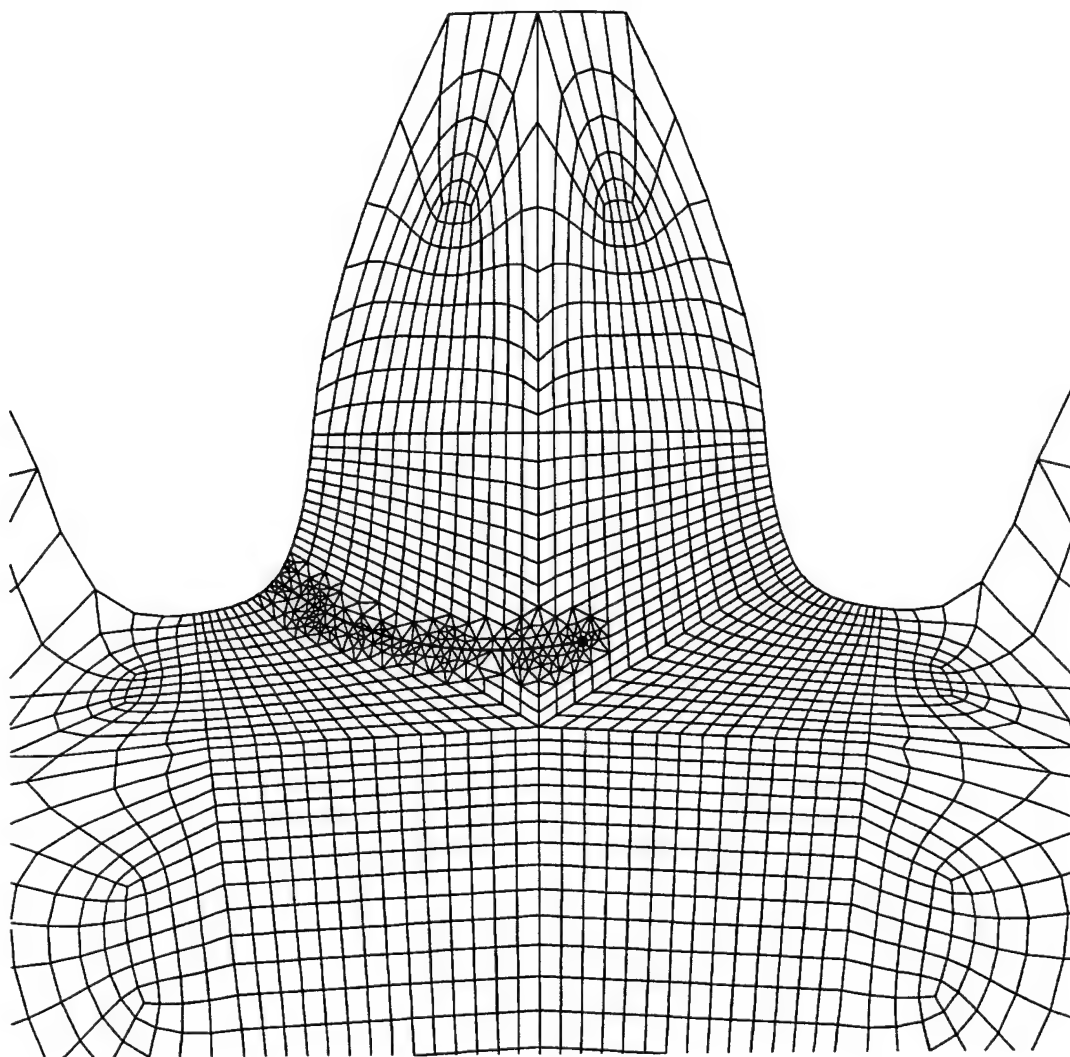


Figure 3.4.2.—Predicted crack path after 15 steps of automated gear tooth crack propagation.

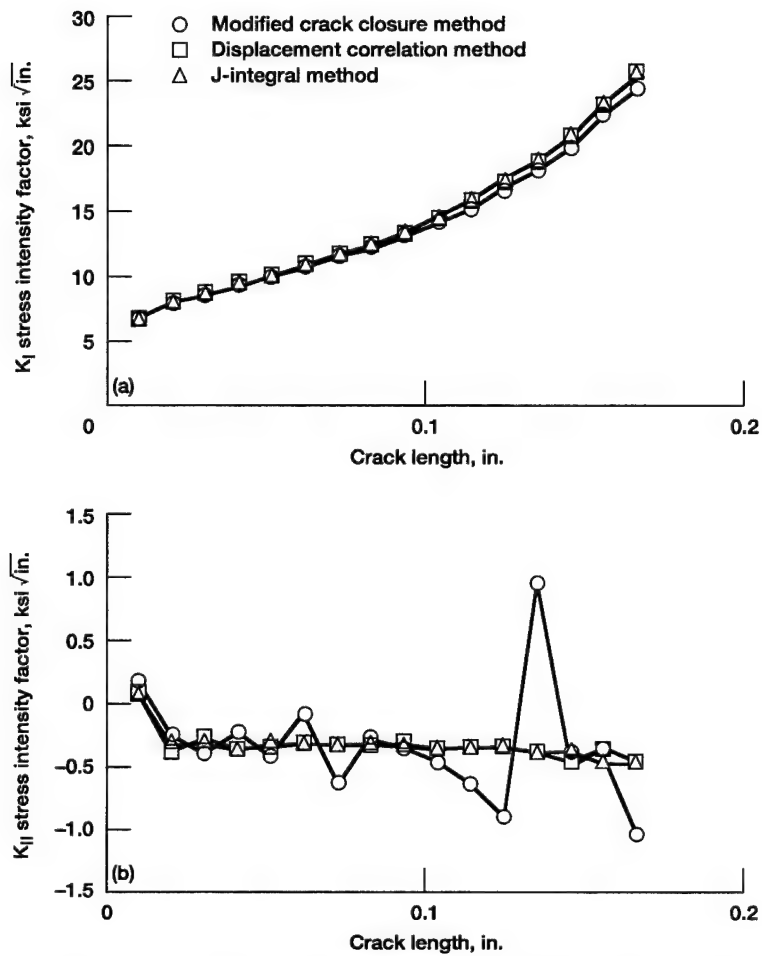


Figure 3.4.3.—Comparison of modified crack closure, displacement correlation, and J-integral stress intensity factor calculation methods after 15 steps of automated gear tooth crack propagation. (a) Mode I stress intensity factors. (b) Mode II stress intensity factors.

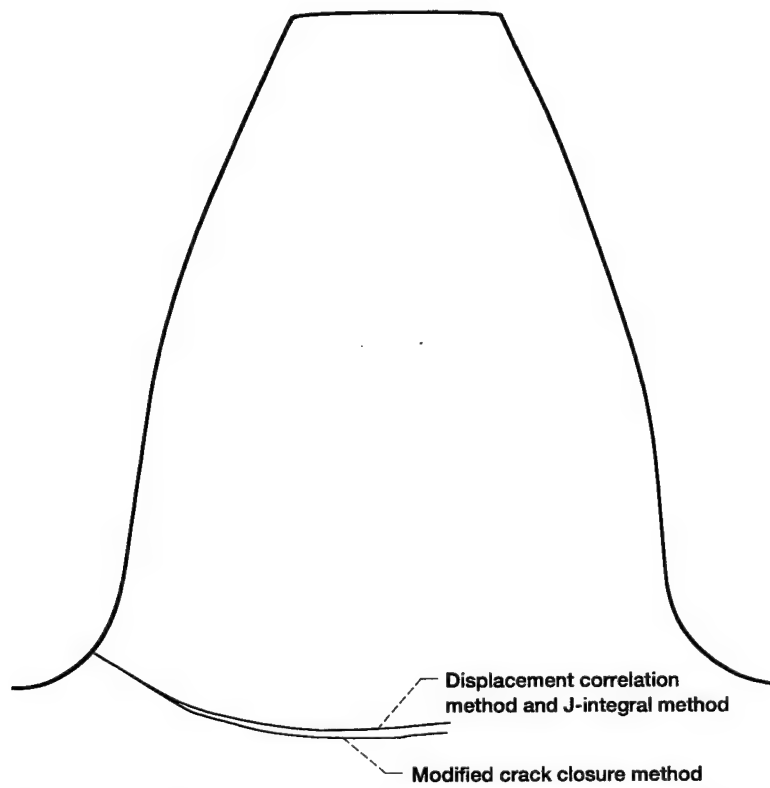


Figure 3.4.4.—Predicted crack path comparison of modified crack closure, displacement correlation, and J-integral stress intensity factor calculation methods after 15 steps of automated gear tooth crack propagation.

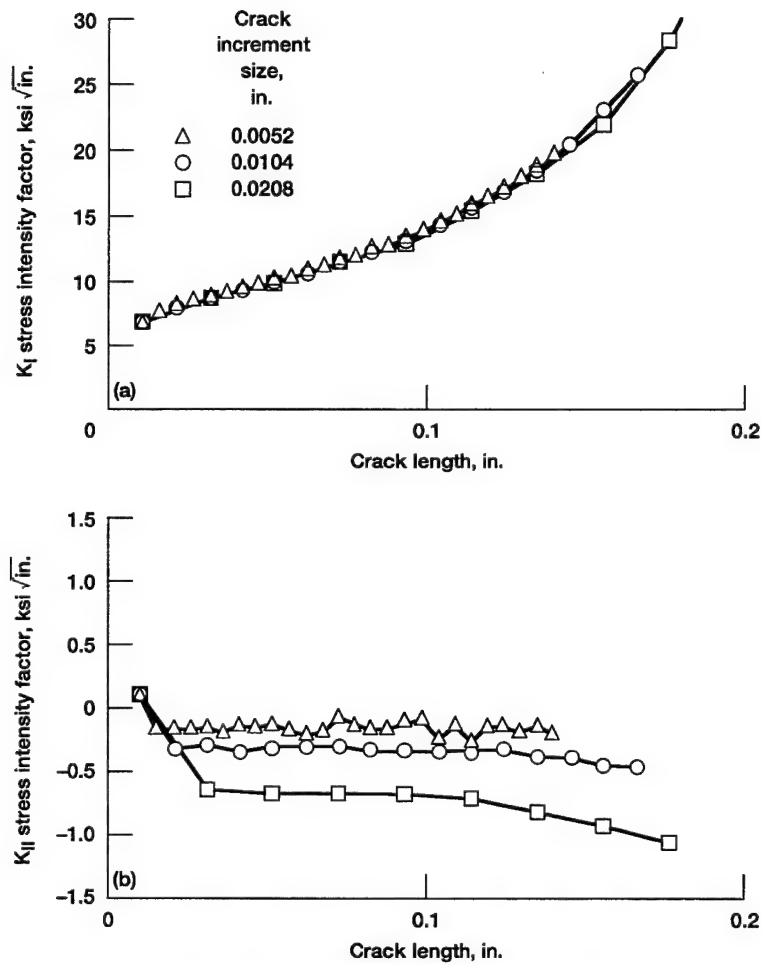


Figure 3.4.5.—Effect of crack increment size on predicted stress intensity factors after 15 steps of automated gear tooth crack propagation. (a) Mode I stress intensity factors. (b) Mode II stress intensity factors.

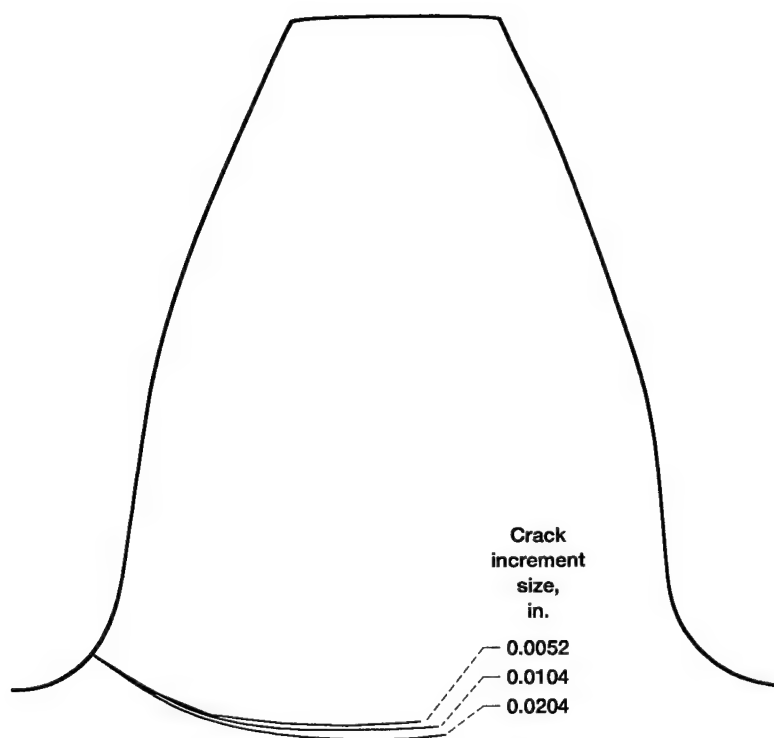


Figure 3.4.6.—Effect of crack increment size on predicted crack path after 15 steps of automated gear tooth crack propagation.

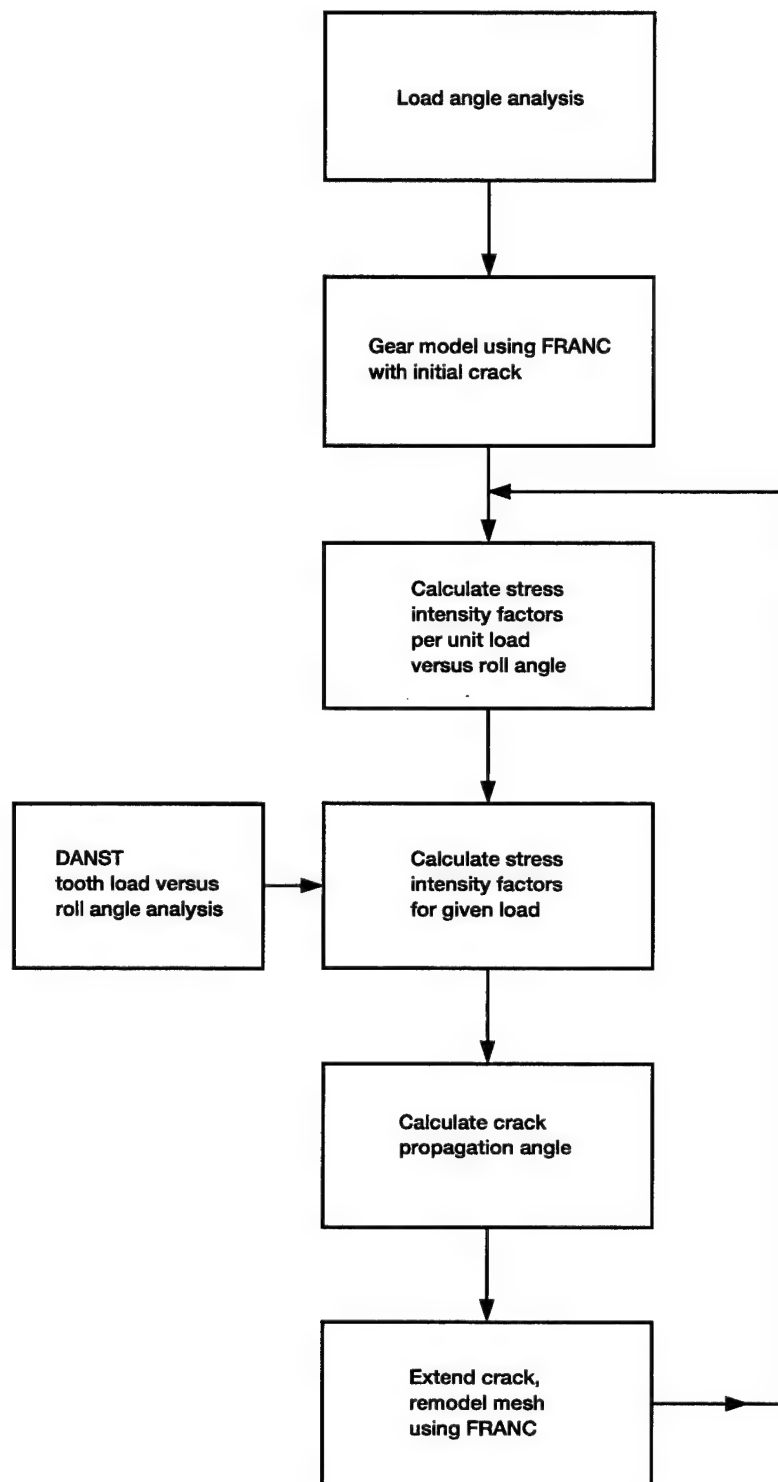
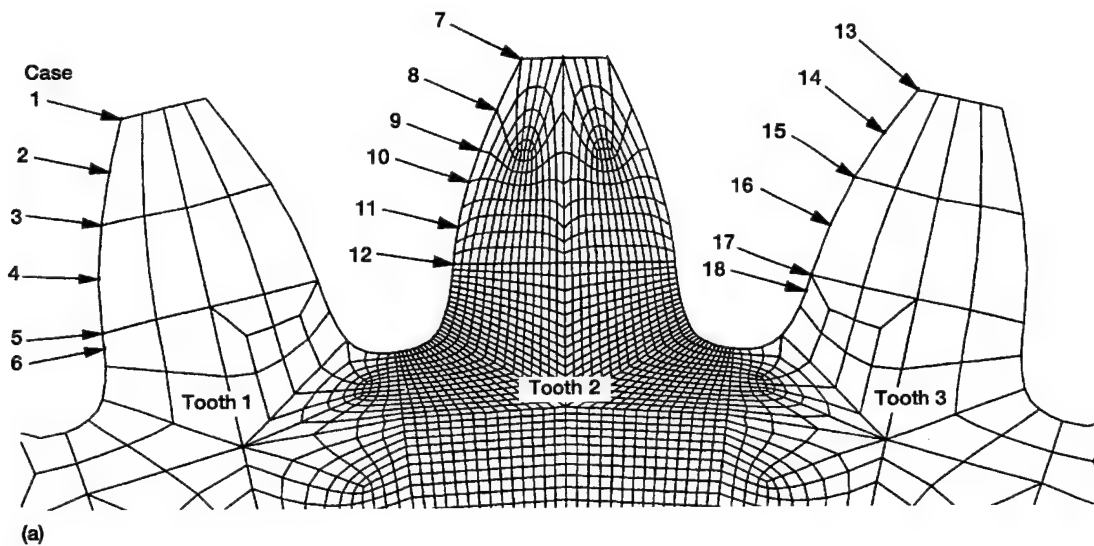


Figure 3.5.1.—Flow chart of manual crack propagation scheme which includes effect of gear tooth load position.



(b)

Case	ϵ , deg	ξ , deg
1	31.4	14.5
2	27.6	11.5
3	23.2	7.9
4	17.7	3.0
5	9.5	-4.8
6	4.6	-9.6
7	31.4	27.4
8	27.4	24.3
9	23.9	21.4
10	20.8	18.7
11	15.6	13.9
12	9.5	8.1
13	31.4	40.3
14	27.6	37.3
15	23.2	33.6
16	17.7	28.7
17	9.5	20.9
18	4.6	16.1

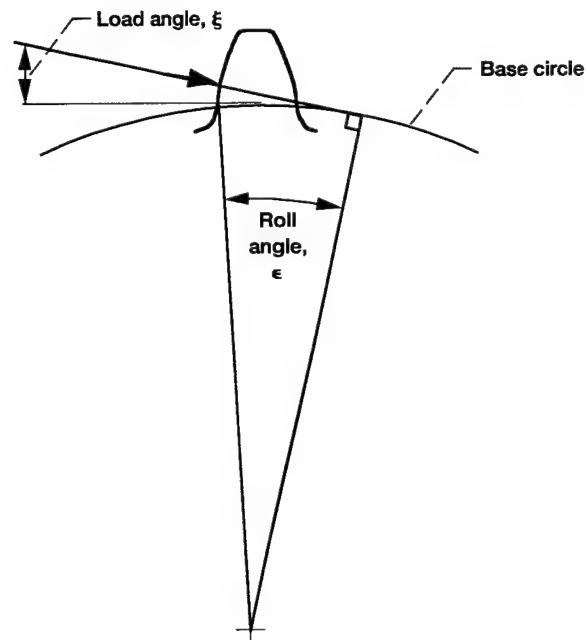


Figure 3.5.2.—Finite element mesh to determine effect of load position on crack propagation parameters.
 (a) Locations of eighteen separate unit load cases. (b) Orientations of load cases.

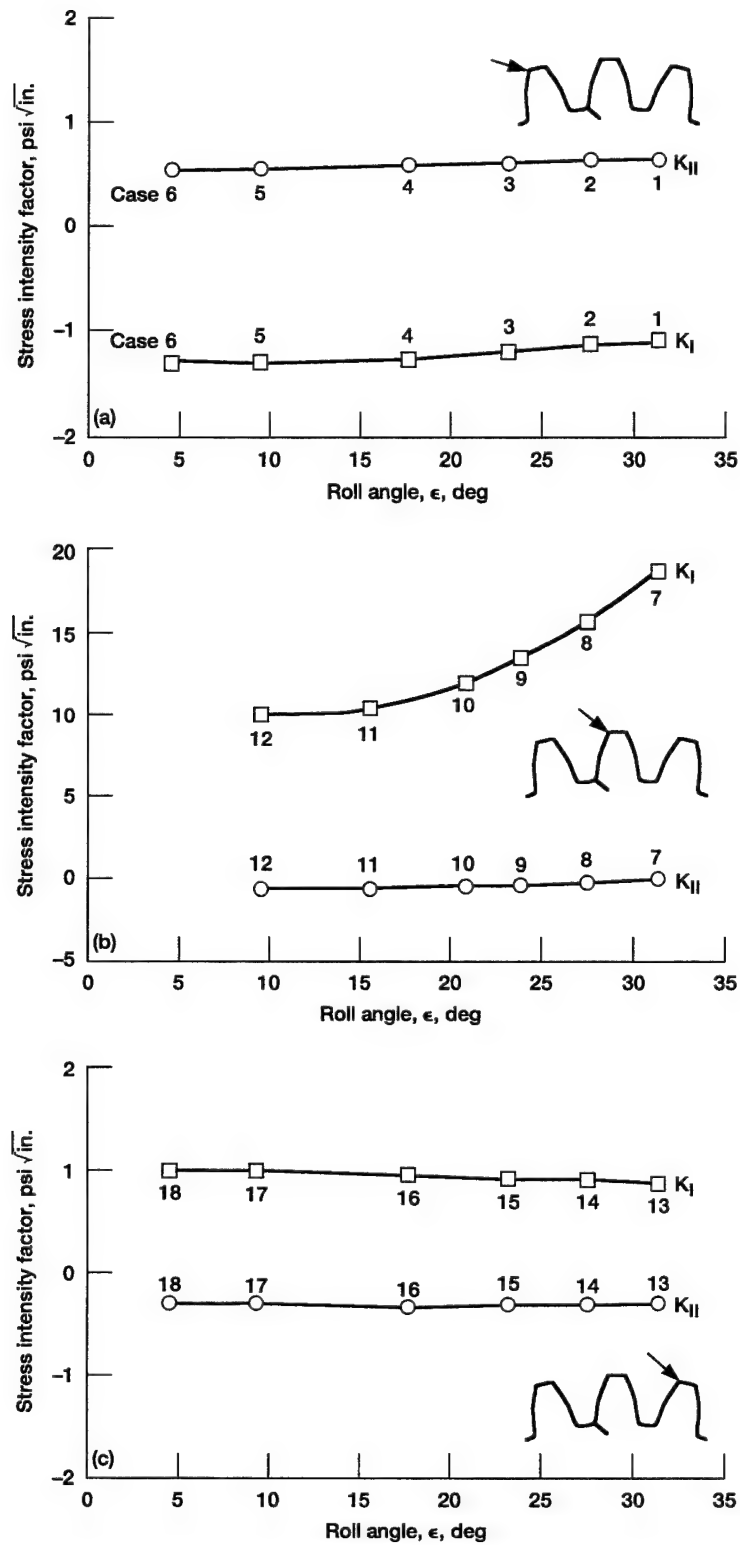


Figure 3.5.3.—Mode I and Mode II stress intensity factors as a function of gear tooth roll angle; unit load cases, 0.0104-in. initial crack size. (a) Load on tooth 1. (b) Load on tooth 2. (c) Load on tooth 3.

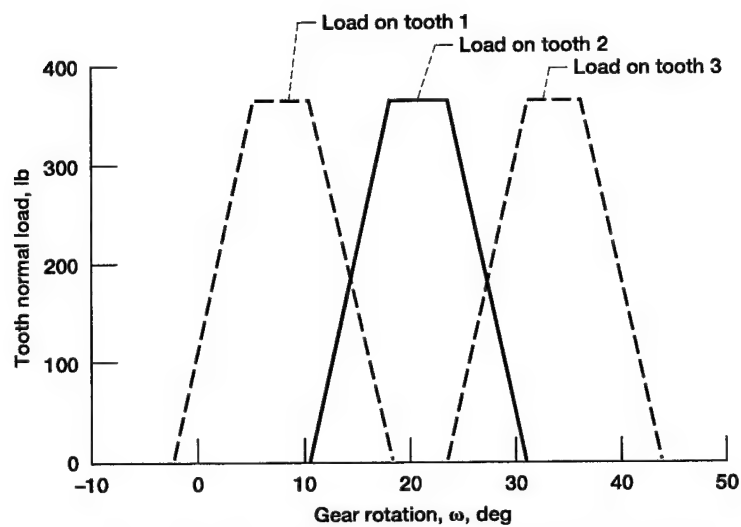


Figure 3.5.4.—DANST computer program output of static gear tooth load.

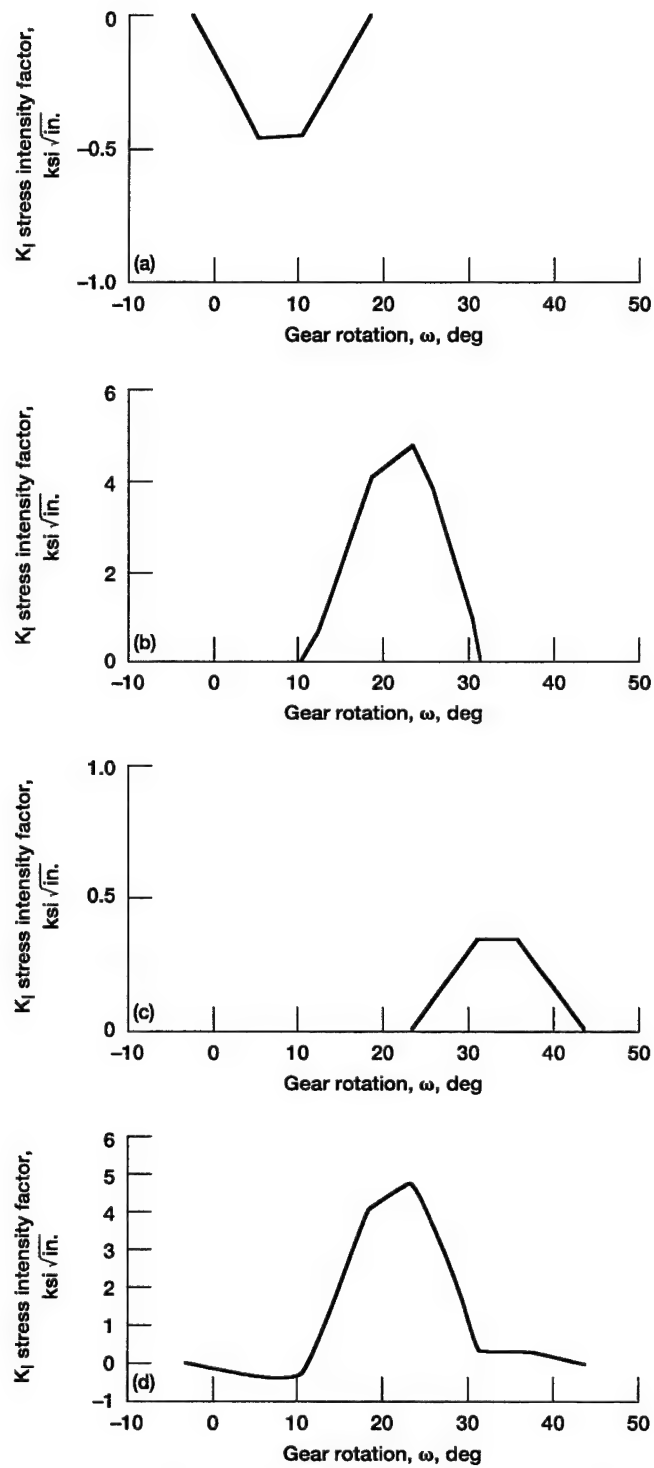


Figure 3.5.5.—Mode I stress intensity factors as a function of gear rotation angle; 599 in.·lb driver torque, 0.0104-in. initial crack size.
 (a) Load on tooth 1. (b) Load on tooth 2. (c) Load on tooth 3.
 (d) Superposition of loads on teeth 1, 2, and 3.

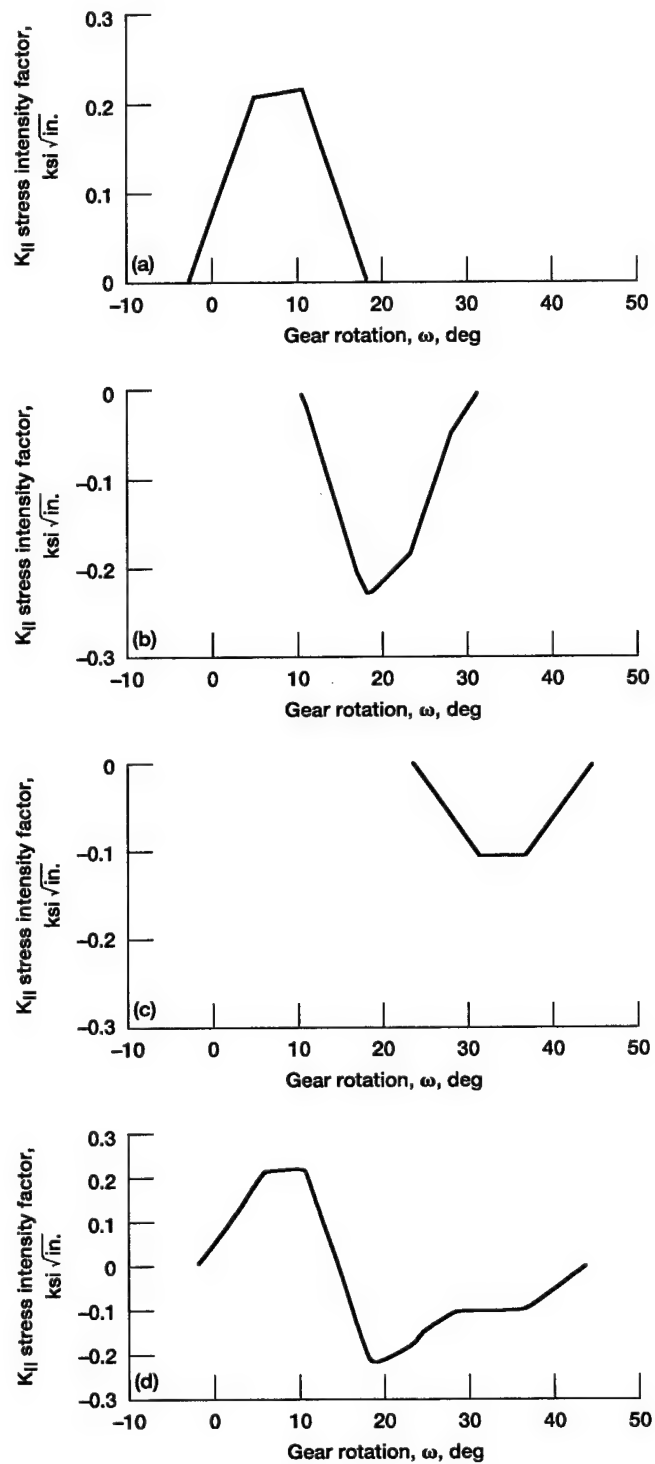


Figure 3.5.6.—Mode II stress intensity factors as a function of gear rotation angle; 599 in.·lb driver torque, 0.0104-in. initial crack size.
 (a) Load on tooth 1. (b) Load on tooth 2. (c) Load on tooth 3.
 (d) Superposition of loads on teeth 1, 2, and 3.

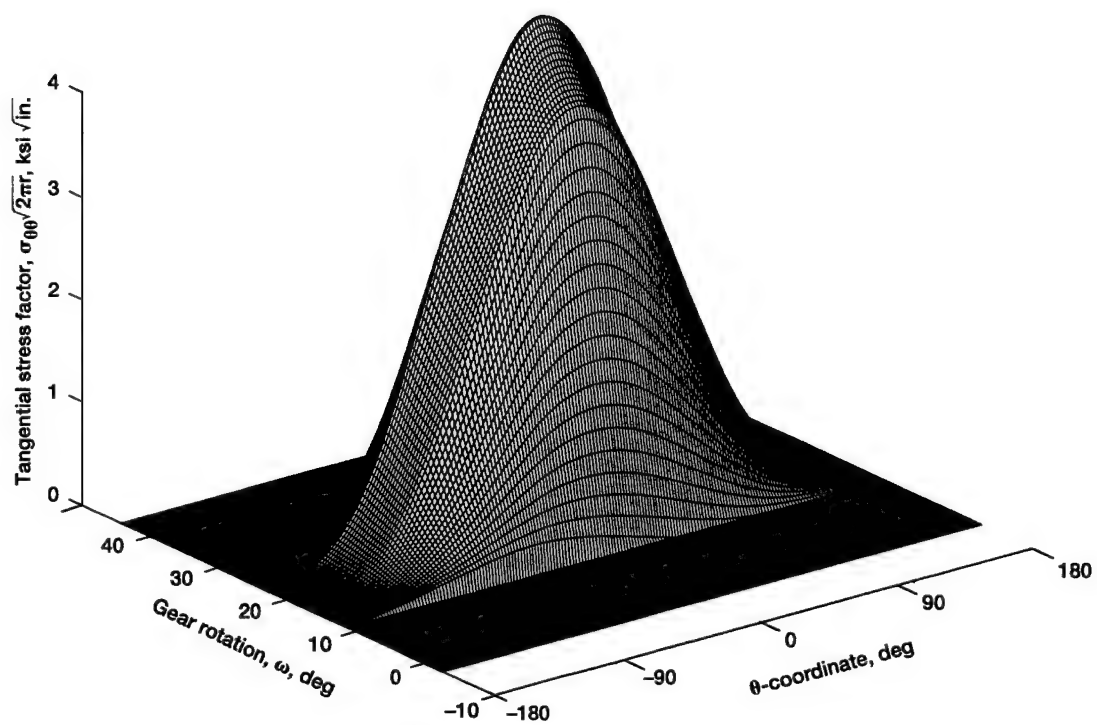


Figure 3.5.7.—Tangential stress factor as a function of gear rotation angle and θ -coordinate; 599 in. • lb driver torque, 0.0104-inch initial crack size.

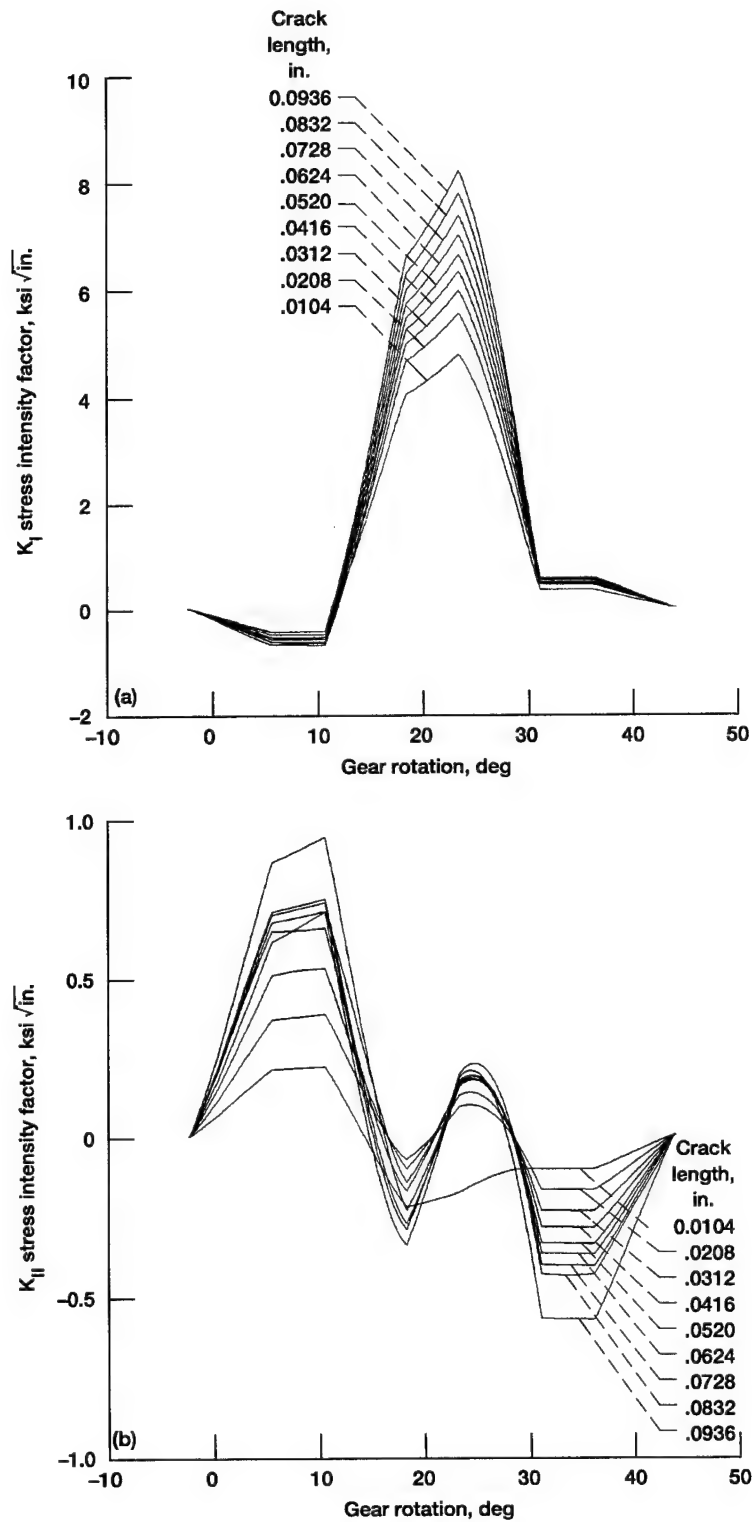


Figure 3.5.8.—Mode I and II stress intensity factors as a function of gear rotation angle; 599 in•lb driver torque, 9 steps of simulated crack propagation. (a) Mode I stress intensity factors. (b) Mode II stress intensity factors.

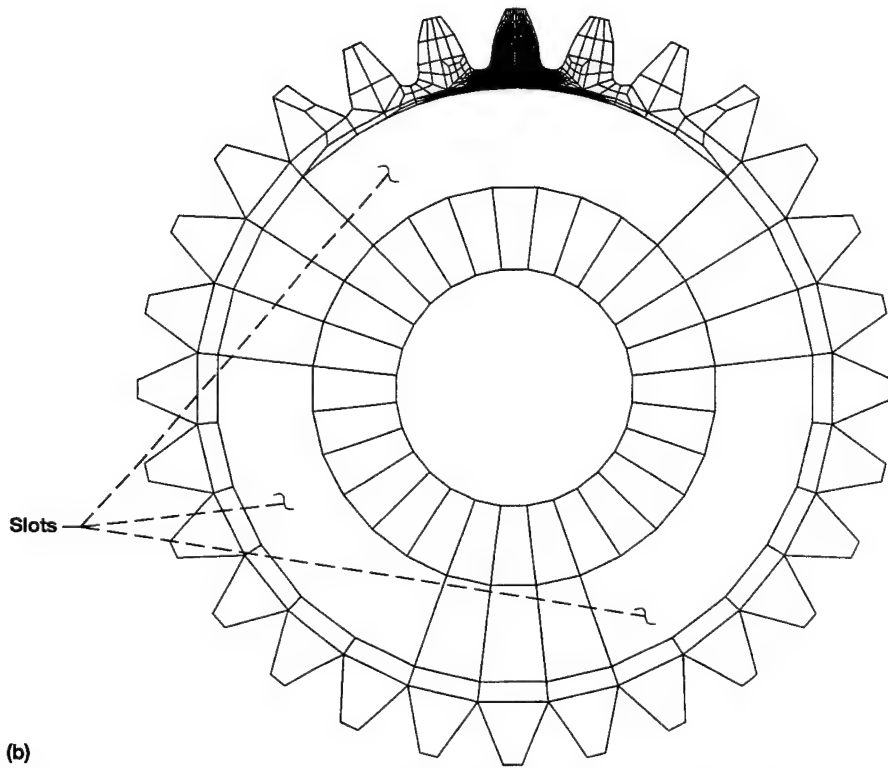
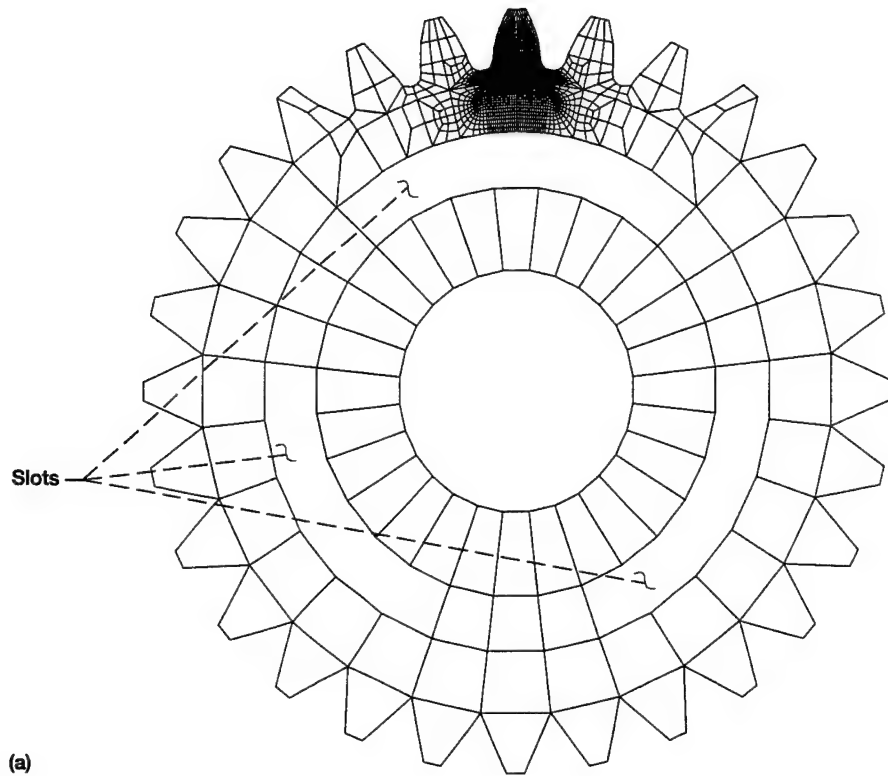


Figure 3.6.1.—Finite element mesh of slotted gears used in crack propagation studies of thin-rim gears. (a) $m_B = 1.0$. (b) $m_B = 0.3$.

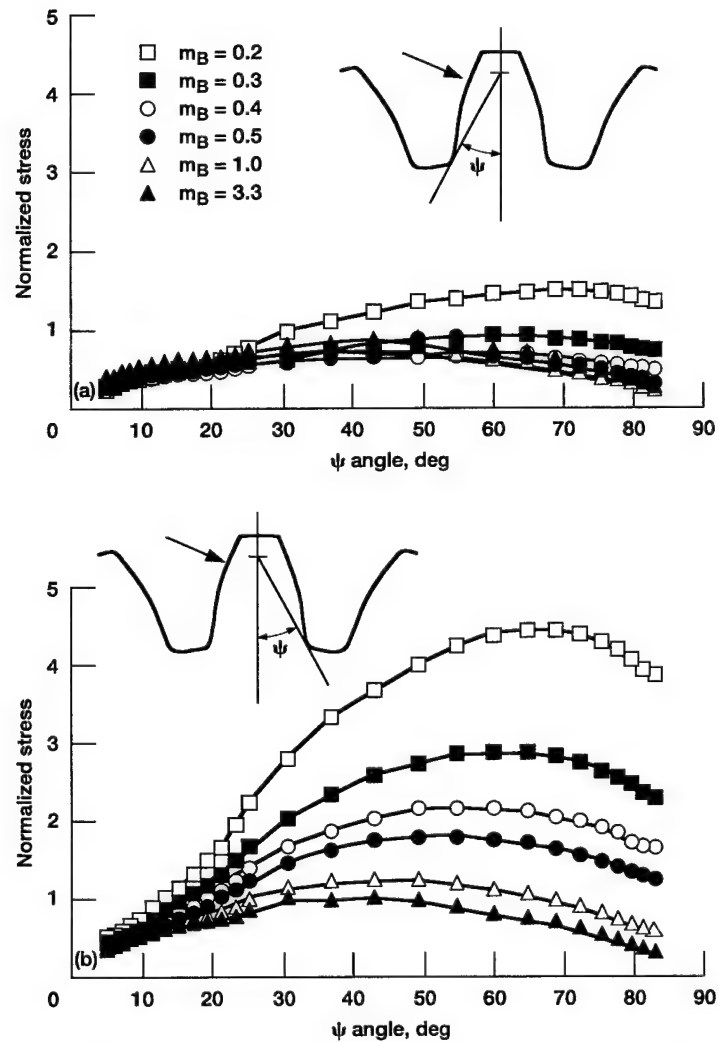


Figure 3.6.2.—Stress distribution of gear tooth fillet surface elements for various backup ratios. (a) Loaded side of tooth (tensile stress). (b) Unloaded side of tooth (compressive stress).

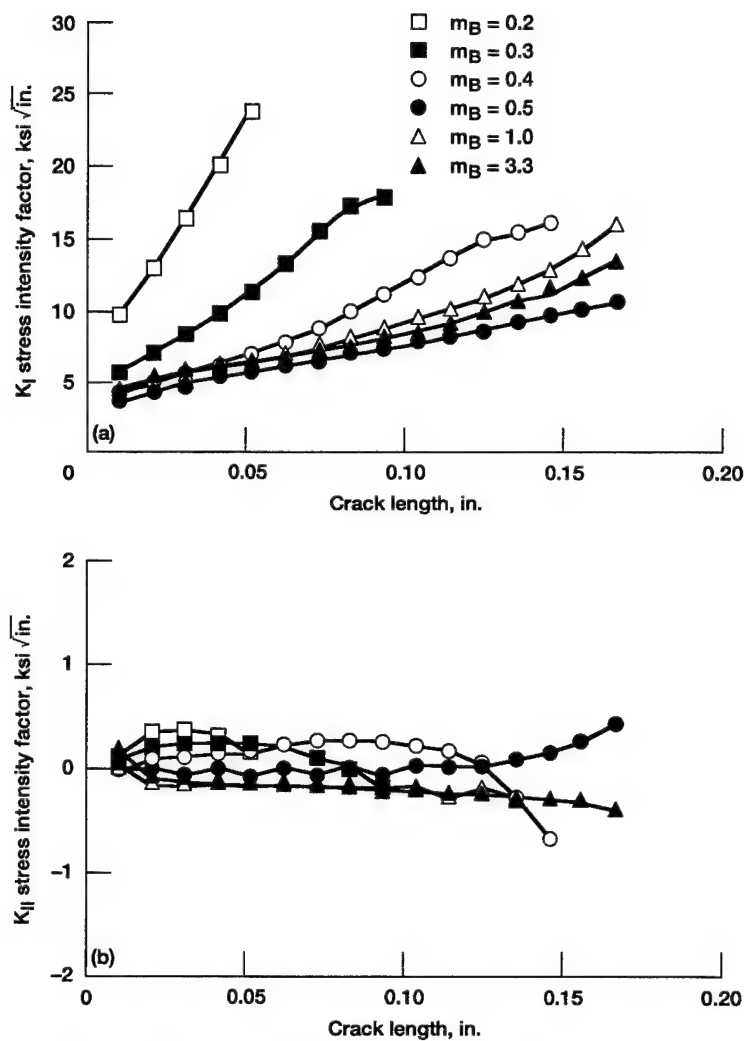


Figure 3.6.3.—Effect of rim thickness on gear tooth crack tip stress intensity factors. (a) Mode I stress intensity factors. (b) Mode II stress intensity factors.

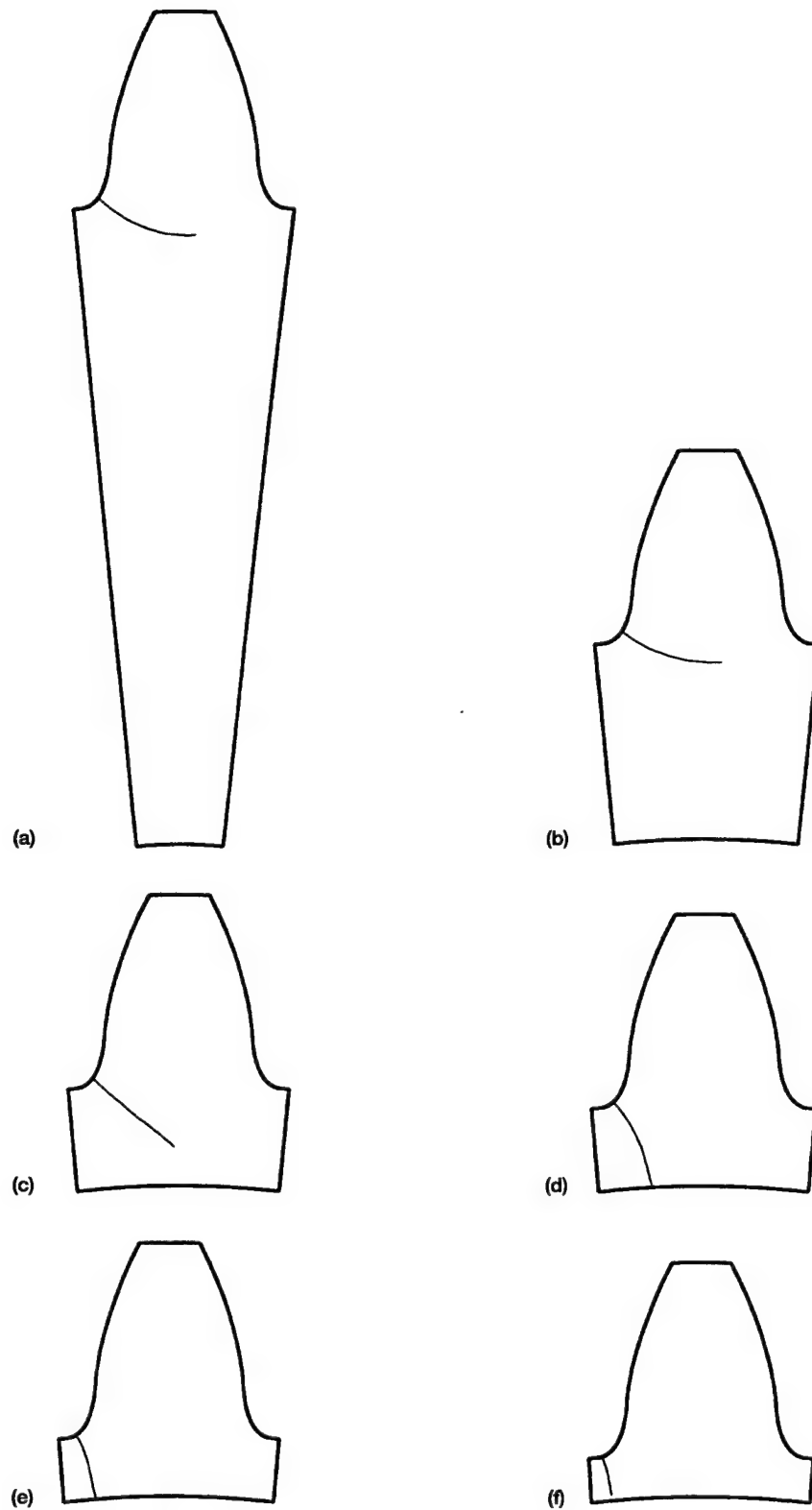


Figure 3.6.4.—Effect of rim thickness on gear tooth crack propagation path. (a) $m_B = 3.3$. (b) $m_B = 1.0$. (c) $m_B = 0.5$. (d) $m_B = 0.4$. (e) $m_B = 0.3$. (f) $m_B = 0.2$.

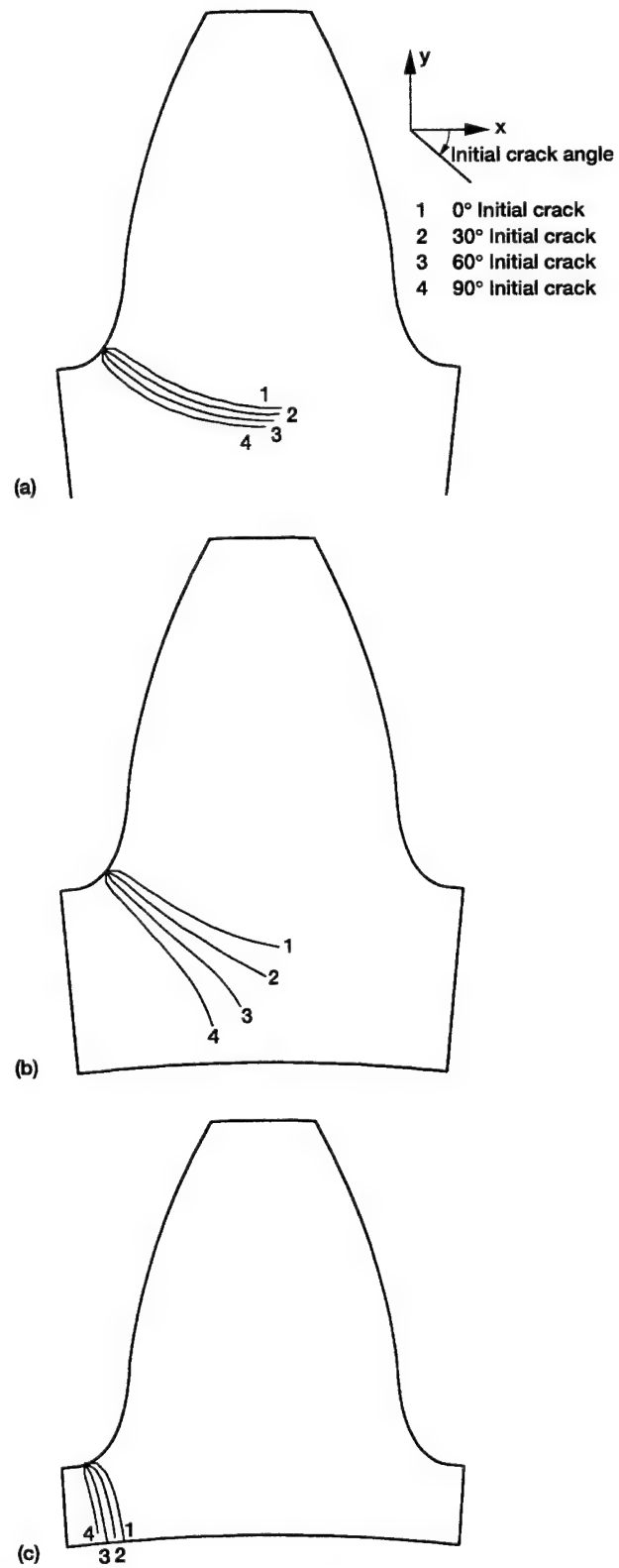


Figure 3.6.5.—Effect of initial crack orientation on gear tooth crack propagation path. (a) $m_B = 3.3$. (b) $m_B = 0.5$. (c) $m_B = 0.2$.

Line	Carburized	Load ratio, R	Test frequency, Hz	Air environment	Paris equation constants	
					n	c*
1	Yes	0.05	1.0	Wet		
2	Yes	.05	3.4	Dry		
3	No	.05	.1	Wet	2.264	1.149×10^{-15}
4	No	.5	3.4	Dry	2.954	6.027×10^{-19}
5	No	.05	1.0	Wet	2.555	2.721×10^{-17}
6	No	.05	3.4	Dry	2.420	1.084×10^{-16}

*Units of in./cyc/(psi $\sqrt{\text{in.}}$)ⁿ

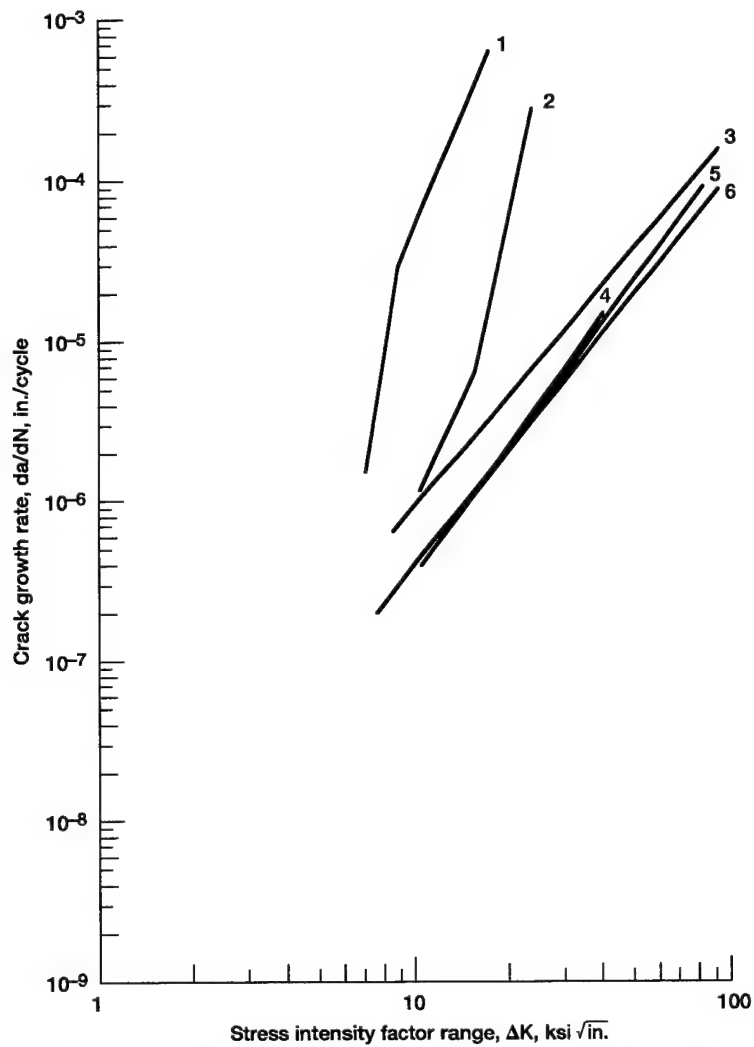


Figure 3.7.1.—Fatigue crack growth for AISI 9310 steel (Au and Ke, 1981).

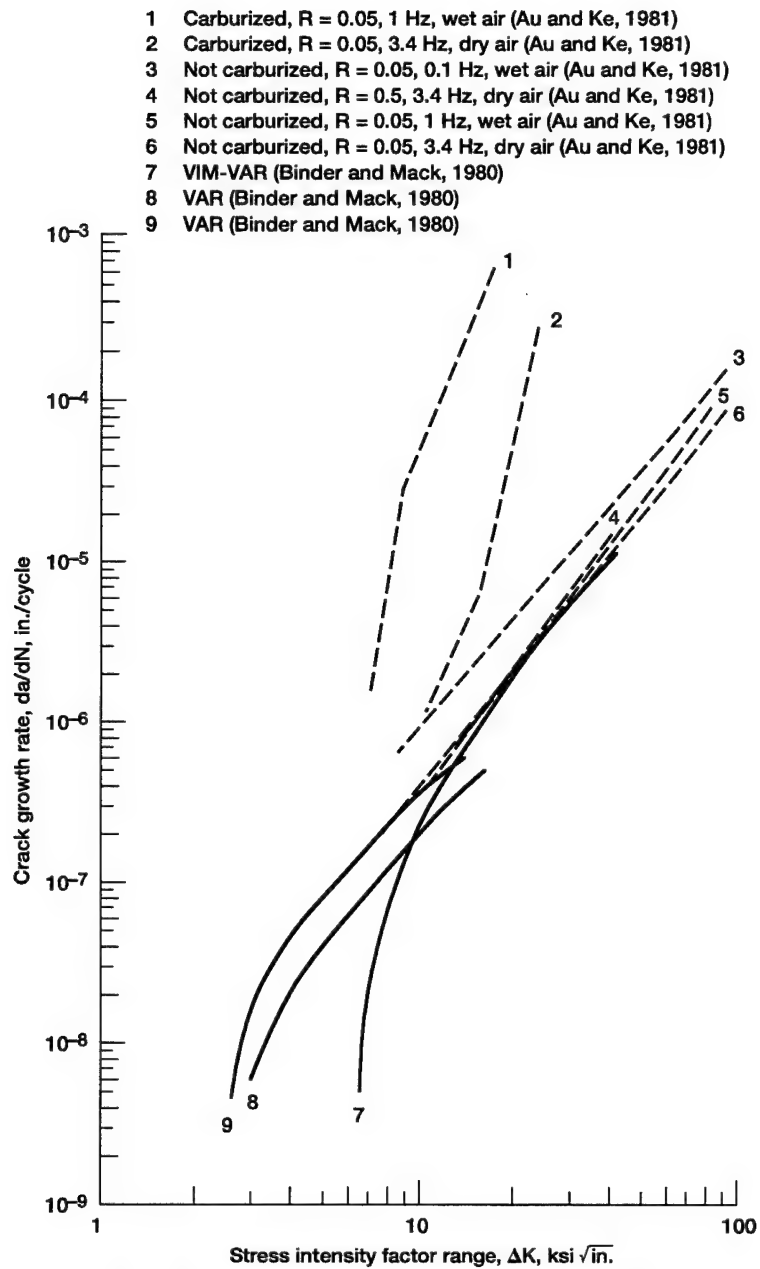


Figure 3.7.2.—Comparison of fatigue crack growth rates for AISI 9310 steel.

- 3 Paris equation, $n = 2.264$, $C = 1.149 \times 10^{-15}$ in./cyc/(psi $\sqrt{\text{in.}}$) n (Au and Ke, 1981)
- 4 Paris equation, $n = 2.954$, $C = 6.027 \times 10^{-19}$ in./cyc/(psi $\sqrt{\text{in.}}$) n (Au and Ke, 1981)
- 5 Paris equation, $n = 2.555$, $C = 2.721 \times 10^{-17}$ in./cyc/(psi $\sqrt{\text{in.}}$) n (Au and Ke, 1981)
- 6 Paris equation, $n = 2.420$, $C = 1.084 \times 10^{-16}$ in./cyc/(psi $\sqrt{\text{in.}}$) n (Au and Ke, 1981)
- 10 Collipriest equation, $n = 1.63$, $C = 8.36 \times 10^{-9}$ in./cyc/(ksi $\sqrt{\text{in.}}$) n , $\Delta K_{th} = 3.5$ ksi $\sqrt{\text{in.}}$,
 $K_{IC} = 200$ ksi $\sqrt{\text{in.}}$, $R = 0$ (Forman and Hu, 1984)

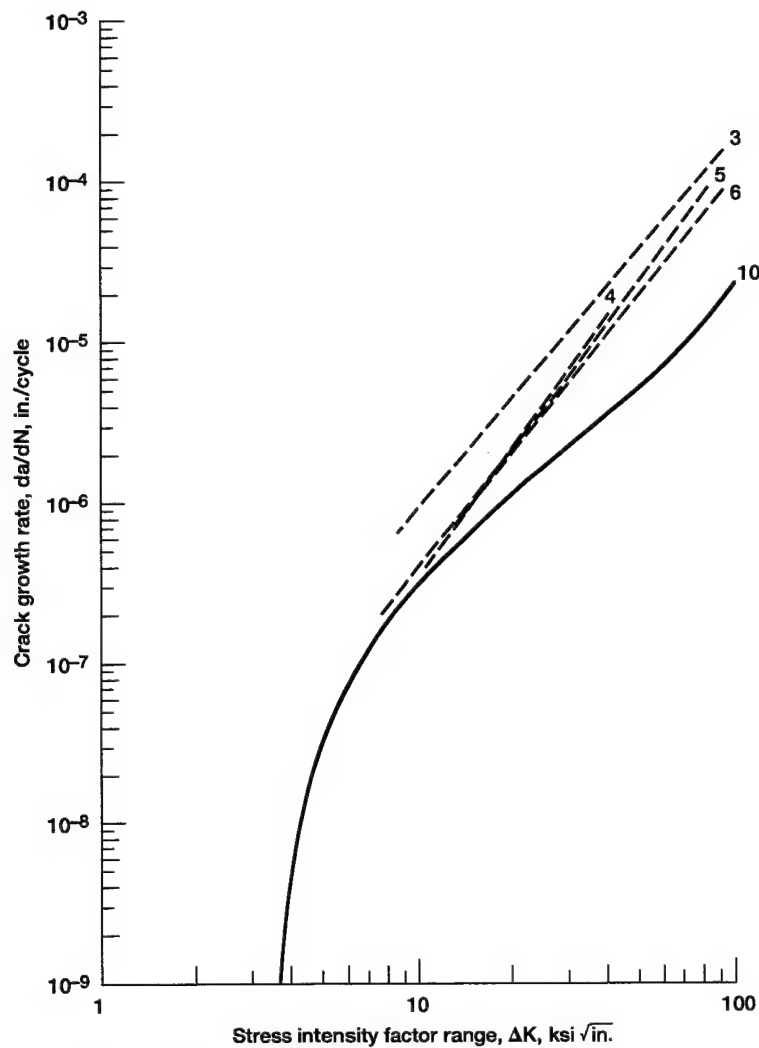


Figure 3.7.3.—Comparison of fatigue crack growth rates using Paris equation and Collipriest equation for AISI 9310 steel.

- 1 AISI 9310, carburized, $R = 0.05$, 1 Hz, wet air (Au and Ke, 1981)
 - 2 AISI 9310, carburized, $R = 0.05$, 3.4 Hz, dry air (Au and Ke, 1981)
 - 3 AISI 9310, not carburized, $R = 0.05$, 0.1 Hz, wet air (Au and Ke, 1981)
 - 4 AISI 9310, not carburized, $R = 0.5$, 3.4 Hz, dry air (Au and Ke, 1981)
 - 5 AISI 9310, not carburized, $R = 0.05$, 1 Hz, wet air (Au and Ke, 1981)
 - 6 AISI 9310, not carburized, $R = 0.05$, 3.4 Hz, dry air (Au and Ke, 1981)
-
- SCM415 (Inoue, et al. 1991)

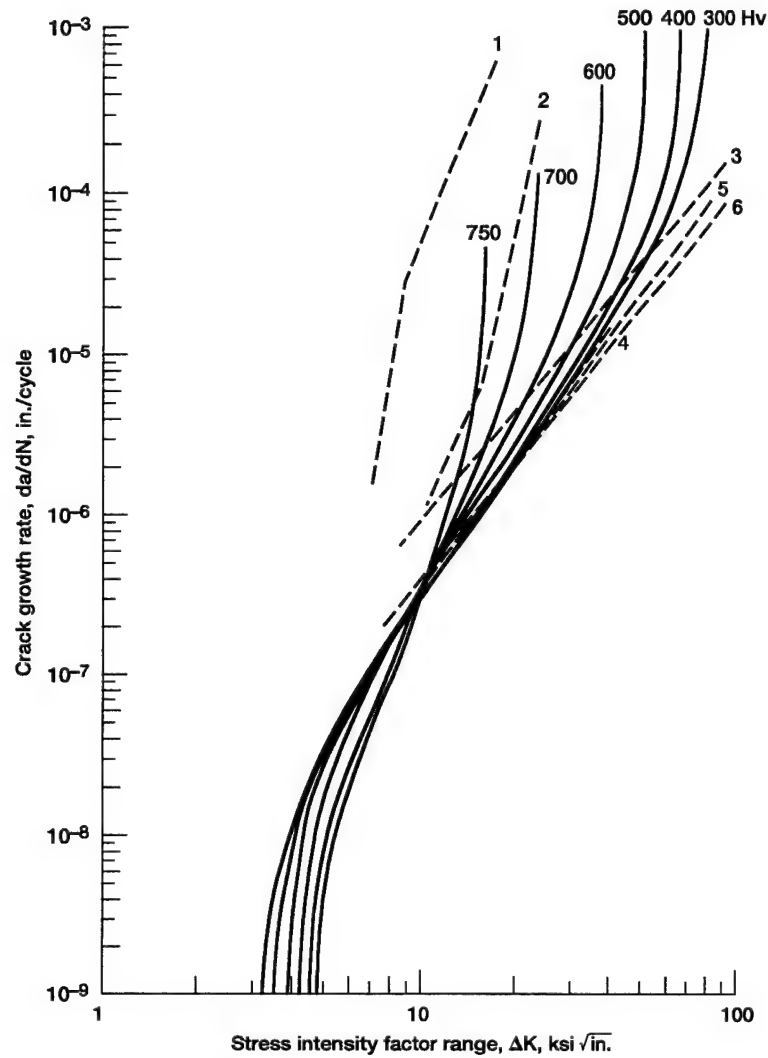


Figure 3.7.4.—Comparison of fatigue crack growth rates for AISI 9310 steel and SCM415 steel.

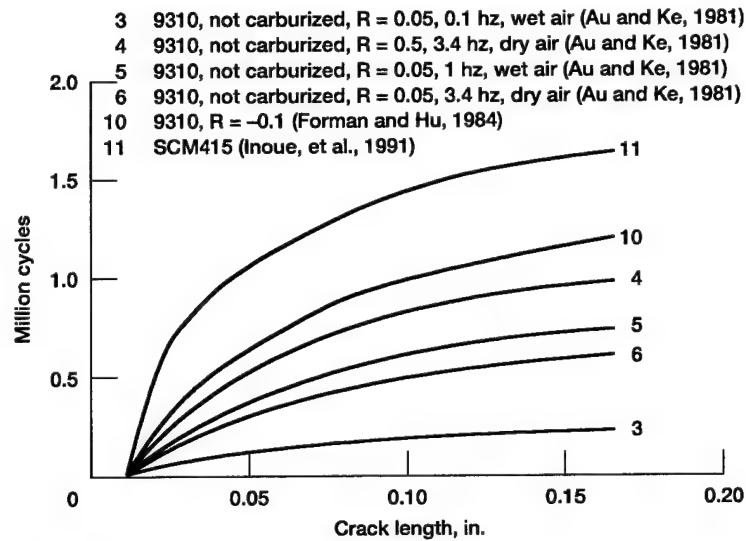


Figure 3.7.5.—Effect of different fatigue crack growth rate calculation methods on predicted number of crack propagation cycles.

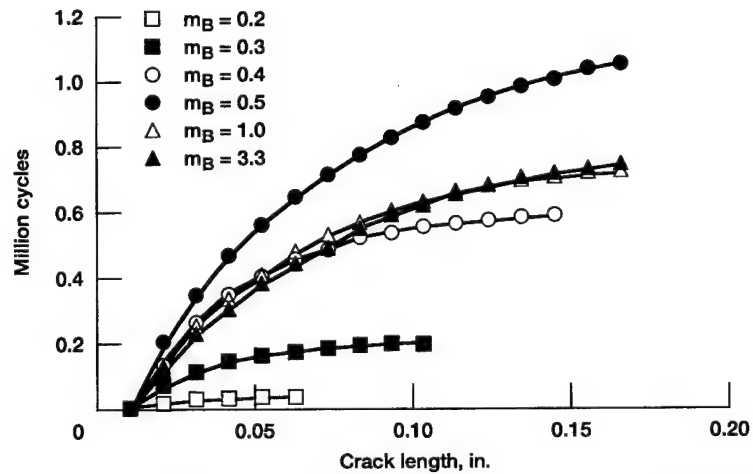


Figure 3.7.6.—Effect of rim thickness on predicted number of crack propagation cycles; Paris equation used, $n = 2.555$, $C = 2.721 \times 10^{-17}$ in./cyc/(psi $\sqrt{\text{in.}}$) n .

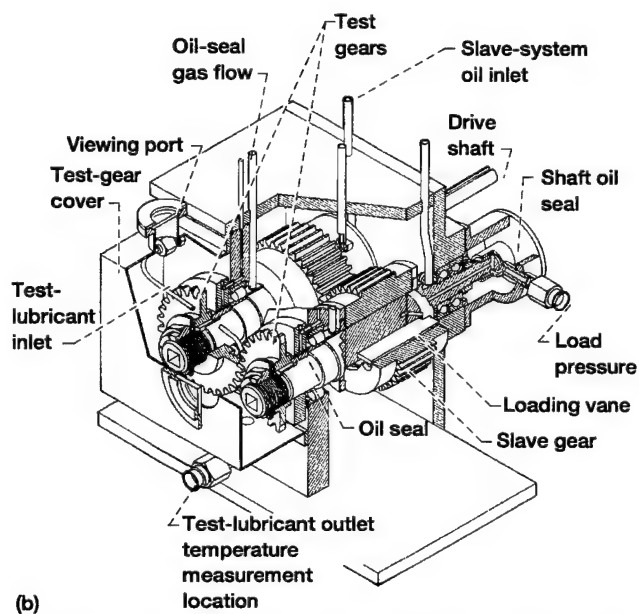
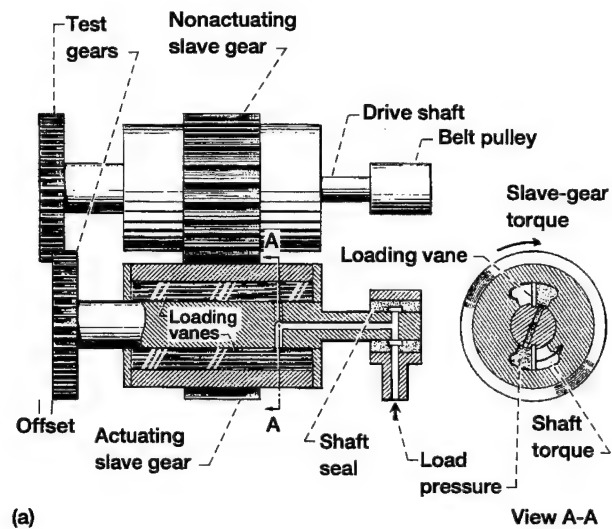
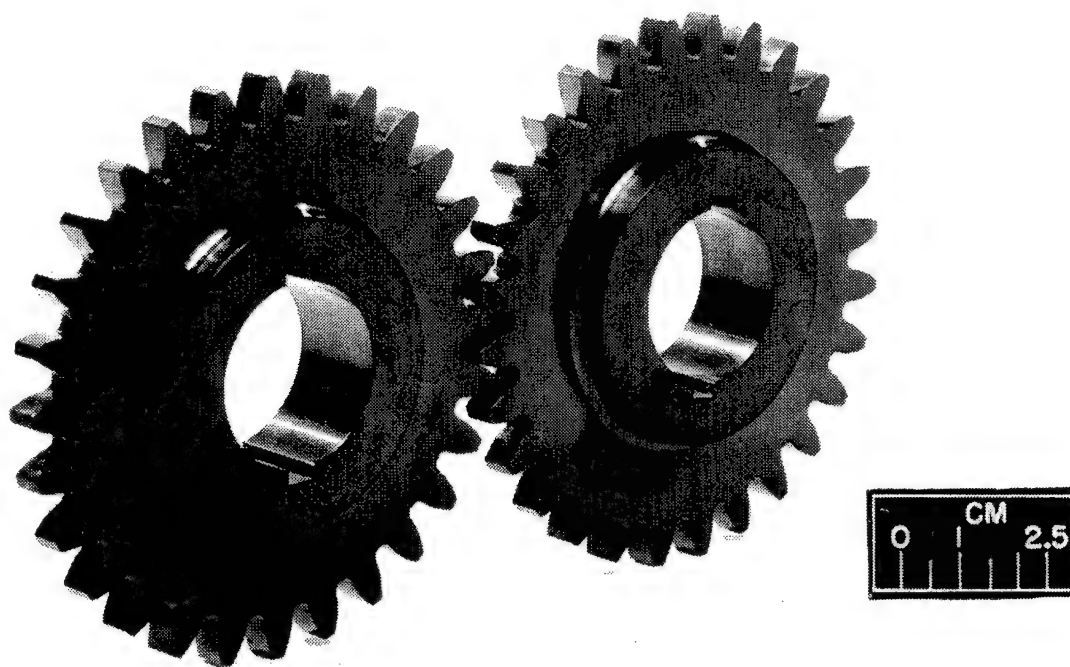


Figure 4.2.1.—NASA Lewis Spur Gear Fatigue Rig. (a) Schematic view. (b) Cutaway view.



C-72-3230

Figure 4.3.1.—Test gears of NASA Lewis Spur Gear Fatigue Rig.

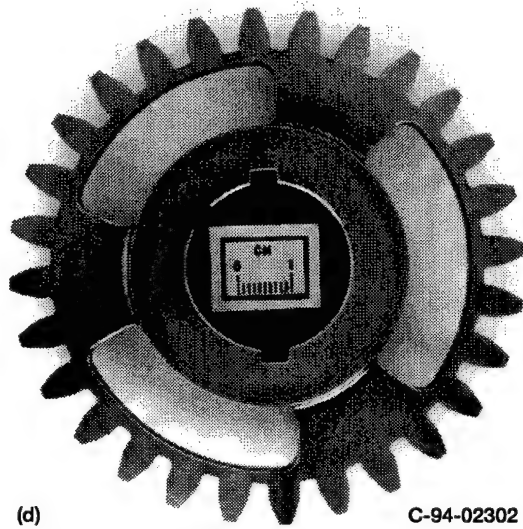
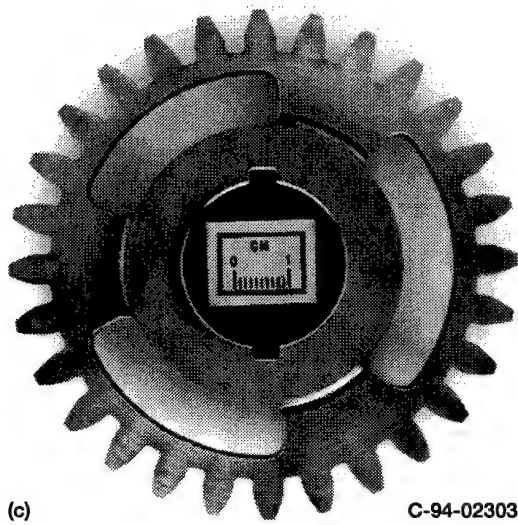
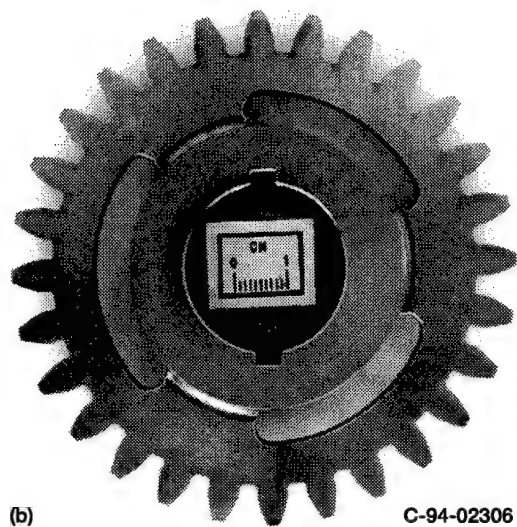
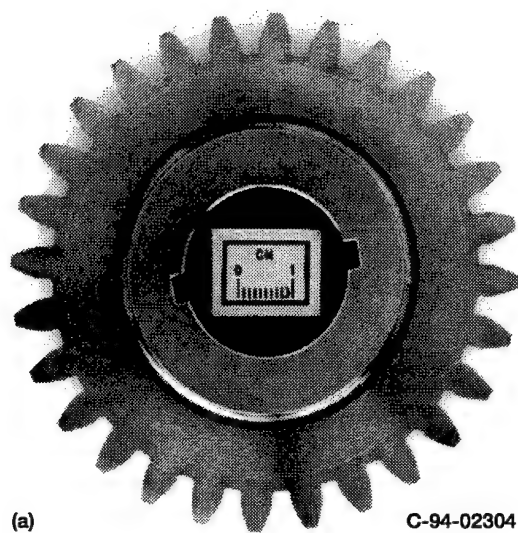


Figure 4.3.2.—Various backup ratios used in tests to determine effect of rim thickness on crack propagation.
(a) $m_B = 3.3$. (b) $m_B = 1.0$. (c) $m_B = 0.5$. (d) $m_B = 0.3$.

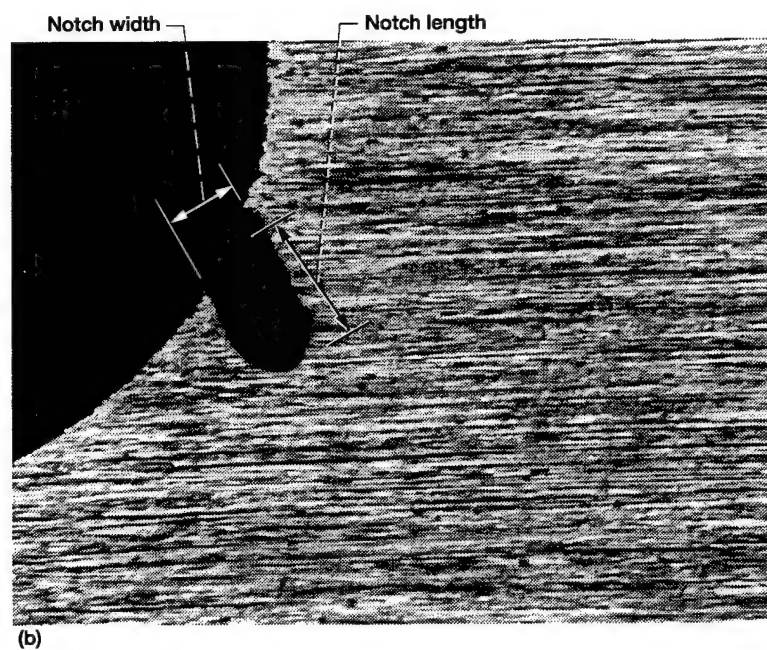
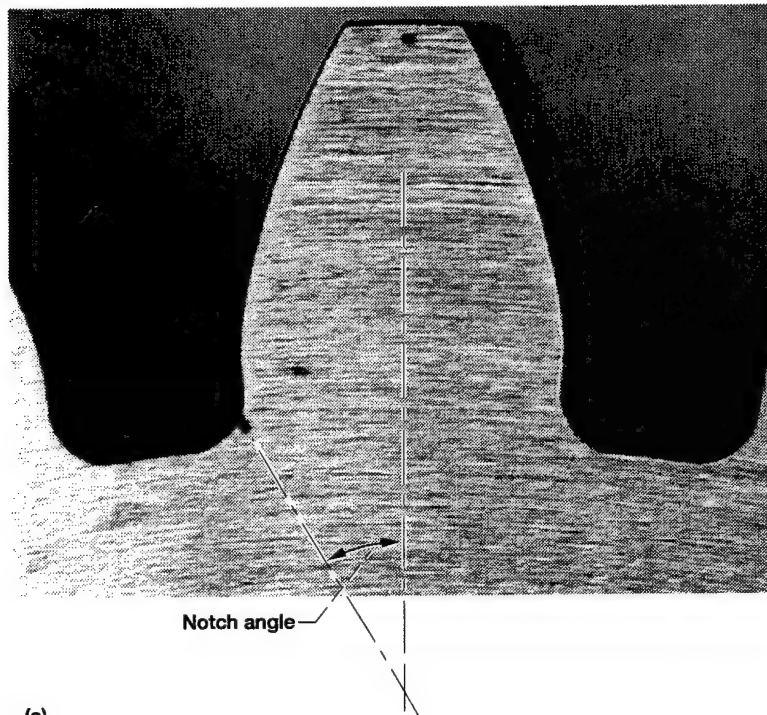


Figure 4.3.3.—Fabricated notch in tooth fillet region of test gears to promote crack initiation. (a) 7.5X. (b) 64X.

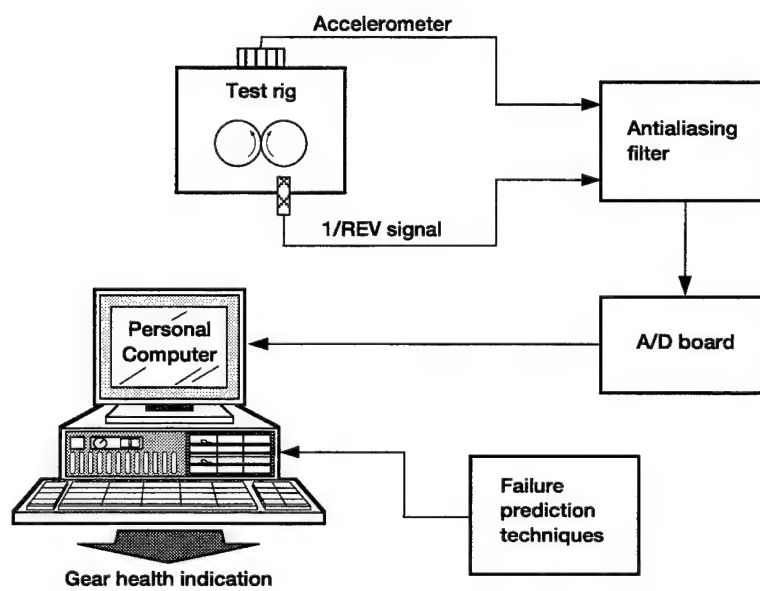
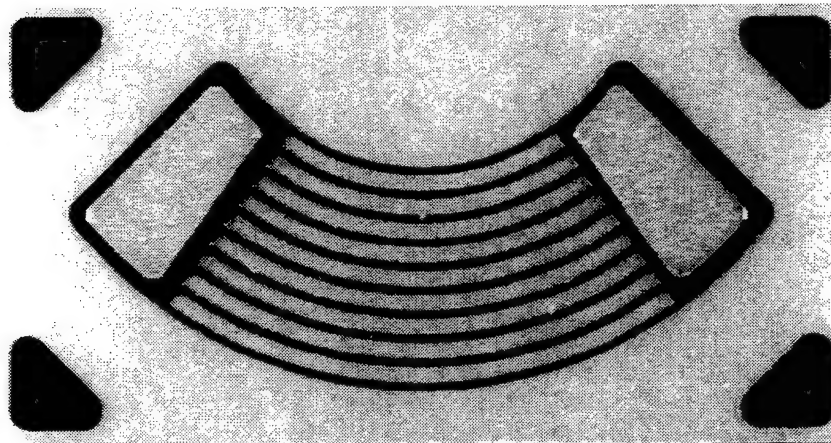
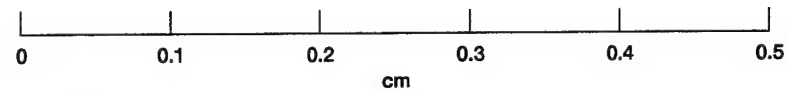


Figure 4.4.1.—Experimental test set-up of advanced vibration processing system to detect crack initiation.



(a)

C-94-05940

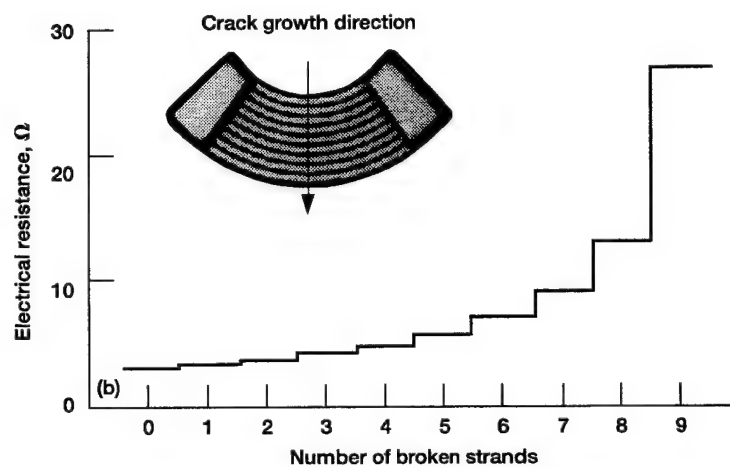


Figure 4.4.2.—Specialized crack propagation gages for gear tooth crack growth measurements. (a) Close-up of gage. (b) Increase in gage electrical resistance as the number of broken strands increase.

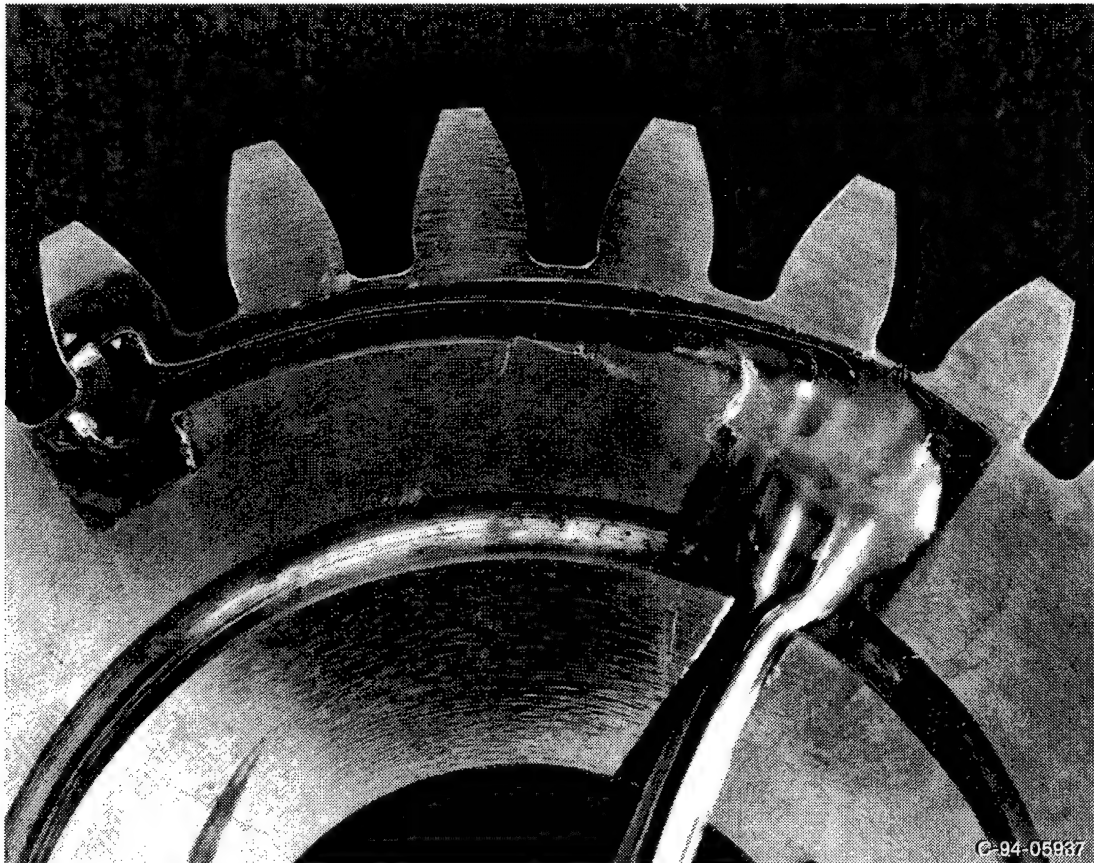


Figure 4.4.3.—Installation of crack propagation gage on test gear.

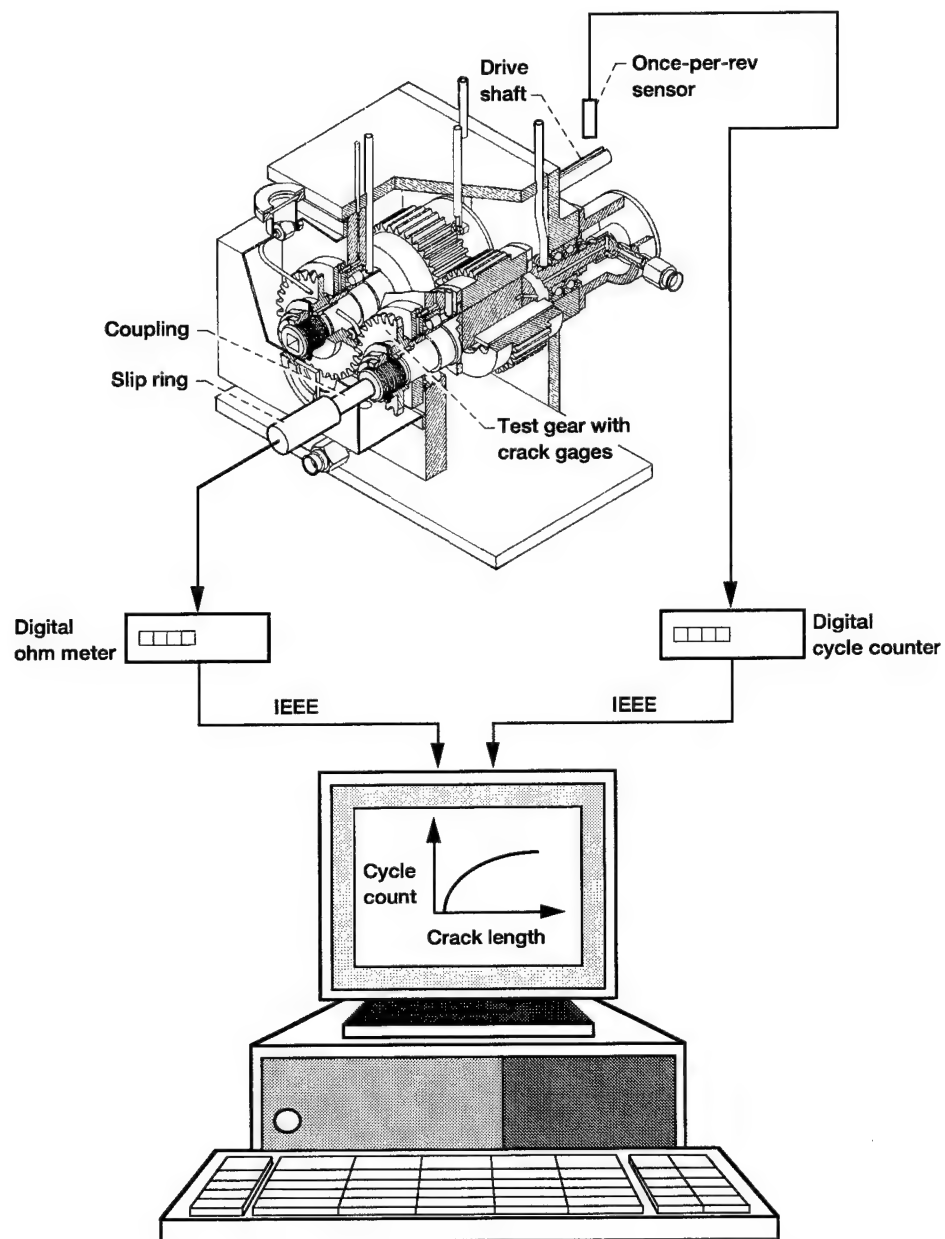


Figure 4.4.4.—Data acquisition set-up of crack propagation gage experiments.

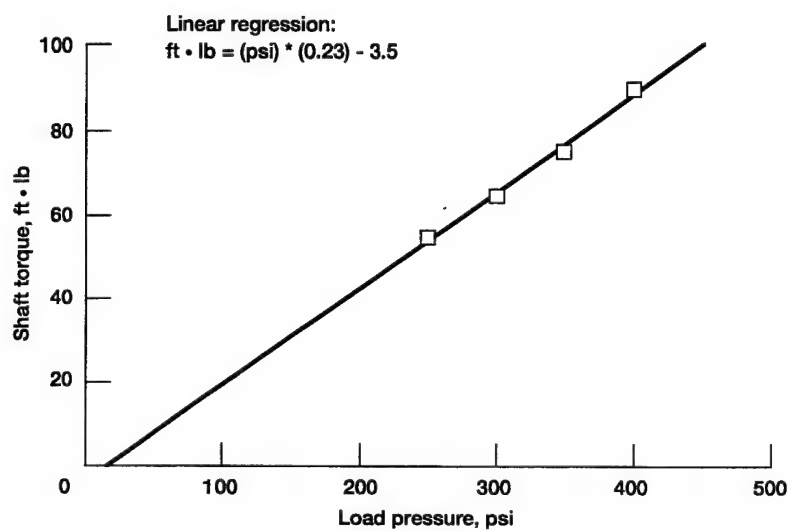


Figure 4.4.5.—Shaft torque-load pressure calibration for NASA Lewis Spur Gear Fatigue Rig.

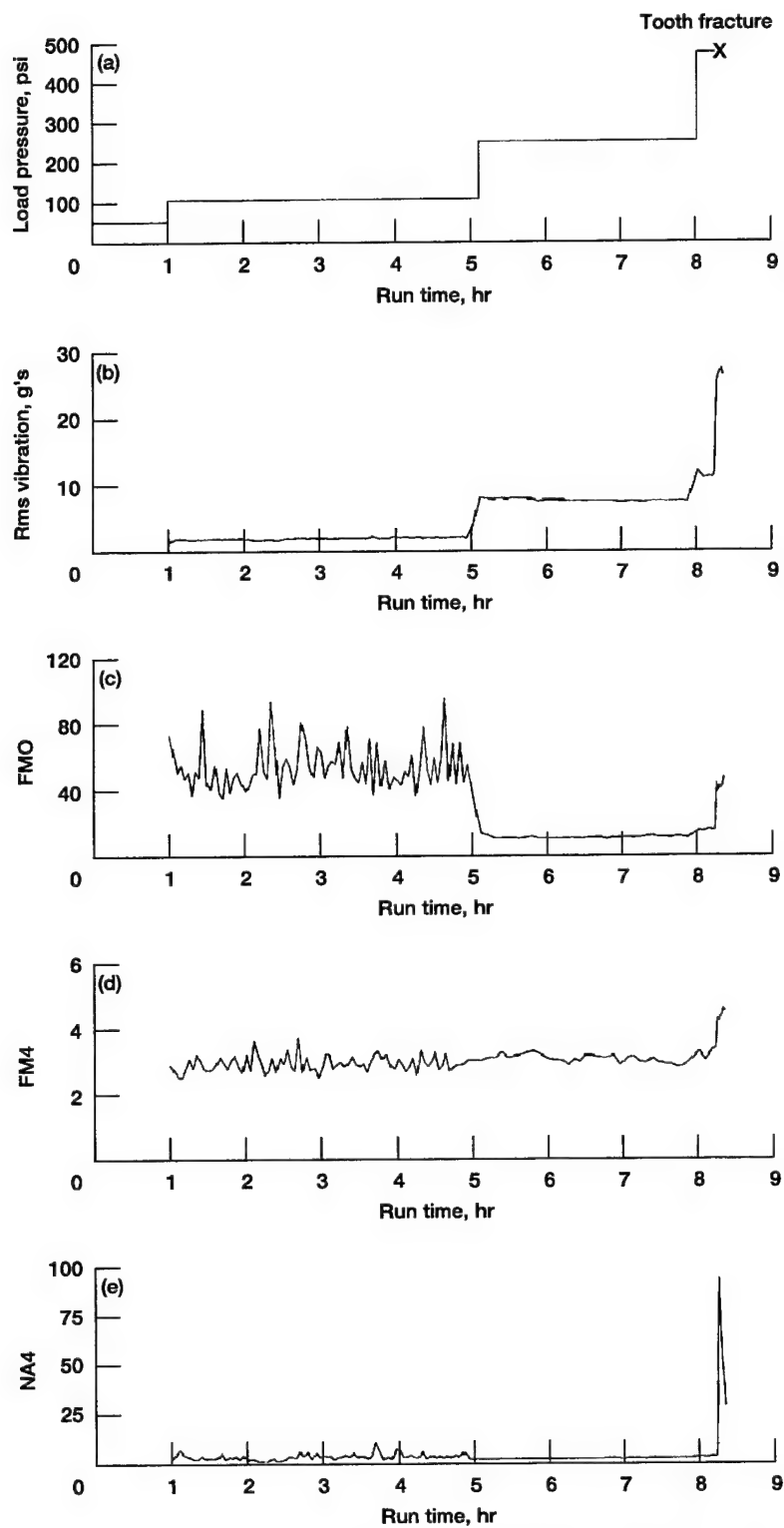


Figure 4.6.1.—Load history and vibration parameters for test 1, S/N 01, $m_B = 3.3$.
 (a) Load pressure. (b) Rms vibration of time-averaged signal. (c) FMO parameter.
 (d) FM4 parameter. (e) NA4 parameter.

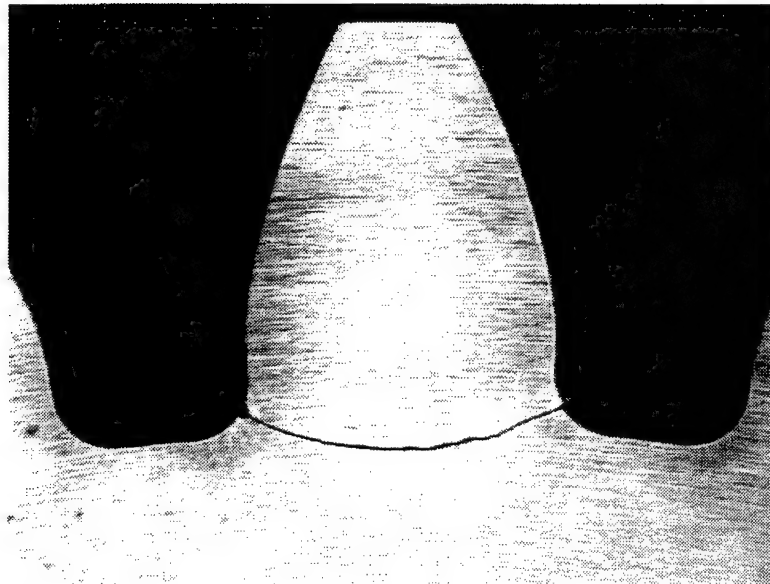


Figure 4.6.2.—Crack propagation path for test 1, S/N 01, $m_B = 3.3$, tooth fracture at 8.4 hr total run time (0.4 hr at 475 psi load pressure).

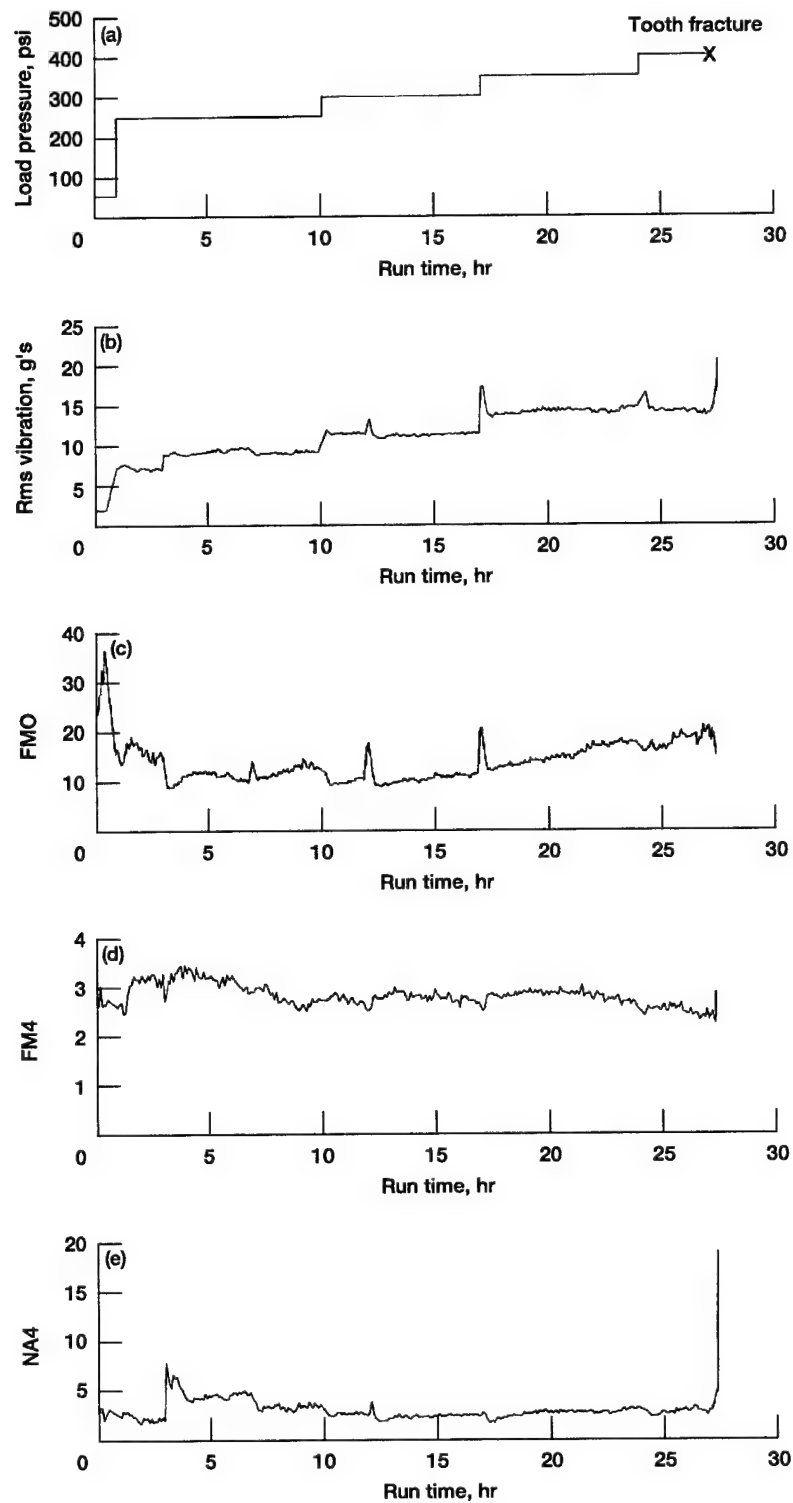


Figure 4.6.3.—Load history and vibration parameters for test 2, S/N 02, $m_B = 3.3$.
 (a) Load pressure. (b) Rms vibration of time-averaged signal. (c) FMO parameter.
 (d) FM4 parameter. (e) NA4 parameter.

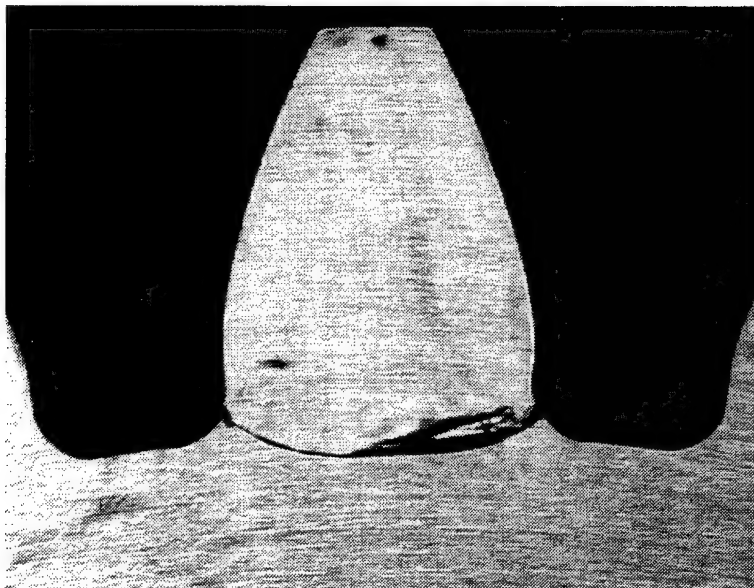


Figure 4.6.4.—Crack propagation path for test 2, S/N 02, $m_B = 3.3$, tooth fracture at 27.4 hr total run time (3.4 hr at 400 psi load pressure).

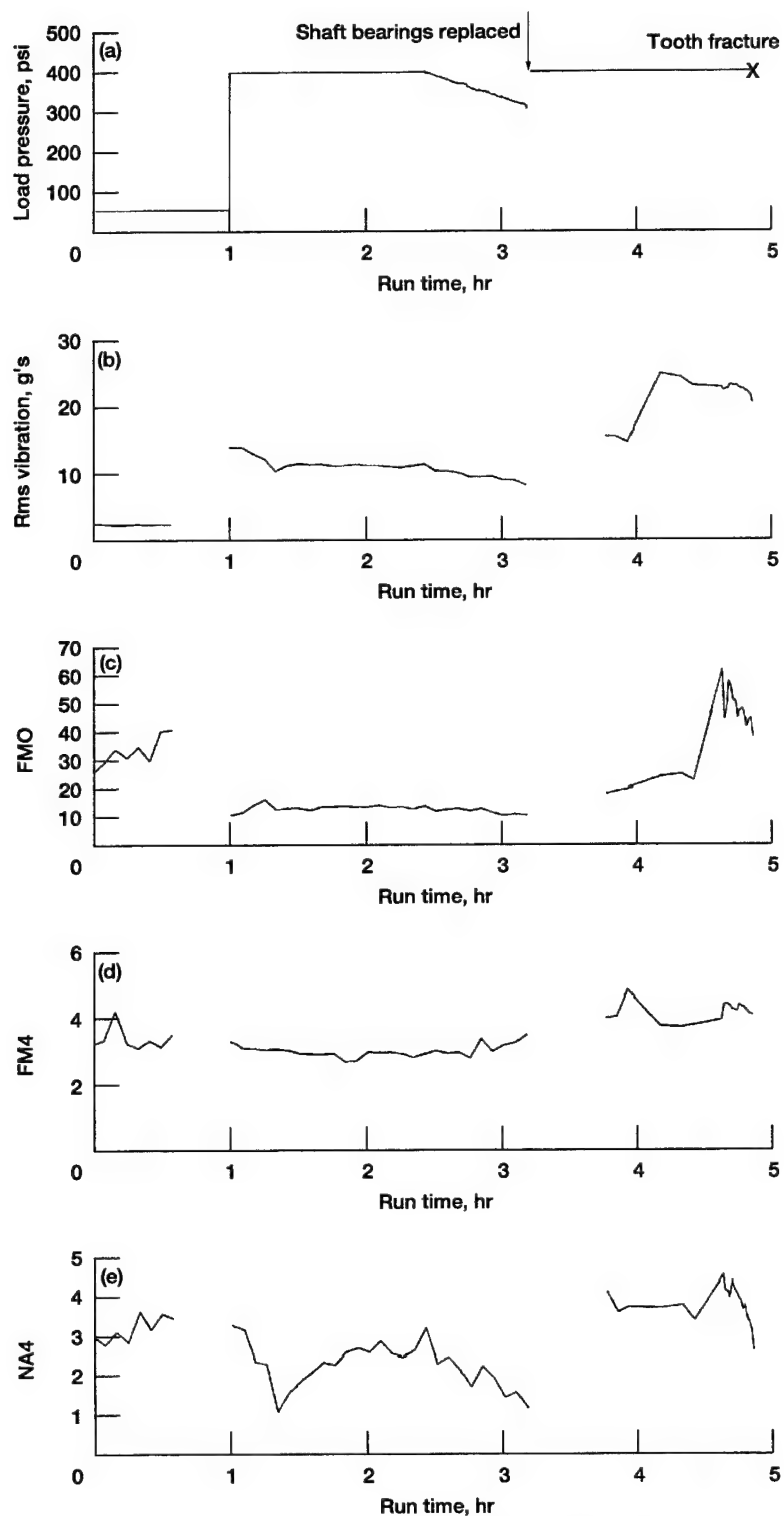


Figure 4.6.5.—Load history and vibration parameters for test 3, S/N 03, $m_B = 1.0$.
 (a) Load pressure. (b) Rms vibration of time-averaged signal. (c) FMO parameter.
 (d) FM4 parameter. (e) NA4 parameter.

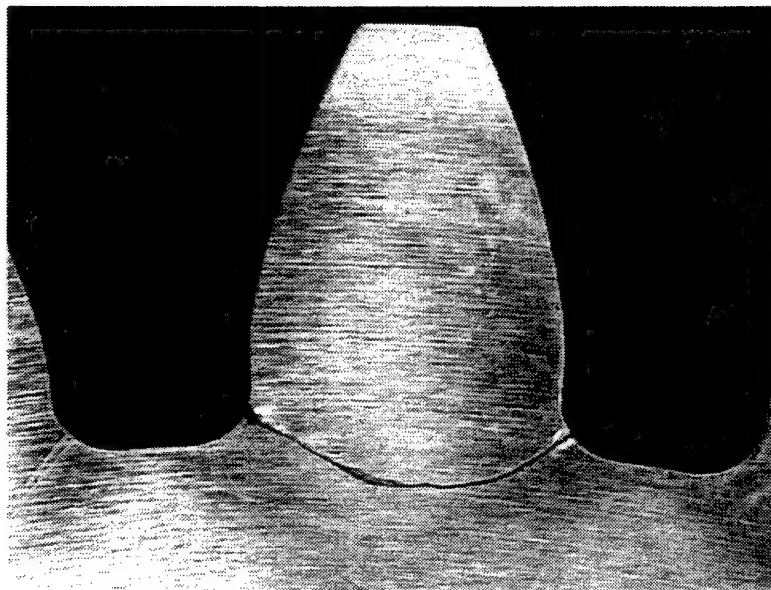


Figure 4.6.6.—Crack propagation path for test 3, S/N 03, $m_B = 1.0$, tooth fracture at 4.9 hr total run time (3.9 hr at 400 psi load pressure).

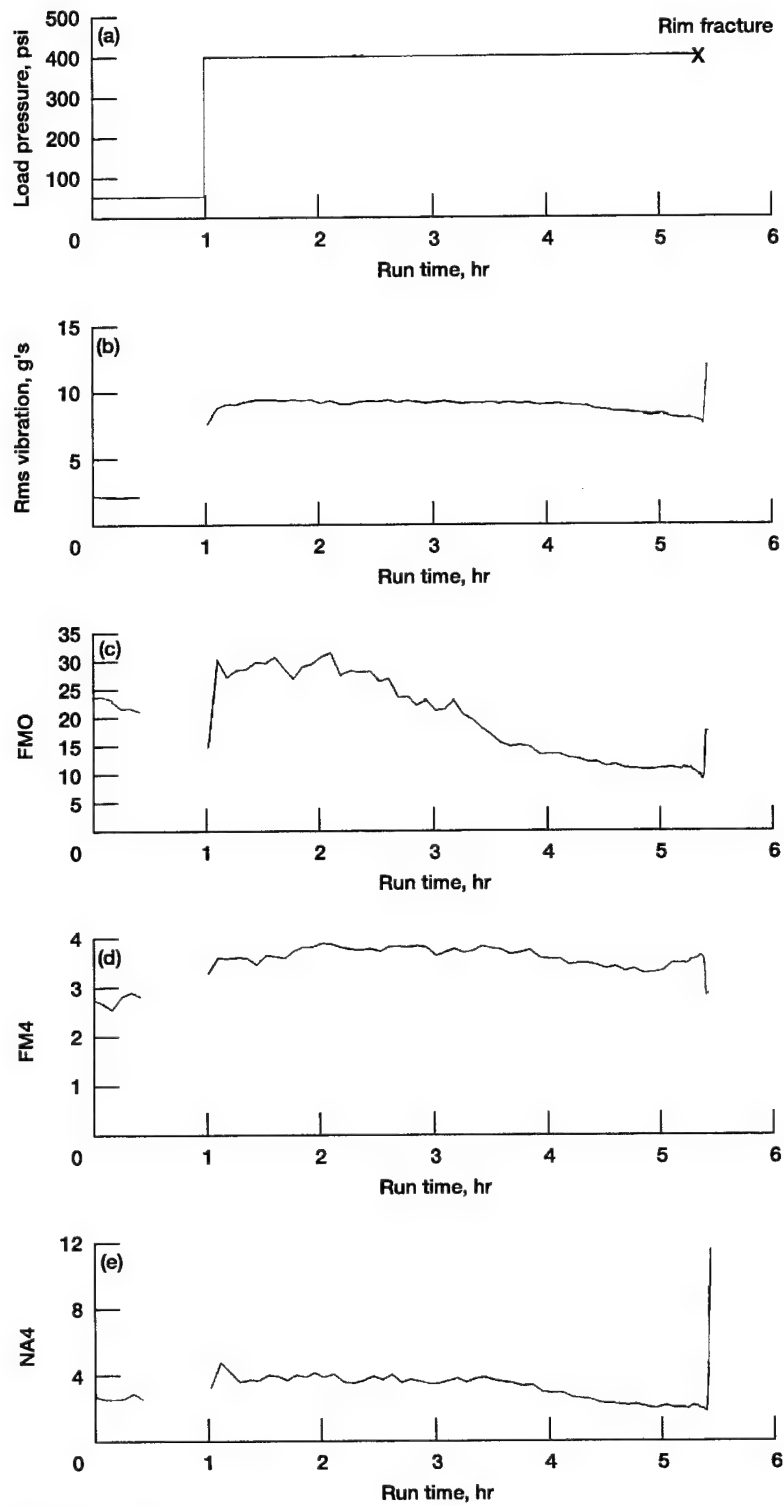


Figure 4.6.7.—Load history and vibration parameters for test 5, S/N 05, $m_B = 0.5$.
 (a) Load pressure. (b) Rms vibration of time-averaged signal. (c) FMO parameter.
 (d) FM4 parameter. (e) NA4 parameter.

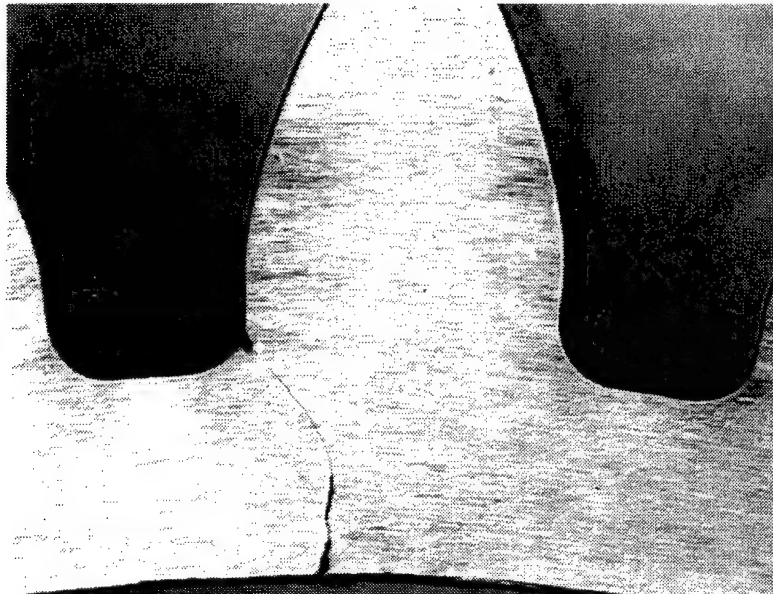


Figure 4.6.8.—Crack propagation path for test 5, S/N 05, $m_B = 0.5$, rim fracture at 5.4 hr total run time (4.4 hr at 400 psi load pressure).

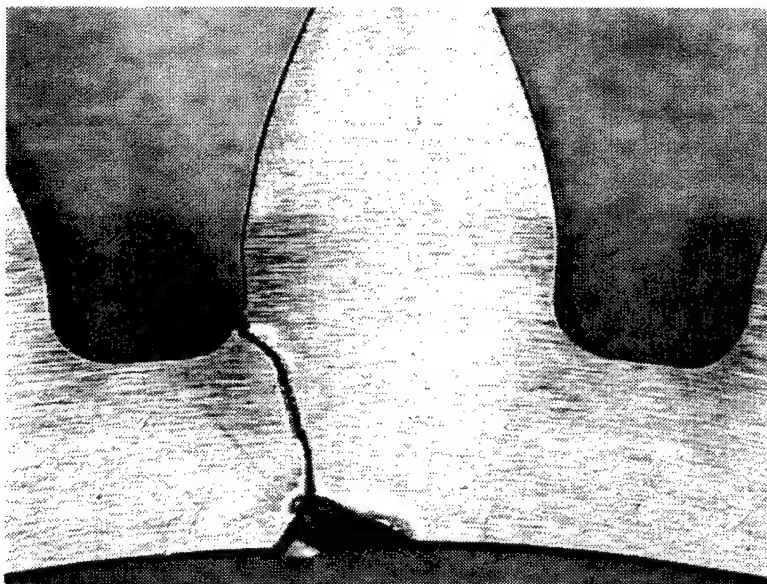


Figure 4.6.9.—Crack propagation path for test 6, S/N 06, $m_B = 0.5$, rim fracture at 31.8 hr total run time (0.9 hr at 475 psi load pressure).

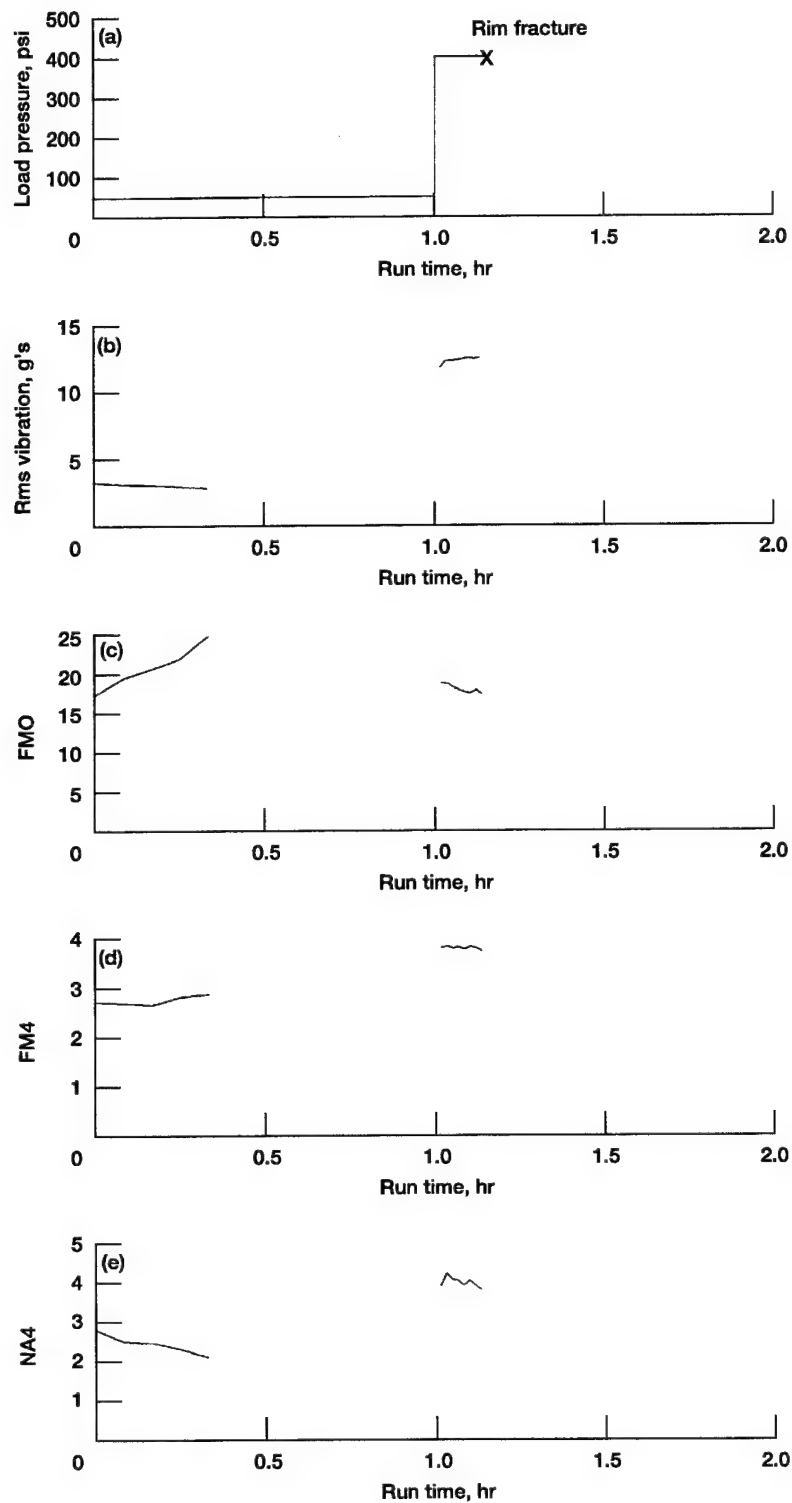


Figure 4.6.10.—Load history and vibration parameters for test 7, S/N 07, $m_B = 0.3$.
 (a) Load pressure. (b) Rms vibration of time-averaged signal. (c) FMO parameter.
 (d) FM4 parameter. (e) NA4 parameter.

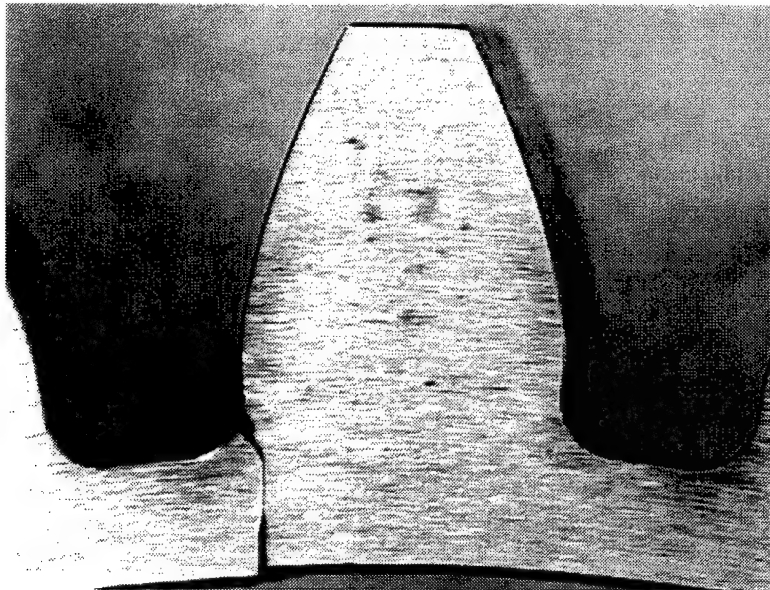


Figure 4.6.11.—Crack propagation path for test 7, S/N 07, $m_B = 0.3$, rim fracture at 1.2 hr total run time (9 min at 400 psi load pressure).

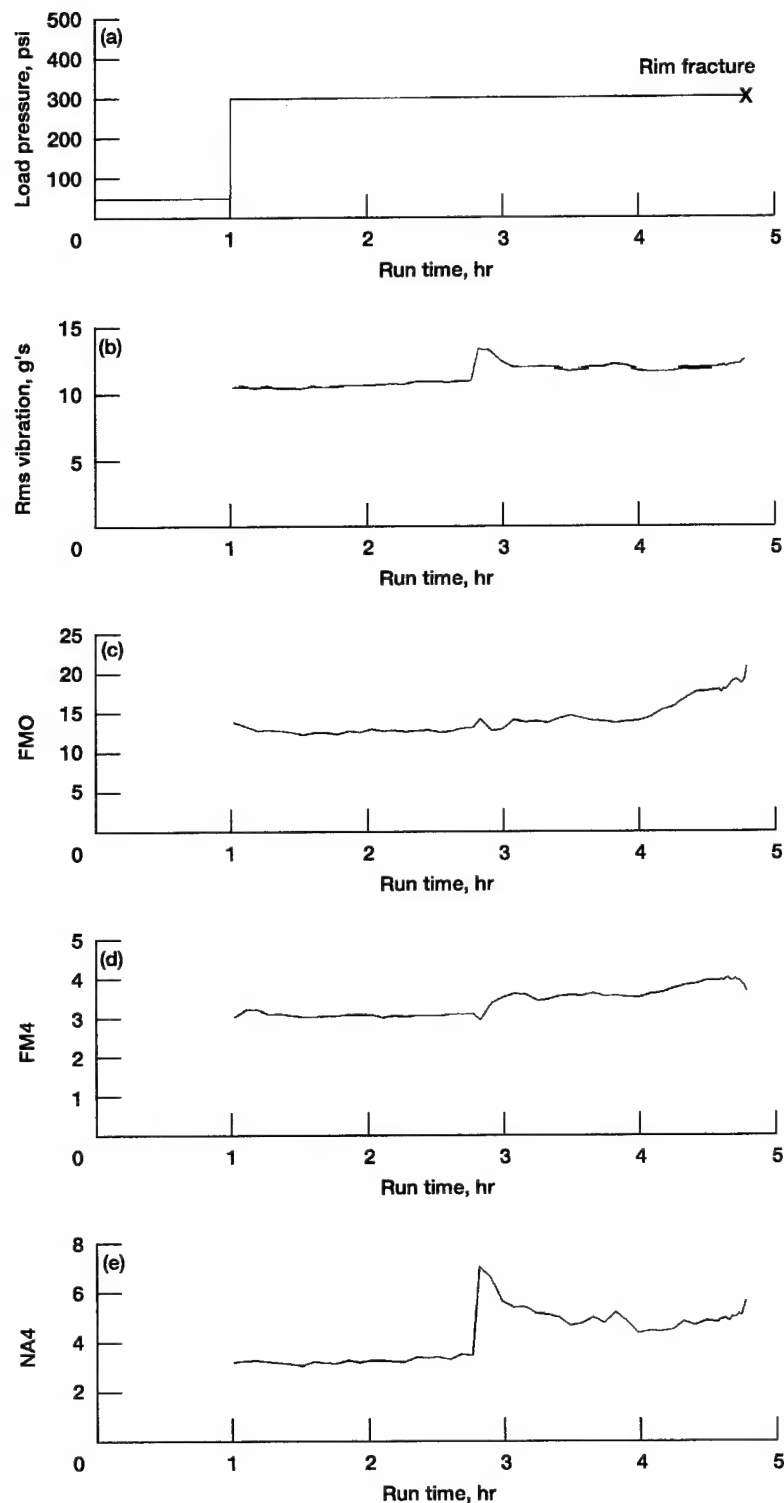


Figure 4.6.12.—Load history and vibration parameters for test 8, S/N 08, $m_B = 0.3$.
 (a) Load pressure. (b) Rms vibration of time-averaged signal. (c) FMO parameter.
 (d) FM4 parameter. (e) NA4 parameter.

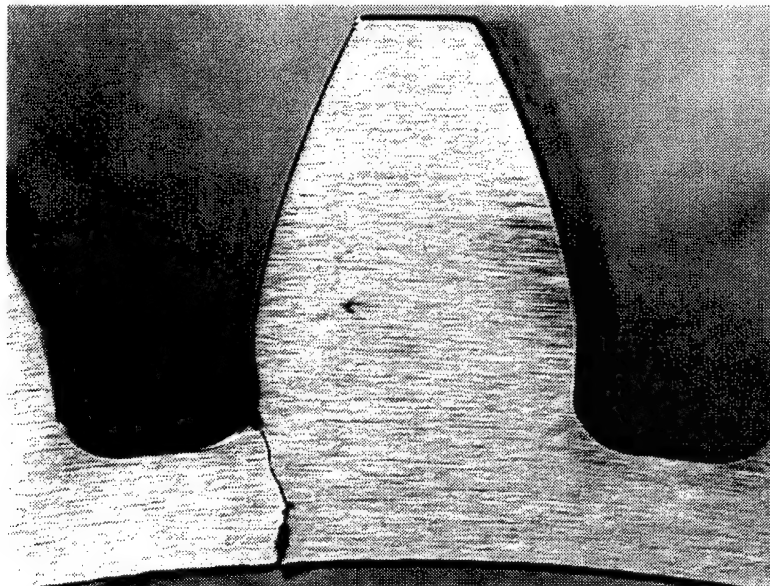


Figure 4.6.13.—Crack propagation path for test 8, S/N 08, $m_B = 0.3$, rim fracture at 4.8 hr total run time (3.8 hr at 300 psi load pressure).

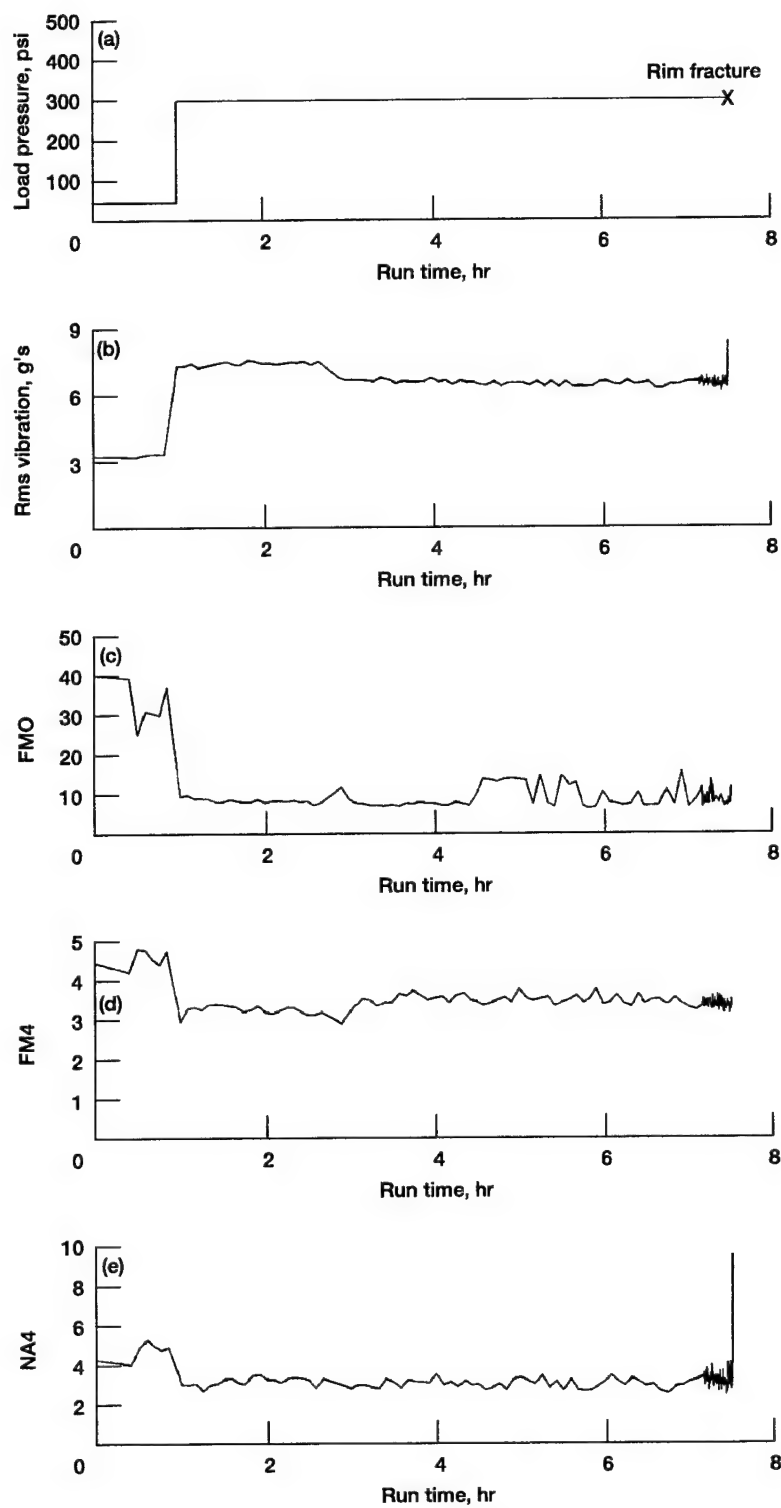


Figure 4.6.14.—Load history and vibration parameters for test 9, S/N 11, $m_B = 0.3$.
 (a) Load pressure. (b) Rms vibration of time-averaged signal. (c) FMO parameter.
 (d) FM4 parameter. (e) NA4 parameter.

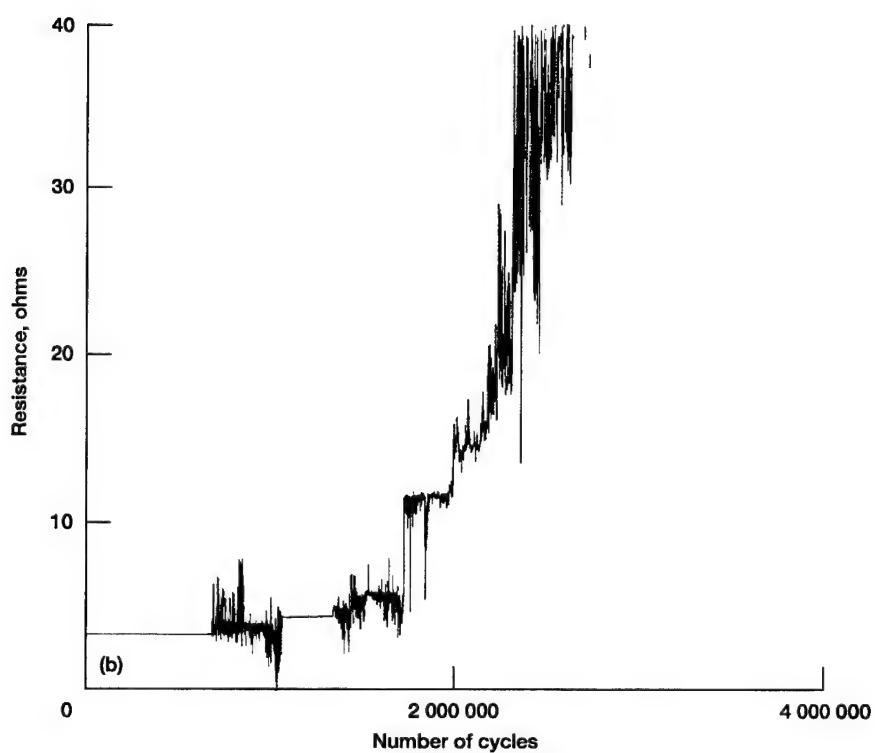
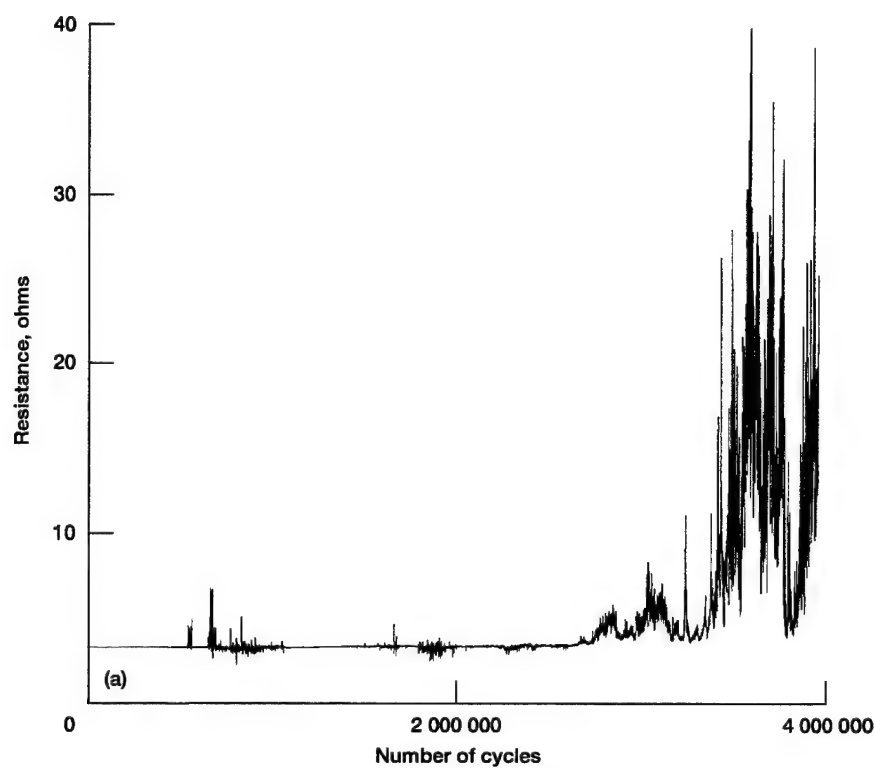


Figure 4.6.15.—Results of crack propagation gages for test 9, S/N 11, $m_B = 0.3$. (a) Gage 1 (front tooth flank). (b) Gage 2 (rear tooth flank).

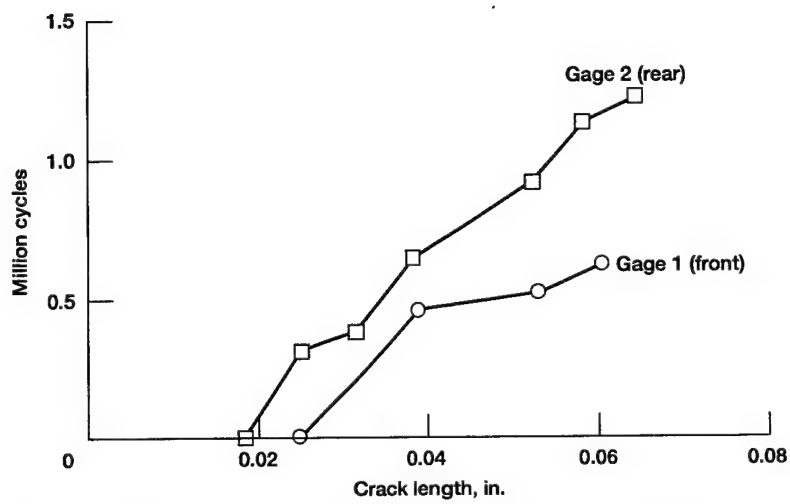


Figure 4.6.16.—Crack propagation fatigue growth rate for test 9, S/N 11, $m_B = 0.3$.

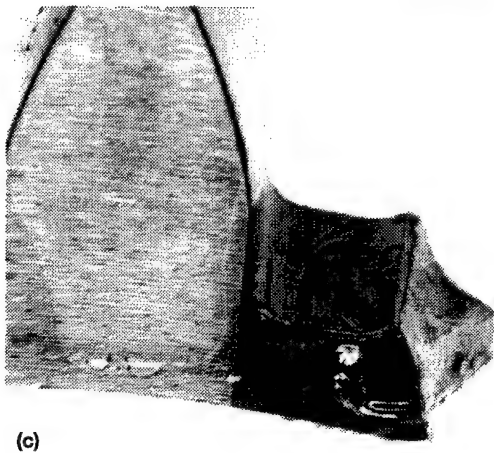
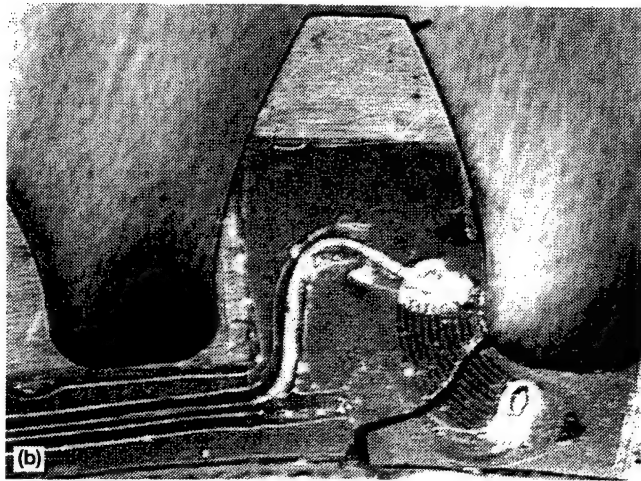
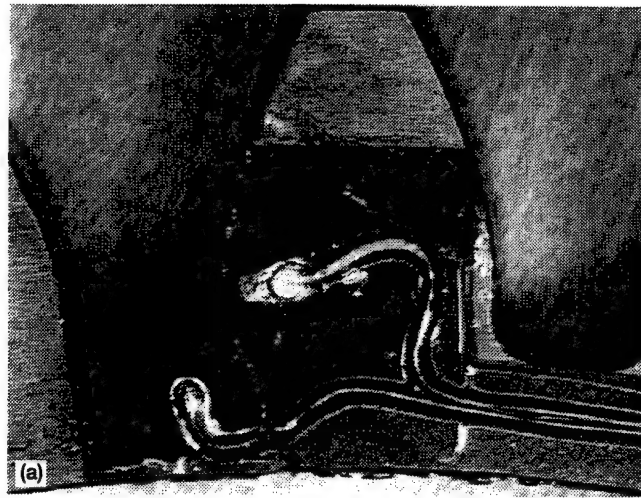


Figure 4.6.17.—Crack propagation path for test 9, S/N 11, $m_B = 0.3$, rim fracture at 7.5 hr total run time (6.5 hr at 300 psi load pressure). (a) Front tooth flank. (b) Rear tooth flank. (c) Isometric view.

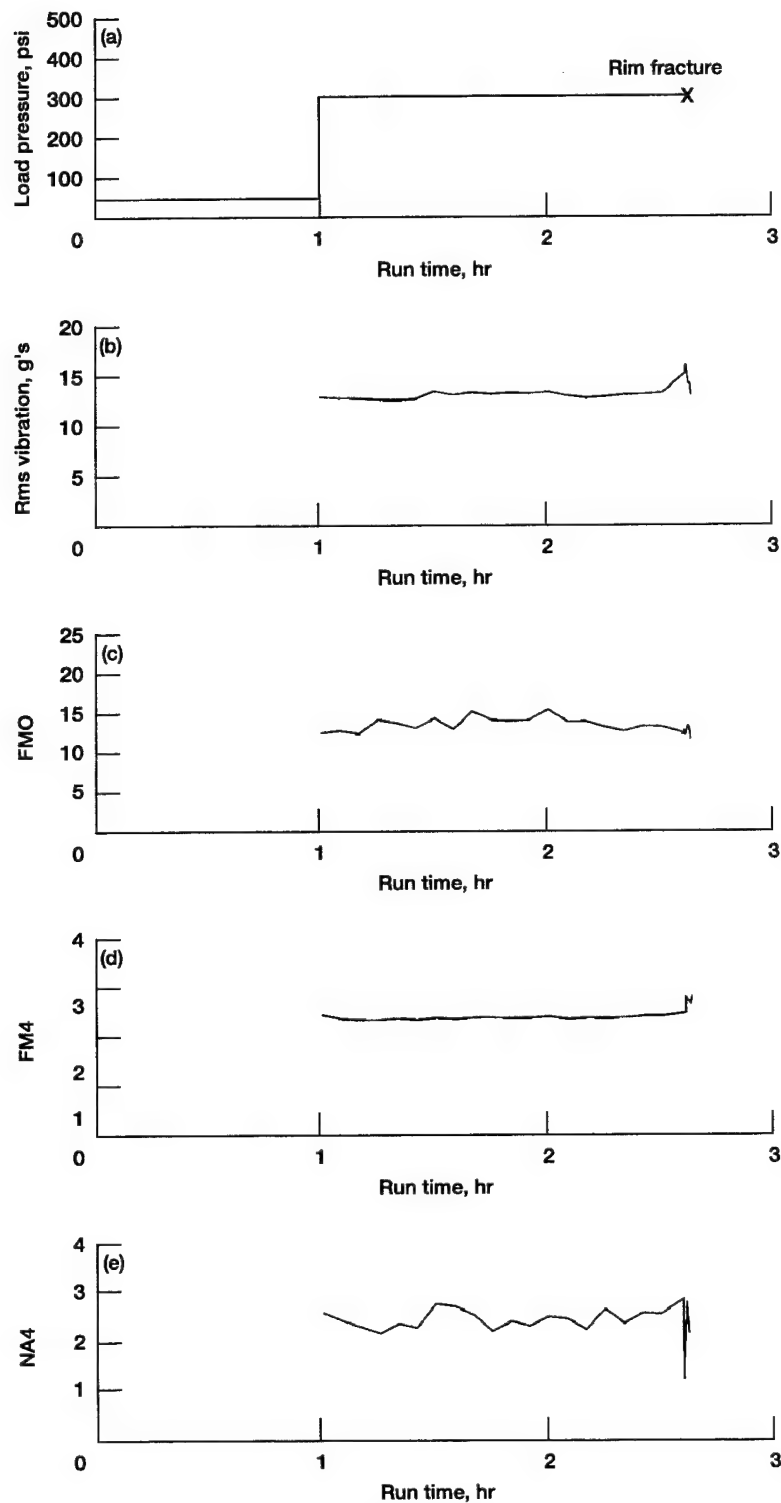


Figure 4.6.18.—Load history and vibration parameters for test 10, S/N 12, $m_B = 0.3$.
 (a) Load pressure. (b) Rms vibration of time-averaged signal. (c) FMO parameter.
 (d) FM4 parameter. (e) NA4 parameter.

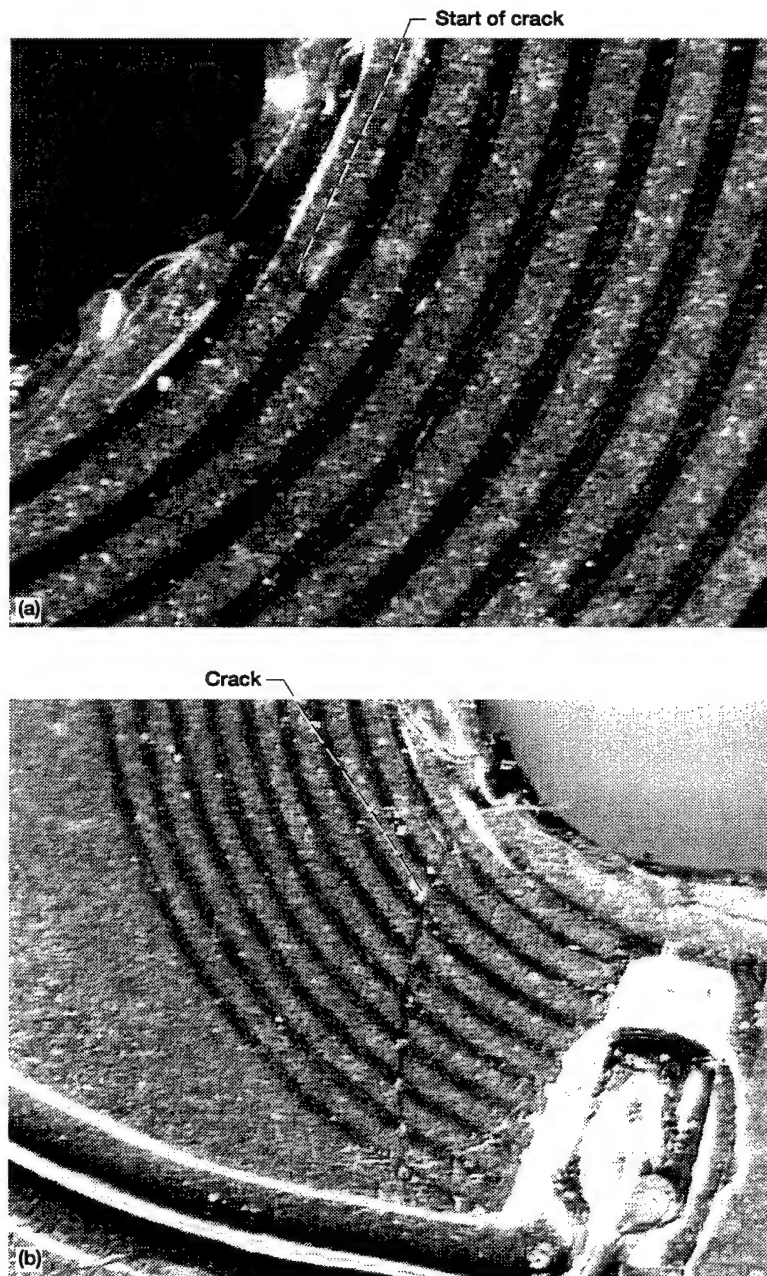


Figure 4.6.19.—Close-up of crack propagation gages for test gear, S/N 12, $m_B = 0.3$, at 2.5 hr total run time of test 10. (a) Gage 1 (front tooth flank). (b) Gage 2 (rear tooth flank).

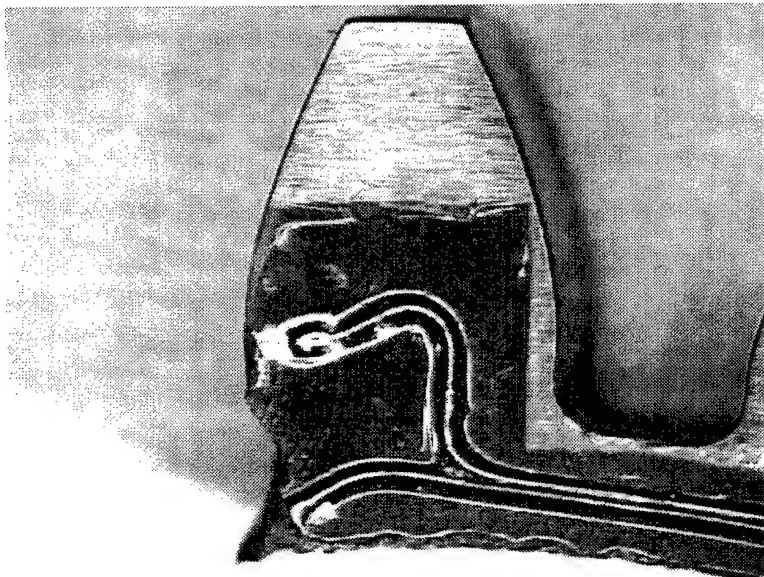


Figure 4.6.20.—Crack propagation path for test 10, S/N 12, $m_B = 0.3$, rim fracture at 2.6 hr total run time (1.6 hr at 300 psi load pressure).

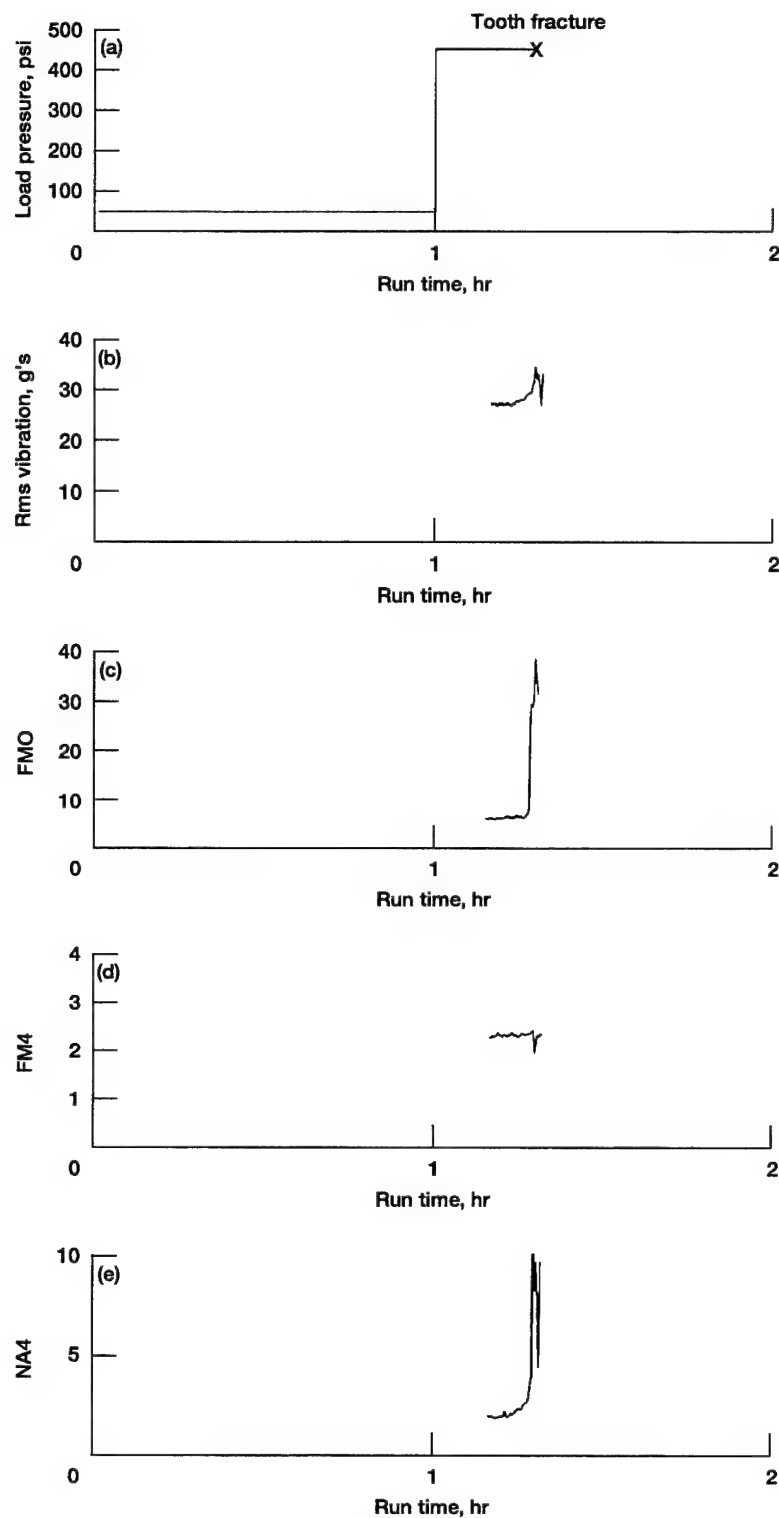


Figure 4.6.21.—Load history and vibration parameters for test 11, S/N 13, $m_B = 3.3$.
 (a) Load pressure. (b) Rms vibration of time-averaged signal. (c) FMO parameter.
 (d) FM4 parameter. (e) NA4 parameter.

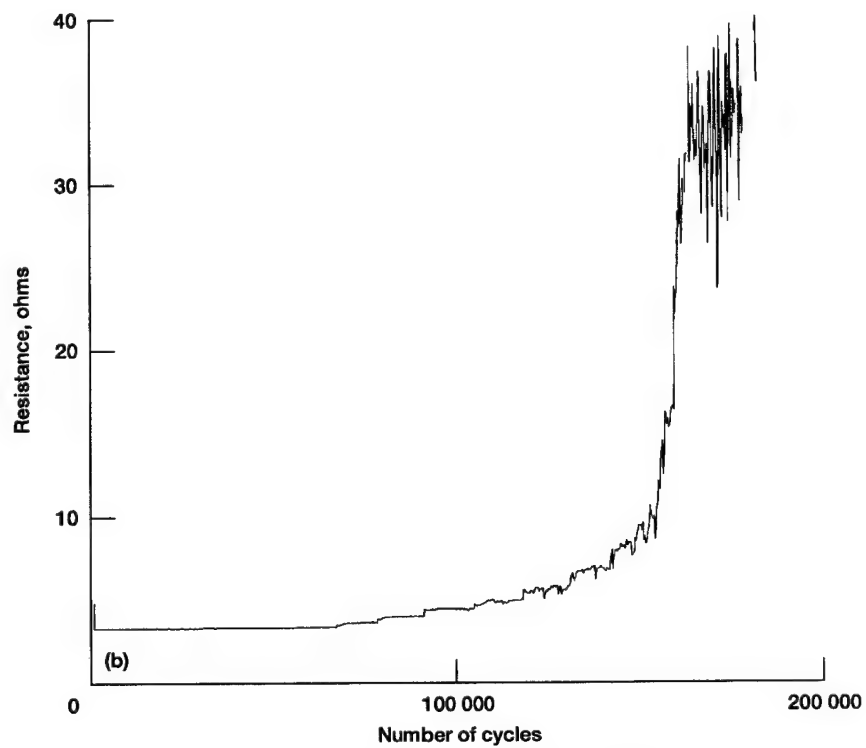
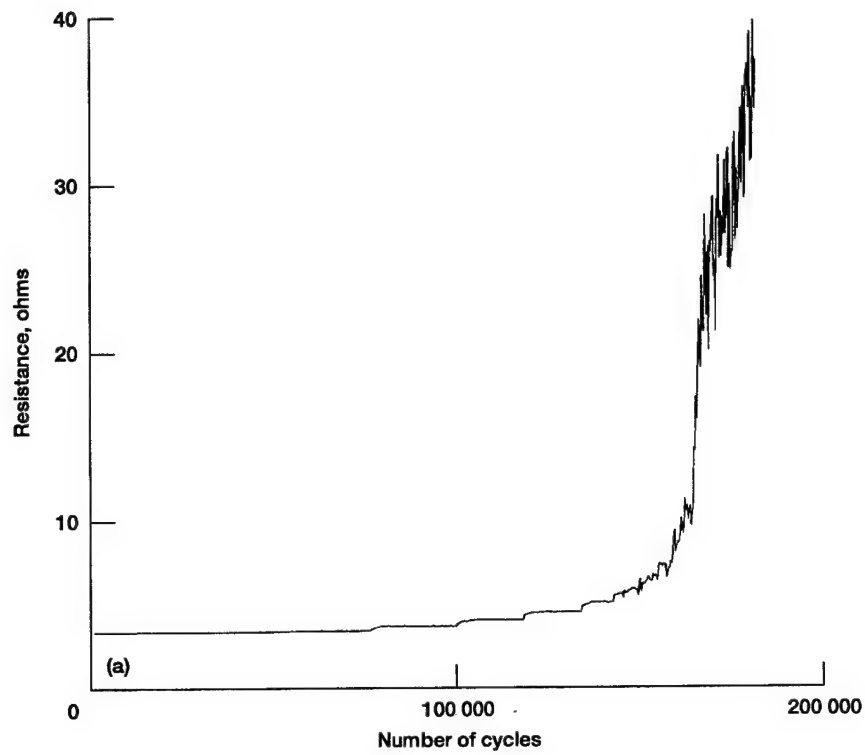


Figure 4.6.22.—Results of crack propagation gages for test 11, S/N 13, $m_B = 3.3$. (a) Gage 1 (front tooth flank). (b) Gage 2 (rear tooth flank).

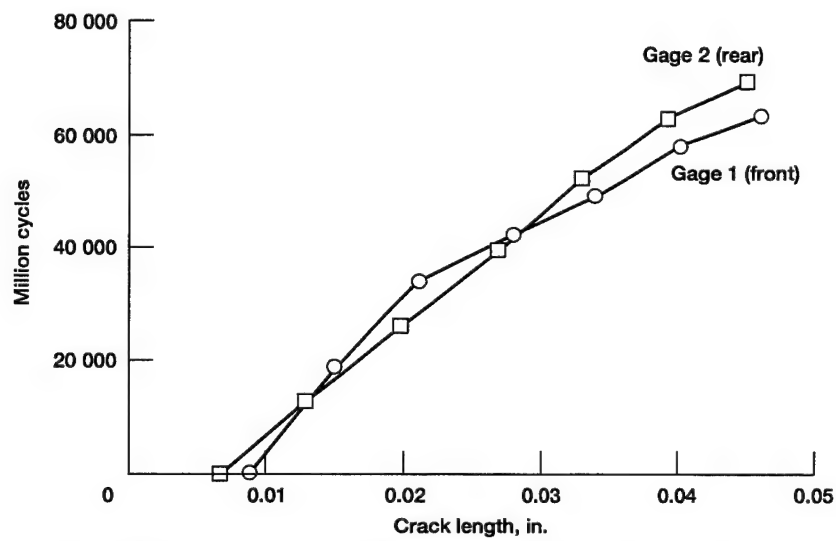


Figure 4.6.23.—Crack propagation fatigue growth rate for test 11, S/N 13, $m_B = 3.3$.

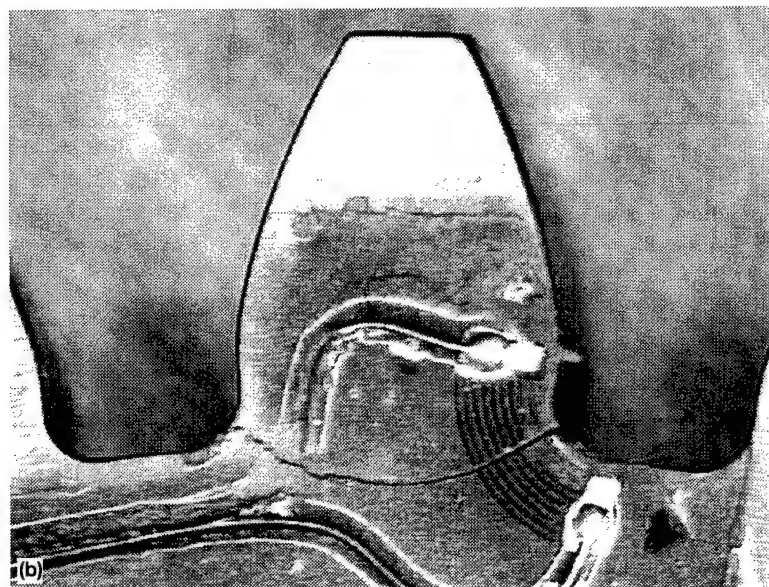
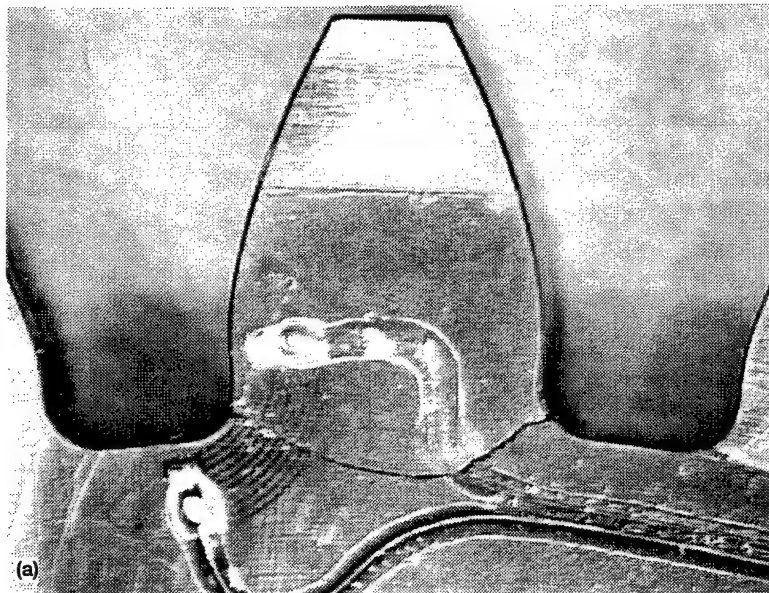


Figure 4.6.24.—Crack propagation path for test 11, S/N 13, $m_B = 3.3$, tooth fracture at 1.30 hr total run time (0.30 hr at 450 psi load pressure). (a) Front tooth flank. (b) Rear tooth flank.

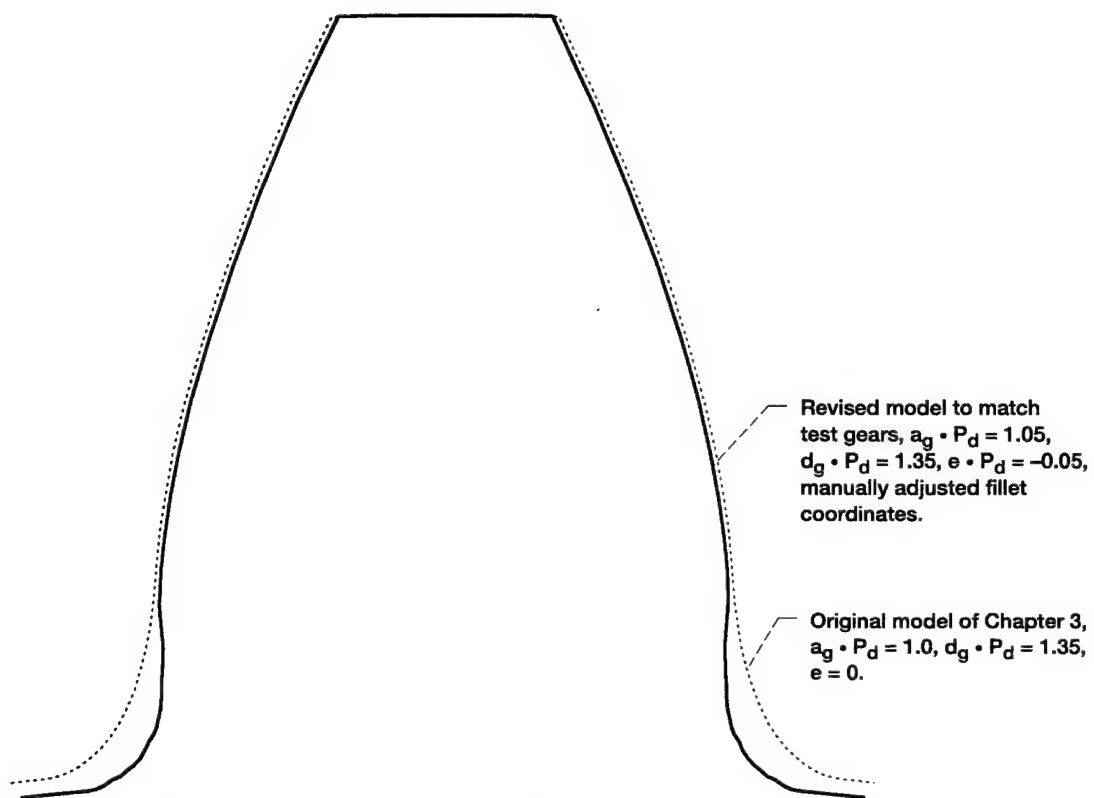


Figure 5.2.1.—Comparison of original tooth model (Chapter 3) to revised model which matched tooth profile of test gears.

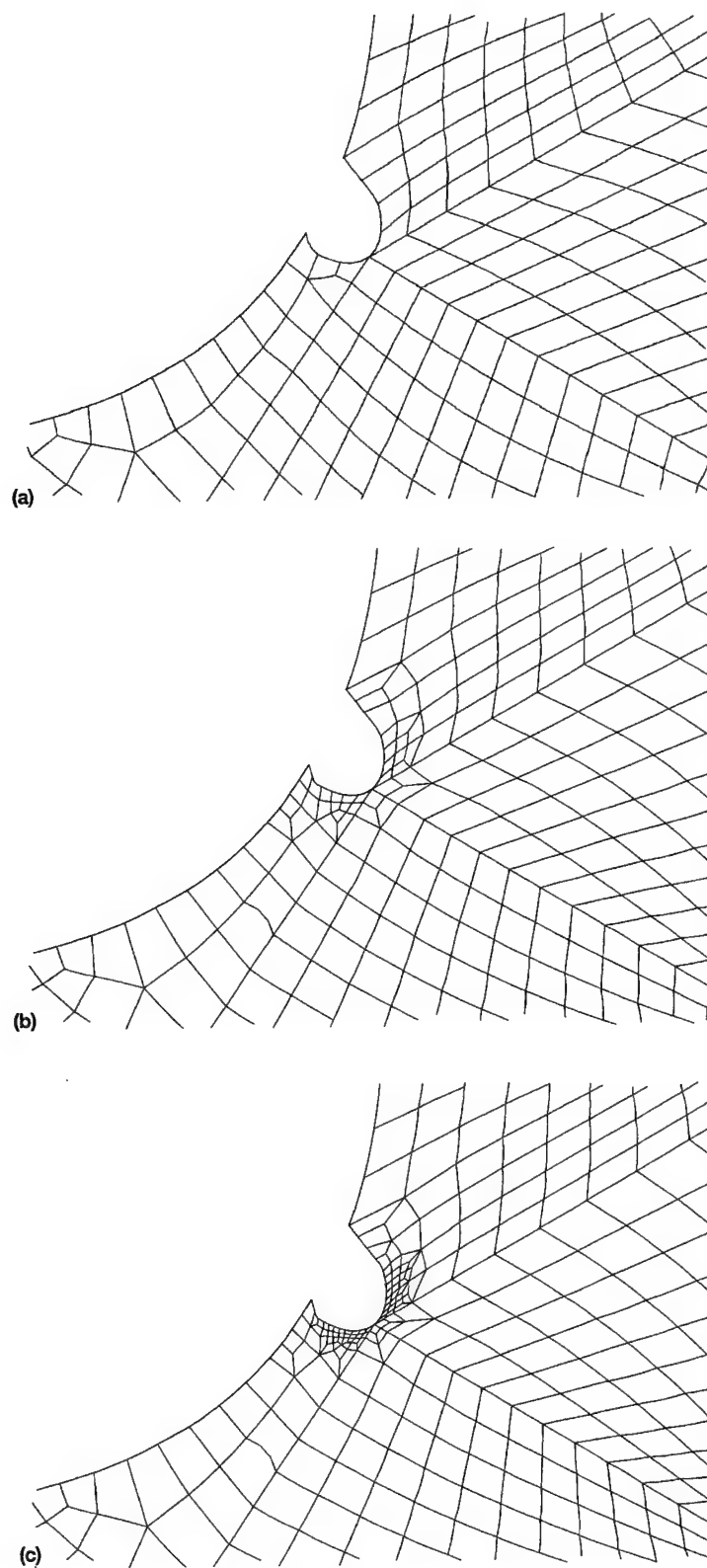


Figure 5.2.2.—Notch in finite element gear model. (a) No refinement. (b) Refinement 1. (c) Refinement 2.

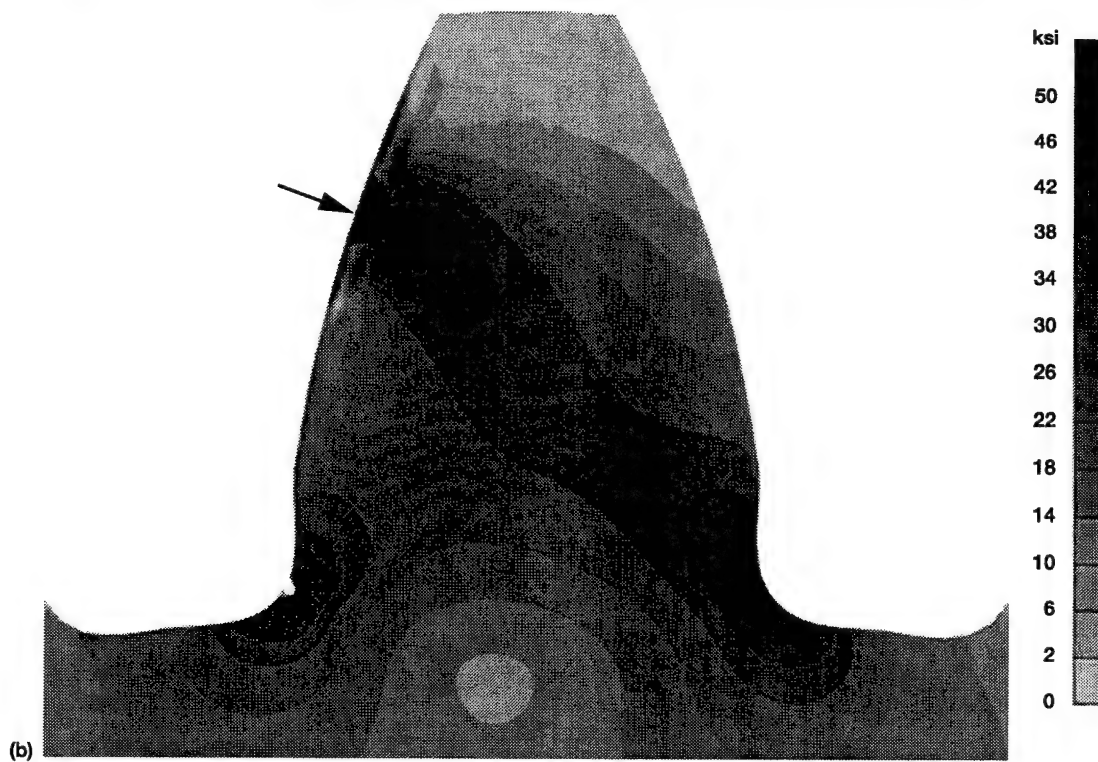
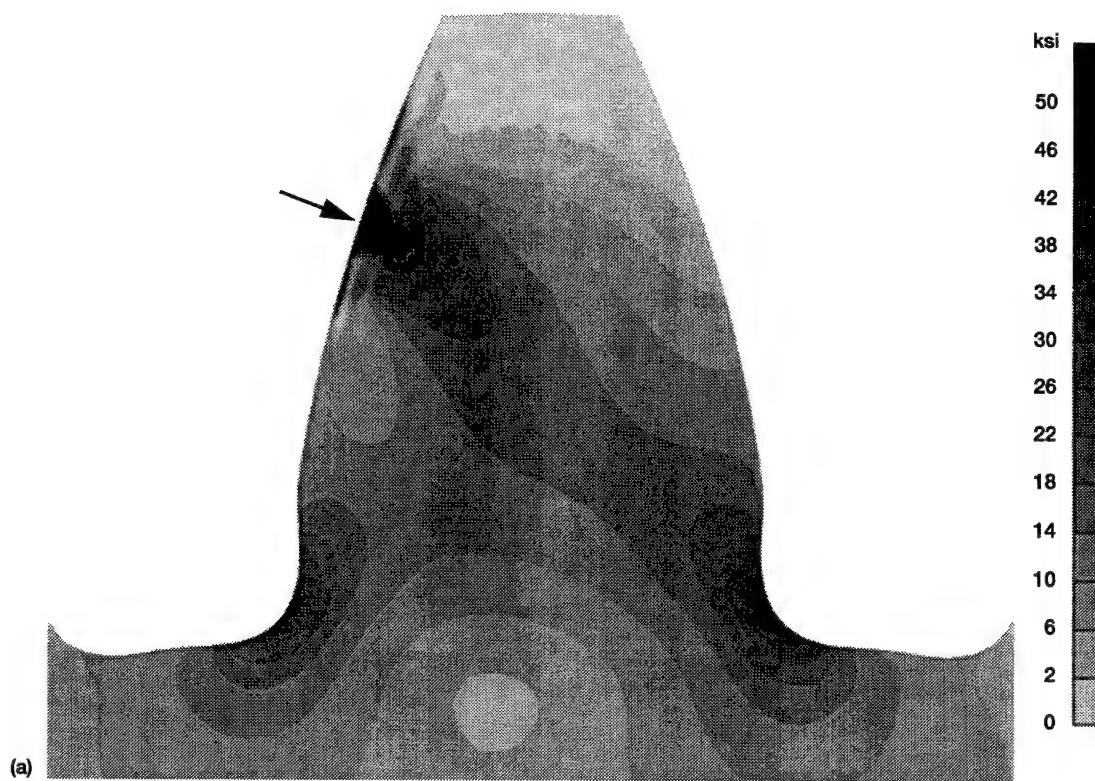


Figure 5.2.3.—Von Mises stress distributions of gear tooth finite element models with and without a notch.
 (a) Without notch in model. (b) With notch in model.

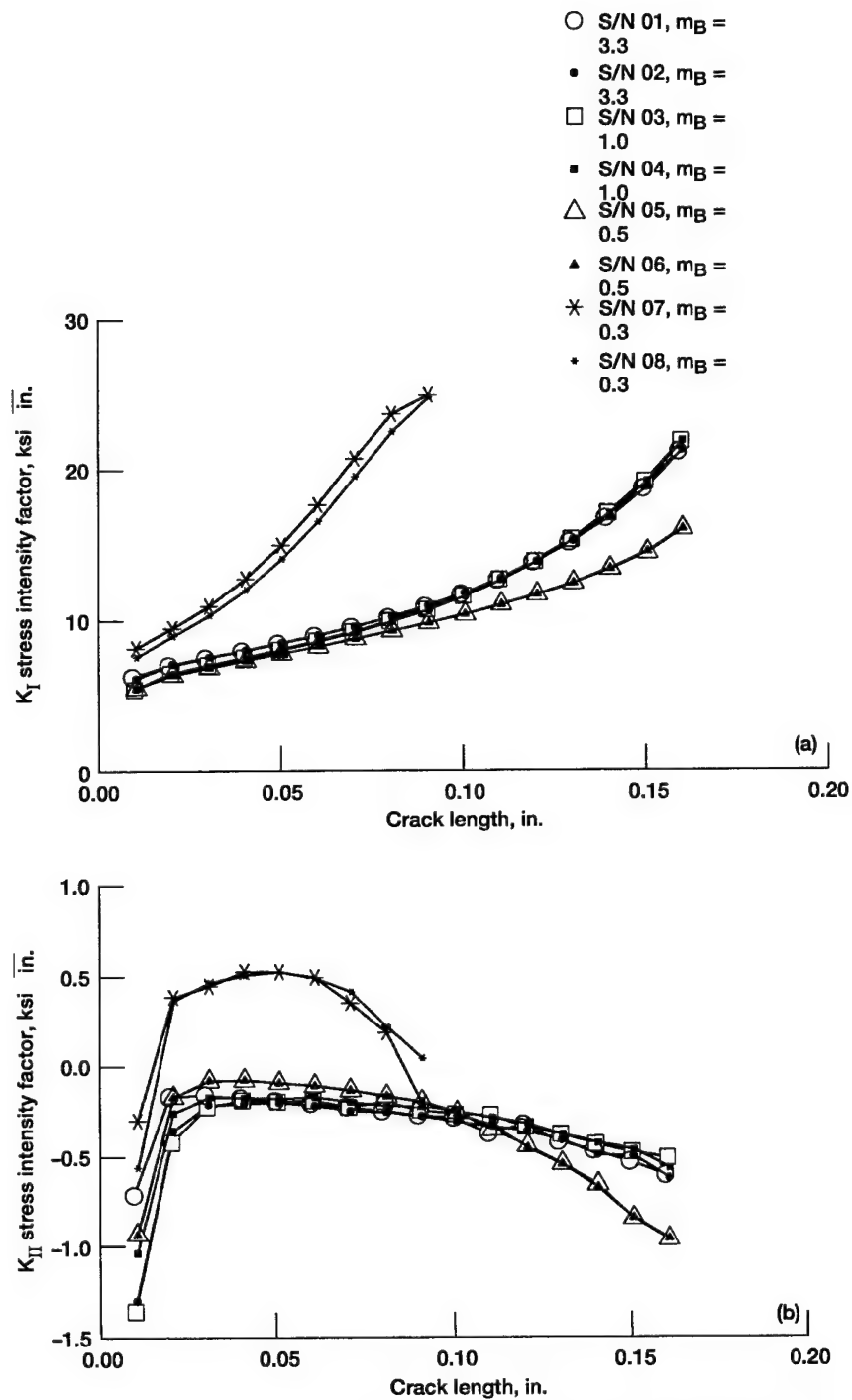


Figure 5.3.1.—Calculated stress intensity factors for test gears S/N 01 through 08.
(a) Mode I stress intensity factors. (b) Mode II stress intensity factors.

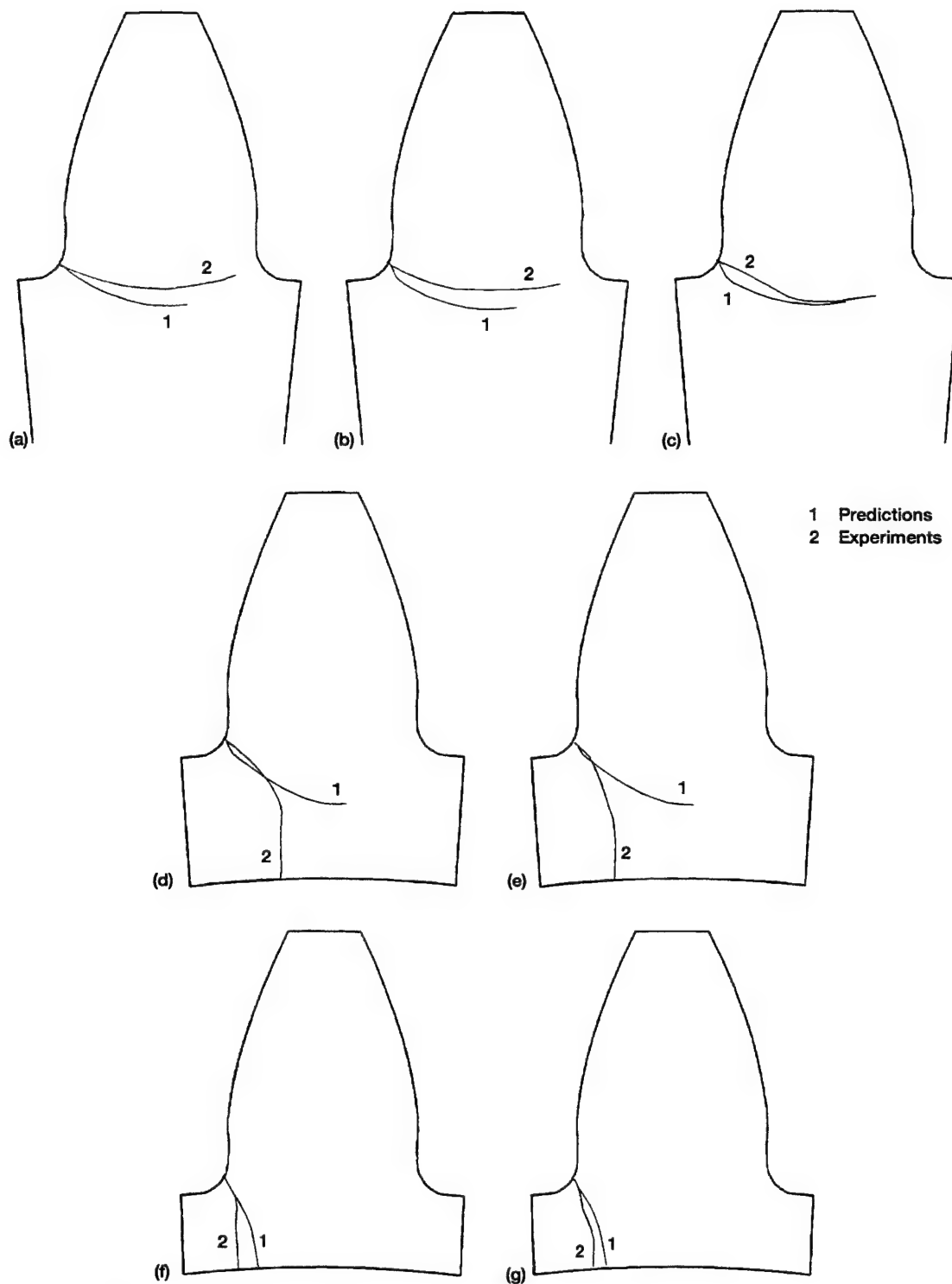


Figure 5.3.2.—Comparison of predicted and experimental crack propagation paths for test gears S/N 01 through 08. (a) S/N 01, $m_B = 3.3$. (b) S/N 02, $m_B = 3.3$. (c) S/N 03, $m_B = 1.0$. (d) S/N 05, $m_B = 0.5$. (e) S/N 06, $m_B = 0.5$. (f) S/N 07, $m_B = 0.3$. (g) S/N 08, $m_B = 0.3$.

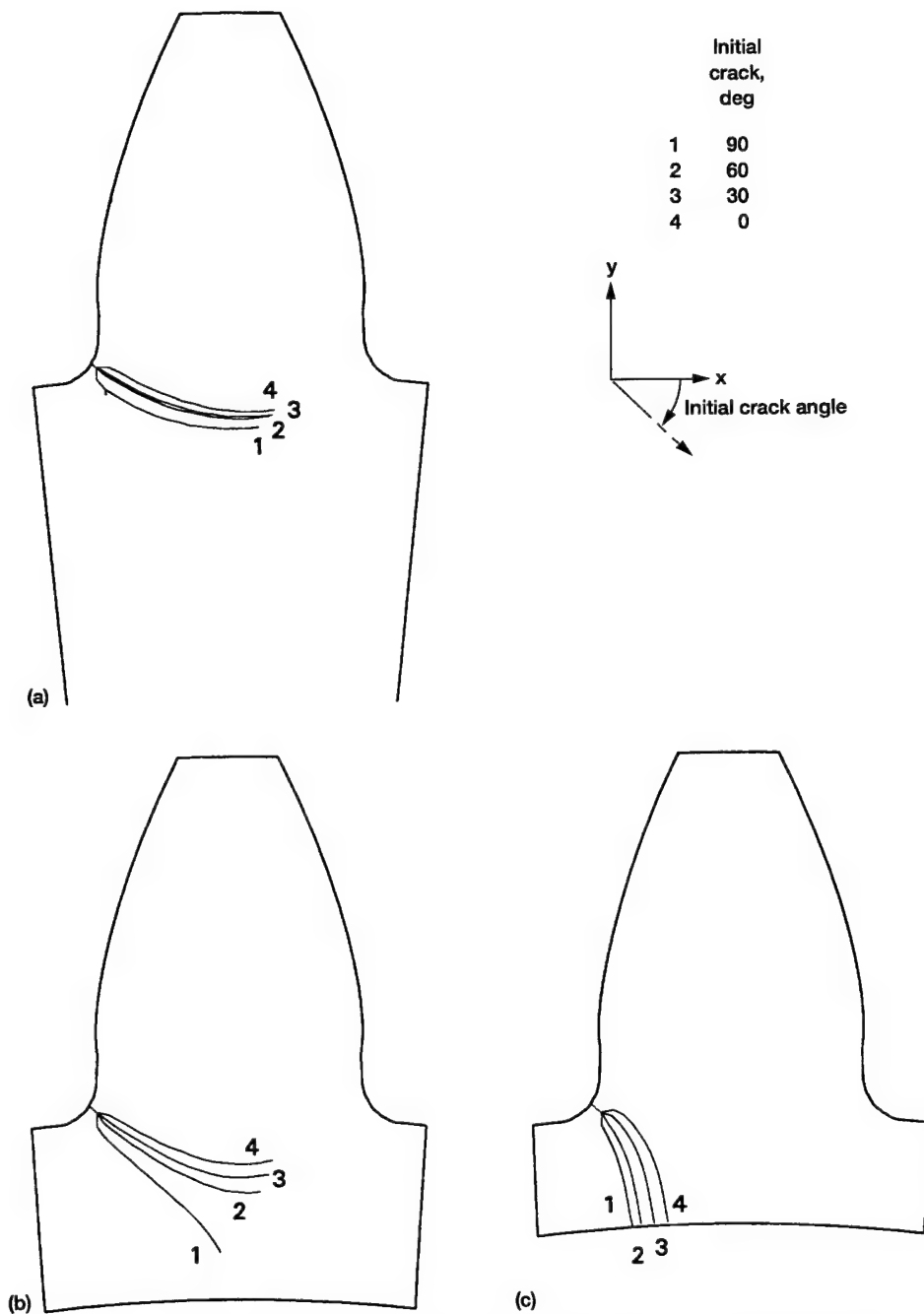


Figure 5.3.3.—Effect of initial crack orientation on predicted crack propagation path. (a) S/N 01, $m_B = 3.3$. (b) S/N 05, $m_B = 0.5$. (c) S/N 07, $m_B = 0.3$.

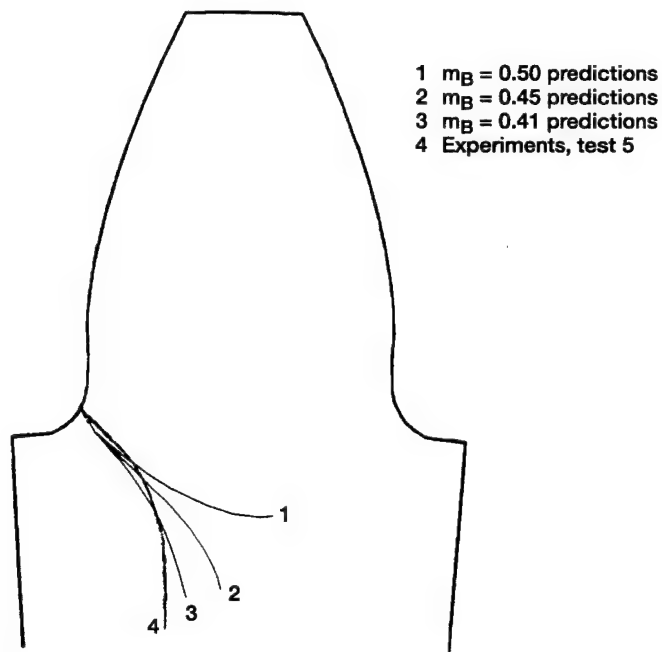


Figure 5.3.4.—Effect of small changes in backup ratio (near $m_B = 0.5$) on predicted crack propagation paths and comparison to experiments.

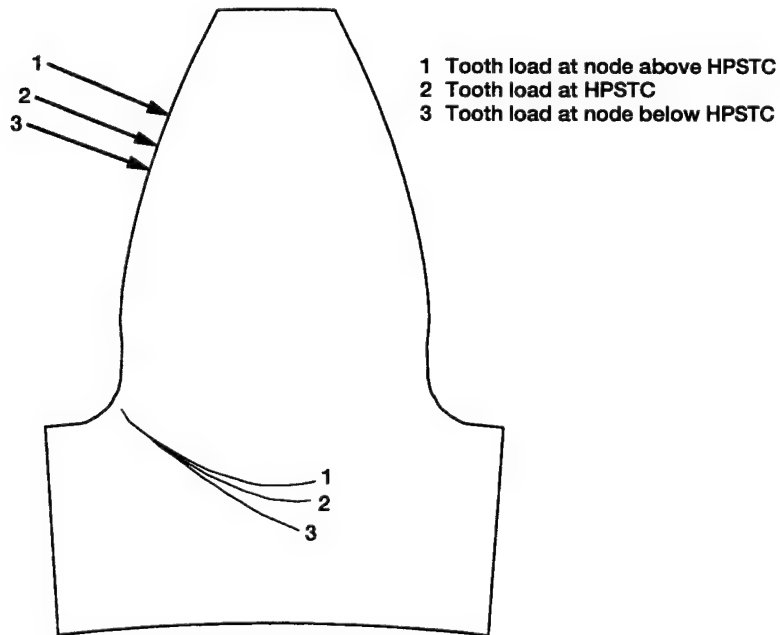


Figure 5.3.5.—Effect of load position of predicted crack propagation paths.

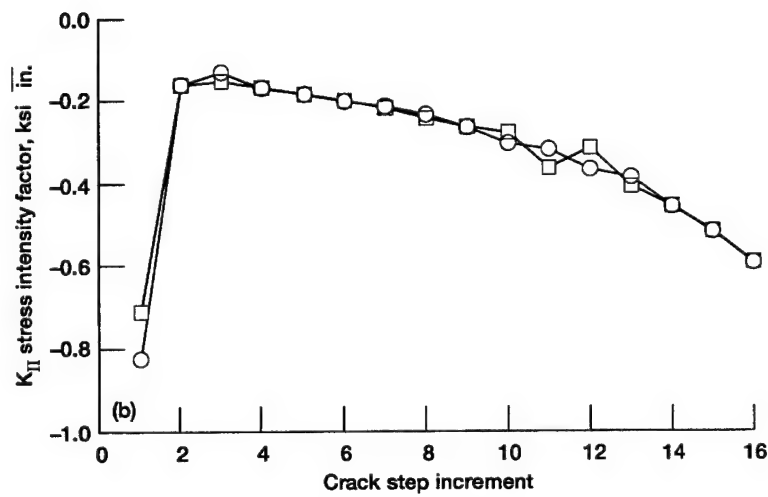
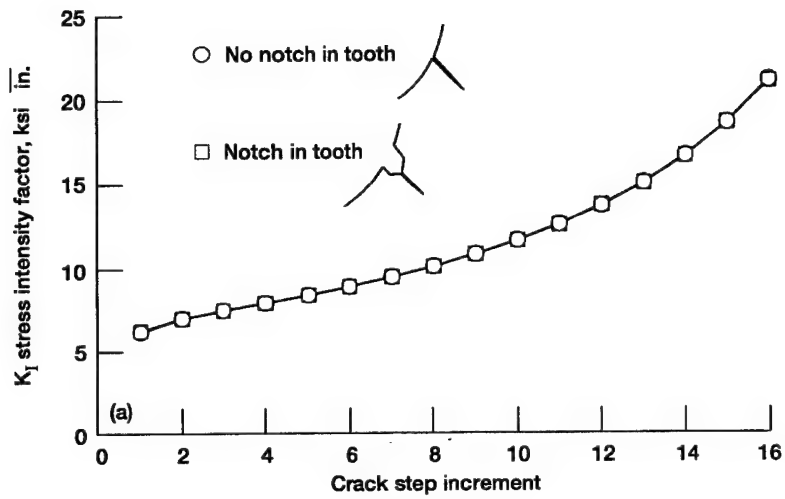


Figure 5.3.6.—Effect of notch on predicted stress intensity factors for test gear S/N 01, $m_B = 3.3$. (a) Mode I stress intensity factors. (b) Mode II stress intensity factors.

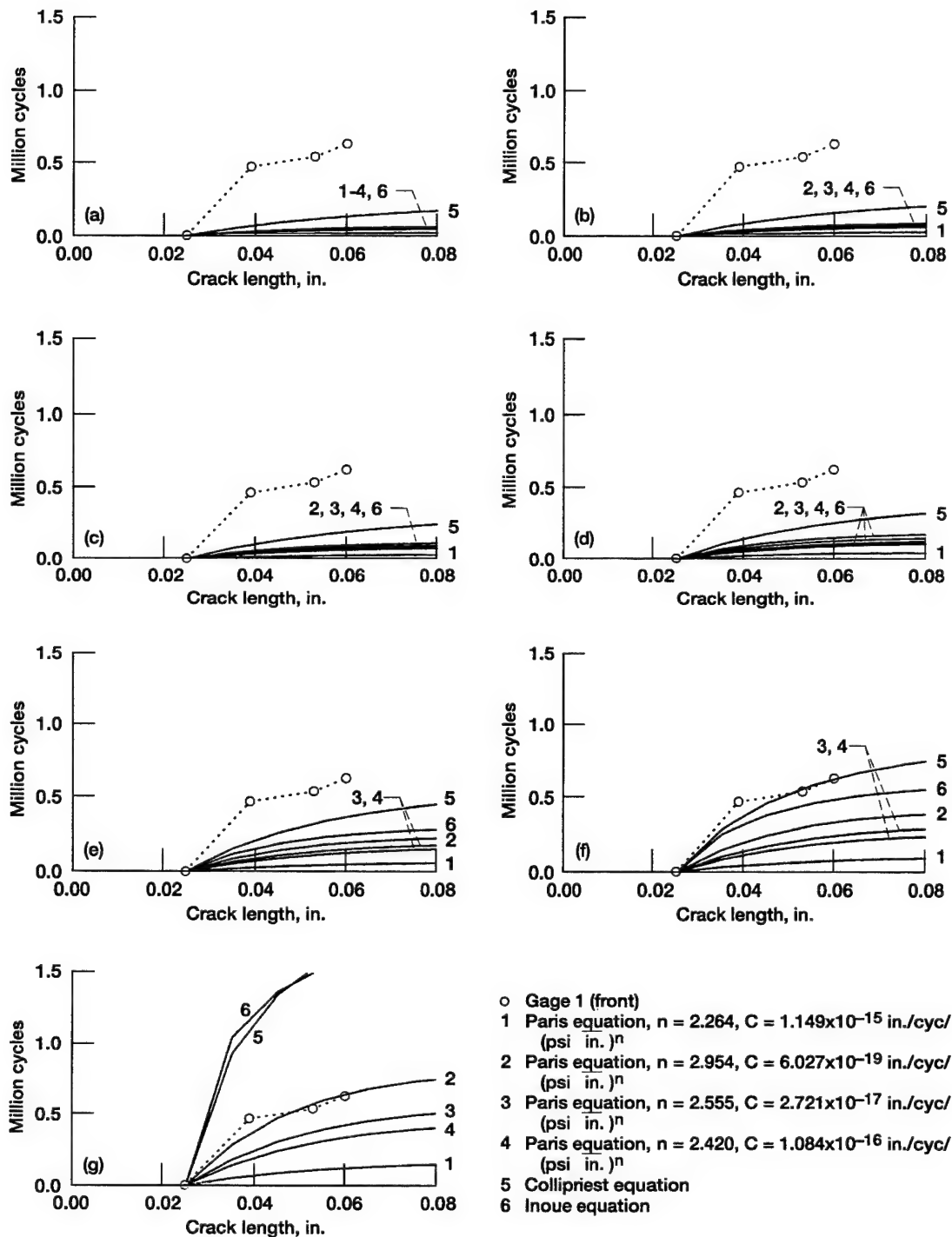


Figure 5.4.1.—Comparison of predicted crack propagation cycles using six different schemes to test 9, S/N 11, $m_B = 0.3$, front tooth flank. (a) $U = 1.0$. (b) $U = 0.9$. (c) $U = 0.8$. (d) $U = 0.7$. (e) $U = 0.6$. (f) $U = 0.5$. (g) $U = 0.4$.

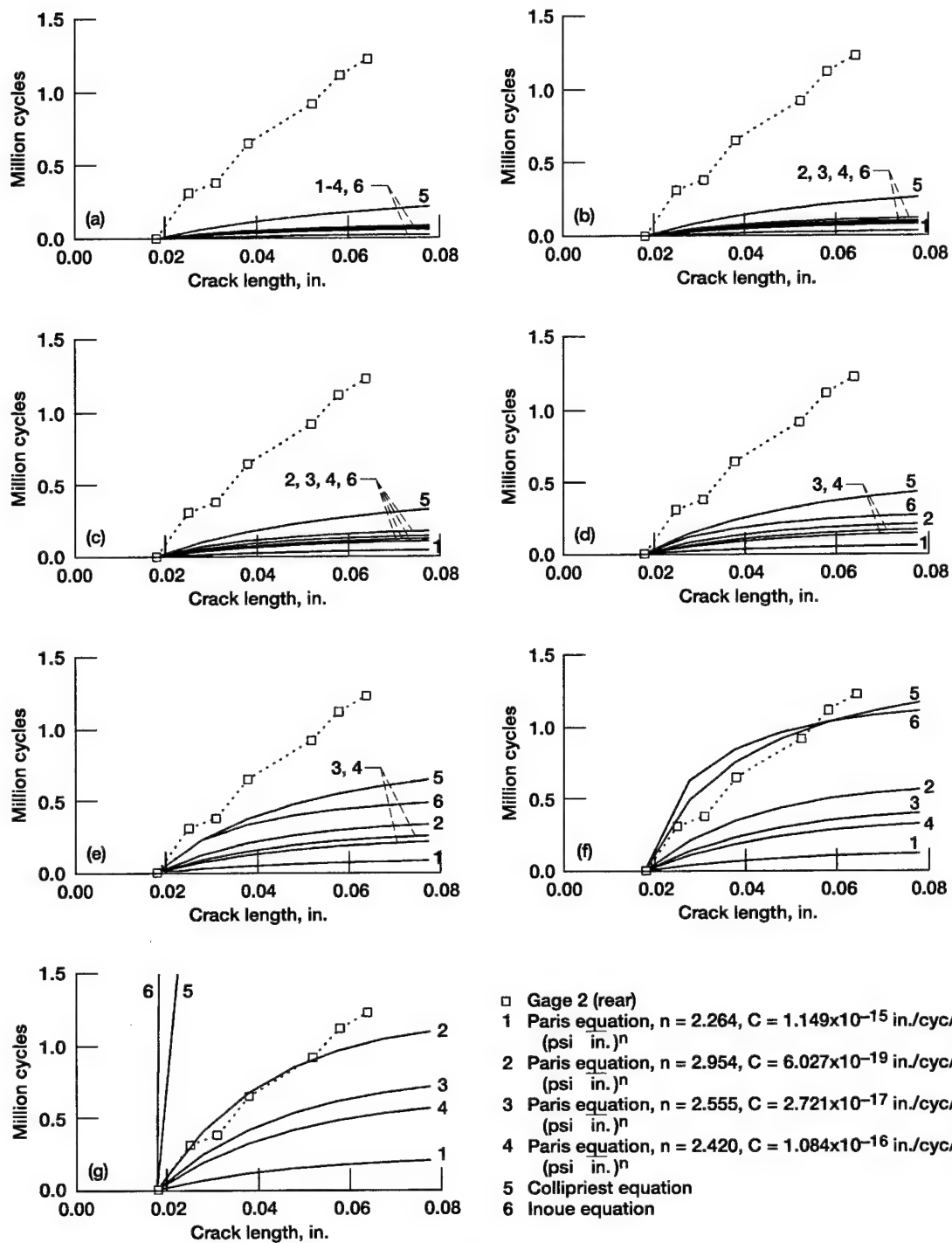


Figure 5.4.2.—Comparison of predicted crack propagation cycles using six different schemes to test 9, S/N 11, $m_B = 0.3$, rear tooth flank. (a) $U = 1.0$. (b) $U = 0.9$. (c) $U = 0.8$. (d) $U = 0.7$. (e) $U = 0.6$. (f) $U = 0.5$. (g) $U = 0.4$.

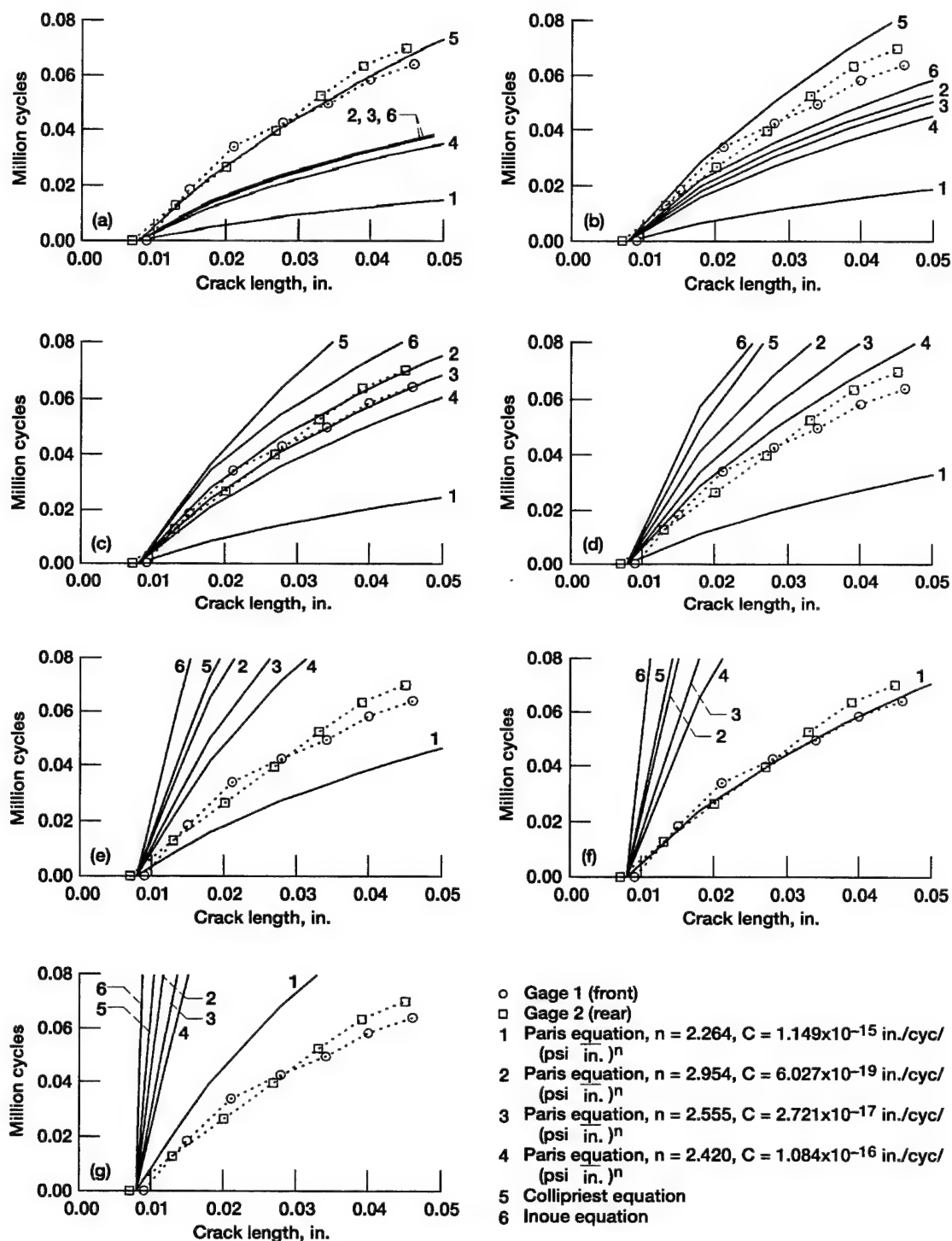


Figure 5.4.3.—Comparison of predicted crack propagation cycles using six different schemes to test 11, S/N 13, $m_B = 3.3$, front and rear tooth flanks. (a) $U = 1.0$. (b) $U = 0.9$. (c) $U = 0.8$. (d) $U = 0.7$. (e) $U = 0.6$. (f) $U = 0.5$. (g) $U = 0.4$.

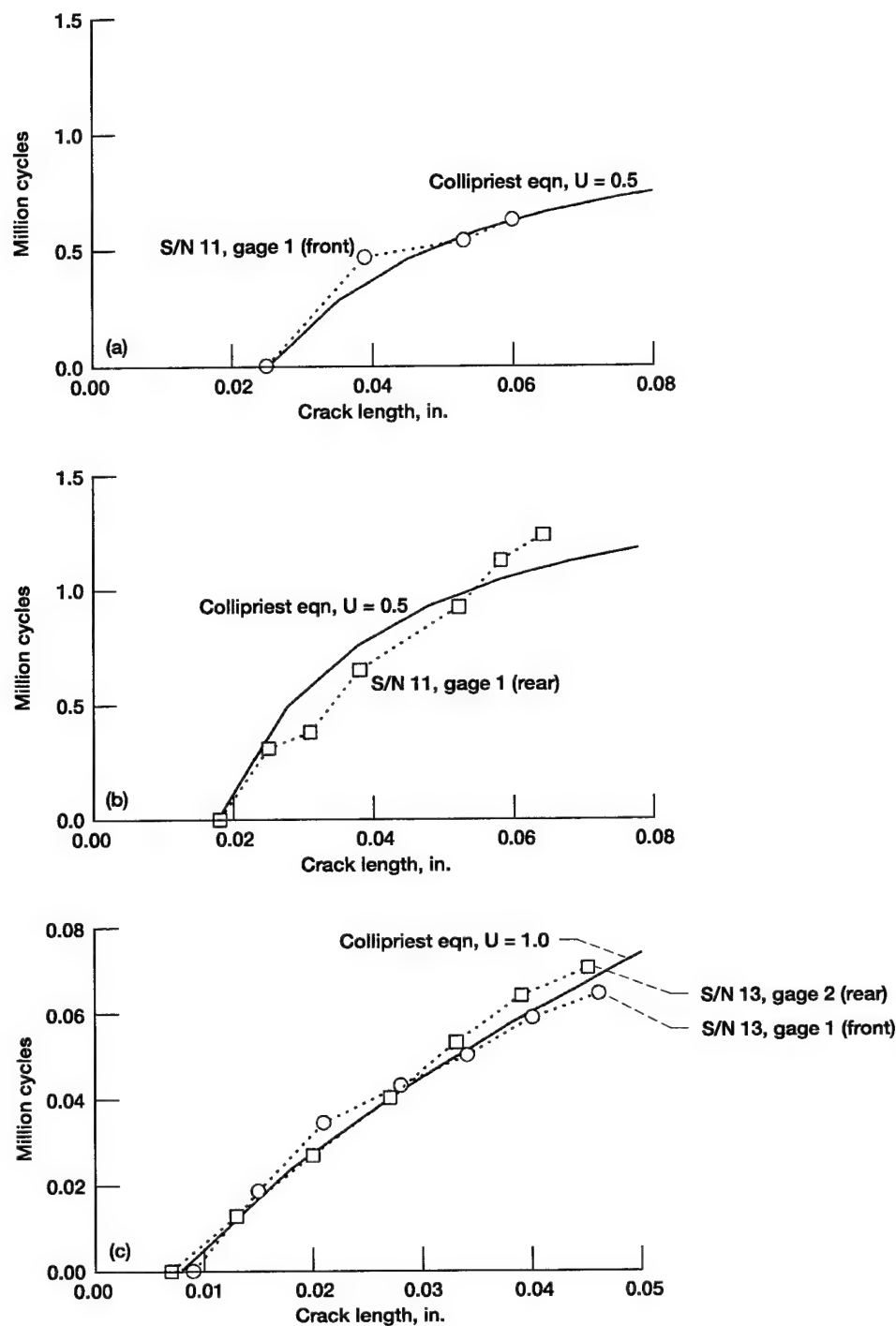


Figure 5.4.4.—Comparison of predicted crack propagation cycles to experiments using Collipriest fatigue crack growth model, $n = 1.63$, $C = 8.36 \times 10^{-9} \text{ in./cyc}/(\text{ksi in.})^n$, $\Delta K_{th} = 3.5 \text{ ksi in.}$, $K_{IC} = 200 \text{ ksi in.}$ (a) Test 9, S/N 11, gage 1 (front flank), $R = -2.6$, $U = 0.5$. (b) Test 9, S/N 11, gage 2 (rear flank), $R = -2.6$, $U = 0.5$. (c) Test 11, S/N 13, gages 1 and 2 (front and rear flanks), $R = -0.1$, $U = 1.0$.

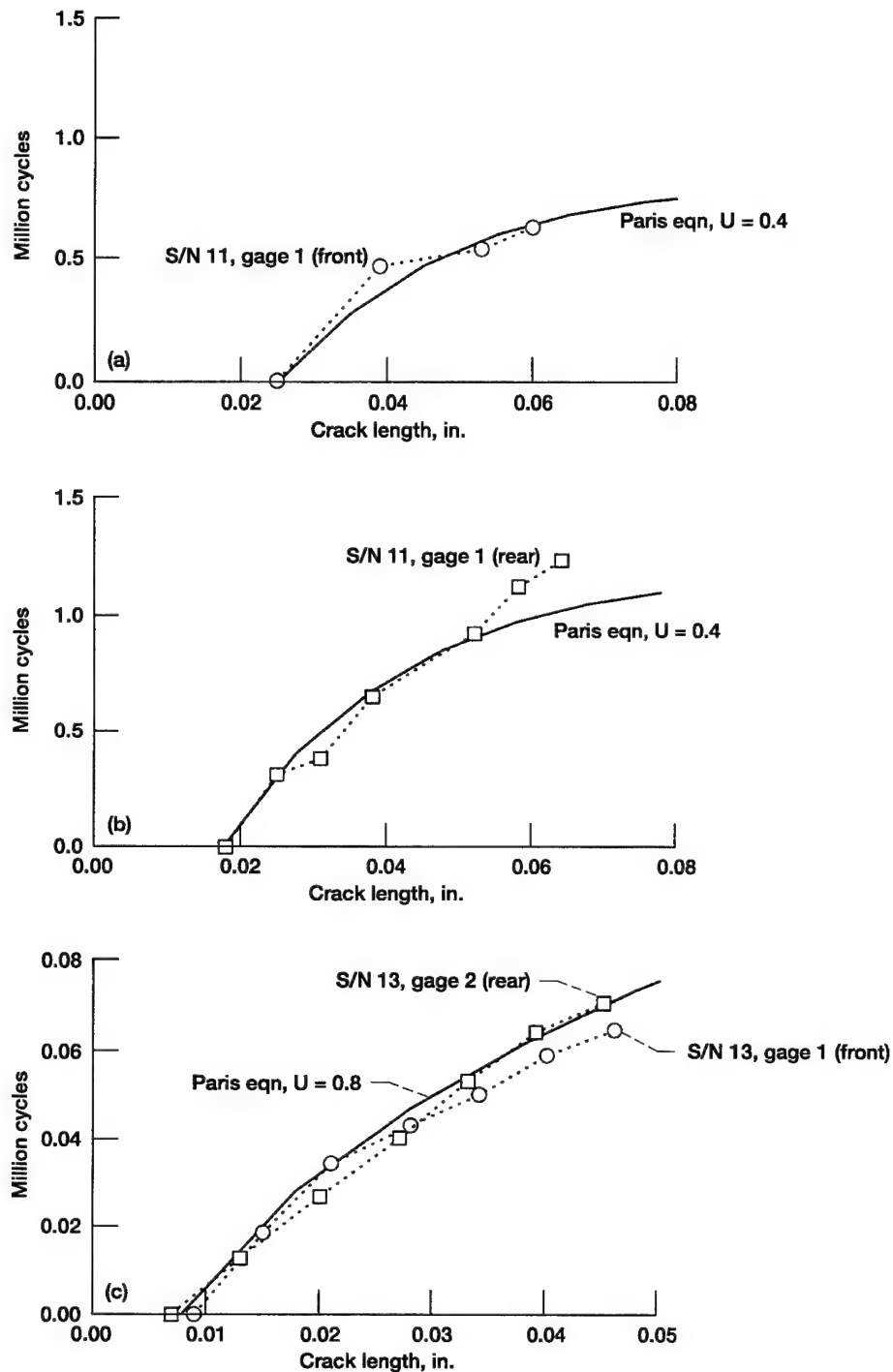


Figure 5.4.5.—Comparison of predicted crack propagation cycles to experiments using Paris fatigue crack growth model, $n = 2.954$, $C = 6.027 \times 10^{-19}$ in./cyc/(psi in.)ⁿ. (a) Test 9, S/N 11, gage 1 (front flank), $R = -2.6$, $U = 0.4$. (b) Test 9, S/N 11, gage 2 (rear flank), $R = -2.6$, $U = 0.4$. (c) Test 11, S/N 13, gage 1 and 2 (front and rear flanks), $R = -0.1$, $U = 0.8$.

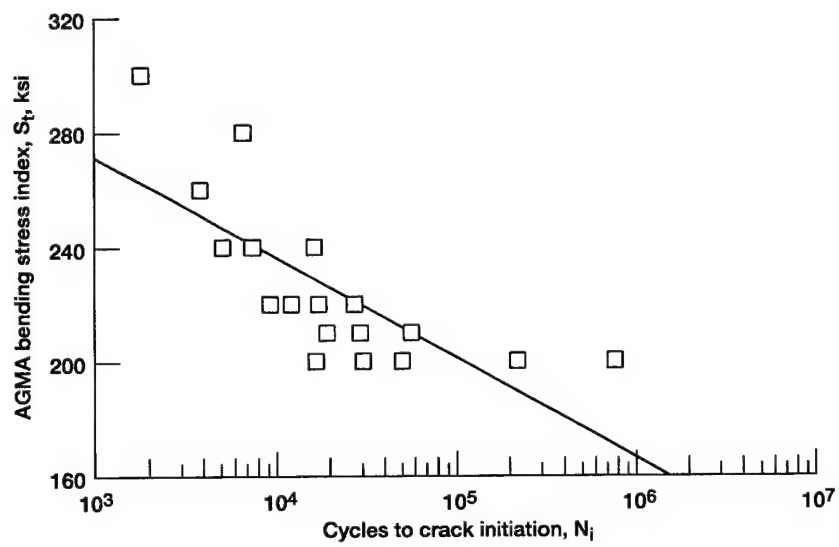


Figure 5.5.1.—Crack initiation life test results from single tooth bending tests for AISI 9310 material (Heath and Bossler, 1993).

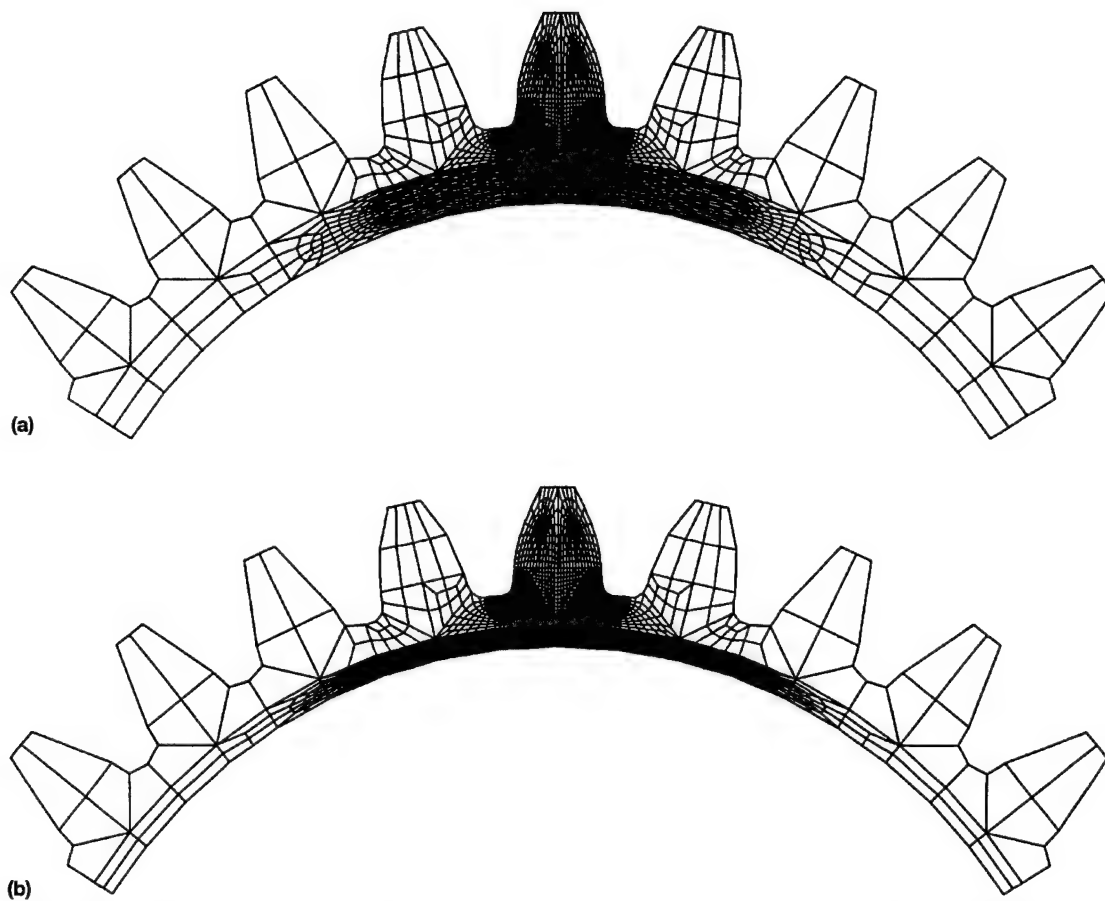


Figure 6.2.1.—Sample finite element mesh for use in analytical parametric studies; $P_d = 8$ teeth/in., $\phi = 20^\circ$, $N_g = 28$ teeth, $r_p = 1.75$ in. (a) Run 1, $m_B = 0.7$. (b) Run 2, $m_B = 0.5$.

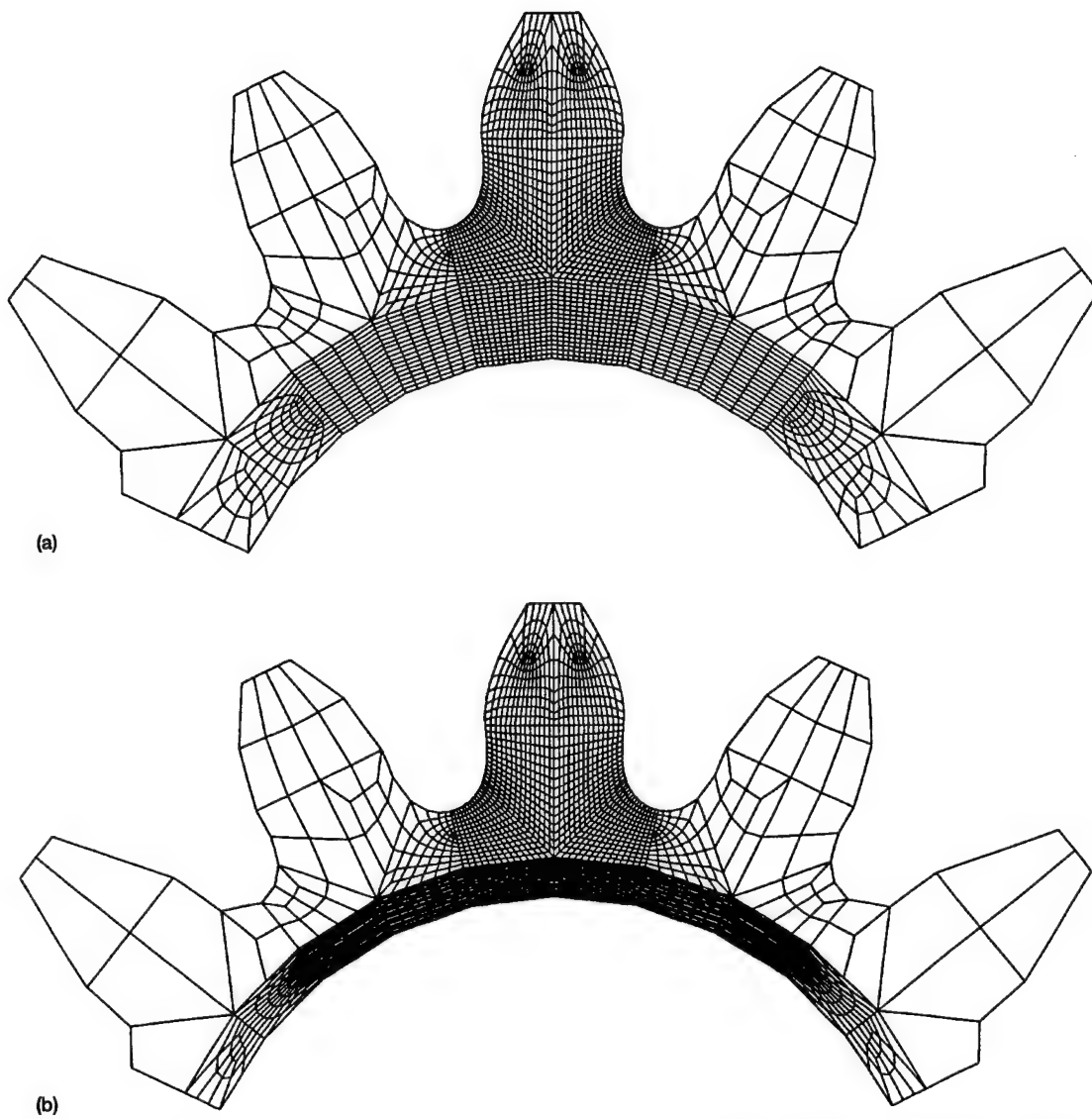


Figure 6.3.1.—Finite element mesh for runs 3 and 4 used in analytical parametric studies; $P_d = 4$ teeth/in., $\phi = 20^\circ$, $N_g = 14$ teeth, $r_p = 1.75$ in. (a) Run 3, $m_B = 0.7$. (b) Run 4, $m_B = 0.5$.

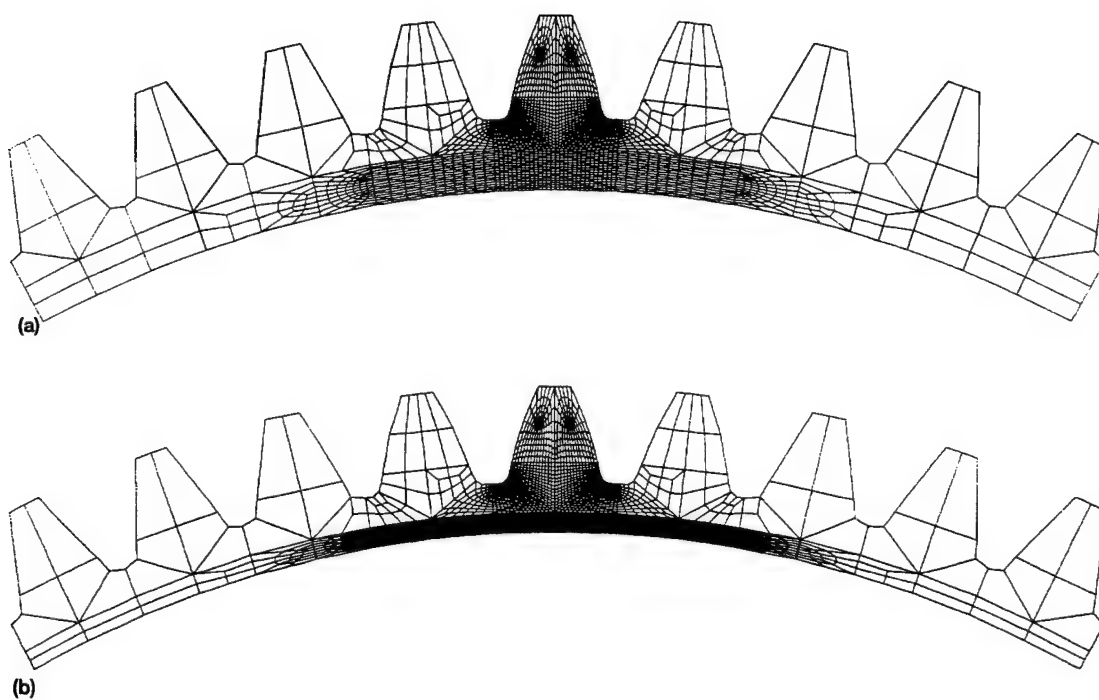


Figure 6.3.2.—Finite element mesh for runs 5 and 6 used in analytical parametric studies; $P_d = 16$ teeth/in., $\phi = 20^\circ$, $N_g = 56$ teeth, $r_p = 1.75$ in. (a) Run 5, $m_B = 0.7$. (b) Run 6, $m_B = 0.5$.

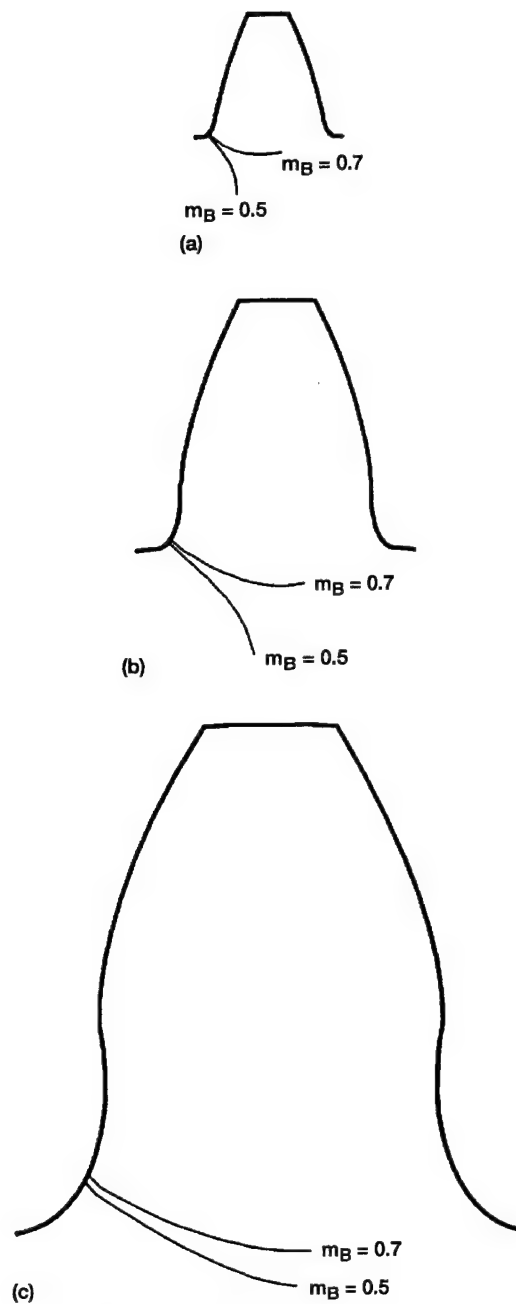


Figure 6.3.3.—Effect of gear tooth diametral pitch on crack propagation path; $\phi = 20^\circ$, $r_p = 1.75$ in. (a) Runs 5 and 6, $P_d = 16$ teeth/in., $N_g = 56$ teeth. (b) Runs 1 and 2, $P_d = 8$ teeth/in., $N_g = 28$ teeth. (c) Runs 3 and 4, $P_d = 4$ teeth/in., $N_g = 14$ teeth.

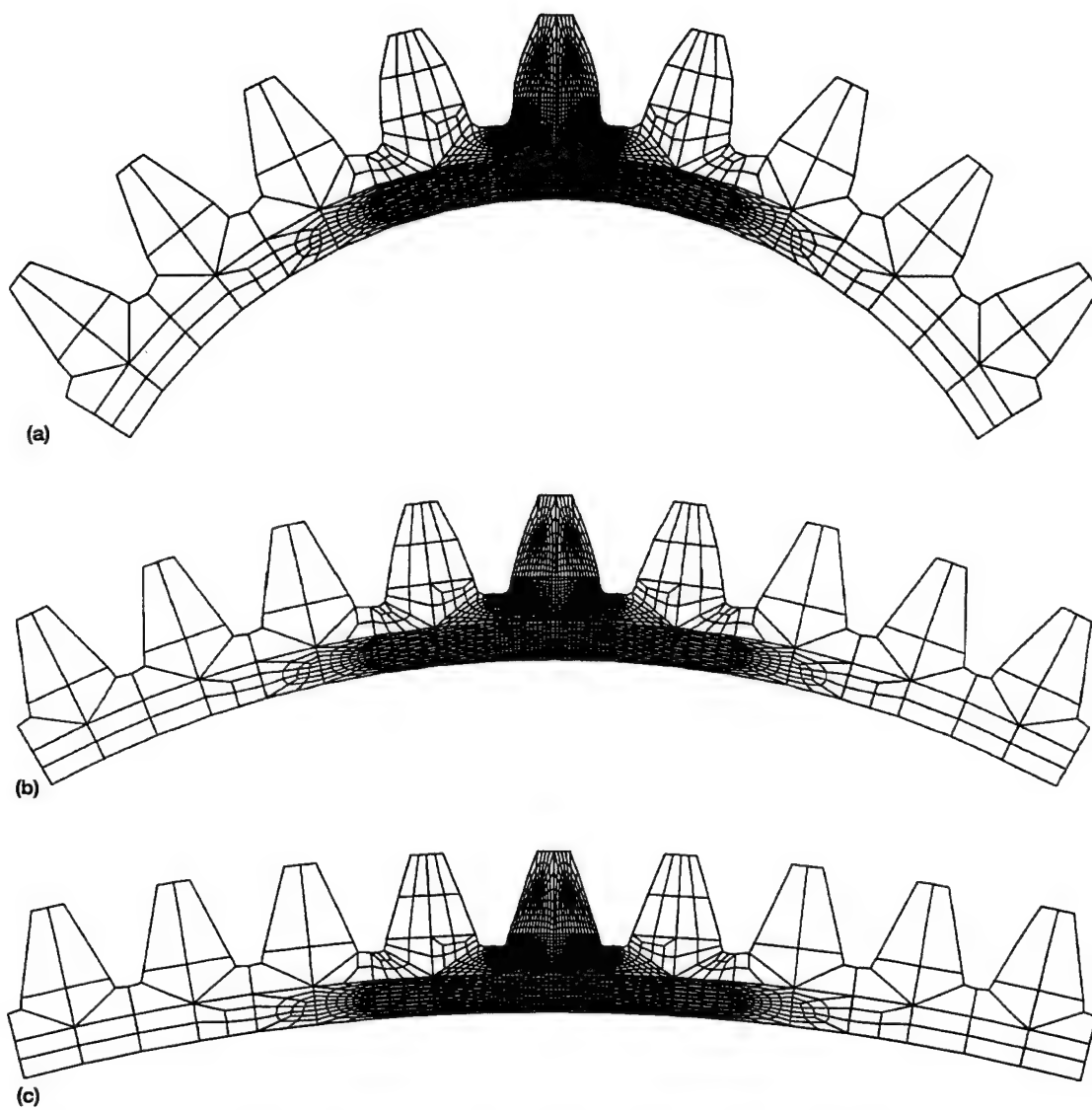


Figure 6.3.4.—Finite element mesh for runs 1, 7, and 9 used in analytical parametric studies; $m_B = 0.7$, $P_d = 8$ teeth/in., $\phi = 20^\circ$. (a) Run 1, $N_g = 28$ teeth, $r_p = 1.75$ in. (b) Run 7, $N_g = 56$ teeth, $r_p = 3.50$ in. (c) Run 9, $N_g = 112$ teeth, $r_p = 7.00$ in.

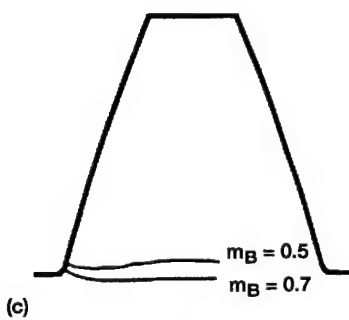
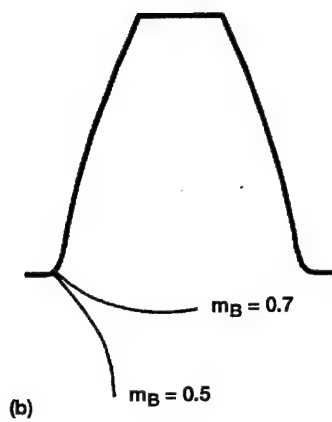
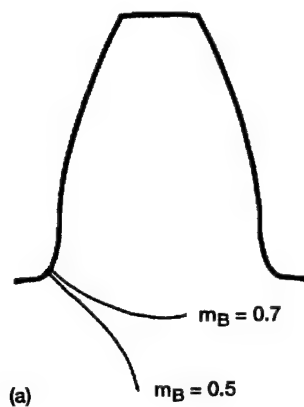


Figure 6.3.5.—Effect of gear pitch radius on crack propagation path; $P_d = 8$ teeth/in., $\phi = 20^\circ$. (a) Runs 1 and 2, $N_g = 28$ teeth, $r_p = 1.75$ in. (b) Runs 7 and 8, $N_g = 56$ teeth, $r_p = 3.50$ in. (c) Runs 9 and 10, $N_g = 112$ teeth, $r_p = 7.00$ in.

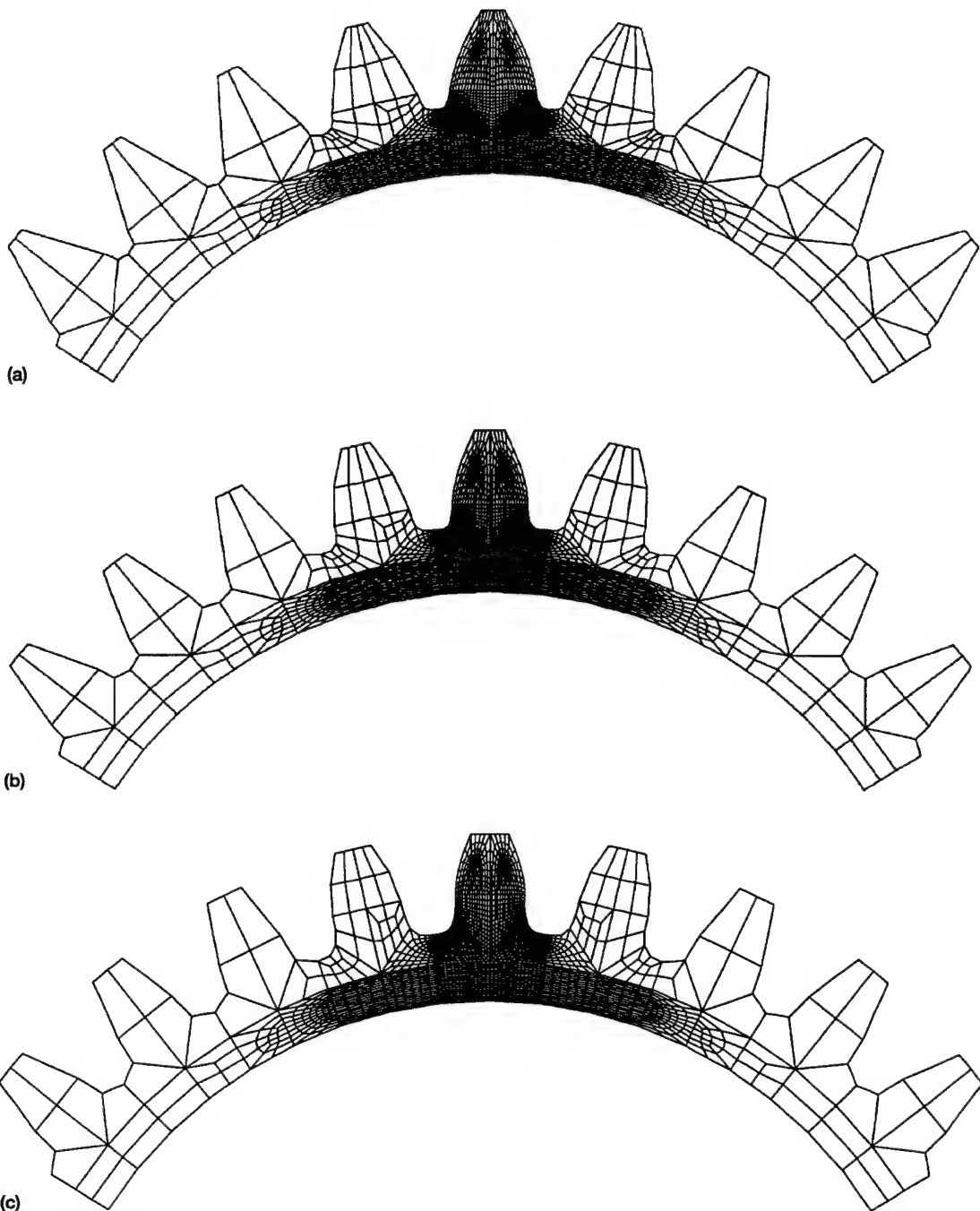


Figure 6.3.6.—Finite element mesh for runs 1, 11, and 13 used in analytical parametric studies; $m_B = 0.7$, $P_d = 8$ teeth/in., $N_g = 28$ teeth, $r_p = 1.75$ in. (a) Run 11, $\phi = 25^\circ$. (b) Run 1, $\phi = 20^\circ$. (c) Run 13, $\phi = 14.5^\circ$.

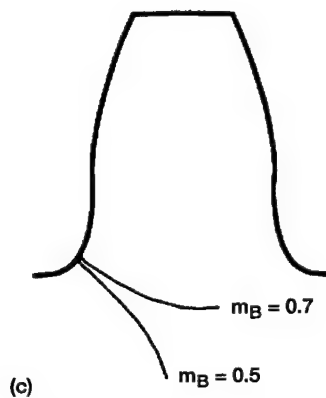
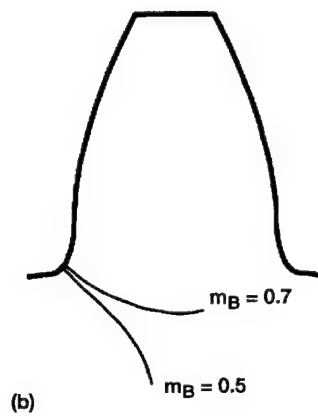
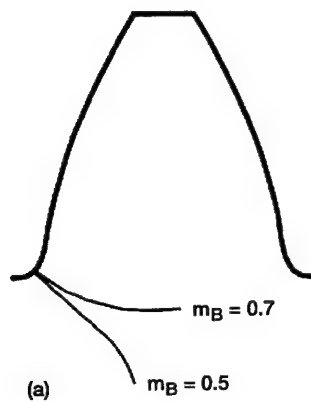


Figure 6.3.7.—Effect of gear tooth pressure angle on crack propagation path; $P_d = 8$ teeth/in., $N_g = 28$ teeth, $r_p = 1.75$ in. (a) Runs 11 and 12, $\phi = 25^\circ$. (b) Runs 1 and 2, $\phi = 20^\circ$. (c) Runs 13 and 14, $\phi = 14.5^\circ$.

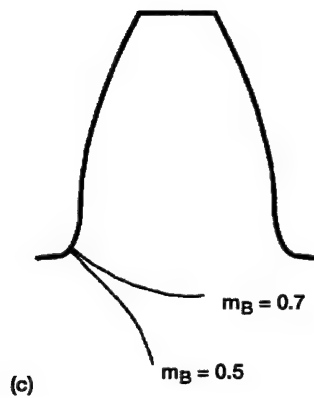
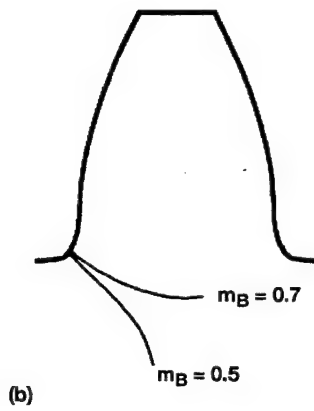
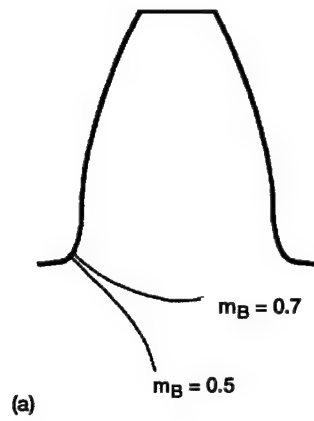


Figure 6.3.8.—Effect of gear reduction ratio on crack propagation path; $P_d = 8$ teeth/in., $\phi = 20^\circ$, $N_{g,1} = 28$ teeth, $r_{p,1} = 1.75$ in.
 (a) Runs 1 and 2, 1:1 reduction ratio.
 (b) Runs 15 and 16, 2:1 reduction ratio.
 (c) Runs 17 and 18, 4:1 reduction ratio.

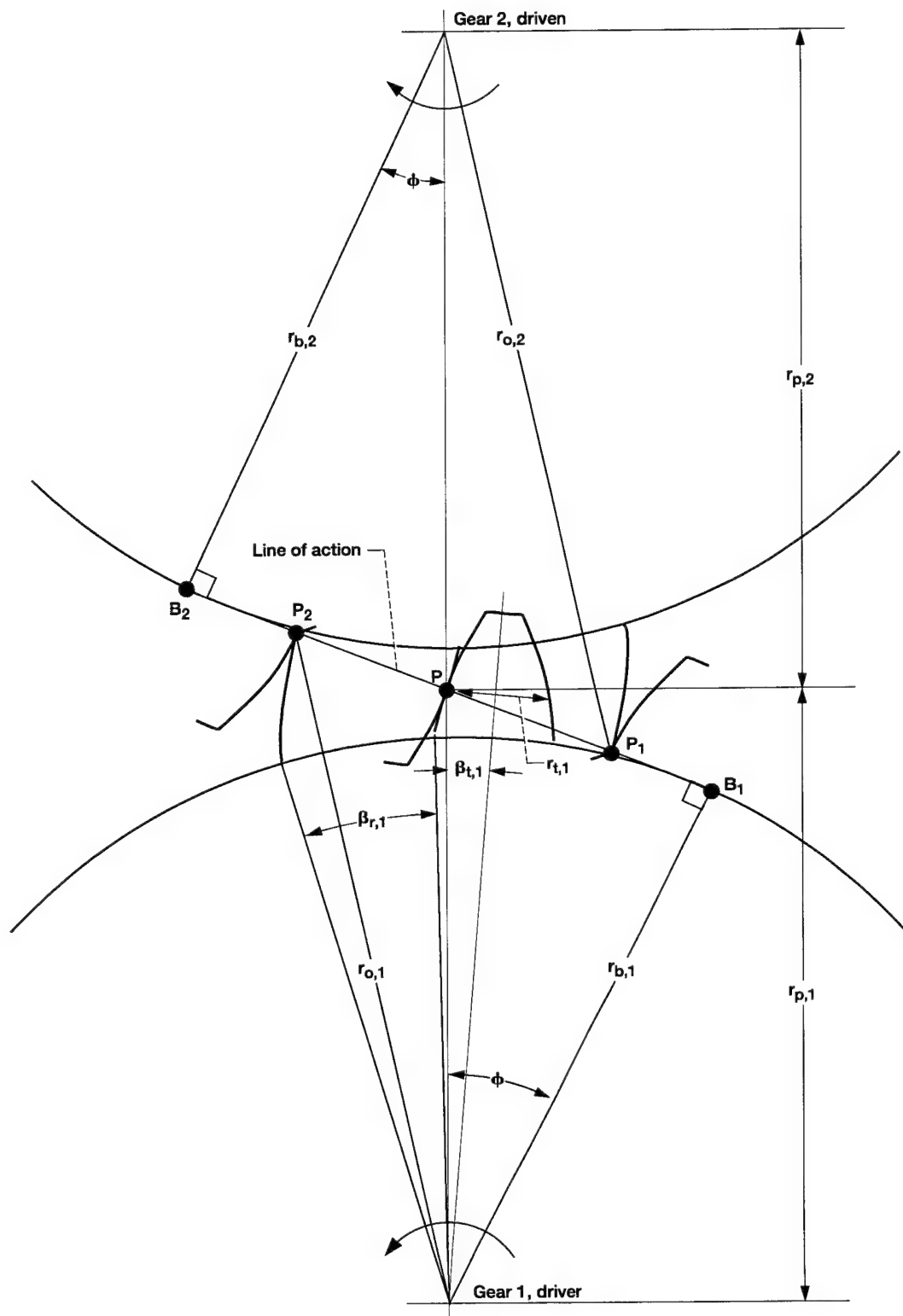


Figure B.1.—Gear nomenclature for load vector orientation analysis.

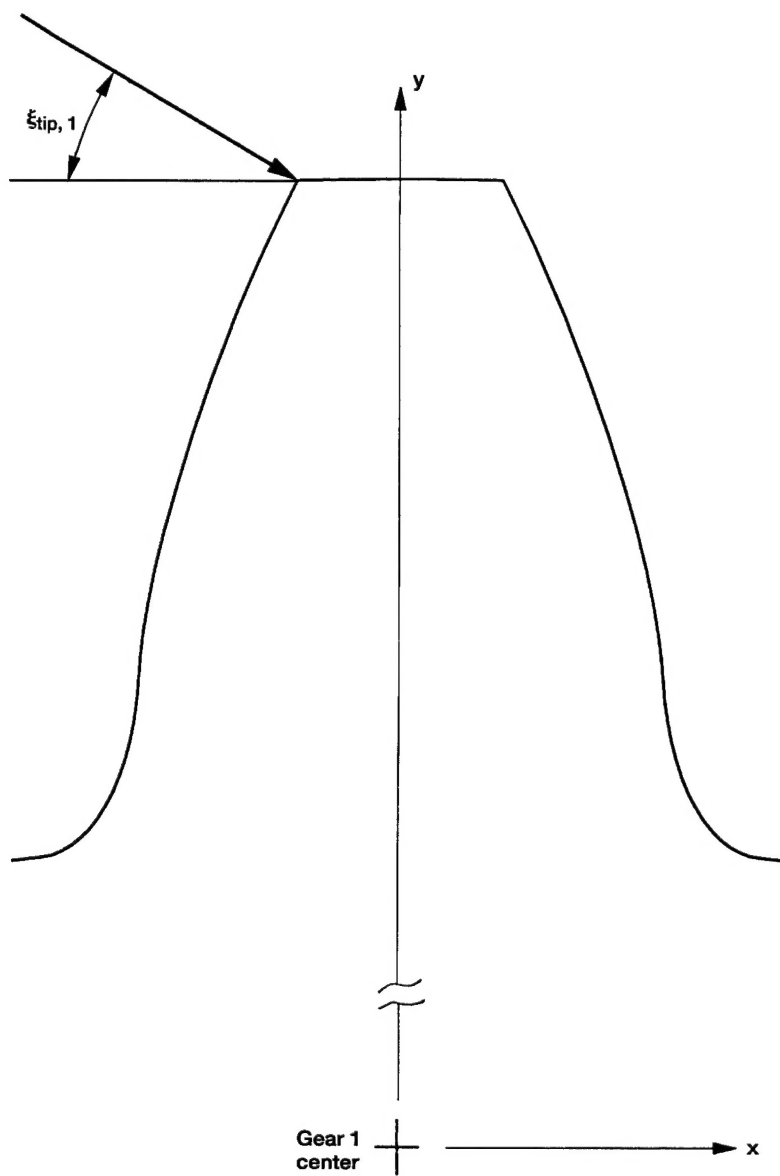


Figure B.2.—Gear tooth load angle orientation.

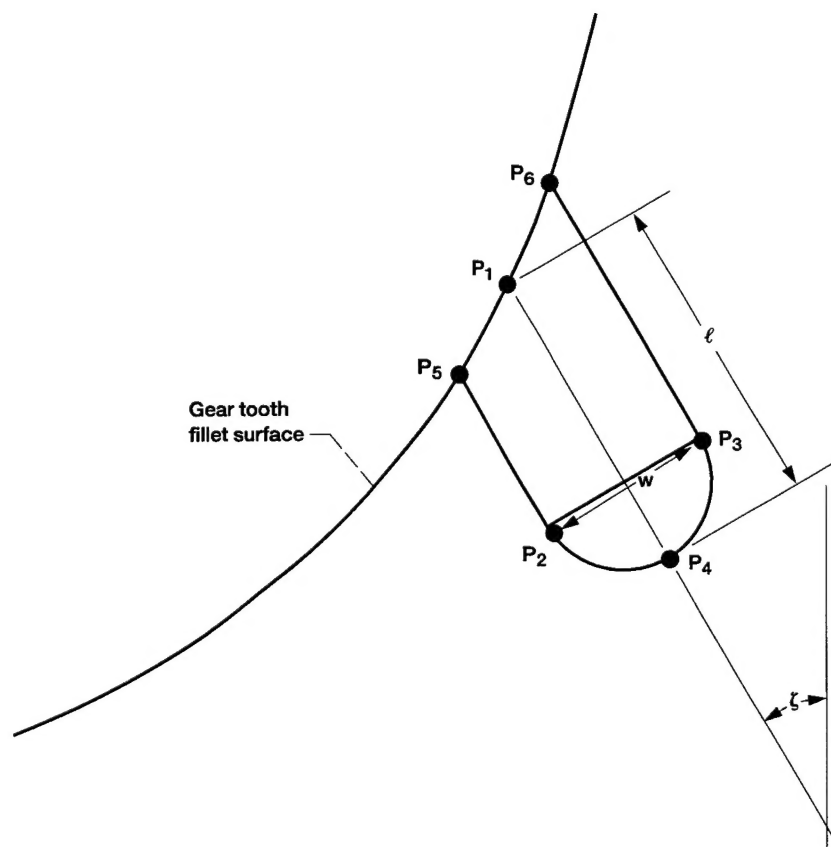


Figure C.1.—Development of notch surface in gear finite element model.

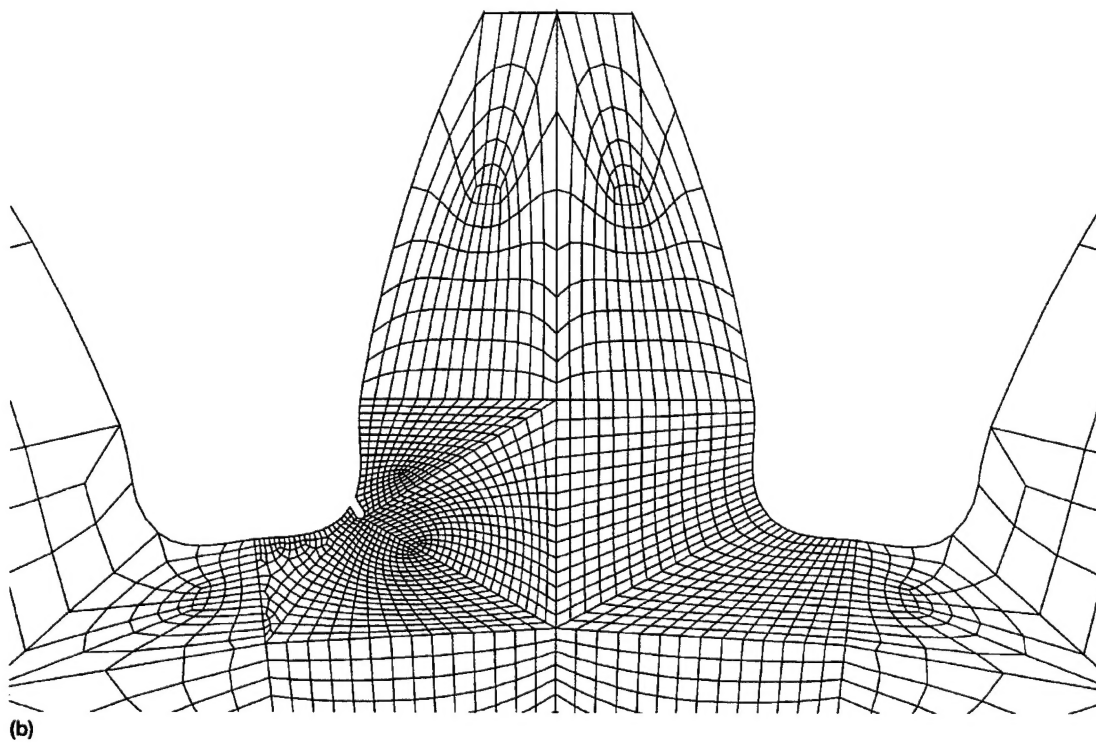
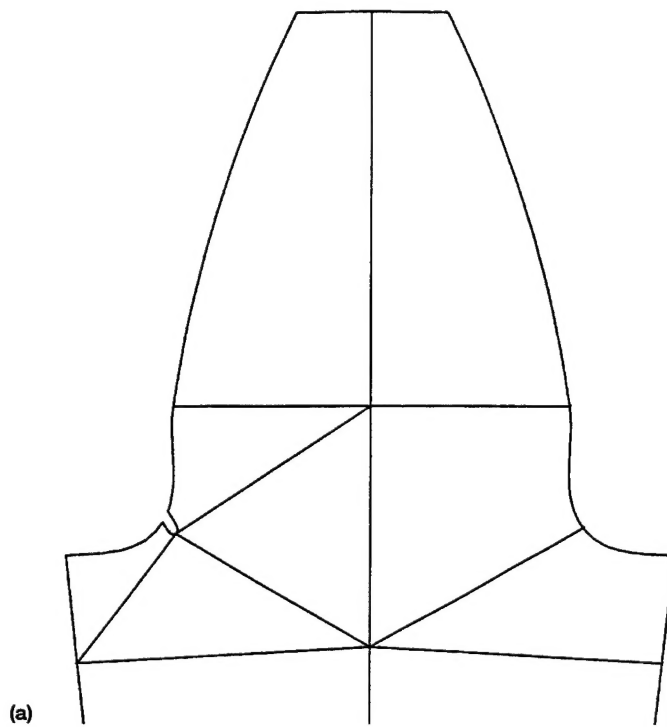


Figure C.2.—Finite element model of gear with notch. (a) Single-tooth sector of P3/PATRAN patches for gear tooth with notch. (b) Finite elements of gear tooth with notch.

REPORT DOCUMENTATION PAGE			Form Approved OMB No. 0704-0188	
Public reporting burden for this collection of information is estimated to average 1 hour per response, including the time for reviewing instructions, searching existing data sources, gathering and maintaining the data needed, and completing and reviewing the collection of information. Send comments regarding this burden estimate or any other aspect of this collection of information, including suggestions for reducing this burden, to Washington Headquarters Services, Directorate for Information Operations and Reports, 1215 Jefferson Davis Highway, Suite 1204, Arlington, VA 22202-4302, and to the Office of Management and Budget, Paperwork Reduction Project (0704-0188), Washington, DC 20503.				
1. AGENCY USE ONLY (Leave blank)		2. REPORT DATE May 1996		3. REPORT TYPE AND DATES COVERED Technical Memorandum
4. TITLE AND SUBTITLE Crack Propagation Studies to Determine Benign or Catastrophic Failure Modes for Aerospace Thin-Rim Gears			5. FUNDING NUMBERS WU-505-62-36 1L162211A47A	
6. AUTHOR(S) David G. Lewicki				
7. PERFORMING ORGANIZATION NAME(S) AND ADDRESS(ES) NASA Lewis Research Center Cleveland, Ohio 44135-3191 and Vehicle Propulsion Directorate U.S. Army Research Laboratory Cleveland, Ohio 44135-3191			8. PERFORMING ORGANIZATION REPORT NUMBER E-9274	
9. SPONSORING/MONITORING AGENCY NAME(S) AND ADDRESS(ES) National Aeronautics and Space Administration Washington, D.C. 20546-0001 and U.S. Army Research Laboratory Adelphi, Maryland 20783-1145			10. SPONSORING/MONITORING AGENCY REPORT NUMBER NASA TM-107170 ARL-TR-971	
11. SUPPLEMENTARY NOTES This report was submitted as a dissertation in partial fulfillment of the requirements for the degree Doctor of Philosophy to Case Western Reserve University, Cleveland, Ohio, May 1995. Responsible person, David G. Lewicki, organization code 2730, (216) 433-3970.				
12a. DISTRIBUTION/AVAILABILITY STATEMENT Unclassified - Unlimited Subject Category 37 This publication is available from the NASA Center for Aerospace Information, (301) 621-0390.			12b. DISTRIBUTION CODE	
13. ABSTRACT (Maximum 200 words) Analytical and experimental studies were performed to investigate the effect of rim thickness on gear tooth crack propagation. The goal was to determine whether cracks grew through gear teeth (benign failure mode) or through gear rims (catastrophic failure mode) for various rim thicknesses. Gear tooth crack propagation was simulated using a finite element based computer program. Principles of linear elastic fracture mechanics were used. Quarter-point, triangular elements were used at the crack tip to represent the stress singularity. Crack tip stress intensity factors were estimated and used to determine crack propagation direction and fatigue crack growth rate. The computer program used had an automated crack propagation option in which cracks were grown numerically using an automated re-meshing scheme. In addition, experimental studies were performed in the NASA Lewis Spur Gear Fatigue Rig. Gears with various backup ratios were tested to validate crack path predictions. Also, specialized crack propagation gages were installed on the test gears to measure gear tooth crack growth rate. From both predictions and tests, gears with backup ratios (rim thickness divided by tooth height) of 3.3 and 1.0 produced tooth fractures while a backup ratio of 0.3 produced rim fractures. For a backup ratio of 0.5, the experiments produced rim fractures and the predictions produced both rim and tooth fractures, depending on the initial crack conditions. Good correlation between the predicted number of crack propagation cycles and measured number of cycles was achieved using both the Paris fatigue crack growth method and the Collipriest crack growth equation when fatigue crack closure was considered.				
14. SUBJECT TERMS Gears; Fracture mechanics; Crack propagation			15. NUMBER OF PAGES 178	
			16. PRICE CODE A09	
17. SECURITY CLASSIFICATION OF REPORT Unclassified	18. SECURITY CLASSIFICATION OF THIS PAGE Unclassified	19. SECURITY CLASSIFICATION OF ABSTRACT Unclassified	20. LIMITATION OF ABSTRACT	